The circumstellar environment of massive young stellar objects - a multi-scale analysis

Abigail Junice Frost

School of Physics and Astronomy

University of Leeds

This dissertation is submitted for the degree of

Doctor of Philosophy

September 2019

"To do things right, first you need love, then technique."

Antonio Gaudí

Declaration

I confirm that the work submitted is my own and that appropriate credit has been given where reference has been made to the work of others.

This copy has been supplied on the understanding that it is copyright material and that no quotation from the thesis may be published without proper acknowledgement.

The right of Abigail Junice Frost to be identified as Author of this work has been asserted by Abigail Junice Frost in accordance with the Copyright, Designs and Patents Act 1988.

The modelling presented in this thesis was undertaken using ARC3, part of the High Performance Computing facilities at the University of Leeds, UK.

The MIDI data used in Chapters 2, 3 and 4 were previously published in Boley et al. [2013] and reduced by them following the procedure detailed in Chapter 2. One configuration of MIDI data was additionally incorporated for the study of NGC 2264 IRS1 and was reduced and previously published by Grellmann et al. [2011]. The VISIR data presented in Chapter 3, 4 and Appendix A were reduced by myself with the use of ESO data reduction pipelines. The COMICS profile in Chapter 2 was electronically lifted from Wheelwright et al. [2012] and the COMICS data presented in Chapter 4 were reduced by Willem-Jan de Wit and had previously been published in de Wit et al. [2009].

The work presented in Chapter 3 was published in Astronomy and Astrophysics (Volume 625, Article Number A44, accepted 6 March 2019). The publication was titled 'A multi-scale exploration of a massive young stellar object - A transition disk

around G305.20+0.21?' and the co-authors were R. D. Oudmaijer, W-J de Wit and S. L. Lumsden. The MIDI data for this publication were from Boley et al. [2013] (as previously stated). The VISIR data reduction, the analysis and initial drafting of the manuscript were all done by myself. W-J de Wit performed spot checks of the MIDI data reduction and provided comments on the manuscript. R.D. Oudmaijer contributed by providing feedback on the manuscript and discussions on the analysis. S.L. Lumsden provided feedback comments for the final version of the manuscript before submission.

Abigail Junice Frost

September 2019

Acknowledgements

First and foremost, I must thank my family. Thank you all so much for helping me over the years and to Grandma and Grandpa for all their assistance throughout my education. I wouldn't be here without any of you, thank you for your continued love, support and everything.

Secondly, I have to say that I would not have gotten through the tough moments of my PhD without my friends. Thank you to all my South Hampstead friends, 8 years since we left school and you're still being awesome! Cheers to the residents of the premier student abode 'Cornerstone' for being the best buds ever and for all the crazy times, even since we went our separate ways from Exeter. Now, to Leeds. I cannot state enough how much of an absolute pleasure it has been meeting, working with and having laughs with such a great group. I'm going to miss Leeds so much mostly because of you lovely lot, so thank you to every single person I've met in E C Stoner 9.64a and b over the past four years, you all made that happen. Thank you to Marc, Rob, Si, Iva, Nando, Karim, Harry, Ignacio, Miguel, Alice Peréz, Evgenia, Katharine, Marcin, Tonye and Jilee for all the extremely professional post-work discussions in the Fenton, generally being great fun and for being so welcoming when I first arrived. A special shout out needs to go to my MYSbrO Rob for convincing me to get more involved in the group and for providing me with sagely advice and lots of laughs from day 1. On the more professional side, thank you to Nando and Marc for listening to all my Python woes and to John for all the help with the job applications and viva prep. Thank you to Chumpon and

Evgenia for being the greatest observing buddies ever, I will always remember our time together at Paranal. Thank you to everyone who has helped me through my many ‘crises’ over these four years, including Katharine, John, James and Evgenia. A special mention needs to go to Alice Booth, for not only supplying endless fun times watching ‘sickening’ reality shows, wine, cheese and being a fantastic friend, but for also letting me live with you for the last month of my PhD. That is something I wouldn’t wish on anyone but thanks, it was a huge help. Lastly, the largest thank you needs to go to James Miley. You have probably (if we’re honest) dealt with the brunt of my PhD related angst whilst simultaneously providing me with some of my happiest times in Leeds. Thank you so much for your never-ending support, patience, kindness, thoughtfulness and for just generally being golden.

Last and certainly not least, I need to extend huge thanks to my supervisors and assessors. To Melvin and Steve, thank you for turning my viva from something I’d been dreading into something I enjoyed. Thank you to my unofficial supervisor, Willem-Jan, for your nuggets of wisdom, the great work visits and all the help you gave me despite your busy schedule. Thank you to Stuart for all your assistance with the final chapter of my thesis and for being open and supportive from the PhD interview stage. And finally, a huge thank you to René. Through all the ups and downs of the past four years you always made the time to chat to me and help me out and even at the latest most stressful stages of my PhD we’ve been able to have some good laughs. Without yourself and Stuart I wouldn’t have been able to spend these four fantastic years in Leeds, make all the aforementioned friends, visit so many amazing places, learn so much and make it to the end of my PhD. Thanks for taking a chance on me and asking me to join the department, I am so very grateful.

Abbreviations

2MASS	Two Micron All-Sky Survey
ALMA	Atacama Large Millimetre Array
AMBER	Astronomical Multi-BEam combineR
APEX	Atacama Pathfinder EXperiment
AT	Auxiliary Telescope
ATCA	Australia Telescope Compact Array
ATLASGAL	APEX Telescope Large Area Survey of the Galaxy
CIAO	Coronagraphic Imager with Adaptive Optics
COMICS	The Cooled Mid-Infrared Camera and Spectrometer
D1 SH	Disk 1 scale height
D2 SH	Disk 2 scale height
ESO	European Southern Observatory
EUV	Extreme UltraViolet
FCRAO	Five College Radio Astronomy Observatory
FFT	Fast Fourier Transform
FORCAST	Faint Object infraRed CAmera for the SOFIA Telescope
FUV	Far-UltraViolet
FWHM	Full width at half maximum
GLIMPSE	Galactic Legacy Infrared Midplane Survey Extraordinaire
GMC	Giant Molecular Cloud
HCHII	Hyper-Compact HII (region)
HMC	Hot Molecular Core
IR	InfraRed
IRAC	Infrared Array Camera on the Spitzer Space Telescope
IRAS	Infrared Astronomical Satellite
IRDC	InfraRed Dark Cloud
IRS	InfraRed Spectrograph on the Spitzer Space Telescope
IRTF	Infrared Telescope Facility
ISAAC	Infrared Spectrometer And Array Camera
ISOCAM	Infrared Space Observatory Camera
ISO LWS	Infrared Space Observatory Long Wavelength Spectrometer
ISO SWS	Infrared Space Observatory Short Wavelength Spectrometer
JWST	James Webb Space Telescope
KAO	Kuiper Airborne Observatory

MATISSE	Multi AperTure mid-Infrared SpectroScopic Experiment
MIDI	MID-infrared Interferometric instrument
MIR	Mid-InfraRed
MRT	Mauritius Radio Telescope
MSX	Midcourse Space Experiment
MYSO	Massive Young Stellar Object
NICMOS	Near Infrared Camera and Multi-Object Spectrometer
NIR	Near InfraRed
NIRS	Near InfraRed Source
OPD	Optical Path Difference
PA	Position Angle
PAHS	PolyAromatic Hydrocarbons
PANIC	Persson's Auxilliary Nasmyth Infrared Camera
PIONIER	Precision Integrated-Optics Near-infrared Imaging ExpeRiment
PNe	Planetary Nebulae
PWV	Precipitable Water Vapour
RMS	Red MSX Source (survey)
RT	Radiative Transfer
SCUBA	Submillimetre Common-User Bolometer Array
SED	Spectral Energy Distribution
SEST	Swedish-ESO Submillimetre Telescope
SFR	Star Formation Rate
SHARC	Shane Adaptive optics infraRed Camera-Spectrograph
SMA	Submillimeter Array
SOFIA	Stratospheric Observatory for Infrared Astronomy
SNe	SuperNovae
TSC	Terebey, Shu and Cassen model
UCHII	Ultra-Compact HII (region)
UKIDSS	UKIRT Infrared Deep Sky Survey
UKIRT	United Kingdom Infrared Telescope
UT	Unit Telescope
UV	UltraViolet
VISIR	VLT Imager and Spectrometer in the InfraRed
VLTI	Very Large Telescope and Interferometer
VSGs	Very Small Grains
VISTA	Visible and Infrared Survey Telescope for Astronomy
VVV	VISTA Variables in The Via Lactea (public survey)
WISE	Wide-field Infrared Survey Explorer
YSO	Young Stellar Object
ZAMS	Zero Age Main Sequence
ZOPD	Zero Optical Path Difference

Abstract

The rarity of young massive stars combined with the fact that they are often deeply embedded has limited the understanding of the formation of stars larger than $8M_{\odot}$. Ground based mid-infrared (IR) interferometry is one way of securing the spatial resolution required to probe the circumstellar environments of massive young stellar objects (MYSOs). Given that the spatial-frequency coverage of such observations is often incomplete, direct-imaging can be supplementary to such a dataset. By consolidating these observations with modelling, the features of a massive protostellar environment can be constrained. By specifically choosing observations which probe different scales of the MYSO environments, their characteristics can be investigated at multiple scales and information on different aspects of the massive star formation process can be obtained. By repeating this analysis for a sample of objects, a reliable set of parameters are obtained for each MYSO. Since the objects have been analysed in the same manner, a consistent comparison between the derived characteristics of the sources can then be made.

This thesis performs the above through the combination of N-band interferometry at $\sim$0.01" resolution, near-diffraction-limited Q-band imaging at $\sim$0.1" resolution and spectral energy distributions. These observations are consolidated by fitting 3D radiative transfer models to all three observables simultaneously. Such an involved methodology constitutes a number of improvements on previous infrared studies of MYSOs, through the use of greatly detailed models and the combined use of different observing techniques, which each provide a unique perspective

on the studied protostellar environments. Specifically, the combination of N-band interferometry and Q-band imaging allows a distinction to be made between the disk and cavity emission of the sources. The Q-band data traces cavity emission at larger scales, whereas the hotter regions are traced by the N-band. With this additional constraint, the N-band data has proven to be an excellent tracer of disk geometry. In particular, the inner rim, flaring and dust content of the disks can have large effects on simulated N-band visibilities. The sensitivity of the N-band interferometric data to the inner rim emission allowed the detection of an inner hole within the disk of the source G305.20+0.21, the pilot object of this study. This could not be rectified by changing the luminosity of the source to move the sublimation radius, the default minimum dust radius, indicating that some other mechanism is responsible for the disruption of the dust in the inner regions of the circumstellar environment. The SED fit for this source also required low densities, implying dispersal of the protostellar environment. These are typical characteristics of evolved transition disks found during the low-mass star formation and the possibilities of this applying to an MYSO are discussed.

When the method was applied to a sample of eight sources, it was discovered that G305 was not alone in its requirement to have a disk in its model. Every MYSO studied required a disk as a model component, and a number of sources within the sample also required inner holes in their environments in addition to G305. Overall, these holes ranged in size between 20-125au across. While diversity exists within the sample, with different cavity opening angles, densities etc., the overall geometry of the sources is the same; an Ulrich-type envelope, bipolar outflow cavities and a dust disk. The fits to the interferometric data of one source could be improved by a gap structure, which is a feature now commonly observed in Herbig Ae/Be disks.

The physical parameters determined through this work were linked to a potential evolutionary sequence through comparison to work done by Cooper [2013]. Cooper [2013] classified just under 200 MYSOs into three different types based on emission

lines in their spectra with each type representing a different evolutionary stage of the MYSO. All the sources classified as the oldest type within Cooper [2013] have substructure in their disks. This is in agreement with low-mass stellar evolution which sees substructure develop at later stages, and therefore has implications for the evolution of massive protostars.

The nature of these massive protostellar environments, as determined by this thesis, show many similarities with various stages of low-mass star formation. Disks of order solar masses in size are components of all the final models for this sample of MYSOs. These disks extend from 10s of au to 1000s of au, and as such could be components of the accretion process, as they are for low-mass stars. The sample studied in this thesis increases the number of MYSOs studied at such a level of detail in the literature eight-fold. Five of the eight studied sources have inner dust rims larger than the sublimation radii expected of the host protostars in their models. Further study is required to directly investigate these holes and substructure found in this work and determine their cause. The application of this method to more sources can expand on these findings to the point where the formation and evolution mechanisms of massive young stars can be characterised in detail.

Table of contents

List of figures

List of tables

Chapter 1

Introduction

Massive stars, that is those more massive than $8M_{\odot}$, are important driving factors within the universe. Within their local environments, the winds, outflows and supernovae (SNe) of massive stars can both inhibit and trigger further stellar formation, replenishing and sustaining turbulence which in turn results in the compression and rarefaction of molecular clouds [Krumholz et al., 2014]. Massive stars generate photons with energies high enough to ionise hydrogen atoms within their surrounding medium, creating features unique to massive protostellar environments such as HII regions [Churchwell, 2002]. Massive stars are important for interstellar chemistry as they emit significant amounts of UV radiation that can drive photochemical reactions and also because they fuse lighter elements into heavier ones through the rapid nuclear process. Massive stellar winds and SNe then distribute this material throughout the interstellar medium, increasing its metallicity. Massive stars have further influence at galactic scales, as they produce the bulk of the observed integrated luminosities of spatially unresolved galaxies [Kennicutt, 2005]. SNe ejecta and massive stellar winds are also influential at these larger scales as they contribute to the galactic super-wind. Leitherer [1994] notes the effects of stars $\geq 50M_{\odot}$ on starburst galaxy outflows and Heckman et al. [1990] present optical spectroscopic

data which connects the characteristics of massive stellar winds to the geometry of galactic super-winds.

Despite their evident importance, the formation of massive stars is poorly understood. Massive stars become zero-age main sequence (ZAMS) stars before their natal clouds have collapsed or dispersed. This means that their entire formation process is obscured and massive protostars are deeply embedded. The formation timescales of massive stars are fast, approximately two orders of magnitude shorter than their lower-mass counterparts. Massive stars are also much less common than low-mass stars meaning that the distance to massive stars averages at a few kiloparsec (kpc). Massive stars are therefore difficult to observe, meaning that detailed surveys of these sources are lacking and high-resolution observations (tracing milli-arcsecond scales) are required to study the details of the few massive protostellar environments that are observable.

In this chapter, the background of star formation relevant to the study of the circumstellar environments of MYSOs is discussed, starting with the theory of star formation, followed by a discussion of the observable phases of massive star formation and finally the background of the observational and modelling techniques used to study MYSOs in the work of this thesis.

1.1 The theory of low-mass star formation

Most of the advances in the study of star formation have concerned low-mass stars that are comparable in mass to the Sun. Due to the observational limitations induced by the embedded nature, distance and rarity of massive stars, our understanding of massive star formation lags behind low-mass star formation. Massive star formation is often discussed in direct comparison with low-mass star formation as a result, and as such the theory of low-mass star formation is discussed first in this thesis.

All stars, no matter their size, form from the same materials - dust and gas. In order for this dust and gas to form a star, the material needs to be compressed from densities comparable to those found in molecular clouds ($\sim 10^{-20}$kgm^{-3}) to those found in stars ($\sim 10^{11}$kgm^{-3} for the core of the Sun). This collapse is a hierarchical process, focusing down to smaller scales through a cascade of substructure generation. Collapse will only begin if the mass of the structure exceeds the Jeans (or Bonner-Ebert) mass, which is the largest mass that an isothermal gas sphere can have while still being in hydrostatic equilibrium (e.g. Ward-Thompson and Whitworth [2015]). The Jeans mass, M_J, can be expressed as:

$$M_J = \left(\frac{3}{4\pi\rho}\right)^{\frac{1}{2}} \left(\frac{5k_BT}{G\mu m_p}\right)^{\frac{3}{2}} \tag{1.1}$$

where temperature is T, gravitational constant is G, mass is M, Boltzmann constant is k_B and proton mass is m_p. This can be written in the form of the equation of hydrostatic equilibrium of a sphere of gas (to which most clouds can be approximated) with a total mass M:

$$\frac{2k_BTM}{\mu m_p} = \int_0^M \frac{GM_r}{r} dM_r \tag{1.2}$$

which essentially describes the interplay between thermal energy (left) and gravitational energy (right).

Huge clouds of dust and gas found in the spiral arms of galaxies [Kolpak, 2003], or Giant Molecular clouds (GMCs), present the starting point of collapse. A GMC is defined as such if it contains greater than $10^5 M_\odot$ of H_2 [Solomon et al., 1980], which is the main constituent of molecular clouds [Carruthers, 1970]. Filaments, which can be defined as elongated structures in the ISM that are significantly more dense than their surrounding material [André et al., 2014], form following the collapse of GMCs. The collapse continues along the filaments in their densest regions leading to the formation of 'clumps' and 'cores'. The densest, largest clumps will serve

as the progenitors of stellar clusters, while individual stellar systems form within gravitationally bound cores [Williams et al., 2000].

When a prestellar core first becomes gravitationally unstable and collapses, its luminosity comes from the release of gravitational potential energy during the contraction, and it maintains more or less a constant temperature. After this isothermal collapse, the core is now centrally concentrated. At its centre, the core becomes opaque to its own radiation, stopping it from efficiently radiating energy away at the same rate at which energy is being generated from the gravitational contraction. This causes the core to heat up rapidly until it is close to hydrostatic equilibrium. Eventually the heating of the opaque hydrostatic core is sufficient to disassociate H_2 in the prestellar material. This process utilises energy that would otherwise be used to support the cloud against the effects of gravity, thereby allowing collapse to continue.

The resultant source of this second collapse is known as the 'protostar'. The protostar will be surrounded by material remaining from the wider prestellar core called the envelope. The protostar will accrete material from this surrounding envelope, allowing it to build mass. Two key components of this process are an accretion disk and outflows. The disk is thought to form from the surrounding envelope material due to angular momentum conservation. The envelope will not be static in space and will possess some amount of angular velocity. As the envelope decreases in size this angular velocity must increase to conserve angular momentum, as the system is not losing significant mass. As this increase in angular velocity occurs, material will be pushed out in the plane of rotation by the centrifugal force, creating a bulge-like structure around this plane from which the disk can form. Along the axis of rotation, infalling material has little angular momentum and infall proceeds relatively unhindered. This causes the molecular cloud to thin along the axis of rotation and causes an anisotropical distribution of the stellar radiation field. Material from the disk can then be accreted directly onto the central source through

processes such as magnetospheric accretion, whereby the field lines of the forming central protostar guide material from the disk onto the central object.

In tandem with accretion, ejection will occur as some of the material moving towards the star is removed from the system at high velocity. Blandford and Payne [1982] were among the first to suggest that a poloidal magnetic field from the accretion disk launches ionised material in its vicinity along the poles as a means of ejecting material. This leads to the formation of bipolar outflows [Machida, 2017] which then carve out cavities within the envelope material. The increased spin of both protostar and protostellar disk creates magnetic vortices, leading to strong magnetic fields along the polar axis which can collimate these outflows and produce jets. These jets may hit the surrounding interstellar medium or the remaining molecular cloud, leading to strong shock fronts or Herbig-Haro objects (HHs). Pudritz and Norman [1986] continued the work of Blandford and Payne [1982] and showed that the generation of these outflows provides an efficient way to remove angular momentum from accreting material. When the protostar has accreted most of its final mass through this accretion-ejection process it is known as a pre-main-sequence (PMS) star.

After a large amount of accretion has occurred, the PMS star ceases to be convective and radiative processes dominate the energy transfer in the object. Eventually the internal densities and temperatures will be so high that fusing hydrogen is now the main source of the object's luminosity. At this point, it stops contracting and reaches the main sequence.

Observationally, the various evolutionary stages of the protostar can be classified according to how the source's flux varies with frequency or wavelength. This is easily displayed in a spectral energy distribution (SED), and previous works have used the appearance of low-mass protostellar SEDs to classify them. Class 0 [Barsony, 1994] describes the protostellar core at the onset of collapse; the core is cold and emitting at far-IR to millimetre wavelengths only. Class I [Shu, 1977] describes the embedded

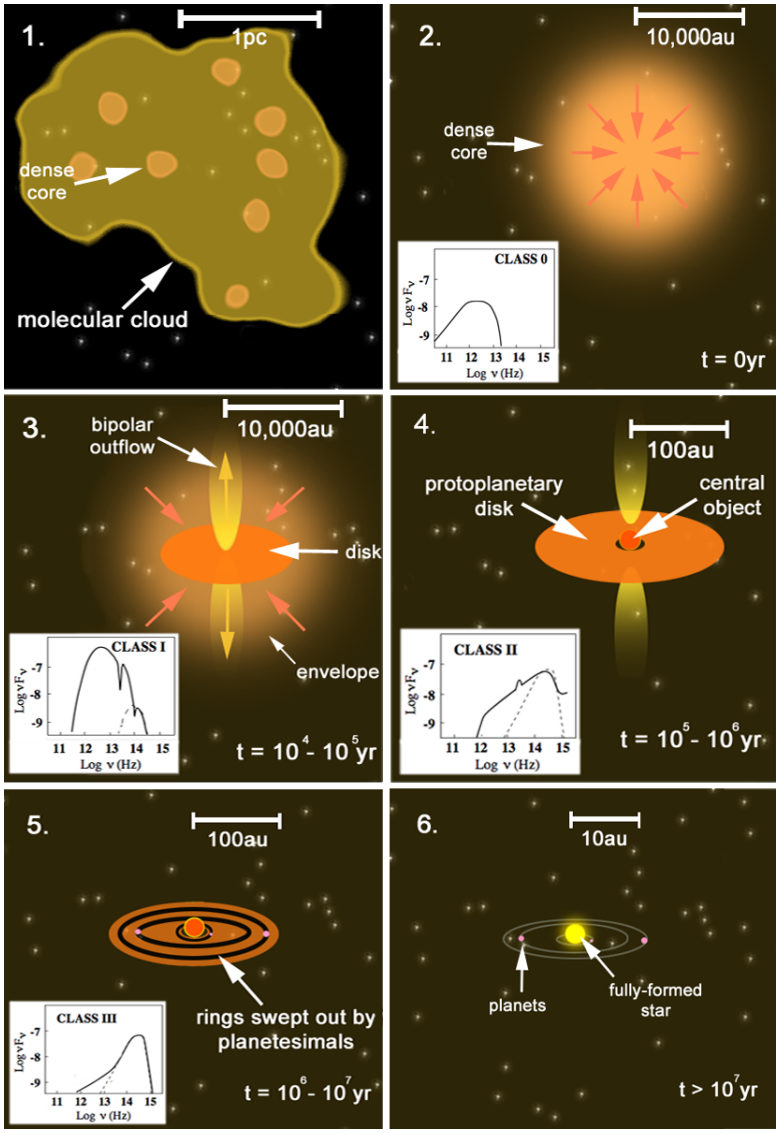

Fig. 1.1 A graphical overview of the various evolutionary stages of low-mass star formation with SEDs from Isella [2007]. Credit: A. J. Frost.

stage, where the envelope and central protostar are indistinguishable. The bulge like structure and outflows will form in the Class I stage, the infall and accretion processes will have led to an increase in the total flux, while the heating of the central material will lead to strong infrared emission. Class II [Shu, 1977] describes the accretion phase, where the so-called 'protoplanetary disk' is feeding material onto the star with less obstruction from the envelope, which has largely dissipated by this point. Due to the lack of envelope material, specific emission features associated

with the accretion process will be more easily observed at this stage. Class III [Shu, 1977] describes the final disk phase of the system - the 'debris disk'. The source is no longer accreting and most of the emission is coming from either the central source or reflection off the remaining disk material. Rings and substructures (e.g. ALMA Partnership et al. [2015]) may also be observed in the disk, perhaps caused by the presence of planetesimals, the amalgamation of dust grains or magnetic trapping. Figure 1.1 presents a schematic of this evolutionary process and the various classes.

1.2 The theory of massive star formation

Massive stars form predominantly in clusters in association with a number of lower mass objects [Lada and Lada, 2003]. However, despite the similarity of their origins to low-mass stars, a clear-cut evolutionary sequence for high-mass stars is yet to be found. Massive star birth begins in parsec-scale molecular clumps with typical masses of 10^2-$10^3 M_\odot$. The collapse and fragmentation of massive clumps give rise to cores with sizes of $<\sim$0.1pc at higher densities.

The high luminosities of massive protostars originate from their contraction, as is the case for low-mass stars. The contraction of the source fuels its luminosity, and as its radius decreases, its temperature increases and it follows a fairly horizontal path in the direction of increasing temperature along a Henyey track on a Hertzsprung-Russell diagram (Figure 1.2).

The Kelvin-Helmholtz timescale describes how quickly a star converts gravitational potential energy into luminosity through contraction and is a good proxy for the formation timescale of a star. For massive stars, this timescale is shorter than the free-fall time of the molecular clouds from which they form. This means that the entire massive star formation process is obscured by natal material and that massive protostars are embedded objects.

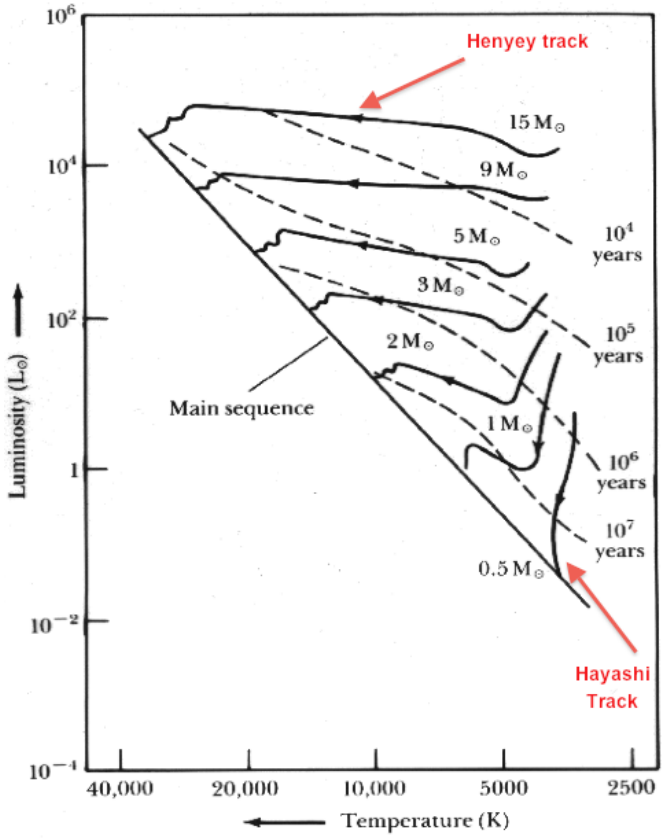

Fig. 1.2 A Hertzsprung-Russell (H-R) diagram, showing the variation in Hayashi and Henyey tracks for different masses of protostar as they evolve into main sequence stars Kaufmann [1991].

A hydrostatic source will still form at the centre of the system and grow through accretion, as in low-mass star formation, but a high mass source will be able to burn hydrogen while it is still accreting. Because of this the central protostar grows even when it has reached the main sequence and will evolve up the main sequence as it continues to gain mass. Low-mass stars do not continue to accrete and so stay in one place on the main sequence once they reach it.

Massive stars will produce a large amount of radiation pressure which will affect their surrounding material. A focal discussion point within the field has been how this affects massive protostellar accretion and it was initially assumed that a limit on the mass of massive stars may exist due to their large radiation pressure.

The acceleration due to gravity of the central source, a_{grav}, felt by accreting material a distance D can be described as:

$$a_{grav} = \frac{GM_{source}}{D^2} \tag{1.3}$$

The acceleration due to radiation pressure acting in the opposite direction on the material can be given by:

$$a_{rad} = \frac{L_{source}}{4\pi cD^2}\frac{n_{dust}\sigma_{dust}}{\rho} \tag{1.4}$$

where c is the speed of light, n_{dust} is the number of dust grains per unit volume, ρ is the density and σ_{dust} is the cross section presented to the radiation by a single dust grain [Ward-Thompson and Whitworth, 2015]. $\sigma_{dust} \sim \pi r_{\text{dust}}^2$ where r_{dust} is the radius of the dust grain and typically holds if $\lambda \leq 2\pi r_{dust}$.

Since D is a common term between the two expressions and the other values remain constant it is the ratio between L_{source} and M_{source} that is important. If a_{rad}>a_{grav} accretion stops. Assuming that $n_{dust} = \rho Z_{dust}/M_{dust}$ (where Z_{dust} is the dust fraction by mass) and considering the previous equations, accretion will stop if:

$$\frac{L_{source}}{M_{source}} > \frac{16\pi cG\rho_{dust}r_{dust}}{3Z_{dust}} \tag{1.5}$$

Therefore, depending on the constitution of the dust, M_{source} should not exceed 8-20$M_\odot$ if accretion is to continue. However, evolved main sequence stars of 60$M_\odot$ [Crowther et al., 2016] to over 100$M_\odot$ [Kashi and Soker, 2010] have been observed. The previous theory assumes that accretion occurs spherically symmetrically which is most likely not the case. Accretion will come almost exclusively from the disk, and since the disk is flat in comparison to the rest of the protostellar environment material will accrete from the equatorial plane, so the amount of radiation (which emits in all directions) experienced by the accreting material will be reduced. The

above upper mass limit uses dust properties that pertain to the ISM, but these could be different. In particular, the densities could be lower in the inner regions if shocks have pushed material to larger distances from the central source. Massive stars also form in clusters and multiples so the gravitational potential could be stronger than assumed, allowing more accretion. Theoretical modelling has shown that the geometrical effects of disk formation [Yorke and Sonnhalter, 2002] and outflows (Krumholz et al. [2005], Cunningham et al. [2011]) can reduce the radiation pressure on accreting gas allowing protostellar formation to continue [Bonnell et al., 1998] and this is discussed in more detail in subsequent subsections.

At the present time, the exact mechanisms of massive stellar formation are unknown. Theoretical work has led to the formation of a number of theories for massive star formation and among these the most robust are monolithic collapse, competitive accretion and, to a lesser extent, stellar collision. While it is not clear which of these theories is the more accurate solution to the massive star formation question or whether a combination of the three is the answer, each of them are discussed in the following subsections.

1.2.1 Monolithic collapse

Monolithic collapse, or core accretion, models are essentially scaled-up versions of low-mass star formation, where one massive core forms one massive star and the initial mass of the core is the main dictator of the final stellar mass. The theory makes the assumption that the pre-stellar core mass function (CMF) displays the same trends as the stellar initial mass function (IMF). This assumption is supported by SPIRE/PACS observations of André et al. [2010] of the star forming region Aquila, although this only considers objects up to 10 solar masses.

The turbulent core model of McKee and Tan [2003] handles clumps as products of fragmentation that exist in quasi-equilibrium. The clumps are maintained by the input

of kinetic energy from outflows and accretion events and the energy cascade from GMC scales. Infall occurs from the clump onto the residing cores at a similar rate as the accretion of material on to the star, increasing over time up to $\sim 10^{-3} M_{\odot} yr^{-1}$. Important characteristics of these cores are that 1) they are much denser than the surrounding clump 2) they have higher pressures than the ISM or their natal cloud and 3) they are supersonically turbulent and can remain in this state as they form stars [Tan et al., 2014]. Disks form due to angular momentum conservation in the same way as low-mass star formation, and this added midplane density component channels radiation towards the poles where jets and outflows are formed. These models produce evolutionary timescales of 10^5yr with a stronger dependence on surface density ($t \sim \Sigma_{cl}^{-3/4}$) than mass ($t \sim M_*^{1/4}$).

Krumholz et al. [2009] have shown through 3D radiation-hydrodynamic simulations of such cores that radiation pressure can escape through optically thin bubbles in the environment, meaning that accretion is not halted. Kuiper et al. [2011] and Kuiper and Yorke [2013] show that the disk also shields itself against radiation, again allowing accretion and removing the upper limit on the mass of stars. Other core collapse models have been performed by Rosen et al. [2016]. Through 3D radiation–hydrodynamical simulations they utilised an algorithm that simulated the absorption of the direct radiation field in order to obtain an accurate solution for the radiation pressure. They again found that radiation bubbles can cause Rayleigh-Taylor instabilities which alleviate radiation pressure, similar to Krumholz et al. [2009]. This applies in cases of both turbulent and laminar flow and the bubbles make the disk more susceptible to fragmentation, allowing the generation of several low–mass companions. However, no outflows, magnetic fields or photoionisation were included in their models.

One limitation of core-collapse models is that they do not account for the possibility that a larger core could potentially fragment into smaller stars as predicted by models by Dobbs et al. [2005]. The Jeans' mass is less than one solar mass for

a typical molecular cloud [Carroll and Ostlie, 1996]. It should then follow that a very large cloud of, say, 100M$_\odot$ should form one hundred solar mass stars instead of a larger protostar. One possible solution is that the luminosity of the accreting protostar raises the temperature to hundreds of Kelvin within a radius of a few thousand astronomical units (au), significantly increasing the Jeans mass and suppressing fragmentation. Fragmentation is not observed in the calculations of Krumholz [2006] and Krumholz et al. [2007].

Hosokawa et al. [2010] created a number of models of massive forming stars with the high accretion rates expected from turbulent core models. The timescales of their models are short, meaning that the energy generated by accretion cannot be efficiently dissipated through radiative cooling. Accretion becomes almost adiabatic, resulting in an increase in opacity as the mass enlarges. The stellar temperature subsequently drops and because the temperature is proportional to $1/\sqrt{R}$ following the Stefan-Boltzmann law, Hosokawa et al. [2010] produce bloated stars in their models as large as $100R_\odot$. Eventually in their models the opacity decreases, the stellar luminosity increases, and the Kelvin–Helmholtz timescale for stellar contraction decreases. The protostar eventually continues its collapse as expected until it can begin burning hydrogen in its core and it reaches the ZAMS. The Hosokawa et al. [2010] bloated models can therefore explain how massive forming stars can have large luminosities but not reach temperatures high enough to form associated ionised regions.

1.2.2 Competitive accretion

In monolithic collapse, competition for material only exists if a multiple system is formed within a core. In competitive accretion, this competition shapes the evolution of all the stars within a forming cluster. The competitive accretion model postulates that massive stars form via accretion onto small protostars that form from the initial gravitational collapse. It assumes that 1) a large reservoir of gas is available from the

clump for accretion 2) this gas is not hampered by the presence of magnetic fields and 3) the gas is under the same gravitational acceleration as the cores. The idea was first discussed by Zinnecker [1982] and has been modelled extensively (e.g. Bonnell et al. [1997]). The type of accretion included in this model is Bondi-Hoyle accretion which describes spherical accretion onto a compact object traveling through the interstellar medium. Accretion from the clump onto the protostars is assumed to occur at a rate described by:

$$\dot{M} = \pi R^2 \rho v \tag{1.6}$$

where ρ is the ambient density, v is the relative velocity of the stars and R^2 is the accretion radius. Two scenarios were modelled by Bonnel et al.; a star dominated regime and a gas-dominated regime. The star-dominated regime is argued to better apply to massive star formation [Bonnell et al., 2001], with the massive stars settling towards the centre of the clusters where high ambient gas densities are fed by infall from the wider clump. Accretion is weak at first, attracting material close to the core, but the influence of the cores expands as they gain mass, extending to more distant areas of the clump. The ultimate mass of the core will depend more on its location within the clump (or its potential area for retrieving material) rather than its initial mass. Disks are expected as part of the accretion methods within competitive accretion models, but these are smaller than those in core-collapse models. Accretion is eventually expected to stop due to stellar feedback or fragmentation.

1.2.3 Stellar collision

The final model, the stellar collision model, has also been investigated through simulations [Bonnell et al., 1998]. It proposes that massive stars form through direct collisions of low mass stars. Since merging protostars are optically thick they are unaffected by the feedback from radiation pressure, avoiding this potential problem.

For collision rates to be in agreement with stellar evolution timescales, exorbitant stellar densities $\geq 10^8 \mathrm{pc}^{-3}$ would be required (e.g. Baumgardt and Klessen [2011]). Thus far simulations including gas accretion and N-body stellar dynamics show that collisions often result in the formation of just a couple of very large sources.

1.3 Observable phases of massive star formation

Various structures are observed which have been determined to be different parts of the massive star formation process. Simply put, massive star formation is suspected to occur through:

1. The collapse of a giant molecular cloud (GMC) into filaments and cores
2. The collapse of cores into protostars
3. A period of accretion where the protostars gain mass from their surrounding environment
4. A period of disruption as the feedback from the (proto)stars echoes through the surrounding environment

as stated by Zinnecker and Yorke [2007]. In this section each of these stages are addressed.

1.3.1 Giant molecular clouds and filaments

As introduced in Section 1.1, giant molecular clouds (GMCs) present the first stage of massive star formation, which then collapse under gravity resulting in fractal density structure on small scales in the form of filaments and high density clumps [Williams et al., 2000]. Figure 1.3 shows each of these stages in one star forming environment. Very few GMCs have been shown to be devoid of star formation [Maddalena and

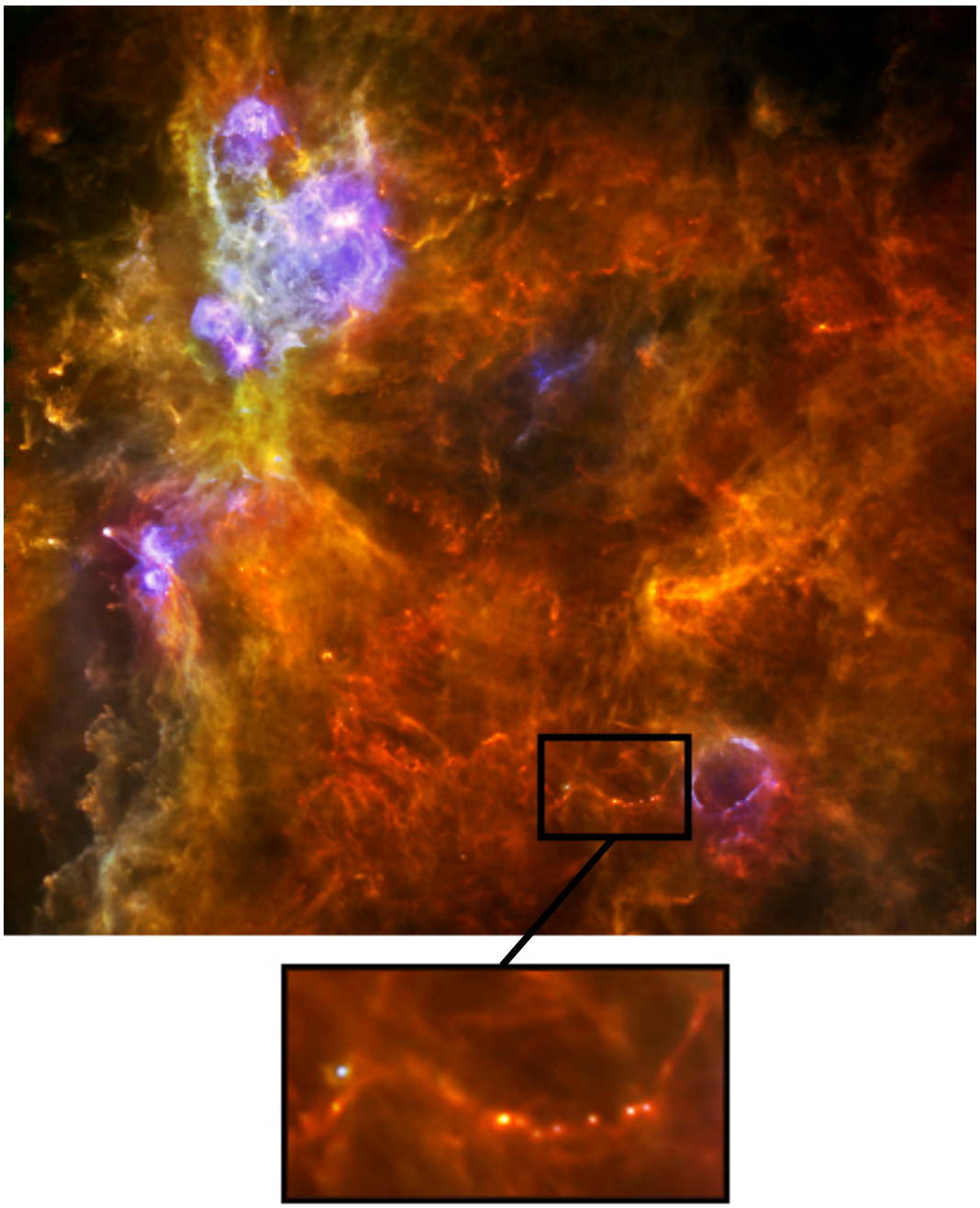

Fig. 1.3 The W3 giant molecular cloud as imaged by PACS (Herschel) [Rivera-Ingraham et al., 2013]. In the box a filament can be seen, with bright cores forming within it. Credit: ESA.

Thaddeus, 1985]. There is debate as to whether some GMCs appear inactive due to source confusion and Blitz [1993] state that with this consideration the youngest 10% of GMCs could not be forming stars. It is thought that the feedback of massive O and B stars disrupts GMCs, shortening their lifetimes [Blitz and Shu, 1980] and it is likely that GMCs are transient objects that are dissipated by star formation.

Observations from the Herschel Telescope Gould Belt Survey [André et al., 2010] have shown that massive filaments are ubiquitous features of GMCs. Filaments are of similar temperatures to their natal GMCs ($\sim$10K) and are long ($\sim$1-100pcs) and thin ($\sim$0.1pc) in structure [Jackson et al., 2010]. If a filament is dense to the point where its mass per unit length is greater than the critical line mass of isothermal structure, it can fragment into cores.

1.3.2 Cores

Massive starless cores, or infrared dark clouds (IRDCs), have been found by both the Infrared Space Observatory Camera (ISOCAM) [Perault et al., 1996] and the Midcourse Space Experiment (MSX) [Egan et al., 1998]. Rathborne et al. [2006] performed an imaging survey of 38 IRDCs at 1.2mm and found all of them to contain at least one compact (<0.5pc) core. The slope of the core mass function in IRDCs is determined to be 2.1$\pm$0.4, similar to that of the stellar IMF, and their deduced SFR is 2 $M_{\odot}yr^{-1}$ (close to the Galactic SFR), suggesting they must be forming stars. Spitzer has also been used to study cores, with Evans et al. [2003] using 400hrs of observing time with the IRAC, MIPS and IRS instruments to investigate star formation from the earliest stages of molecular cores. More recently, Henshaw et al. [2016] and Henshaw et al. [2019] presented evidence of filamentary structure for two IRDCs, implying that massive starless cores are susceptible to fragmentation and future star formation, despite their quiescent appearance.

The hot molecular core (HMC) constitutes the next observable phase of massive star formation. They can be detected using submillimetre emission lines, generated by the reactions of complex molecular species on the surface of their dust grains enabled by their higher temperatures. Cesaroni [2005] find that HMCs lie in the centres of parsec-sized clumps where the density and temperature are highest and that their masses are comparable to those of embedded clusters.

1.3.3 Massive Young Stellar Objects (MYSOs)

A massive young stellar object (MYSO) is a relatively short evolutionary phase towards the end of the hot molecular core phase. MYSOs are deeply embedded and therefore not visible in the optical, but are mid-infrared bright. Their centimetre continuum emission is weak, indicating that they cannot be sufficiently ionising their surrounding material. Bipolar outflows are ubiquitous around MYSOs, implying that accretion is ongoing, making them ideal candidates for studying the physics and nature of the accreting regions of massive stars (Oudmaijer and de Wit [2014], Lumsden et al. [2013]).

Evidence of accretion disks is slowly arising for MYSOs. Ilee et al. [2013] found evidence for disks around a number of MYSOs by successfully fitting Keplerian disk models to CO first overtone bandhead emission. Through K-band interferometric observations and radiative transfer modelling, Kraus et al. [2010] detected a compact disk at scales of $\sim$10au around the MYSO IRAS 13481-6124, confirming observationally that an accretion disk could exist around an MYSO. Disks have also been observed at larger scales. For example, Johnston et al. [2015] and Ilee et al. [2016] present findings of Keplerian-type disks of 12$M_{\odot}$ and 1-2$M_{\odot}$ respectively around two MYSOs. Beltrán and de Wit [2016] present a detailed examination of the types of the disk-like objects around varying sizes of protostar, including MYSOs, and their accretion properties. Caratti o Garatti et al. [2017] detected an accretion event around

the MYSO S255 NIRS 3, observing a radio burst after a maser/IR accretion event and interpreting this as an accretion event of the order $10^{-3}M_{\odot}yr^{-1}$ and Cooper et al. [2013] detected near-IR line tracers indicative of accretion processes. The objects also display activity from powerful jets (e.g. Purser et al. [2016]), winds (e.g. Bunn et al. [1995]) and outflows (e.g. Shepherd and Churchwell [1995]) which are also associated with accretion-ejection processes.

The study of the aforementioned features within the environments of MYSOs has been limited by their large typical interstellar extinctions (A_v=42 mag median found by Cooper et al. [2013]), large distances (of order kpc) and their rarity. Systematic studies have been difficult and only the highest resolution instruments resolve the spatial scales required to study MYSOs in detail. One of the first attempts to catalogue MYSOs used the IRAS satellite [Neugebauer et al., 1984] and Campbell et al. [1989] identified 115 YSOs from IR colour selection criteria. Molinari et al. [1996] and Molinari et al. [1998] performed follow-up studies to this work using NH_3 and radio observations of the IRAS sources, but only studied sources over 30° north of the celestial equator and those 1' away from HII regions, meaning a number of MYSOs were excluded. Follow-ups with far-infrared, radio continuum, molecular line data and masers were performed by Sridharan et al. [2002] and Beuther et al. [2002b]. Here, objects with similar densities and luminosities to UCHII regions and low-radio fluxes (<25mJy, to avoid confusion with UCHII regions) were the focus, but again due to their restrictions the study resulted in a bias against sources inside large HII regions or wider star forming areas. They found only some MYSOs display maser emission and that the types of maser transition vary across MYSOs, implying that the molecules producing maser emission are being destroyed throughout the MYSO phase. As a result, methods which use maser detections as a way of cataloguing MYSOs may be at risk. Robitaille et al. [2008] used the GLIMPSE point source catalogue (with colour selection criteria) to identify 11000 candidate YSO sources across the mass range, but no follow-up studies have been

performed to prove that planetary nebulae and HII regions are not also included in the data set. Churchwell [2006] and Churchwell et al. [2007] found 600 HII regions and bubbles in GLIMPSE data and that 10% of these had associated YSOs and 12% displayed a morphology suggestive of triggered star formation.

The Red MSX (Midcourse Space Experiment) Source survey was designed to catalogue as many young massive protostars as possible within the galactic plane of our galaxy. The objects were classified by colour using the criteria of Lumsden et al. [2002] and approximately 2000 candidates were found. Follow-up observations were performed to exclude other objects which satisfied the colour requirements such as planetary nebulae (PNe), UCHII regions and evolved stars contaminated the sample. UCHII regions produce radio emission and can be resolved at 1" resolution in the MIR. This meant that radio continuum observations [Urquhart et al., 2007a, 2009] and MIR observations [Mottram et al., 2007] could be used to remove them from the sample. Evolved stars are surrounded by dust but this takes the form of a shell as opposed to the continous envelope/core expected for massive forming stars. As a result, their continua are bluer, allowing them to be separated from the MYSO sample [Cooper et al., 2013]. Ultimately, $\sim$650 MYSOs were found. The kinematic distances were determined using ^{13}CO line emission observations [Urquhart et al., 2007b, 2008, 2012] and Mottram et al. [2011a] estimated their luminosities using the grid of model SEDs generated by Robitaille et al. [2007]. Mottram et al. [2011b] also estimated the number of objects per unit volume per unit luminosity across the galaxy (the Galactic luminosity function). The main results of the survey are presented in Lumsden et al. [2013]. All the aforementioned calculations and data are available as part of the RMS database, supplemented with public data from other surveys such as the SCUBA (Submillimetre Common-USer Bolometer Array) Legacy Catalogue, ATLASGAL (Atacama Pathfinder EXperiment Telescope Large Area Survey of the Galaxy) and UKIDSS (UKIRT IR Deep Sky Survey). The RMS

survey database therefore provides a comprehensive, multi-wavelength source of information for many MYSOs.

1.3.4 HII regions

HII regions occur in a variety of different sizes but are all essentially structures created by the ionisation of hydrogen in massive protostellar environments. Hypercompact HII regions (HCHIIs) are the first to form when pockets of ionised gas form near the star (potentially coinciding with the photoevaporation of a protostellar disk). This phase is observable through broad radio recombination lines and their sizes are of order ∼0.01pc/5000au [Kurtz, 2005]. Ultracompact HII regions (UCHII) can contain multiple stars and occur when the ionisation spreads and disrupts the natal cloud. They are therefore much larger in both size and mass than HCHIIs, with ionised masses ∼10 times larger and densities a factor of 100 lower than HCHIIs. Hydrogen recombination line widths are observed for UCHIIs of order 10km/s [Hoare, 2005], while HCHIIs line widths are ∼75km/s [Kurtz, 2005]. Strong radio free-free emission is observed from both compact HII regions (<0.5pc) and classical HII regions, which are huge bubbles of ionised material at scales of 100s of parsec [Kurtz, 2005].

1.4 Ground-based observing in the mid-infrared

As stated in previous sections, MYSOs are embedded sources. While this makes them invisible at optical wavelengths, the irradiated dust of their circumstellar environments emits in the infrared, providing an opportunity to observe them. Infrared space telescopes such as Herschel have provided high-sensitivity images of MYSOs (e.g. Olguin et al. [2015]), but space telescopes (even the soon to be launched JWST) cannot be built to such a size that allows them to reach the spatial resolution required

to study the local environments of massive star formation at milliarcsecond scales. Therefore the most powerful infrared observatories are currently ground-based.

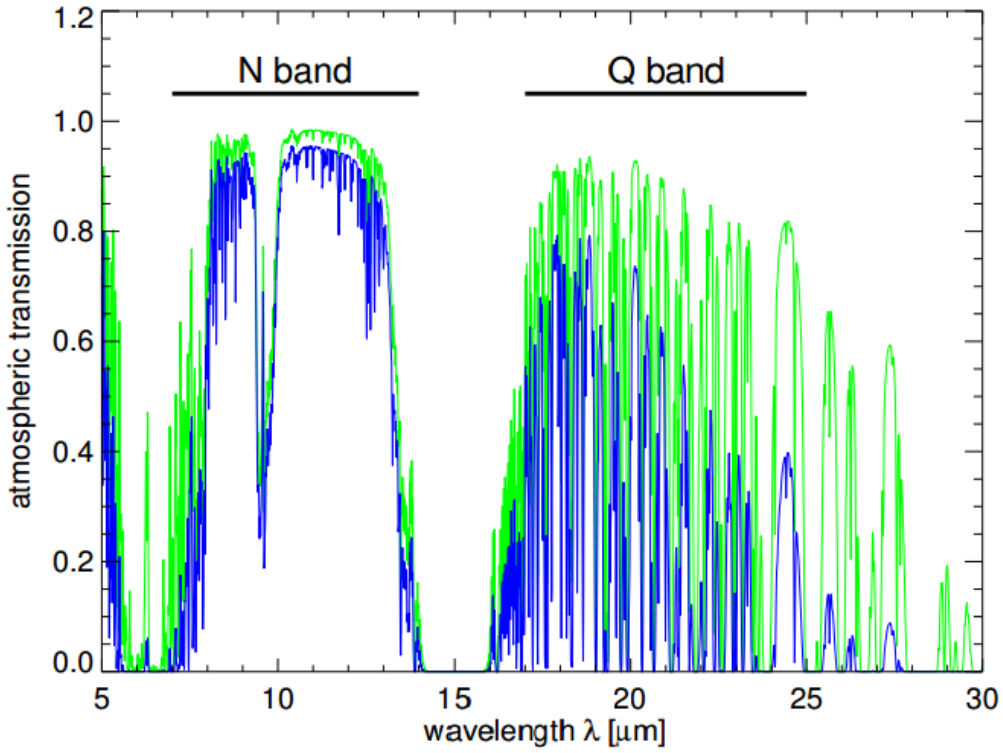

Fig. 1.4 The transmission of radiation across the mid-infrared as measured at Paranal Observatory (see Section 1.4.3). The green line corresponds to measurements taken with different conditions. The green line (better conditions) has precipitable water vapour (PWV) of 1mm and the blue line (worse conditions) has PWV=3mm. Credit: ESO user manual.

Any ground-based telescope falls victim to absorption from the Earth's atmosphere and mid-infrared radiation is particularly effected. Water has the largest effect, with molecules such as methane, carbon dioxide, carbon monoxide, oxygen and ozone (O_3) presenting further problems. Observing at the driest site possible can enhance infrared observing and most observatories operating at these wavelengths are high-altitude. Even with the best Earth conditions possible, the mid-infrared wavelength range, which is approximately between 5-30μm, is almost completely absorbed by the atmosphere save for a few select spectral windows, the N and Q band. These two spectral transmission windows are shown in Figure 1.4. The atmosphere

also contaminates observations by emitting in the mid-infrared. Additional background noise comes from the detectors in the instruments themselves, and cryostats are often used to cool these to keep contamination to a minimum.

The resolution of a telescope relies on its diffraction limit and atmospheric seeing. The diffraction limit (θ) is measured as the diameter of the first Airy ring, or the first minima in the diffraction pattern of the light as it enters the telescope. $\theta \propto \lambda/D$, where λ is the wavelength of the incoming radiation and D is the diameter of the telescope. For an interferometer, D is substituted for B, the projected baseline between the telescopes. Therefore, the larger the primary mirror of a telescope or the larger the baseline between the telescopes in an interferometric array, the smaller the angular scales on the sky that can be resolved and the more powerful the telescope. The atmospheric 'seeing' describes the sharpness of an image after atmospheric interference and depends on wavelength.

Once a suitable observing site for infrared observing has been obtained, different high-resolution techniques can be exploited to probe massive protostellar environments. In the subsequent subsections two such methods, interferometry and imaging, are introduced and an observatory which can perform both.

1.4.1 N-band Interferometry

Interferometry is an observing technique which in its simplest form can be compared to Youngs' double slit experiment. In this experiment, wavefronts from a source of light pass through two holes in a screen some distance from that source. As the light passes through the holes, it is split into two new wavefronts and dispersed. If a second screen is placed in front of the two new wavefronts a sufficient distance away, the wavefronts will meet once again and as they do, their light will interfere. This leads to a fringe-like pattern of maxima and minima, resulting from the overlapping of the waves. Interferometry works in much the same way, except it is individual telescopes

that detect the original wavefronts and then a correlator (radio) or combiner (infrared) which brings them together to generate the fringe pattern. In 1868, Fizeau used this phenomena to study stars and his methods allowed Stephan to find well-constrained upper limits of the diameters of stars and this work was then used by Michelson and Pease [1921] to measure the diameter of Betelgeuse. Over subsequent years, radio interferometry quickly evolved (see Thompson et al. [2017] and their references for examples) but it was not until much later through the efforts of Labeyrie [1975] that short-wavelength interferometry was pursued as a viable technique. Several technical advances were required before infrared and optical interferometry could be routinely used by observers, as for many years the instrumentation was not sophisticated enough.

When an interferometer detects wavefronts of light from a target using multiple telescopes, the telescopes are at separate locations and the distance between them is referred to as the baseline vector of the observations. The projected baseline (the projection of the baseline vector onto a plane perpendicular to the line-of-sight) and the wavelength of the observations dictate the angular resolution of the interferometer. The larger the baseline and/or the shorter the wavelength, the smaller the scales that can be resolved by the instrument. Once obtained, the wavefronts at each telescope are directed to a relay system, which transmits the signal using mirrors to the detector, where the beams are combined (Fig. 1.5). Many short wavelength interferometers are of the Michelson type. This means that they use a beam splitter to divide and recombine the beams from the telescopes. This optimises the optical paths between the beams [Bass, 1995]. Delay lines are used to ensure that the signals reach the detector at the same time.

Once the beams are combined, constructive and destructive interference occurs between the wavefronts, leading to an interference pattern which holds the infor-

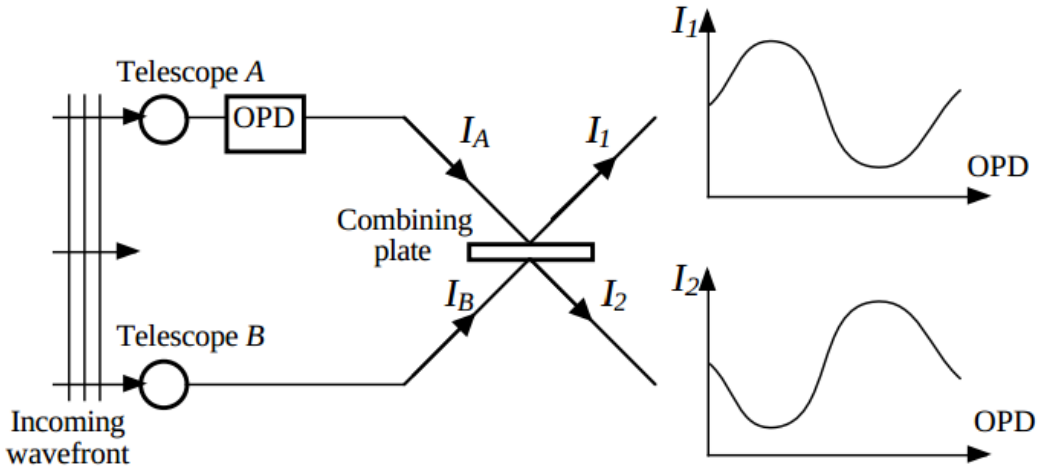

Fig. 1.5 Schematic showing how the beams are combined in a two-telescope optical/infrared interferometer. OPD is optical path difference induced by the atmosphere, the incident intensities from Telescopes A and B are labelled I_A and I_B respectively, and I_1 and I_2 are the intensities from the two outputs of the beam combiner. Credit: ESO.

mation of the observed source. The primary observable of an interferometer is the complex visibility, which can be expressed as:

$$\Gamma = Ve^{i\Phi} = \hat{O}(u,v) \tag{1.7}$$

where $\hat{O}(u,v)$ is the Fourier transform of the target's brightness distribution $O(x,y)$. u and v constitute the coordinates of sampled points within the Fourier plane and can be described as $u = B_x/\lambda$ and $v = B_y/\lambda$ where (B_x,B_y) are the coordinates of the projected baseline at that sampled point. V is the visibility of the fringes and can be described as:

$$V = \frac{I_{max} - I_{min}}{I_{max} + I_{min}} \tag{1.8}$$

where I is the fringe brightness and Φ is the phase and related to position. The visibility can be obtained either from the fringe contrast in an image plane or by

varying the internal delay and quantifying the subsequent variations in intensity. In the latter case the intensities are described by:

$$I_1 = I_{A1} + I_{B1} + 2V\sqrt{I_{A1}I_{B1}}(\frac{2\pi OPD}{\lambda} + \Phi) \tag{1.9}$$

$$I_2 = I_{A2} + I_{B2} + 2V\sqrt{I_{A2}I_{B2}}(\frac{2\pi OPD}{\lambda} + \Phi) \tag{1.10}$$

where I_1 and I_2 are the intensities from the two outputs of the combiner, I_{xy} is the intensity from telescope x mixed for the channel y of the combiner, and OPD is the path difference introduced by the atmospheric turbulence and by the modulator used to generate interferograms. Often V^2 is used as an observable instead of V, as it is more robust to smearing effects induced by atmospheric fluctuations.

1.4.2 Mid-infrared imaging

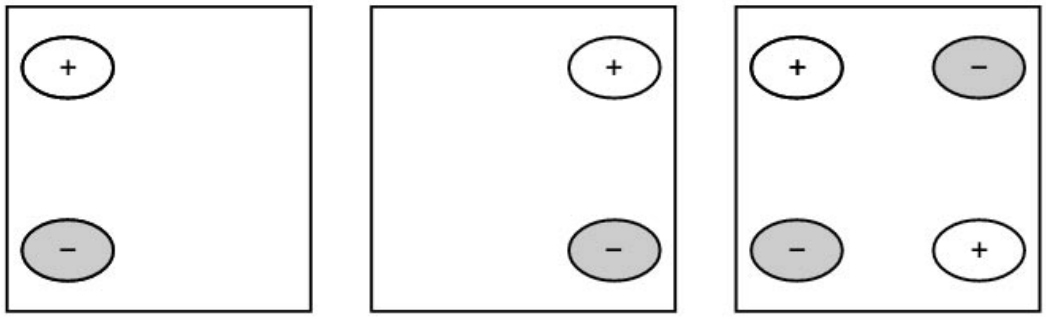

Fig. 1.6 Schematic showing how the images taken in the chopping and nodding process are combined. Credit: ESO User Manual.

Mid-infrared imaging is decidedly simpler than mid-infrared interferometry as the signal from a single telescope is handled and no combination is required. In order to minimise contamination from the detector, imaging instruments are cooled to close to absolute zero. In order to reduce the effects of the mid-infrared

background of the sky/atmosphere, a technique known as chopping and nodding is used. In chopping, two sets of exposures are taken, one including the source and one of a piece of sky without the source. In order to be effective, the two sets must be alternated at a faster rate than the fluctuation of the background. Background fluctuations usually occur over several seconds resulting in chopping frequencies of a few Hz. Chopping alone can significantly reduce the background effects, but the optical path is not the same in both chopping directions leading to a residual remaining background. Nodding reduces this, by moving the telescope off-source and performing the same chopping observations as in the on–source position. Given that there are four positions observed during this process, a partially reduced image from a telescope will show the source four times, as illustrated in Figure 1.6.

1.4.3 The Very Large Telescope and Interferometer

Fig. 1.7 Paranal Observatory and the VLT/I. Credit: G. Hüdepohl/ESO

The Very Large Telescope and Interferometer (Haguenauer et al. [2010], Figure 1.7) performs both of these observing techniques. Operational since 1998, the obser-

vatory harbours eight different telescopes and is operated by the European Southern Observatory. The telescopes are located on Cerro Paranal in the Atacama Desert of northern Chile at an altitude of 2635m. This area sees some of the driest conditions on Earth, limiting the atmospheric effects associated with optical and infrared observing. The total wavelength range observable with the observatory is 300nm to 20μm. Four of the eight telescopes are Unit Telescopes (UTs), with primary mirror sizes of 8.2m and focal lengths of 14.4m. Each UT harbours a number of instruments including spectrographs, imagers and spectropolarimeters and currently thirteen different instruments are operational on these telescopes. The remaining telescopes are called Auxiliary Telescopes (ATs) and are 1.8m in size. These telescopes are movable and form a key-component of the Very Large Telescope Interferometer (VLTI), allowing observations in small, medium and large configurations thanks to their flexibility, with baseline capabilities from approximately 40-120m. The VLTI currently uses three different instruments to perform interferometric observations (MATISSE, GRAVITY and PIONIER) and has previously been home to the beam-combining instruments AMBER and MIDI.

1.5 Radiative transfer modelling

Modelling, or the generation of simulated environments to approximate observed phenomena, is an invaluable tool in practically all fields of astrophysics. It creates synthetic astrophysical situations which, when examined, can provide valuable comparisons and constraints on real objects. Radiative transfer describes the nature of heating, cooling and energy transport. Astrophysical systems cool by emitting radiation, transfer energy within themselves through radiative processes and this radiation can be observed. Radiative processes also drive photochemistry through the photodissociation of molecules. Radiative transfer (RT) modelling is therefore an imperative aspect of the simulation of protostellar systems. In the next subsections, a

short review of radiative transfer and how it has been and can be applied to the study of MYSOs is presented.

1.5.1 Radiative transfer: a short summary

In the absence of any intervening material or obstruction, radiation transfer essentially describes the intensity along a beam of radiation and will remain constant as it propagates in a certain direction. Once an interfering medium is in place, radiative transfer describes the interaction of the ray with that medium. As a photon journeys into a medium, three things can happen: 1) it can hit the medium and be absorbed, 2) it can hit the medium and be scattered, or 3) it can never hit anything.

The efficiency of the medium to absorb a photon is described as the mean free path (l), and is a function of frequency v and position s. The denser the medium, the shorter the mean free path. The number of mean free paths the photons can travel through the medium is the optical depth (τ). If $\tau \gg 1$ the medium is optically thick, if $\tau \ll 1$ it is optically thin. The reciprocal of the mean free path is the extinction coefficient, κ_ν, or the opacity. The optical depth between two points along a ray can be expressed as:

$$\tau_\nu(s_0, s_1) = \int_{s_0}^{s_1} \kappa_\nu(s) ds \tag{1.11}$$

The intensity of an object is determined by its temperature, internal processes and other properties. How this intensity varies can be illustrated through the radiative transfer equation (RTE):

$$\frac{dI_\nu}{d\tau_\nu} = -I_\nu + S_\nu \tag{1.12}$$

$S_\nu = j_\nu/\kappa_\nu$ is the source function, where j_ν is the emissivity and κ_ν is the opacity. If a system is in thermodynamic equilibrium, the intensity is uniform and equal to

the source function, the Planck function and $j_\nu = \kappa_\nu B_\nu(T)$. A general solution of the RTE is given by:

$$I_\nu(\tau_\nu) = I_\nu(0)e^{-\tau_\nu} + \int_{\tau_\nu=0}^{\tau_\nu=\tau_\nu'} S_\nu(\tau_\nu)e^{-\tau_\nu-\tau_\nu'}d\tau_\nu \tag{1.13}$$

If the medium is uniform this means that the source function and the emissivity will be constant, so the solution becomes:

$$I_\nu(\tau_\nu) = I_\nu(0)e^{-\tau_\nu} + S_\nu(1-e^{-\tau_\nu}) \tag{1.14}$$

If the medium is optically thin the solution goes as $I_\nu(\tau_\nu) = I_\nu(0)(1-\tau_\nu) + S(0)\tau_\nu$ and the observer receives emission from throughout the medium. If the medium is optically thick the solution goes as $I_\nu(\tau_\nu) \approx S_\nu^0$ and only emission from the outer-most layer of the medium is observed. These solutions assume that there is background intensity to some degree ($I_0 > 0$), which is to be expected of all star forming regions.

The scattering of photons can have large effects on the propagation of radiation and is caused by a variety of objects from charged particles to dust grains. Scattering can be included in the RTE (quantified as the coefficient σ_ν) but the solution to the equation in this case can only be solved numerically [Rybicki and Lightman, 1986]. Its inclusion results in an extinction coefficient which is the sum of κ_ν and σ_ν.

1.5.2 The Monte Carlo method

Predicting how a single photon will behave as it moves throughout a medium, such as a protostellar envelope, is very difficult. In order to adequately simulate a protostellar envelope, millions of photons are often required. The behaviour of such a number of photons can be estimated based on their statistical properties. The Monte Carlo method uses repetitive random sampling to obtain numerical results, allowing it to

be used to determine the position, behaviour and effects of millions of photons. It follows this approximate procedure:

1. Emit some number of 'packets' (in this case, photons)
2. Track the progress of each packet through the defined medium.
3. As the packets exit the medium, capture them on a pre-defined image plane and see how they have changed.

The photons themselves take a random 'walk' throughout the material - each time they reach a dust grain or particle a random interaction will occur (an absorption, emission or scattering) which will affect where the photon 'walks' next. The locations of the photons during Step 2 are found by constantly sampling the optical depth of the system, and the scattering and absorption of the photons is found by sampling albedo and phase functions. This sampling makes use of probability distributions which are a core feature of the Monte Carlo technique. In the case of astrophysics, the probability distributions are based on properties of the dust in the grid [Whitney, 2011]. Lucy [1999] and Bjorkman and Wood [2001] present methods of determining the temperature distribution of medium. When the photons reach the edge of the grid their properties can be used to calculate images or SEDs. In order to make high signal-to-noise images one can use the peel-off method (where a photon is thrust in the direction of the observer weighted by the probability that it can travel in that direction) or by ray-tracing (which solves the RT equation of the grid in the line of sight).

According to the above steps, the Monte Carlo Radiative Transfer used within this thesis can be explained as follows. A central protostar is defined in terms of its temperature and radius and as such it will produce photons of a certain energy. These photons will be emitted from this central protostar into a predefined dusty medium, constituting of an envelope with outflow cavities and potentially a disk all within a

grid which encases the system. As the photons hit the dusty material they can be scattered, absorbed and re-emitted. When the photons reach the edge of the grid they are projected onto a predefined image plane which can used in post-processing. The information obtained while the photons interacted with the protostellar environment can also be used in post-processing.

1.5.3 Applications to star formation

In the case of star formation RT modelling is employed to model irradiated protostellar environments. Through the use of these models a detailed parameter space of the simulated environment is generated, and if the model well fits the observational data these parameters can be linked to real star forming regions. RT modelling has been frequently exploited in the study of MYSOs. de Wit et al. [2010] and Wheelwright et al. [2012] used 2D radiative transfer in the study of various MYSOs, simulating N and Q band data. Robitaille [2017] presents a grid of RT models (compiled into different groups based on different protostellar geometries) run using a code of the authors' making, Hyperion [Robitaille, 2011]. This code has been used in a number of multi-wavelength studies of massive star formation such as Olguin et al. [2015]. Harries et al. [2017] combined radiative transfer modelling with hydrodynamical modelling to study the formation of a 25 solar mass star but while the combination of the codes produces impressive results, the combination of two already complex codes results in model run times too long to perform work on a sample of objects.

1.6 The motivation for and structure of this thesis

As outlined previously in this chapter, the MYSO phase presents a crucial and observable phase of the massive star formation process. Given their embedded nature, mid-infrared studies at high-resolution are able to trace the details of MYSO

environments. A number of studies have probed the circumstellar environments of massive young stellar objects using mid-infrared observations in an attempt to discern their evolutionary processes. This thesis was motivated by three such studies in particular. The first, de Wit et al. [2007], studied the MYSO W33A by fitting one configuration of mid-infrared interferometric data of the source and its SED with a 1D RT model. The interferometric data had the required resolution to probe the innermost regions of the source, unveiling its characteristics, but was limited as only two *u*-*v* points of the full *u*-*v* plane were probed. The second study, de Wit et al. [2010], expanded upon this work by including more configurations of interferometric data and using a 2D RT model. This vastly improved the constraints that could be made on the source, confining the mid-infrared emission to outflow cavities specifically. The third work, Wheelwright et al. [2012], tested whether this model could be applied to a number of MYSOs, by fitting the successful W33A model to longer wavelength imaging data taken at $\sim$20μm. They found that this model satisfied this longer wavelength data, and that the radial profiles and SEDs from 15 other MYSOs could be successfully fit by this same model. This begs the question - is there a model, and therefore a protostellar geometry/type, which fits all MYSOs? The goal of this doctorate work was to determine whether this is indeed the case by building upon the aforementioned works and increasing the complexity of the approach.

As different processes occur at different scales, using different wavelength observations provides a more complete look of a studied source. By consolidating observations with RT modelling, the physical properties of the protostellar environment can be investigated and observations and theory compared. This work of this thesis combines high-resolution MIR observations at multiple wavelengths with SEDs and fits all these observables simultaneously using a 3D radiative transfer code. By fitting one model to the different kinds of observation simultaneously

the characteristics of different MYSOs are obtained on a case-by-case basis and a consistent, comparative analysis can be performed.

The remainder of this thesis is structured as follows. In Chapter 2, the methodology used to study the circumstellar environments of MYSOs is described in full, alongside the fitting results of one MYSO as an example. In Chapter 3, the results for another source, which potentially constitutes an example of a transition disk around an MYSO, are presented. In Chapter 4, the results for a sample of sources which have been subject to the same analysis (the largest number of objects for which this has been done) are shown. In Chapter 5, all the MYSOs discussed in the thesis are analysed as a group, and the trends found between them described. Finally, the thesis is concluded in Chapter 6.

Chapter 2

Multi-scale methodology

2.1 Introduction

As presented in Chapter 1, the massive star formation process is not clear. One of the most critical aspects of the process which remains to be constrained is how massive protostars accrete and arrive at their final mass. Infall and accretion happen on a number of scales throughout the massive protostellar environment and observations at different wavelengths, which probe these different scales, allow the study of the important regions where these processes occur. A number of high-resolution, single-object studies of MYSOs have been performed (e.g. Kraus et al. [2010], Caratti o Garatti et al. [2017]), allowing investigations into these environments. Each has provided a valuable 'snapshot' of the massive formation process, but since each study utilises a different observable, methodology, modelling approach or perspective, these cannot be directly combined nor the findings from each of the studies directly compared. This prevents us from determining whether these glimpses of massive star formation are indicative of the wider evolutionary sequence or whether they are special cases. Groups of massive stars have been studied in single works (e.g Boley et al. [2013]) however working with larger samples means it is more difficult to employ a time-consuming, in-depth analysis, and as a result studies

often use simpler models (e.g. geometric vs. full radiative transfer) and are limited to simply commenting on the group of MYSOs rather than reliably constraining their individual characteristics.

Longer wavelength observations in the sub-millimetre and millimetre regimes probe cool material that is further from the protostar. Shorter wavelength observations in the infrared (IR) trace the inner regions of protostellar environments, which are hotter due the presence of accretion luminosity and their proximity to the central protostar. Millimetre wavelengths observation for example trace material of $\sim$10K, while infrared radiation at 10μm traces material at $\sim$280K. Spectral energy distributions (SEDs) contain multi-wavelength information and as such have the potential to trace a protostellar environment from its smallest to largest regions. However SEDs provide no information on the geometry of a source. For example, it is not immediately evident whether millimetre wavelength emission is coming from a cool massive toroid or just the envelope from examining an SED alone. Spatially resolved observations are required to break the SED degeneracy and confirm the origin of protostellar emission.

Infrared observing is particularly suited to MYSOs as they are dust-rich and because the short wavelengths of the infrared benefit the angular resolution. Using these benefits, a number of previous works (e.g. Linz et al. [2008], Vehoff et al. [2008]) present studies of MYSOs using mid-IR interferometry in particular. Boley et al. [2013] present a survey of 20 MYSOs with the MID-infrared Interferometer (MIDI) instrument. Nearly every observed object has reasonable u-v coverage despite the two-telescope nature of the instrument, supplemented in some cases by aperture-masking N-band data from the Long Wavelength Spectrometer (Keck-1 telescope). Using geometrical models they derive the sizes of the emitting regions and the elongation of the circumstellar material. de Wit et al. [2010] and de Wit et al. [2011] investigated two MYSOs, W33A and AFGL 2136, by fitting a RT model to the SED and MIDI visibilities, concluding that most of the mid-IR emission

originates from the outflow cavity walls, in agreement with other works such as De Buizer [2006]. At slightly longer wavelengths, Wheelwright et al. [2012] and de Wit et al. [2009] present surveys of MYSOs at 20 and 24.5μm respectively using diffraction limited imaging. de Wit et al. [2009] find a shallower density distribution than expected for their objects and postulate that this flattening could be due to envelope rotation. Wheelwright et al. [2012] on the other hand attribute the shallow intensity profile gradients to be indicative of emission from the outflow cavity walls, but note that the envelope-cavity model proposed in de Wit et al. [2010] seems to apply to the wider sample. This thesis exploits both the N and Q band data utilised in these works simultaneously to probe multiple scales of MYSOs and see whether one master model can replicate the environment of many MYSOs at multiple scales.

The method of this thesis aims to obtain radiative transfer (RT) models that optimally fit high-resolution observations at 10mas scales, 100mas scales (for typical MYSO distances of a few kpc) and the SEDs of MYSOs. The type of observations used to trace 10mas scales is interferometric data taken with the MIDI instrument between 7-13μm. Diffraction-limited $\sim$20-25μm imaging data at 100mas resolution was obtained using the VLT Image and Spectrometer (VISIR) and the Cooled Mid-Infrared Camera and Spectrometer (COMICS). The Red MSX Source (RMS) survey [Lumsden et al., 2013] and the literature were used to compile SEDs from near-infrared to millimetre wavelengths, tracing the total flux of the observed objects. By combining spatially resolved observations with the SED the previously mentioned degeneracy is broken, and when the observations are consolidated with RT modelling the geometry of the accretion regions of an MYSO can be reliably constrained. This chapter describes the methodology in full.

2.2 N-band interferometry with the MID-infrared Interferometer (MIDI) at the Very Large Telescope Interferometer (VLTI)

MIDI is a Michelson-type, two-telescope interferometer at the European Southern Observatory's (ESO) Very Large Telescope (VLT), able to combine light from the 8m Unit Telescopes (UTs) or the 1.8m Auxiliary Telescopes (ATs) into two interferometric channels. The channels have a phase difference of π radians, due to the half-reflecting combiner plate of the instrument, and the beam-combination is done near to the pupil plane. Hence, one can subtract the two images and remove background contamination whilst retaining the correlated flux. In order to minimise contamination of the data due to background and instrumental thermal emission, the optics are cooled to 35K using a helium closed-cycle cryostat and the array detector is cooled to 10K. MIDI measures both the correlated flux and total flux in the N-band using one of two possible dispersive elements, prism or grism (a combination of a grating and a prism). Two modes of observation are possible - HIGHSENS and SCIPHOT. In HIGHSENS mode the correlated and total flux measurements are taken sequentially as opposed to SCIPHOT mode where a beam splitter is used to simultaneously measure the individual beams from each telescope and the combined/interferometric beam. For the photometric (or total flux) measurements light is passed sequentially from each of the two used telescopes through the VLTI optical train to MIDI, where it is dispersed and recorded on the detector. The relative contribution of each beam to the interferometric beam is estimated, allowing visibilities to be obtained from the correlated flux.

Most of the MIDI data used throughout this method are from Boley et al. [2013] and the typical observing sequence for these data was as follows. MIDI can function as an N-band imager and acquisition images could be obtained and used to period-

ically check the beam position on the chip. Images were also taken with MIDI's imaging mode on occasion (without the use of its beam combiner and prism) in order to adjust the position of the stars and maximise overlap of the images before interferometric measurements [Leinert, 2003]. After this, the prism/grism was introduced into the optical train. The used prism delivers $\lambda/\Delta\lambda \approx 30$. Only one dataset used within this thesis (for the object NGC 2264 IRS1 - see Section 4.1) was taken with a grism. To find the location of zero optical path difference (ZOPD) a small region of millimetre size around the point of path length equalisation was scanned by varying the position of the delay lines and internally stepping the OPD over a few wavelengths. After determining that the geometrical position of the delay-line for the two beams was equal, the fringe tracking could be started. The mirrors within MIDI are used to scan over a range of OPD, and after each scan the position of the fringe packet was measured and the VLTI delay lines adjusted to re-centre the fringe packet for the next scan. Photometric data were then recorded by blocking the light from one telescope and then the other. For these photometric measurements, the chopping technique is used to obtain sky and background subtraction, but no chopping is used during fringe search and tracking as the sky signal will not correlate.

All observations were taken in the HIGHSENS mode and the photometric observations immediately followed the uncorrelated flux measurements to produce the final visibilities. HIGHSENS measurements are useful when observing faint targets or low visibilities, however they are limited by the sky brightness variation between the photometric and interferometric measurements which can result in as much as a 15% uncertainty in V^2. Calibrator stars of known brightness and diameter were observed immediately before or after the source observation in order to correct for the internal instrumental contrast and convert the photometry to Jy. Calibrators were chosen from Leinert [2004].

The data from Boley et al. [2013] were reduced using version 2.0Beta1 (8 Nov. 2011) of the MIA+EWS data reduction package [Jaffe, 2004] and their final

reduced data are what are presented in this thesis. Calibrated correlated fluxes were calculated from the measured instrument values of all calibrator measurements in a single night. A wavelength-dependent calibration function relates the counts per second of correlated flux to Jansky, takes the mean over all calibrators and allows the calibration of the science data. The statistical error from MIA+EWS based on the variation of the correlated flux over the time of the fringe tracking and from individual transfer functions derived from the calibrator measurements were considered in the total uncertainty.

In addition to the data from Boley et al. [2013], one configuration of MIDI data from Grellmann et al. [2011] was used for one source and the MIDI data from de Wit et al. [2010] for another. The additional data from Grellmann et al. [2011] (2005) were taken in the SCIPHOT mode using a grism with a spectral resolution of $\lambda/\Delta\lambda \approx 230$. The observations from de Wit et al. [2010] were observed using a similar sequence to the aforementioned Boley et al. [2013] data, using HIGHSENS mode and the same prism. They used calibrators from Cohen et al. [1999] as well as version 1.6 of MIA+EWS, but the observing procedure followed was very similar to that of Boley et al. [2013]. The correlated flux spectra were extracted from the raw data using EWS by Grellmann et al. [2011]. An estimate of the sky background was made and subtracted over an area corresponding to the size of the mask over which the correlated spectra were extracted. The final spectrum is the sum of the two geometric means of the four individual spectra and agrees with what was obtained for the correlated flux after beam combination, thus confirming the consistency of the derived visibilities.

MIDI was decommissioned in March 2015 to make way for the next generation of interferometric instruments at the VLTI.

2.3 Q-band Imaging

The next size scale of the MYSO environments is traced using imaging at $\sim$20μm. Two instruments are used, the Very Large Telescope Imager and Spectrometer for the InfraRed (VISIR) and the Cooled Mid-Infrared Camera and Spectrometer (COMICS). The instruments are similar but not identical and each are introduced here.

2.3.1 The Very Large Telescope Imager and Spectrometer for the InfraRed (VISIR)

The VLT spectrometer and imager for the mid-IR (VISIR, Lagage et al. [2004]) is mounted on the Cassegrain focus of the UT3 (although at the time of writing it is temporarily mounted on UT4). It provides near-diffraction-limited imaging at high sensitivity in two mid-IR atmospheric windows; the N-band between 7-13μm and the Q-band between 17-25μm. The observations employed throughout this methodology use the Q3 filter, which has a central wavelength of 19.5μm and a half-band-width of 0.4μm, reaching a 0.6" resolution FWHM and observing with 0.076"/pixel. To remove the high thermal background from the atmosphere and telescope the VISIR detector is cooled to $\sim$9K and short exposure times are used. The chopping and nodding technique is performed with chopping frequencies between 2-4Hz and amplitudes of $\sim$13". VISIR presents two kinds of imaging mode, a normal imaging mode where the data over each nod is averaged and a burst mode where every single frame from each chop and nod position is saved. The burst mode can be useful for observing quickly varying objects on the sky and for selecting the best frame for optimal stacking. The sample of objects included in this thesis are not known to vary and as such the normal imaging mode was used for all the observations presented throughout this thesis. The observations followed an upgrade of the instrument. The introduction of a new detector (a Raytheon 1024x1024 pixel Aquarius array),

designed for space-based mid-IR observations, was introduced, providing a field of view of 38.0 × 38.0 arcsec^2 with a pixel scale of 0.045 arcsec^2. This improved the instrument's efficiency by a factor of six and increased its sensitivity by nearly 60% [Käufl et al., 2015]. The science verification observations for this upgrade were taken in February 2016, the same year as the VISIR observations included in this thesis. The sensitivities of VISIR are checked against the observations of mid-infrared calibration stars [Cohen et al., 1999] using the chopping and nodding method discussed in the previous section.

The VISIR images presented in this thesis were reduced using ESO pipelines version 4.3.1. The data reduction pipeline recipes combine a stack of chopped and nodded exposures into a final image of the source and can compute the sensitivity for standard star observations. In order to produce an image with one source (as opposed to the 4 sources present in a combined chop/nod image) it repacks the data, detects objects, corrects shifts and adds the frames together.

2.3.2 The Cooled Mid-Infrared Camera and Spectrometer (COMICS)

The COMICS instrument resides at the Cassegrain focus of the 8.2m Subaru Telescope (located at Mauna Kea, Hawaii) and observes with ∼0.13" per pixel when imaging at the diffraction limit of 0.3". Like VISIR, it observes in both the N and Q band, with 5 bands between 8.8–12.4μm, 4 bands between 17.7–24.5 μm and has some additional narrow band filters (8.6μm, 11.24μm, ArIII, SIV, and NeII). When imaging, COMICS uses a Raytheon 320 × 240 Si:As IBC array, which is cooled by a Sumitomo Gifford-McMahon-type cryostat that typically operates at 7-8K. The camera provides images at 24.5μm with a pixel size of 0.13 × 0.13 arcsec^2 and a field of view of approximately 40 × 30 arcsec^2. The 24.5μm images presented in this thesis were taken using the Q24.5-NEW filter and the Q24.5-OLD filter, with

the former providing a better fit to the narrow 24.5μm transmission window and being more robust to saturation than the latter. Through the COMICS data reduction sequence flat-fielding is used to remove the effects of gain in the detector pixels, subtraction of the chopped and nodded images is performed, the frames are added to increase the signal-to-noise and finally flux-calibration with standard stars is performed (again using Cohen et al. [1999]) to turn image counts into brightness. The data presented here were reduced as part of de Wit et al. [2009]. The chopping and nodding was performed in a similar way to that of VISIR, and the subsequent frames were stacked using IRAF [Tody, 1986]. An atmospheric extinction relationship measured on 2002/12/15 (the earliest observation) UT was 0.57 mag per airmass and on 2003/11/12 UT was 0.56 for the Q24.5-OLD filter. The overall uncertainty in flux calibration was estimated to be of the order of 10% with the largest contribution assumed to originate from the absolute calibration uncertainty in the standard flux templates.

2.4 Spectral Energy Distribution (SED)

A spectral energy distribution allows the total flux of a source to be investigated and describes how much the source is emitting at different wavelengths. The Red MSX (Midcourse Space Experiment) Source, or RMS, survey [Lumsden et al., 2013] that was introduced in Chapter 1 provides a large amount of photometric information for a number of MYSOs. Using the RMS database, the online database VizieR [Ochsenbein et al., 2000] and the literature, fluxes were obtained from near-IR to millimetre wavelengths to compile observational SEDs for the sources studied in this thesis. Fluxes included those from the 2MASS, GLIMPSE, MSX, IRAS surveys and measurements taken by instruments such as PACS (Herschel) and SIMBA. Sources other than the main MYSO target could be contaminating the data for large aperture flux measurements and where necessary they were not considered in the

fitting process. This is discussed on an object-by-object basis in Chapters 3 and 4. In addition to the previously mentioned datasets the fluxes associated with the high-resolution MIDI, VISIR and COMICS datasets are also included in the SEDs. The total flux measurements from the MIDI instrument were calculated using the correlated flux and visibility measurements from the reduced data sets and the fluxes from the VISIR and COMICS data were also included. The Graphical Astronomy and Image Analysis Tool (GAIA, Currie et al. [2014]) was used to perform aperture photometry on the images and on other calibrator objects observed at the VLT. The number of counts detected within the apertures were compared to the recorded fluxes of the objects and the difference in aperture size was accounted for, resulting in a flux density which could be added to the SED.

2.5 Radiative Transfer Modelling with HO-CHUNK 3D

Once observations have been obtained, they must be consolidated in order to relate them to physical characteristics of the MYSOs. By generating a synthetic MYSO environment through modelling and using this to produce simulated observables, comparisons can be made between models and observations. Radiative transfer modelling provides the means to simulate complex dusty environments which can be compared to the dusty environments of MYSOs. The code used to do this in the methodology of this thesis is the HO-CHUNK 3D radiative transfer code developed by Whitney et al. [2013]. This code has gone through a number of updates and was originally only 2D (as presented in Whitney et al. [2003]) and this version was used in the number of studies of MYSOs (e.g. de Wit et al. [2010]). Various forms of output are generated which can either be directly compared to observations or post-processed and then compared to the observables. In this section the capabilities

of the code and how simulated observations were generated from its output are described.

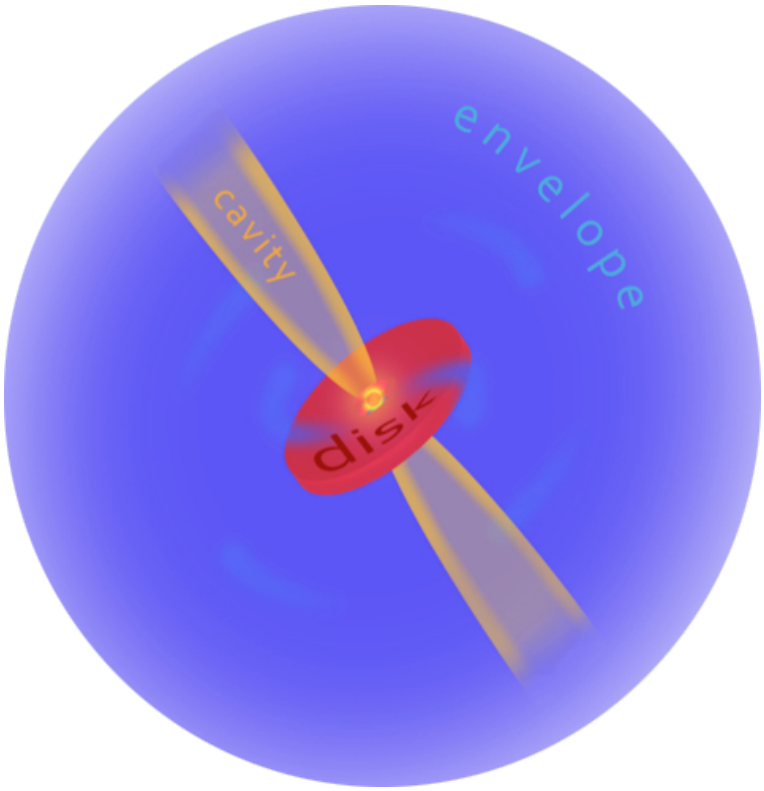

Fig. 2.1 Schematic showing the general geometry of the models used to fit the observational data. The protostar is at the centre of the system (within the disk), disk accretion was included and the envelopes are infalling. The specific details of the cavity, disk, envelope and star varied between the sources. Credit: A. J. Frost.

2.5.1 Included geometrical components

HO-CHUNK allows the user to simulate various protostellar environments. The models used in this thesis follow a schematic of an MYSO developed in Whitney et al. [2003]; a central protostar surrounded by an envelope, a bipolar outflow cavity and potentially a disk. This is illustrated in Figure 2.1. This is a generalisation of the low-mass star formation geometry of Class I objects [Shu, 1977]. Given the number of disks present in recent observations of MYSOs (e.g. Maud et al. [2018], Johnston et al. [2015], Ilee et al. [2018]) and the fact that outflows and dusty envelopes are

nearly ubiquitous around MYSOs (e.g. Purser et al. [2016], Beuther et al. [2002a]) this is a reasonable approximation of the protostellar environment. The code was designed to incorporate as accurate a geometry as possible, and presents a variety of choices as to which of these the user can employ to replicate a source.

The protostellar envelope

Previous works find that a variety of different density distributions can be applied to protostellar envelopes. Many authors (e.g. de Wit et al. [2009]) are able to fit models which describe the density of an envelope as a power-law distribution to observations. Other studies detect infall signatures in their observations of protostellar envelopes (e.g. Ohashi [2004]), indicating that a more complex density distribution will exist within these envelopes. The code provides the user with the option of both types of envelope; an Ulrich (or TSC) type envelope (Ulrich [1976], Terebey et al. [1984]) which is rotating and infalling, or an envelope that follows a simple power-law density distribution described by:

$$\rho = \rho_1 r^{-a} \tag{2.1}$$

where ρ_1 is the fiducial density at 1au and a is the density exponent. The density structure for the Ulrich-type envelope within the infalling radius is described as:

$$\rho = \frac{\dot{M}_{env}}{4\pi}\left(\frac{GM_*}{R_C^3}\right)^{-\frac{1}{2}}\left(\frac{r}{R_C}\right)^{-\frac{3}{2}}\left(1+\frac{\mu}{\mu_0}\right)^{-\frac{1}{2}} \times \left(\frac{\mu}{\mu_0}+\frac{2\mu_0^2 R_C}{r}\right)^{-1} \tag{2.2}$$

where $\dot{M}_{env}$ is the envelope infall rate, R_C is the centrifugal radius, $\mu = cos\theta$ and μ_0 is the cosine polar angle of a streamline of infalling particles as r tends towards infinity. The equation for said streamline is $\mu_0^3 + \mu_0(r/R_C - 1) - \mu(r/R_C) = 0$. R_C is set by the user and not solved for within the code. Tobin et al. [2012] also discuss

Ulrich infall signatures and produced a plot which displays these streamlines (shown in Figure 2.2). The centrifugal radius here is 100au, and it can be seen that the streamlines converge to this radius. Mass will flow down the streamlines through the infall process and collect at this radius.

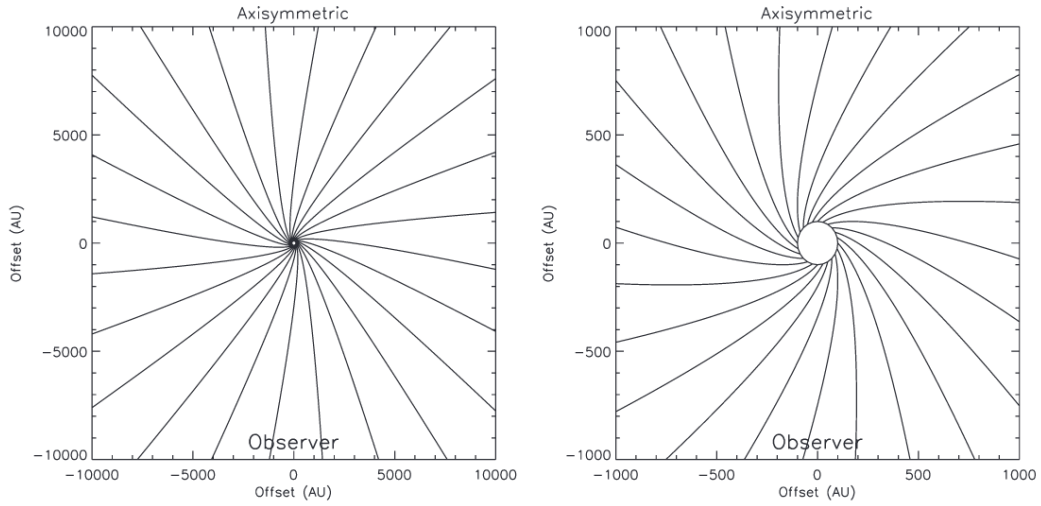

Fig. 2.2 Plots from Tobin et al. [2012] showing how the streamlines according to Ulrich's solution appear for an axisymmetric envelope, similar to those modelled in this thesis. The left shows the streamlines at scales of 10000au and the right shows their appearance at 1000au scales. Here, R_C is 100au.

The envelope infall rate takes the value of solar masses per year and is set by the user. It is essentially a proxy for the distribution of dust within the envelope and therefore has large effects on the SED. The ambient floor density is the minimum density the envelope density will trail off to at it maximum radius, so the density in the central regions will be higher than this.

A full list of the parameters which can be specified within the envelope is given below:

- the main dust type of the envelope
- the dust type for grains smaller than 200Å
- the minimum radius of the envelope

- the maximum radius of the envelope
- the type of envelope (Ulrich vs. power law)
- the envelope infall rate (Ulrich only)
- the centrifugal radius R_C (Ulrich only)
- the fiducial density (power-law only)
- the envelope exponent (power-law only)
- the ambient/floor density

Outflow cavities

Outflows are ubiquitously observed components of the massive protostellar environment and outflow activity carves bipolar cavities out of the envelope. Cavities which are conical/streamlined and those whose walls follow a curved shape are observed around YSOs (e.g. Padgett et al. [1999], Reipurth et al. [2000]) and both cases can be modelled with HO-CHUNK. A streamline is described by $\mu_0^3 + \mu_0(r/R_C - 1) - \mu(r/R_C) = 0$. The curved cavity shape for both walls follows:

$$z_i = z_{0i} + a_i \varpi^{ex_i} \tag{2.3}$$

where ϖ is the cylindrical radius, z_{0i} is the z-intercept for the outer cavity surface at $w = 0$ and ex_i is the exponent which defines the polynomial shape of the cavities. The density within the cavity follows a power-law relation $\rho = \rho_{fid,i} \times r^{exf}$. A full list of the parameters which can be specified within each cavity wall is given below:

- the main dust type within cavity
- the dust type for grains smaller than 200Å
- the opening angle of the surface of the cavity wall, θ

- the z-intercept of the cavity surface at $w = 0$
- the exponent of the cavity wall (if applicable)
- the exponent of the cavity density power-law
- the coefficients of the cavity density distribution, $\rho_{fid,i}$

Disks

The disks available for incorporation within the code are flared dust disks. These follow the density of works such as Shakura and Sunyaev [1973], Lynden-Bell and Pringle [1974], Bjorkman [1997] and Hartmann [1998] which goes as:

$$\rho = \rho_0 \left(1 - \sqrt{\frac{R_*}{\varpi}}\right) \left(\frac{R_*}{\varpi}\right)^{-\alpha} exp\left\{-\frac{1}{2}\left[\frac{z}{h(\varpi)}\right]^2\right\} \tag{2.4}$$

where ϖ is the radial coordinate in the disk midplane and the scale height h increases with radius as per $h = h_0(\varpi/R_*)^{\beta}$.

Two disk components can be included which follow these specifications, dubbed the 'large grains' and 'small grains' disks (also referred to as 'disk 1' and 'disk 2' respectively throughout this thesis), to allow the user to experiment with dust distribution (an upgrade from the original 2003 version of the code). The individual properties for each of these disks can be changed independently. The scale-height of the disk essentially alters the volume of the disk by adjusting its flaring and height above the midplane. The disk radial density exponent affects how the density distribution of the disk varies with radius, and the disk scale-height exponent dictates how the shape of the disk varies with height and radial distance.

Disk accretion can also be included in the model by utilising a hot-spot and alpha disk section of the parameter space. Hot-spots are thought to be an important component of magnetospheric accretion which is known to occur within Herbig and T-Tauri disk accretion, but the lack of magnetic activity detected around massive

stars and MYSOs makes this an unlikely disk accretion mechanism. As a result, the decision was made to not use disk accretion in the final fitting of the MYSOs in this thesis, although some tests were done and are discussed in Chapter 3. The reader is referred to Whitney et al. [2013] for a full discussion of this aspect of the code.

A full list of the parameters which can be specified within the disks is given below:

- the main dust type of the disks
- the dust type for grains smaller than 200Å
- the fraction of the mass of the disk composed of small grains
- the scale height of the disk, z
- the minimum radius of the disk
- the maximum radius of the disk
- the disk radial density exponent, α, which dictates the density variation of the disk with respect to distance from the central source
- the disk scale height exponent, β, which dictates the height of the disk with respect to distance from the central source

In addition to these basic specifications (which applied to the single disk in the 2003 version of the code and the two disks in the 2008 version of the code) a variety of additional disk features were added to the 2013 version including gaps, puffed-up rims/walls, curved inner rims/walls, warps and spirals. Warps are again, thought to occur in low-mass disks, but given that a warp was detected in a disk around a massive protostar by Sanna et al. [2019] it seems that some mechanism may be able to warp massive disks too. HO-CHUNK simulates warping by adopting

a parameterised, variable form of the scale height that ultimately lines up with the stellar accretion hotspots but this was not experimented with during in the fitting.

Puffed-up rims are included by using a parameterisation similar to the warp which adds to the scale height of the disk depending on cylindrical radius. Curved inner rim/walls are handled in a similar way by subtracting from the scale height depending on cylindrical radius. Gaps are included and Whitney et al. [2013] suggest to set the gap density to 0.01% of the density in the disk where the gap is not present based on their work. The position of the gap is specified in terms of au, and both the curved and inner rims can be applied to the rims of gaps as well as the inner rim of the disk. Spirals can also be induced and are included through a combination of the scale height functions for warped disks, puffed up rims and curved inner rims.

Varying this parameter space

Given that there are over 50 parameters within the model which can be varied, some decisions had to be made within the fitting process. Within the parameter space of the envelope it was decided to start with the Ulrich-type density distribution of the envelope given its success in the work of Wheelwright et al. [2012] and to vary the parameters therein. It was decided that if through the variation of the Ulrich-type envelopes parameter space no suitable fits could be found, that power-law envelopes would then be investigated.

For the bipolar outflow cavities, the cavity opening angle and density were widely varied. The cavity shape exponent b was experimented with during early fitting. It was found that changing the exponent from 1.5 (curved) to 1 (streamlined) increased the amount of $\sim$20μm emission slightly. Ultimately it was found that no deviation from the 1.5 default exponent value was required to obtain fits to the datasets. The density exponent was varied in a similar way, but had bigger effects on the observables. Increasing the density exponent from 0 essentially increases

the density in the bottom of the cavity, therefore making the 20μm more compact and significantly reducing the amount of simulated extended 20μm emission. This proved an important aspect of fitting the image profiles of barely resolved sources.

The disk parameter space is extremely large and as a result a number of parameters were not varied throughout the fitting. Both the disk components (large and small grain) were utilised during the fitting. The percentage of the dust in the large grains disk, otherwise known as the dust fraction, was also varied. The disk radial density exponent α and disk scale height exponent β, which dictate how the density profile and scale height of the disk vary with r were not varied and fixed to match the results of hydrostatic equilibrium modelling by D'Alessio et al. [1998]. The scale height of the disk z was widely varied. The minimum and maximum disk radii were varied widely but the maximum disk radius and the centrifugal radius were kept equal, as infall from the envelope will provide the material to form the disk. The constraint on the inner rim of the disk is greater than it is for the outer radius as the inner radius was traced by the higher resolution, more sensitive MIDI data, while the outer radius was traced by the image profiles and SED. The capabilities of the code which deal with 3D substructure were not heavily used throughout the modelling. Only if a suitable fit could not be found for the majority of the MIDI fits were these parameters investigated. Ultimately this was only the case for one source. Many of these substructures such as puffed-up rims and curved inner rims traces exist at scales too small to probe (<1au) with our observables and so were not a focus of the fitting.

2.5.2 Dust

The specific features of an MYSO's environment will be dependent on the specific physical and chemical processes happening within it which in turn depend on its composition. Different types of dust are found in protostellar environments and so

to consider the total emission of the object, the code ascribes different dust types to each distinct geometry. It was decided, to simplify matters, not to experiment with different dust files throughout the fitting. The dust files used are those suggested and used by Whitney et al. [2013] and these are described in this section. Figure 2.3 shows the opacity of each of the dust types included in the fitting process.

Four different dust types are used within the code, pertaining to different aspects of the protostellar environment. The cavity and 'small grains' disk share the same dust type, based on that of Kim et al. [1994] for the diffuse ISM (with maximum grain sizes of 0.01μm). For the envelope grains, Whitney et al. [2003] produced a size distribution of grains in agreement with $R_v = 4$, which is typical of dense regions of molecular clouds [Whittet et al., 2001]. To include the effects of ices in the cooler outer regions of the envelope a layer of water ice was included as the outer 5% of the grains' surface. This final percentage was decided upon after variation testing and comparison to polarisation observations in Whitney et al. [2003]. For the large grains disk, a dust distribution based on models from Wood et al. [2002] were used, with grain sizes ranging between 5μm and 1mm.

Polyaromatic-hydrocarbons (PAHs) and very small grains (VSGs) are additional components added to the 2013 version of the code. If these are included, dust files which are identical to the above files are used, with the exception that they do not include the grain population with sizes smaller than 200Å as they are calculated in a separate very small grains file. The model for these small grains is that of Draine and Li [2007]. As most of the sources studied in this thesis are well known and previously studied, it could be determined from infrared spectra of the sources whether PAHs were present within the MYSO environments. The fraction of the grains in each protostellar component is set to 0.1937; $\sim$5% due to PAHs and $\sim$15% in VSGs. This is in accordance with standard Galactic abundance values as quoted by Draine and Li [2007]. The PAHs/VSGs files were used if evidence of them was

reported for the MYSO in the literature, and this is discussed further in Chapters 3 and 4.

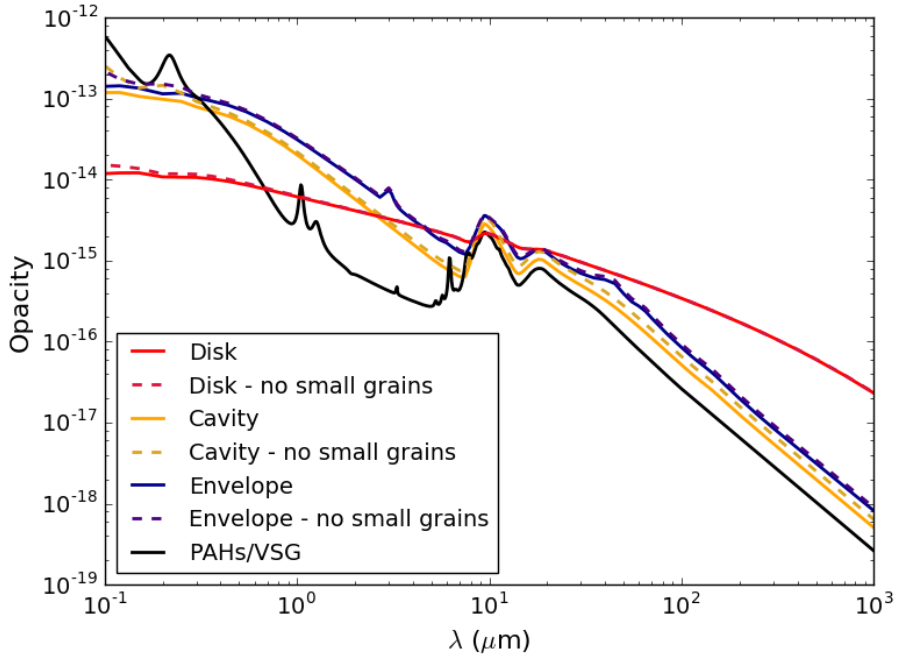

Fig. 2.3 Opacities of the different types of dust used in the RT models. Where PAHs/VSGs were included with the code, the models indicated by dashed lines were used instead of the those with solid lines.

The dust sublimation, or destruction, radius is calculated as $\frac{R_{sub}}{R_*} = (\frac{T_{sub}}{T_*})^{-2.085}$ where the dust sublimation temperature is chosen as 1600K, to be consistent with the included dust types [Barvainis, 1992]. This relationship between dust and stellar temperature was determined analytically by Whitney et al. [2003] through the calculation of a series of two-dimensional radiative transfer simulations of disks around young stars, which included re-radiation and a distribution of dust grain sizes based on Wood et al. [2002].

2.5.3 The method of radiative transfer

To solve the radiative transfer equations, HO-CHUNK code builds upon the Monte Carlo radiative equilibrium routines of Bjorkman and Wood [2001]. The code of Bjorkman and Wood [2001] used a numerical optical depth integrator which acts

analytically on a predefined density. To allow the HO-CHUNK code to handle arbitrary density distributions (which apply to features such as outflow cavities or 3D envelopes) the Bjorkman and Wood [2001] code was employed within the 3D spherical-polar grid code of Whitney and Wolff [2002]. Each cell within the grid effectively has a constant density, allowing the optical depth integration to be performed in a straight-forward manner. Because this means the density only needs to be calculated once at the beginning of the processing of each cell, complex density formulations across the entire grid can be employed. The spacing of the grid varies across different components of the protostellar environment. For example, for modelling a protostellar system with an envelope and a disk, the radial spacing of the grid in the disk regions is handled logarithmically, while the outer edges of the envelope follow a power-law spacing.

In the models, the luminosity is produced by the central star and is absorbed, re-emitted or scattered by the surrounding disk/envelope/cavity material. The Lucy method [Lucy, 1999] is used to efficiently calculate the temperature and emission spectrum in each grid cell as photons are absorbed. This method uses Monte Carlo techniques to iteratively compute the radiative equilibrium temperature of a material in local thermodynamic equilibrium in one to three dimensions. A radiative equilibrium algorithm corrects for the temperature in each grid cell by calculating the difference between the new temperature and previously calculated temperature and energy is conserved throughout. The Henyey-Greenstein function (HGθ) weights photons by the scattering phase function (where θ is the angle through which the photon is forced to scatter towards the observer). The forward-scattering parameter g and albedo ω are computed at each wavelength from the relevant dust grain models. Polarisation is calculated assuming a Rayleigh-like phase function for the linear polarisation [White, 1979].

The Monte Carlo codes allow the production of results at all inclinations simultaneously. 'Peeling-off' is also utilised (e.g. Yusef-Zadeh et al. [1984]). This process

uses weighted photons to allow the user to obtain high resolution images at particular inclination/direction and works as follows.

Direct photons are emitted towards the observer with weight:

$$W_{direct} = e^{-\tau/4\pi d^2} \tag{2.5}$$

where τ and d are the optical depth and distance from the point of emission to the observer. To calculate the scattered light contribution, a random direction is chosen and the optical depth τ_1 is calculated from the point of emission to the edge of the grid. The photons are then forced to scatter at an optical depth less than τ_1 sampled from:

$$\tau = -log[1 - \varepsilon(1 - e^{-\tau_1})] \tag{2.6}$$

This reproduces the correct probability distribution for optical depths and ensures that all photons scatter at least once. After this the photons are allowed to scatter until they exit the medium or are absorbed, which is checked by comparing a random number with the albedo at each interaction location. At each scattering location a portion of the photon's energy is 'peeled-off' and directed towards the observer. The weight of this is:

$$W_{scatter} = a(1 - e^{-\tau_1})e^{-\tau_2}HG(\theta) \tag{2.7}$$

where τ_2 is the optical depth from the scattering location to the observer. The total intensity is the sum of the weights of the direct and scattered photons.

2.5.4 Simulating Observations

HO-CHUNK produces a wide variety of output after calculating the RT, and scripts are packaged into the code which allow the post-processing of said output. Intensity

images can be generated and it is from these images that the MIDI, VISIR and COMICS data were simulated. In order to simulate the MIDI observations, model images were generated at 7.5, 8.5, 9.5, 10.5, 11.5 and 12.5μm so as to sample the N-band wavelength regime. Images 0.52" (for UTs) or 2.29" (for ATs) in size were generated, corresponding to the MIDI slit width, with a pixel size of $\sim$0.01". In previous work (e.g. de Wit et al. [2010]) the UT-airy disk was used as the field-of-view and the model images were multiplied with a Gaussian of this size in order to account for the effects of the telescope. For this thesis their methodology was revised and the slit-width is used as the size of the simulated N-band images with no Gaussian multiplication. This choice was made because the MIDI data reduction process accounts for the effects of the telescope and removes them, meaning that multiplying the model images to include telescope effects is not necessary, if the final aim is to simulate the visibilities (the final product of the data reduction). It is ultimately the slit size that determines the amount of observed emission from the object, and as such this is used as the size of the model images.

Once the model images are generated they were post-processed in Python in order to allow a direct comparison to the observations. Taking the fast Fourier Transform (FFT) of the images provides a fully-filled u-v plane from which the visibilities corresponding to the position angle and baseline of the observations can be extracted. The position angle of the source (or its orientation) on the sky was also taken into account at this stage, as the model images are automatically generated with a 0° orientation. If the PA on the sky was obvious from previous work, this was used in the consideration of the final PA. If there was no obvious way to determine this PA (e.g. previous works show the source to be face on) and no value was stated in the literature, the PA was varied between 0-360° in 20° intervals in order to find a PA that allowed a good fit to the MIDI data and then narrowed down if required.

At lower densities gridding effects exist in the model images, creating ring-like structures within the cavity. In order to quantify the effect this may have on the final

visibilities the model images were convolved with a Gaussian with a FWHM of 10 pixels to remove any high frequency structure and then subtracted from the original model image to isolate the rings and quantify their contribution to the emission. The rings constitute $\sim$4% of the overall image counts and therefore any effects they may have on the model visibilities are negligible. These difference were included in the errors on the simulated visibilities.

In order to simulate the Q-band images a model image of the same field of view as the observations was generated at 19.5 or 24.5μm, depending on whether VISIR of COMICS data was available for the specific source. The model image was then convolved with the observed PSF standard star from the same night as the observations in order to accurately include the effects of the sky on the modelled object. An azimuthally averaged profile was taken from the images to allow easy comparison to the source, PSF and model. Previous works such as de Wit et al. [2011] convolve their model images with Gaussian PSFs but it was found through the work of this thesis that a more accurate fit, especially are larger radii, is obtainable by using an observed PSF.

It was straight-forward to edit the SED generation routines to allow the inclusion of the observed fluxes. To generate an SED the post-processing script written by Whitney et al. [2013] was utilised which extracts the flux and wavelength data from the RT output. Fluxes from the RMS and the MIDI observations were overlain on the model SED to allow comparison. Thanks to the 'peeling-off' nature of the code, SEDs could be viewed at multiple inclinations with no addition to the computation time. The Monte-Carlo thermal file, which sets-up and executes the code and model runs, allows the specification of the apertures generated in the SED so that they could be aligned with those of the observations. As such, minimal additional post-processing had to be performed in order to compare the simulated and observational SEDs.

2.6 Fitting Process

In the previous section the parameter space available to use throughout the fitting of the objects was described and various choices can be made as to how to best utilise this. The total number of variable parameters within the code amounts to $\sim$50 and varying all of these completely would have not been sensible, or workable, given the number of parameters which are traceable by the observables included in the methodology. Additionally, running codes which solve for hydrostatic equilibrium would also take an unsustainable amount of computing time (a disk run without solving for HSEQ runs in about 20-40minutes on a supercomputer node, whereas a model solving for HSEQ takes a minimum of around 4hours). Given that the disk components of the code were originally designed based on results from hydrostatic-equilibrium calculations, it can be argued that this is indirectly taken into account without the need for computationally expensive HSEQ modelling. Since outflows are ubiquitous around MYSOs, no models without bipolar outflow cavities were run. The Ulrich-type envelope was the original envelope type included in the code as infall signatures are observed for envelopes [Ohashi, 2004] and because this type of envelope has been successfully used in previous works (e.g. de Wit et al. [2010], Wheelwright et al. [2012]). For no source was the fit unsatisfactory to the point where switching to a power-law envelope was required during the fitting process. A polynomial cavity with b=1.5 was the starting point for the fitting and, similarly, for no source was the fit unsatisfactory to the point where the parameter space needed to be expanded to vary this value.

The dust types for each protostellar section were kept constant, unless PAH emission was observed in the spectrum of the sources, in which case they were experimented with (discussed in Chapters 3 and 4). Two disk components, the large and small grains disks or disk 1 and disk 2, were included in the fitting process. The simplest disk geometry was always the starting point. Often, a fit could be

found by just varying the scale heights, mass, inner and outer radii of the disks. The radial and scale height exponents were not varied through the fitting process. Were a fit unobtainable with the simple disk geometry, the substructures section of the code was engaged. Puffed-up rims and curved inner rims were tested, but these had negligible effects as all the sources are too distant for this sub-au-scale geometry to be detectable. Spiral structures were also investigated where necessary and had marked effects on the simulated visibilities when they harboured the majority of the disk mass.

In terms of the observables, SEDs are degenerate (as previously discussed) and in principle the easiest to fit, so this observable was the starting point for the fitting process. The fitting of the MIDI and VISIR/COMICS data followed and the simulated visibilities and profiles were checked simultaneously as each parameter was systematically varied. Extreme testing (e.g. varying cavity angle by 25° or cavity density by an order of magnitude) was done to determine whether an observation was going to affect the datasets. If a change occurred in the simulated observables the values were changed in smaller intervals to then constrain the fit and improve the model. It was often the case that the higher the resolution of the dataset, the more stringent the constraint on the parameters it could trace. For example, the inner disk radius which traced by MIDI ($\sim$0.01" resolution) could be constrained down to 5au scales, whereas the maximum disk radius and centrifugal radius (traced by the VISIR/COMICS data of $\sim$0.6") envelope radius could be constrained down to a few hundred au.

Given the success of the envelope-only model of de Wit et al. [2010] in fitting the VISIR profiles of a range of MYSOs in Wheelwright et al. [2012] and the MIDI visibilities of MYSO W33A [de Wit et al., 2010] the same central object, envelope and cavity parameters were used as a starting point for the modelling of W33A (which is discussed later in this chapter) and G305 (which is discussed in Chapter 3). The model did not immediately present a satisfactory fit, so a large portion of

the parameter space was varied in attempts to fit the observational data. A range of parameters were systematically tested covering the envelope properties, cavity properties and disk properties in order to constrain the MIDI and VISIR/COMICS fits.

2.6.1 Constraining model fits - examples from previous work

When combining a variety of observations, the balance between the fits of those observations needs to be considered. When the SED alone is utilised, a common method of uncertainty quantification has been the chi-square minimisation. The SED Fitter tool of Robitaille et al. [2007], which uses a large grid of models and has been used to analyse the data of many protostars, uses this minimisation. Once a method is expanded past SED considerations, which as previously discussed is important to better constrain protostellar environments, the uncertainties in the fit parameters must be and have been considered differently. This is because different observations at different wavelengths using different techniques will all trace different scales of MYSO environments in contrasting ways. Few papers dedicated to MYSOs in the literature fit RT models to more than one set of observation, but some of those which best translate to the work of this thesis are discussed here.

One work which uses multiple types of observable and is Linz et al. [2009]. In this paper the environment of one MYSO is studied through the use of MIDI interferometric data and an SED. They use the aforementioned SED Fitter tool to constrain the fits on their SED and compared the model visibilities associated with a variety of acceptable models from that process in order to decide upon their best fitting model. A similar approach was taken in de Wit et al. [2010], where again the SED Fitter was used to provide some quantitative analysis of the SED fits but the overall fit between the MIDI and SED was determined by eye. Similarly, in de

Wit et al. [2011] where one MIDI dataset and an SED were used, the overall fit was determined by eye.

Johnston et al. [2013] modelled the SED and 2MASS image profiles of the MYSO AFGL 2591 using a Monte Carlo radiative transfer code. The reduced combined chi-square was calculated for the line profiles and their SEDs, giving equal weight to each observation within the final chi-square. They studied the constraints on their parameter space by systematically varying a few key parameters and investigating how the chi-squared varied with each parameter.

Boley et al. [2013] determined the best fits among the 2D Gaussian models they fit to their MIDI data by performing a grid search over their parameter space and the chi-square minimisation. The uncertainties on the fitting parameters were found using a Monte Carlo approach. This involved generating synthetic observations which were normally distributed about the mean visibility of their observations and repeating this to optimise. This was a viable approach given that only one observable (their MIDI data) was being used in their work. In Boley et al. [2016] a variety of different models were applied to a combined dataset of MIDI observations, T-ReCS aperture masking data and K-band interferometric data for MYSO. Gaussian modelling was again used to fit their visibilities and the chi-square minimisation (as in Boley et al. [2013]) was used to determine good fits with a different fit found for the different wavelength datasets. Temperature-gradient disk models were also used to fit to their K-band visibilities and N-band correlated fluxes and a reduced chi-squared was calculated across the different observations, although the weighting of this not explicitly explained. Finally, radiative transfer models were employed via the use of the 2003 version of HO-CHUNK [Whitney et al., 2003]. They did not attempt to reproduce the SED throughout this modelling; only the K-band visibilities and N-band fluxes were modelled. No errors are formalised on their final parameters and the chi-square is not utilised.

In Liu et al. [2019], the model grid of Zhang and Tan [2018] was used to fit the SEDs of a number of MYSOs. Following the method of De Buizer et al. [2017] they performed the chi-square minimisation to find five best fitting models for each of the MYSOs. Five parameters alone were varied within the fitting process in order to investigate how the SED is affected by models corresponding to different evolutionary phases that occur within the turbulent core model.

The aforementioned works constitute those most similar to the work of this thesis. Hardly any of these works calculate a global chi-square for different datasets, nor do they derive formal errorbars on their parameters when RT codes are used. This appears to be the inherent compromise of combining many datasets and using a complex modelling approach. Including multiple observations and a large model parameter space provides a much better picture of a source, but formalising the combined error using these methods becomes unfeasible. Calculating an overall chi-square and giving each observation equal weight, as has been done in some of the works mentioned in the previous subsection, is not an appropriate approach for the case of this thesis. The MIDI spectrum and VISIR profiles have dozens of points covering a very small wavelength regime while the SED covers a wavelength regime from 1 to 1000s of micron with a small number of data points. This means that there will be an obvious bias within any chi-squared value calculated for the combined datasets, in favour of the 7-13μm and $\sim$20μm datasets. Another reason to not combine the chi-squared is that each observation traces very different scales, so similarly the innermost and smallest geometrical features of the source, which is traced by the data-rich MIDI spectrum, will be unfairly focused on through the use of a combined chi-square. With this in mind the data in this thesis were ultimately fit by eye as per previous works which have handled multiple and similar observations to this thesis such as de Wit et al. [2010] and de Wit et al. [2011]. However, the chi-square was calculated for each observable, and in the next section the information provided by this process is discussed.

2.6.2 Comments on the fits of this methodology

In order to comment on the uncertainties involved in the fitting of the wide parameter space provided by the RT code, the chi-squared was calculated for each observation. The chi-squared was calculated separately for each configuration of the MIDI observations and then averaged. The VISIR chi-squared was calculated from the radial profiles up to the point where the background noise exceeded the rms. The SED chi-squared was calculated by convolving the model SED with filter fluxes corresponding to the available data points. While the SED was the starting point for the fitting (like de Wit et al. [2010] and Linz et al. [2009]) the SED fitter tool is not made use of. As such the fits of these models avoid the inherent biases of the Robitaille grid of models which are discussed at length in Robitaille [2017].

The chi-square can provide insight into how tightly constrained various parameters are by the methodology of this thesis. This is illustrated in this section by plotting the chi-square against various parameters using models used during the fitting process of the source W33A, which is discussed later on in this chapter. Figures 2.4 to 2.10 show how the fit to each different observable varies with a few key parameters involved in the fitting process through the use of the chi-square. The chi-square has been normalised so as to highlight the change that occurs between the best fitting model and others as a single parameter is varied.

Figure 2.4 illustrates how the chi-square varies with minimum disk radius. When the plots for the MIDI, image profile and SED are compared, it is evident that the MIDI data is the only observable which can constrain the inner radius of the disk in a model. A clear minimum is observed in the MIDI chi-square at the sublimation radius for this particular model (which is based on that of W33A which will be discussed later in this chapter) but this is not observed for either the image profile or SED chi-square. This suggests that for the 2.4kpc distance of this source, the disk is too small in scale to have significant effects on the $\sim$20μm image profile. Additionally,

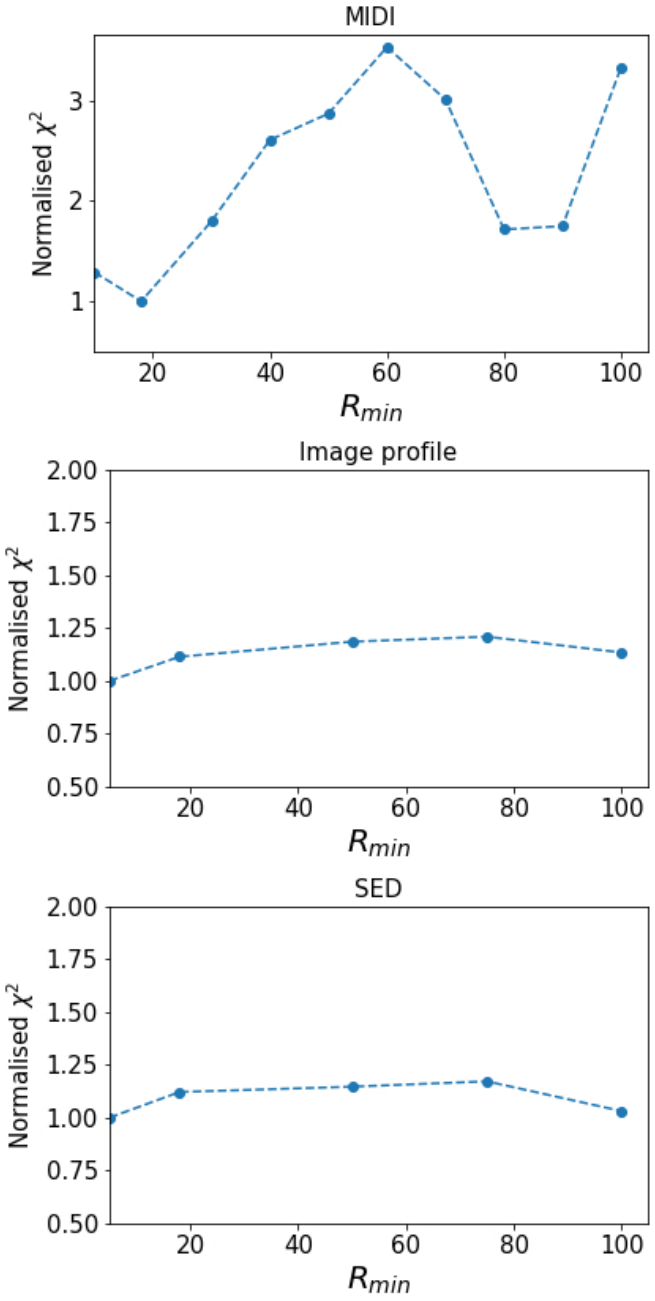

Fig. 2.4 Plots showing how the chi-square for each observable varies with disk minimum radius and that MIDI is most sensitive dataset to this parameter.

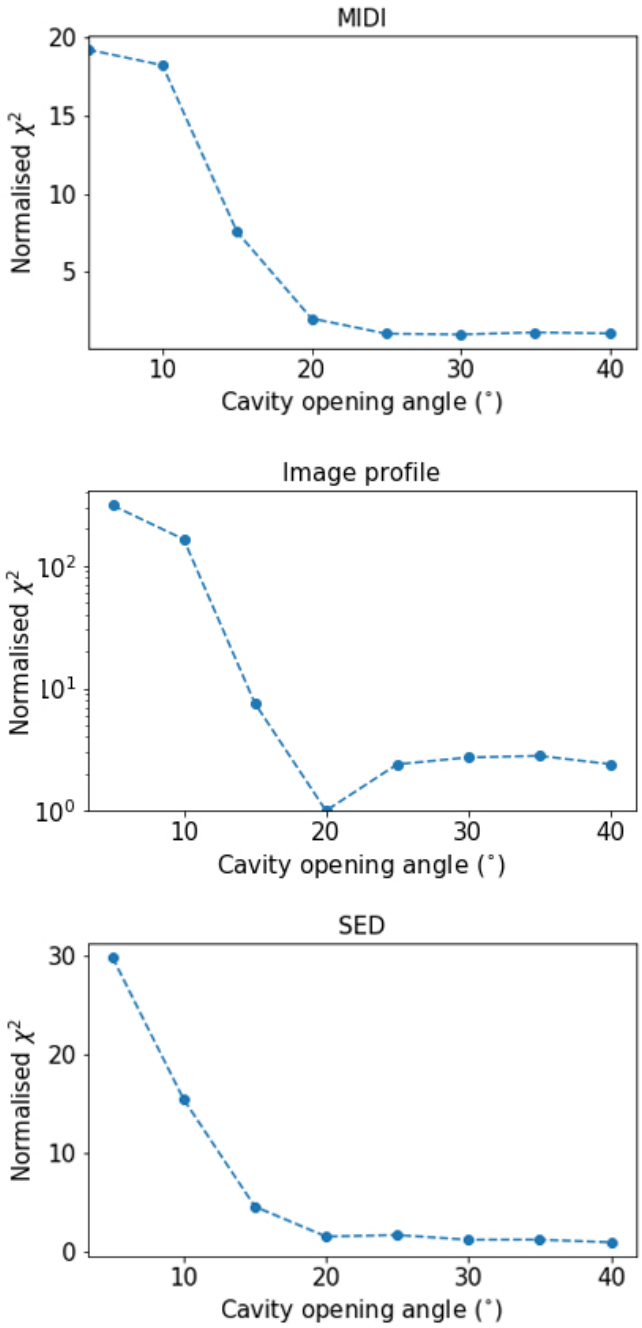

Fig. 2.5 Plots showing how the chi-square for each observable varies with cavity opening angle. In this case, the COMICS profile is the most sensitive dataset to this parameter.

this highlights the embedded nature of the MYSOs and its effect on the SED, as the disk has negligible effects on an MYSO SED whilst being the dominant source of emission for low-mass protostars, especially Class II and III sources. Finally this demonstrates MIDI's merit in determining the inner geometry of an MYSO. The normalised chi-squared value doubles at 31au, providing an indication of the range of possible values for this parameter. It corresponds to an error on the minimum radius of approximately 13au.

Figure 2.5 illustrates how the image profiles at $\sim 20 \mu$m help to constrain the cavity opening angle of the source. Whilst the MIDI and SED chi-square trail off and therefore do not place a tight constraint on the cavity opening angle, a clear minimum is seen in the image profile chi-square, centered on 20°. This implies that $\sim 20 \mu$m emission traces cavity wall emission which has been concluded by other studies such as Wheelwright et al. [2012]. Considering the cavity opening angles at which the chi-squared gets twice as bad, the cavity opening angle here is constrained to $\sim 4^{\circ}$ of accuracy.

In some cases a minimum is observed across different observables showing an overlap between the areas traceable by each observation. Figure 2.6 clearly shows how as the cavity density exponent increases, the fit for each observable worsens for this source. This implies that a constant density cavity best satisfies the observables, perhaps suggesting that outflow activity is constant for this MYSO. Similarly, the MIDI, image profile and SED chi-square all show minima in similar places when examining the envelope infall rate (Figure 2.7). For the image profile and SED, an envelope infall rate of 1×10^{-3} $M_{\odot}yr^{-1}$ is best, while for the MIDI this is 5×10^{-4} $M_{\odot}yr^{-1}$. The level of improvement for all the chi-squares between the 1×10^{-3} $M_{\odot}yr^{-1}$ and 5×10^{-4} $M_{\odot}yr^{-1}$ values is less than a factor of two, but given that two observables reach a minimum at 1×10^{-3} $M_{\odot}yr^{-1}$, this would be the final value. Past 10^{-3} $M_{\odot}yr^{-1}$, the chi-square rapidly worsens for all observables. This is because for higher envelope infall rates, too much material is being fed into the

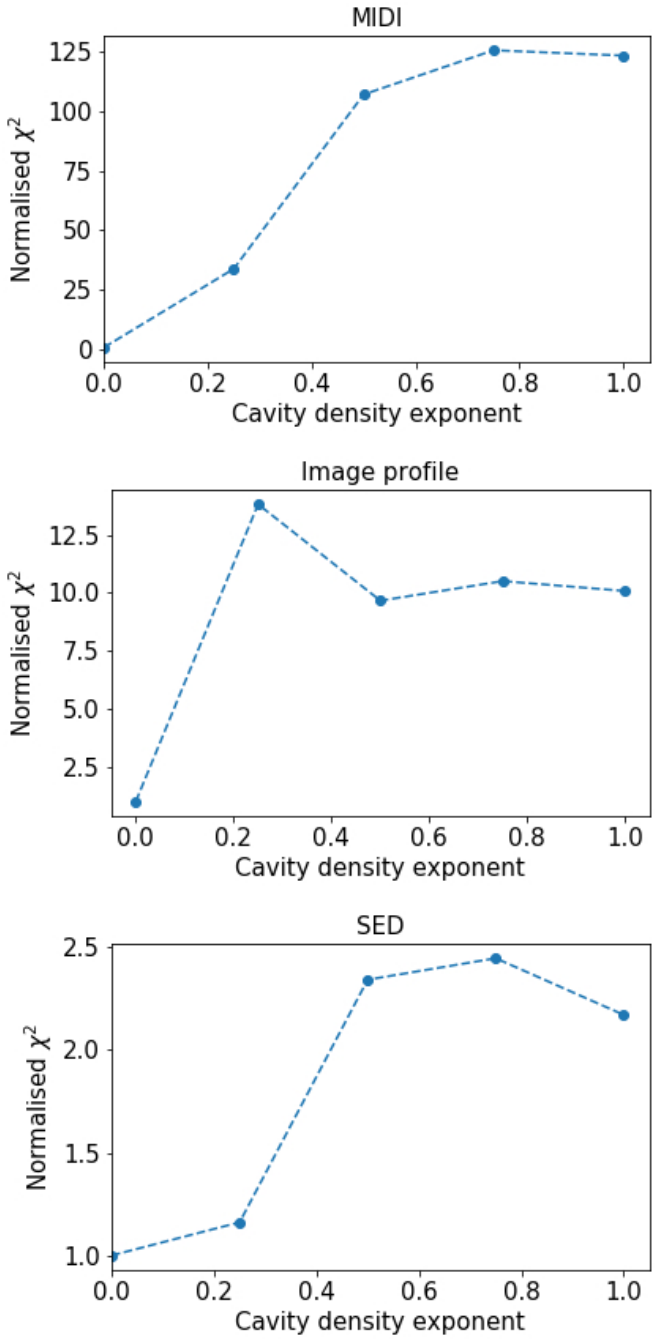

Fig. 2.6 Plots showing how the chi-square for each observable varies with cavity density exponent. Although variation is observed across all datasets, MIDI is the most sensitive.

centre of the environment. This worsens the fit by increasing the density of its central regions to the point where far-IR and sub-mm emission dominates for the source, reducing the emission at N-band and Q-band wavelengths and making the SED resemble that of a Class 0 source as opposed to a Class I or II.

Figure 2.8 shows how each of the individual chi-squares vary with the disk mass. The MIDI chi-square is the only one to show any obvious variation, and even this is small when it is considered that the chi-square changes by a factor of $\sim$4 for a two-order-of-magnitude change in disk mass. When varying between 10, 20 and 30 solar masses, negligible variation in the chi-square is observed, even though this change in mass will obviously have important effects for the physics of the disk. The lack of sensitivity of the observable to disk mass is due to the fact that as the disk gets more massive (and therefore denser since other disk parameters are kept constant during this exercise) it will also get cooler. Eventually the density will be such that only the innermost rim of the disk will be hot enough to be re-radiating at MIDI wavelengths and the rest of the disk will be emitting at much longer wavelengths. Since the geometry of the inner rim is not changing, once this disk mass is reached the change in the MIDI emission will be marginal, which the chi-square illustrates. Therefore, disk mass is not a property which is well constrained by the methodology of this thesis and if anything can only be used to determine a minimum mass.

Figure 2.9 outlines another parameter that is not well constrained - the outer disk radius. Minimal variation for each observable is found and all lower than a factor of two. This is to be expected. The outer regions of disks have been shown to be well traced by millimetre and sub-mm emission in studies such as Ahmadi et al. [2017], Johnston et al. [2015] and Ilee et al. [2016], so the fact that the infrared datasets used in this methodology do not well constrain this parameter is unsurprising.

Figure 2.10 shows how changing the scale-heights of the disks in the models affects the fit. In the models used for this plot, two disks were used but the scale-height for the large grains disk (the flatter disk) is plotted. The small grains disk was

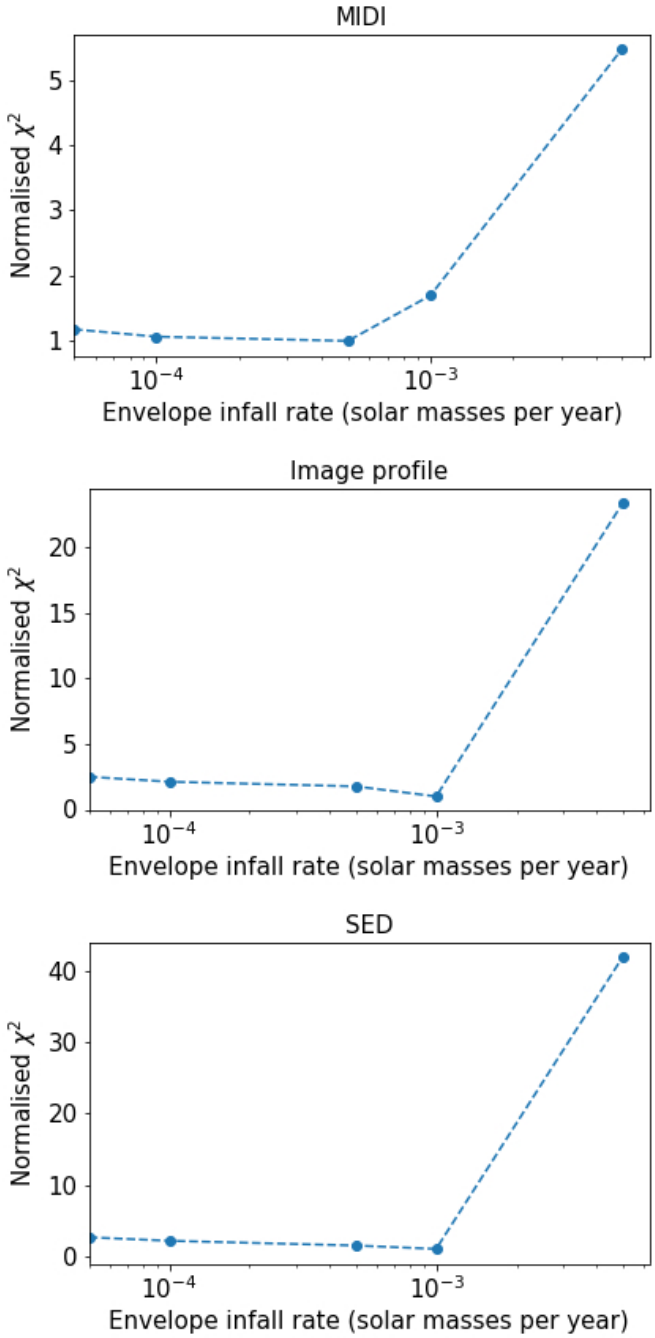

Fig. 2.7 Plots showing how the chi-square for each observable varies with envelope infall rate.

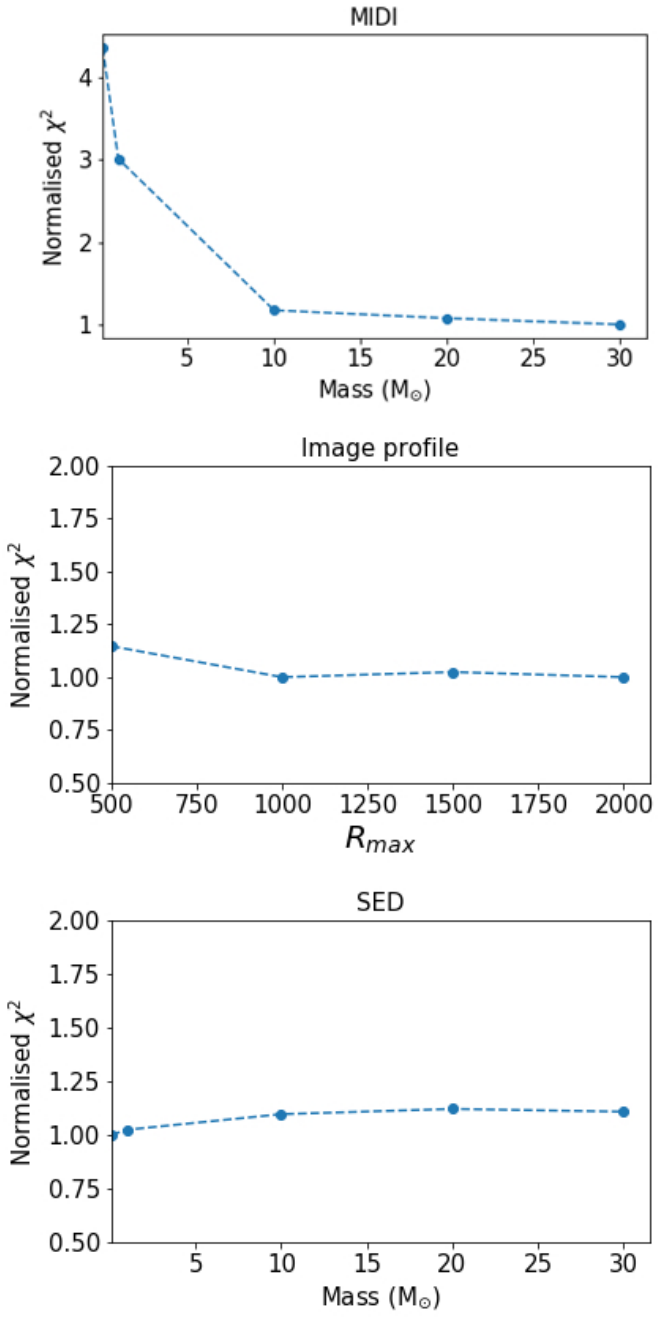

Fig. 2.8 Plots showing how the chi-square for each observable varies with changing disk mass. Little variation is seen, implying that this parameter is not well investigated by the observables.

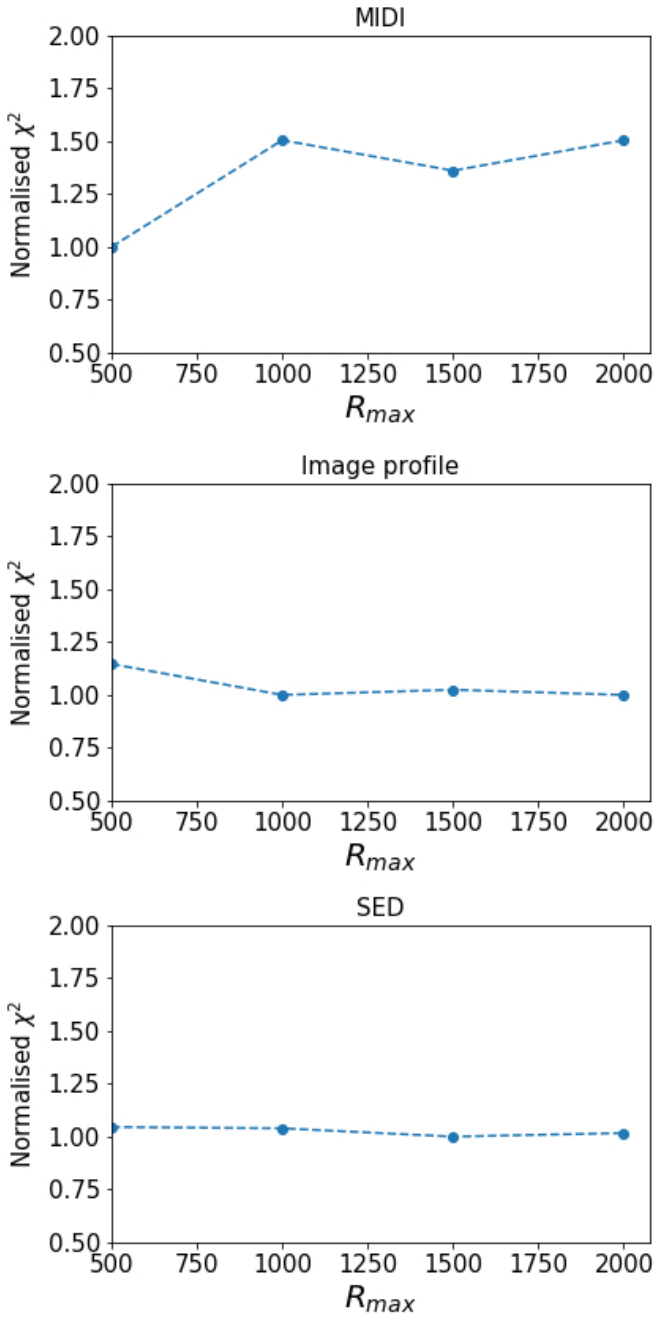

Fig. 2.9 Plots showing how the chi-square for each observable varies with disk maximum radius. Little variation is seen, implying that this parameter is not well investigated by the observables.

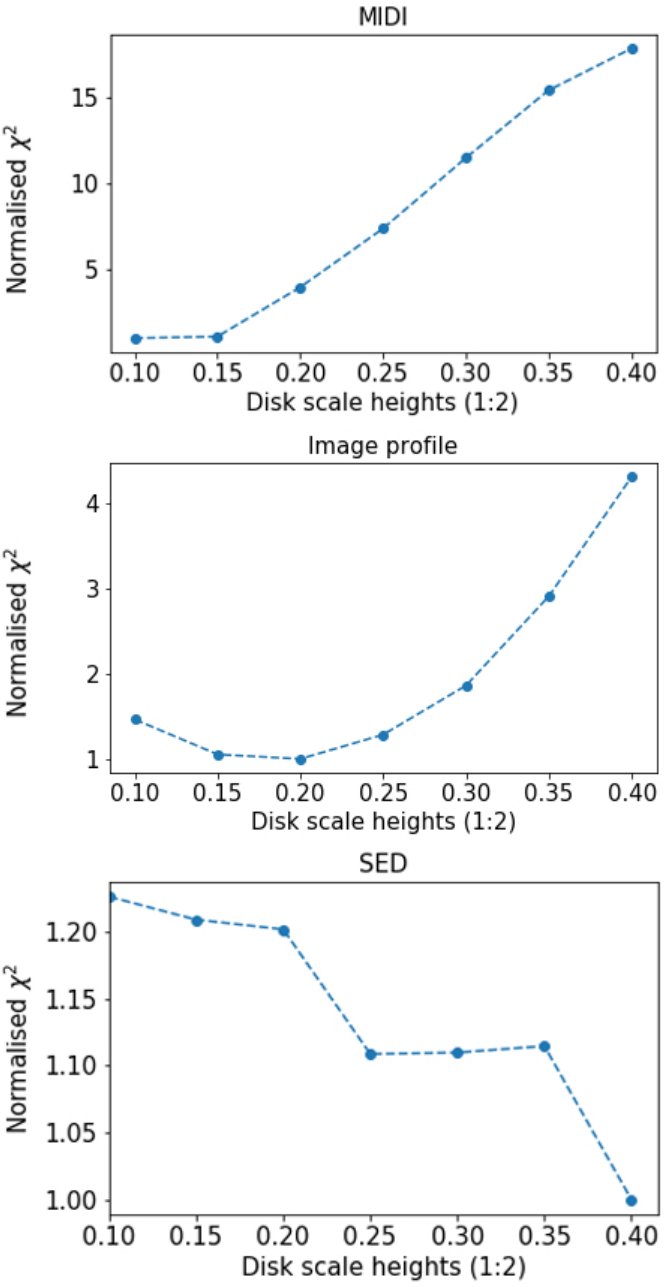

Fig. 2.10 Plots showing how the chi-square for each observable varies with disk scale-height.

included with a scale-height double that of the large grains disk. This is done based upon the hydrostatic calculations of D'Alessio et al. [1998]. Figure 2.10 shows an interesting case where increasing the disk scale-height worsens the fit to the MIDI data but improves the SED fit. A minimum is seen for the image profile chi-square, but given the small variation (less than a factor of two) between 0.1 and 0.3, this is not a high level of constraint. Given the distance for the source in this example is 2.4kpc, the disk is unlikely to be having significant influence on the $\sim$20μm emission, so this poor constraint is understandable. The SED is also poorly constrained, as the chi-squared varies within a factor of two across the whole parameter space. However, increasing the scale-height exposes a larger surface of the disk to radiation from the central source, which will lead to an increase in near-IR flux which improves the SED fit. Increasing the scale-height whilst maintaining the same disk mass lowers the density of the disk overall. Similarly this increase in scale-height will provide a larger area for irradiation at MIDI wavelengths, worsening the fit to the MIDI visibilities for this source. Even though opposing trends are observed in the variation of the chi-square for between the different observables, it is evident that the improvement in the MIDI when varying this parameter is the most significant. This is again consistent given that MIDI is the most likely dataset to be sensitive to this inner disk geometry.

Overall, it can be concluded that while the chi-squared may not be an appropriate way to provide a blanket estimate of a fit when multiple observations that trace different scales are used, it can assist in the determination of which observables are key for tracing different physical characteristics of MYSOs.

2.7 Example dataset

Throughout this section the works of de Wit et al. [2007] and de Wit et al. [2010] have been referenced, which studied the source W33A using a methodology similar

to the one presented throughout this chapter,. The key differences between their methodology and the one presented here are that here, the slit-width is used as the field of view of the MIDI data (which is not multiplied by a UT Airy disk), that different dust files are used and that the version of HO-CHUNK used in this work has many more features. This object therefore presented a good opportunity to demonstrate these differences and illustrate the fitting process relevant to this thesis.

2.7.1 W33A

W33A is a well studied source due to its plethora of ices which make it interesting for spectral studies (e.g. Gibb et al. [2004]). de Wit et al. [2010] found that the source's MIDI data and SED could be satisfied by an envelope-only geometry with two bipolar outflow cavities. Ilee et al. [2013] attribute the CO bandhead emission to a 1-2au disk. Davies et al. [2010] find a Brγ jet perpendicular to a disk found in CO emission and absorption using NIR adaptive optics integral field spectroscopy. At longer wavelengths, two large continuum sources are observed within W3, the brighter of which is MM1 [Galván-Madrid et al., 2010] or W33A. Maud et al. [2017a] studied the source with ALMA to investigate whether a Keplerian disk may be present. Their SMA data indicated a change in position of the blue-shifted and red-shifted emission close to the peak of the continuum emission which could be indicative of rotation and thereby a rotating disk. Ultimately they probed complex large-scale structure, with hints of a disk at smaller scales.

The luminosity of the source is listed as $3.4\times10^4 L_\odot$ by the RMS survey [Mottram et al., 2011c]. The kinematic distance to W33A was thought to be 3.8kpc [Faúndez et al., 2004] but water maser measurements by Immer et al. [2013] recalculate this as 2.4$\pm$0.2kpc. In order to provide a consistent comparison to the work done in de Wit et al. [2010] and to be consistent with the latest measurements, fits for both distances are discussed and included. The observations for the source consist of

Table 2.1 List of MIDI observations of W33A

Configuration Label	Date (UTC)	Telescopes	Projected baseline (m)	Position angle (°)
A	2008-06-21	UT2-UT3	42.03	15.04
B	2008-04-22	UT3-UT4	57.95	119.69
C	2008-04-21	UT3-UT4	61.08	114.57
D	2005-09-16	UT2-UT3	45.58	47.31

the MIDI observations from de Wit et al. [2010], the COMICS image presented in Wheelwright et al. [2012] (shown in Figure 2.12) and an SED. The MIDI observations are presented in Table 2.1 and the SED is comprised of fluxes from the RMS survey and previous work (de Wit et al. [2010] and references therein) which are included in the appendicies.

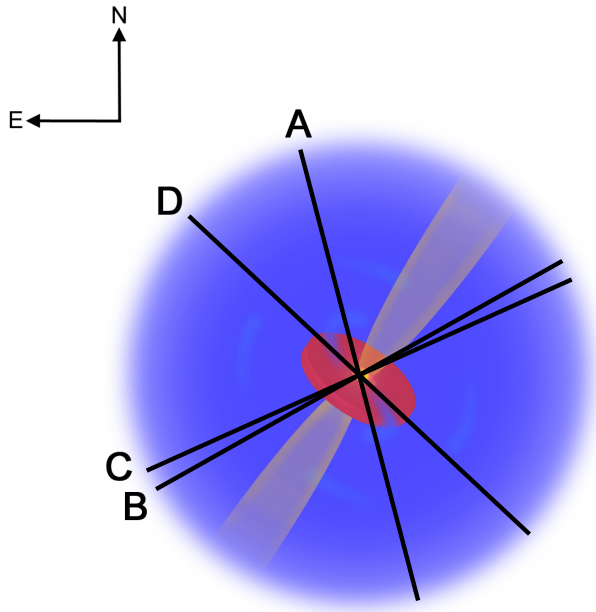

Fig. 2.11 Schematic of the suspected geometry of W33A overlain with the position angles of each configuration of the MIDI data. The envelope is shown in blue, the cavity in yellow and the disk in red.

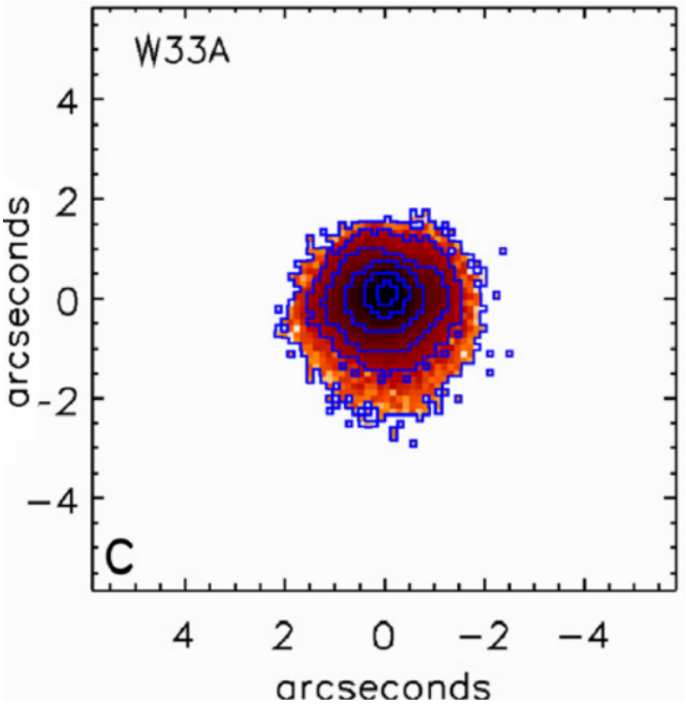

Fig. 2.12 The COMICS image of W33A as presented in Wheelwright et al. [2012].

2.7.2 Comparison to previous work - 3.8kpc distance

For a distance of 3.8kpc, it was found that the best fitting model of de Wit et al. [2010] provides a satisfactory fit to the SED and COMICS data for the source, but cannot immediately provide a satisfactory fit to the MIDI data when using the new version of HO-CHUNK and the new method. All the visibilities are exceedingly low and the overall profile is flat and in complete disagreement with those that are observed. However, the MIDI fit can be improved to the point where it is of comparable quality to the fit presented in de Wit et al. [2010] if 1) PAH emission is included in the model or 2) if a disk is included.

PAHs were not a built-in capability of the 2003 version of the code used by de Wit et al. [2010], however it was possible to include user-specified dust files. In that work, dust-files from the radiative transfer code DUSTY [Ivezic and Elitzur, 1997] were used instead of the suggested dust files by Whitney et al. [2003] or Whitney et al. [2013]. It was found that the dust files suggested by Whitney et al.

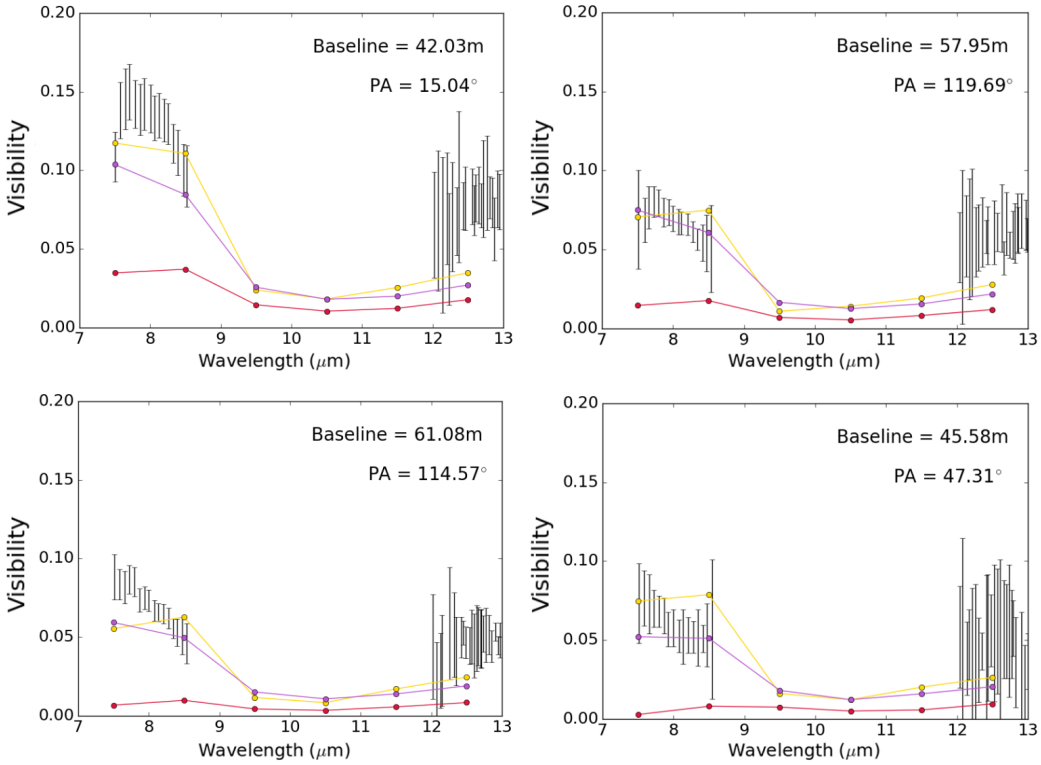

Fig. 2.13 The observed visibilities for each configuration (black) with the simulated visibilities for different models to show the effects different components on the simulated MIDI data. The red data are the de Wit et al. [2010] model, the gold data are the model when PAHs are added and the purple data are the model when a disk is added.

[2013] without PAHs could not produce a satisfactory fit using the model of de Wit et al. [2010]. The inclusion of PAHs increases the visibilities, improving the fit of the envelope-only model. This could be due to the fact that that very small grains and particles will be more easily heated by the central protostar, and that the central regions closest to the star will be therefore hotter, brighter and present a more compact emitting region. A PAH signature is only tentatively mentioned in Gibb et al. [2004], however, so whether this should be an included component of the code is debatable. The MIDI fit for the model with PAHs is shown Figure 2.13 to illustrate the improvements PAH emission makes to the fit.

The effects of including a disk in the model on the simulated MIDI visibilities was discussed in de Wit et al. [2010], where they included a plot displaying how

Table 2.2 Parameters of the preferred final model for W33A

$M_\star$ ($M_\odot$)	$L_\star$ ($L_\odot$)	Temp. (K)	i (°)	d (kpc)	$R_{\rm env}^{\rm min}$ (au)	$R_{\rm env}^{\rm max}$ (au)	R_c (au)	$\dot{M}_{infall}$ ($M_\odot yr^{-1}$)	θ_{cav} (°)
25	49270	30000	60	2.4	18 (R_{sub})	5×10^5	500	7.4×10^{-4}	20

the inclusion of the disk heightens the visibilities. When a disk is added to the envelope-only model of de Wit et al. [2010] (with no PAHs) a similar increase in visibilities is observed which vastly improves the fit to the MIDI data. Figure 2.13 also shows the improvements to the MIDI data a disk is added to the final model of de Wit et al. [2010].

The reason why these fixes must be employed to fit the MIDI data may be due to the differences between the methodology of de Wit et al. [2010] and that of this thesis. To reiterate what was said earlier in this chapter, in the method of this thesis the model images are not multiplied by a Gaussian but in de Wit et al. [2010] they are. The inclusion of a Gaussian multiplication heightens the emission in the inner regions of the image, essentially creating a compact component. This increases the visibilities, with the largest changes seen outside of the silicate absorption window (where emission is suppressed). As such, the inclusion of a Gaussian component also has a similar effect to adding a disk or PAHs to the model.

To conclude, using the methodology of this thesis (using MIDI slit-width as the interferometric FOV with no Gaussian multiplication) the envelope-only model of de Wit et al. [2010] could only fit the observed visibilities if PAHs or a disk were included. Since PAHs are not indubitably observed in the literature, they are not carried through to the refitting procedure for the new distance of W33A, which is discussed in the next section and supersedes the fits of this section and of de Wit et al. [2010].

Table 2.3 Parameters of the preferred models of W33A (cont.)

n_{cav} (gcm^{-3})	Cav exp	M_{disk} ($M_\odot$)	$R_{\rm disk}^{\rm min}$ (au)	$R_{\rm disk}^{\rm max}$ (au)	Dust Fraction	Scale height Disk 1	Disk 2
1×10^{-19}	0	1	18 (R_{sub})	500	0.2	0.11	0.22

2.7.3 Best fitting model using the new distance of 2.4kpc

Immer et al. [2013] recalculated the distance to W33A as 2.4kpc using water maser parallaxes after the work on the source by de Wit et al. had been published. This constitutes a difference in distance of factor ∼1.6 and affects all observables, and as such changes in the model are to be expected. In this section, the source is refitted using the methodology of this thesis and the new distance.

A test was done to see if the fit could be reproduced by simply reducing the luminosity of the central source according to the change in the distance. When done, the simulated visibilities for all the MIDI configurations increased between 8.5-10.5μm and the visibility at 7.5μm for configuration A), taking them outside of the observed errorbars and worsening the fits. This may be because the sublimation radius of the source will have become smaller, presenting a more compact component for emission resulting in increased visibilities. The COMICS profile was also too broad and the silicate absorption feature of the SED became deeper and in violation of the observed MIDI spectra.

When improving the fit past this initial test, recent literature was taken into account. Maud et al. [2017a] studied W33A with ALMA, tracing its wider environment. In their work they note the turbulent and messy nature of the source and image a spiral on scales of ∼5000au. Although Keplerian signatures at the centre of the source are weak, they also state that while they do not detect a disk on scales of the spiral, a disk component could be viable at scales ≤500au. During the fitting of this source for the work of this thesis, including a disk within the model was experimented with, and improvements were found to the fits of the MIDI data. A

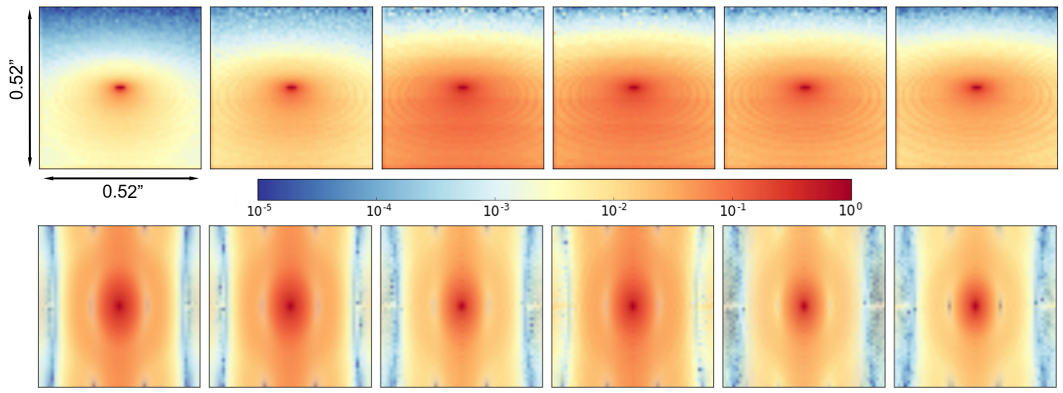

Fig. 2.14 Logarithmically scaled model images (top row) at 7.5, 8.5, 9.5, 10.5, 11.5 and 12.5μm and their corresponding Fourier transforms (bottom row) of the best fitting model for the 2.4kpc distance. Image size is 0.52" corresponding to the interferometric field of view. The colour bar applies to both sets of images and represents the number of counts.

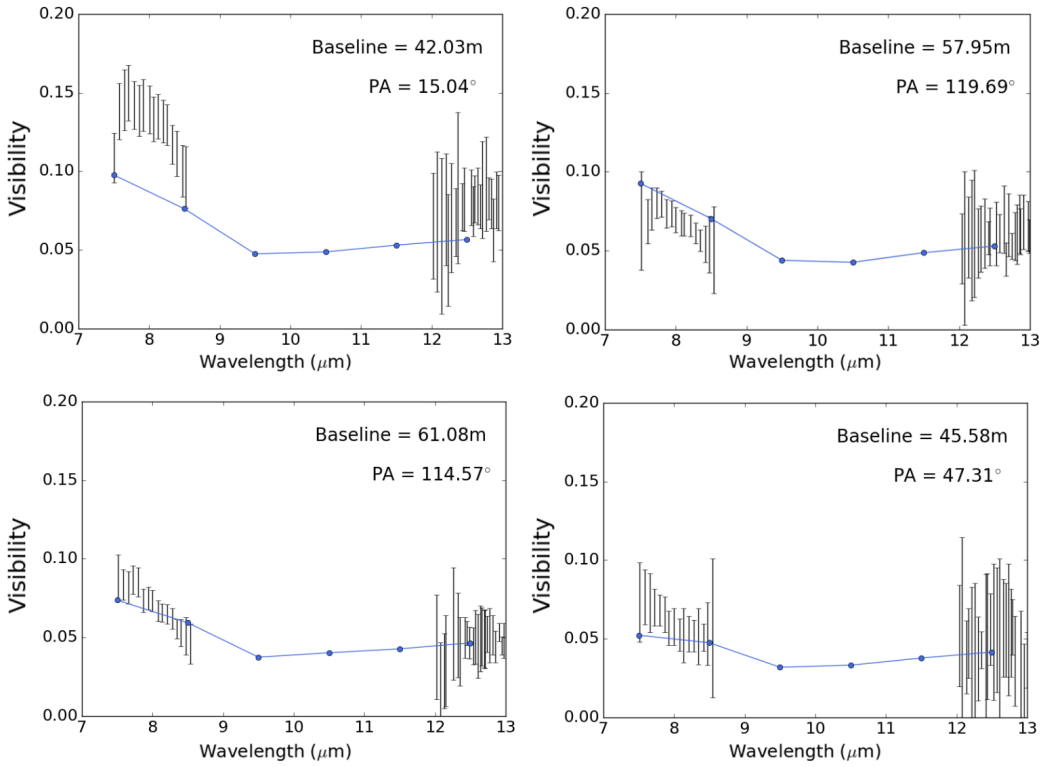

Fig. 2.15 The observed visibilities for each configuration (black) with the simulated visibilities (coloured) of the preferred model for the 2.4kpc distance of W33A.

disk can be included in the model with a maximum radius of 500au, in agreement with the suspected scales of Maud et al. [2017a]. The disk can be made smaller than this without violating the fits but given the size of the protostellar environment and the suspected mass of the source, 500au is used as the final maximum disk value. This implies that the disk's emission from its inner regions is more important than the emission from its outer regions, which is consistent as the outer regions of a dense feature like a disk will be too cold to be traced by our high-resolution infrared data. The disk is flat, with the large grains disk component scale-height set to half that of the smaller grains disk, as discussed earlier in this chapter. The model envelope has outflow cavities carved out at a 20° opening angle, twice that of de Wit et al. [2010], but with a similar cavity density. The envelope infall rates are identical between the two works. The inclination from de Wit et al. [2010] for the 3.8kpc distance satisfies all observables for the closer distance. The model images and FFTs of the final model are displayed in Figure 2.14, the visibilities are displayed in Figure 2.15, the model 24.5μm image and the radial profiles are displayed in Figure 2.16 and the SED is displayed in 2.17.

2.8 Summary

In this chapter the methodology used to probe the environments of MYSOs at multiple scales was presented. The details of the observations included in this methodology have been described, as well as the code used to consolidate them. Given the wide parameter space of HO-CHUNK, choices were made throughout the fitting process as to which to focus on. The starting parameters were selected based on the work of de Wit et al. [2010] and Wheelwright et al. [2012] and the suggestions of Whitney et al. [2013] and varied from there. The constraint on the derived parameter space appears to depend on the resolution of the data. A comparison was made between previous work done by de Wit et al. [2010], who fit MIDI data and an

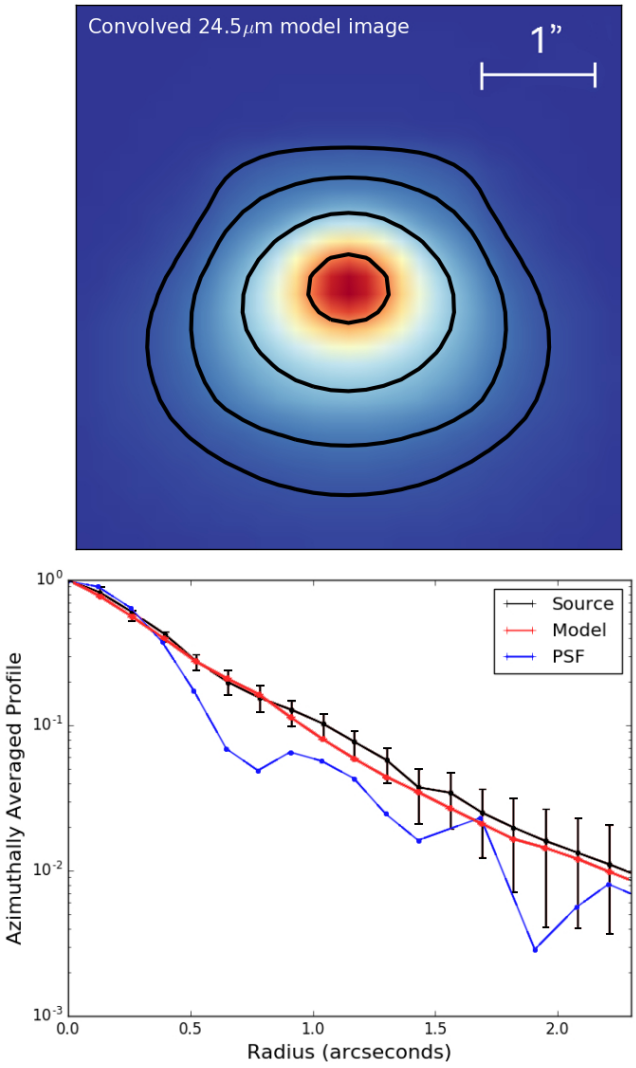

Fig. 2.16 The convolved model image (top, contours represent 5, 10, 25 and 75% of the peak flux) and the radial profile (bottom) of the best fitting model for the 2.4kpc distance.

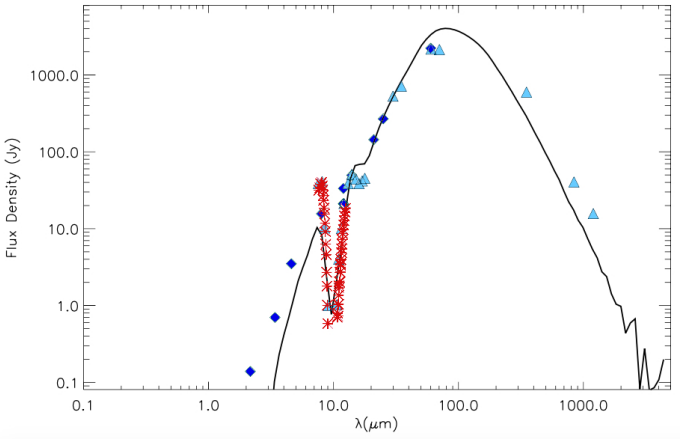

Fig. 2.17 The SED of the preferred final model. Data from the RMS survey is shown as diamonds, the MIDI spectra is shown as red crosses and data points from de Wit et al. [2010] are shown as triangles.

SED with an older version of the HO-CHUNK code, and the methods of this thesis by refitting the source in that paper W33A. The main methodical change between the two works is in the consideration of the field of the view when simulating the MIDI data. It was found that their model and method could not satisfy the MIDI data using the new version of the code and the method of this thesis, due to different considerations of the field-of-view. Further investigation was made in to the effects of distance on the observables as well, given than a new distance for W33A had been calculated since the publication of de Wit et al. [2010]. The geometry of the model changed due to this distance change and a disk was a required component of the model. This highlights the need for accurate distance measurements in the study of MYSOs.

The following chapters in this thesis present the results obtained when the methodology outlined is this chapter is applied to different MYSOs.

Chapter 3

A potential transition disk around an MYSO

3.1 Introduction

Disks have been proven to be a crucial aspect of the low-mass star formation process. As described in Chapter 1, disks form as a result of angular momentum conservation and allow accretion of material onto the protostar and eventually the birth of planetesimals. Various stages of disk have been observed around low-mass stars. Williams and Cieza [2011] detail how a disk evolves between the Class II and III stages described in Chapter 1 and this is illustrated in Figure 3.1. The disk begins as a large flared disk. As it starts to evolve, the disk loses mass through a combination of accretion towards the star and far-UV (FUV) photoevaporation of the outer disk, whose scale-height is large enough at these radii to be irradiated directly by the protostar. Simultaneously, grains within the disk collide and coalesce into larger bodies that fall towards the midplane of the disk due to gravity and the disk becomes settled. As the mass of the disk and accretion rate continue to decrease, photoevaporation due to extreme-UV (EUV) photons destroys the smaller particulates in the inner regions of the disk at such a speed that the outer disk is unable to replenish it. The inner disk

drains on a viscous timescale ($\sim 10^5$ years) and a hole forms between the protostar and disk, the accretion stops and the disk dissipates rapidly from the inside out. Once the remaining gas photoevaporates, the small grains are removed by radiation pressure and Poynting-Robertson drag. Only large grains, planetesimals, and/or planets are left, leaving a debris disk. The stage where the inner regions of the disk are clearing is often referred to as the 'transition disk' stage (e.g. Cieza et al. [2010], van der Marel et al. [2015]). Wyatt [2008] describes the first stage of the transition disk as a phase where accretion is ongoing with the presence of gas but absence of small dust grains and Tang et al. [2017], van der Marel et al. [2014], van der Plas et al. [2017] and Fedele et al. [2017] show inner radii of order 10s of au for low-mass transitional objects. An additional disk phase is also proposed for lower-mass stars known as the pre-transitional disk. During this phase a very small gaseous inner disk (scales of order 0.1au) remains close to the inner star [Espaillat et al., 2010] as material is removed at larger radii, so the inner cleared region is referred to as a gap. Instrumentation is now sophisticated enough that evolved disks, like the transition disk, are being resolved around lower mass objects (e.g. van der Marel et al. [2016]), however evolved disk stages are yet to be confirmed for MYSOs.

In this chapter, the results obtained through the application of the methodology described in Chapter 2 to the source G305.20+0.21 are presented, which infer the presence of a transitioning system around an MYSO. G305.20+0.21 (henceforth G305) is located at RA 13:11:10.45, DEC -62:34:38.6 (J2000 co-ordinates). The region that houses G305 is littered with Class II maser emission (e.g. Urquhart et al. [2013], Hindson et al. [2010]), which has been shown to be exclusively associated with massive star-forming regions (e.g. van der Walt [2011], Pandian et al. [2011]). A separate compact HII region is present $\sim$18" west of the source [Walsh, 2002], again implying the presence of massive star formation. A very bright source is also visible $\sim$22" east of G305 in 870μm maps from the ATLASGAL survey [Schleicher et al., 2011]. Walsh and Burton [2006] detect ^{13}CO and HCO+ line wings in the

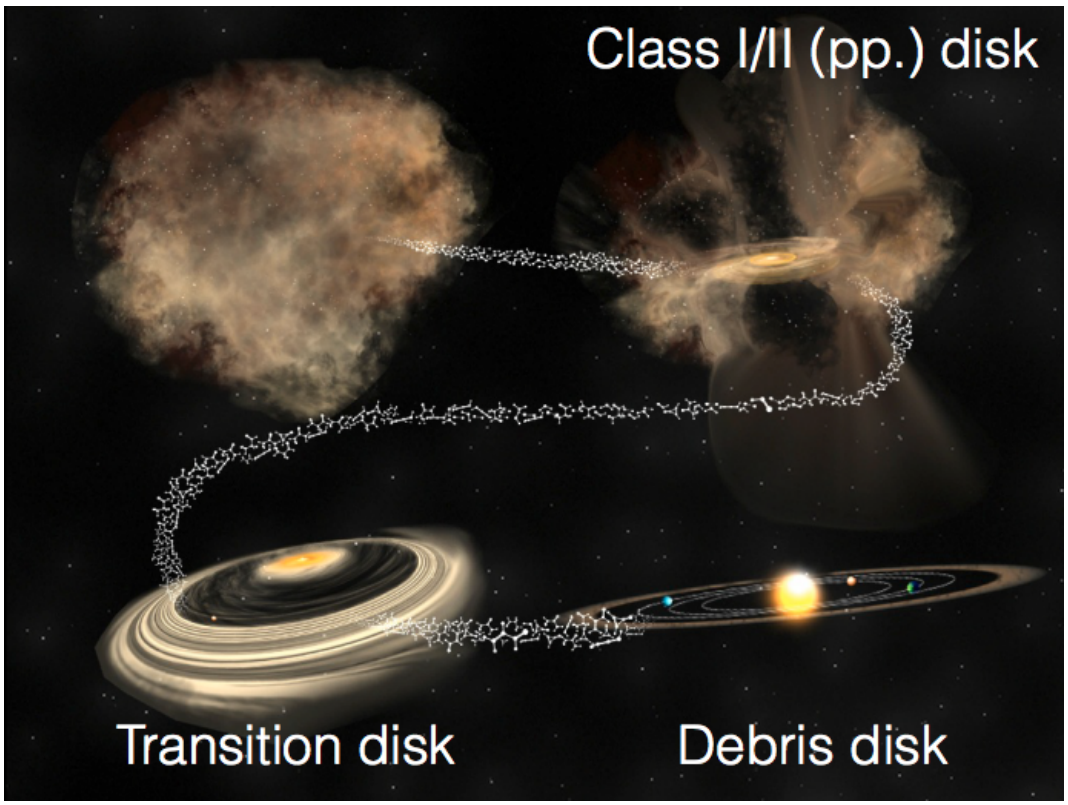

Fig. 3.1 A schematic displaying how a Class II protostellar disk system evolves into a transition disk before becoming a Class III object. Credit: L. Pérez

area surrounding G305 implying the presence of outflows, but due to the spatial resolution of their data they cannot discern which source would be powering these emission features. G305 is classified as an MYSO in the Red MSX Source (RMS) survey [Lumsden et al., 2013] and has a listed bolometric luminosity of 4.9×10^4 $L_\odot$ [Mottram et al., 2011d] at a kinematic distance of 4kpc [Urquhart et al., 2014a]. Krishnan et al. [2017] determine a distance of $4.1^{+1.2}_{-0.7}$ kpc for a maser parallax of 0.25±0.05mas. Hindson et al. [2010] find v_{LSR} = -42.0 kms^{-1} from observations of the NH_3(3, 3) line at 24 GHz, corresponding to a kinematic distance of 4.74±1.70 kpc. Walsh [2002] find G305 to have a deeply embedded near-infrared source and determine its luminosity to be $2.5\times10^5 L_\odot$ at a distance of 4.5kpc based on IMF models and Class II maser emission. Liu et al. [2019] included G305 (named as G305B in their paper) in a SOFIA survey of massive star formation supplemented by radiative transfer modelling and their findings are discussed in relation to those of

this thesis in Section 3.5.1. The source was also included in a study of a number of MYSOs by Ilee et al. [2013] where the CO band-head emission of the MYSO (as part of a large sample) was modelled and the presence of a disk inferred.

3.2 Observations

Table 3.1 MIDI observations of G305.20+0.21

Config. Label	Date/time (UTC)	Telescopes	Projected baseline (m)	Position angle (°)	Average visibility
A	2005-06-26 01:20	UT1-UT2	42.5	48.1	0.03
B	2005-02-27 03:35	UT2-UT3	44.7	4.8	0.03
C	2005-03-02 05:26	UT3-UT4	56.7	83.4	0.02
D	2005-03-02 06:10	UT3-UT4	58.9	93.4	0.03
E	2005-03-02 07:13	UT3-UT4	61.0	106.9	0.03
F	2005-06-24 02:46	UT3-UT4	62.3	146.7	0.01

G305 was observed in 2005 in six distinct telescope configurations using three different telescope pairs (the details of which are listed in Table 3.1). The prism mode was used for configurations A-D and F and the grism mode was used for configuration E. Each configuration has a different projected baseline and position angle. In order to help illustrate the regions of the protostellar environment each configuration may trace, Figure 3.2 presents a VVV (VISTA Variables in The Via Lactea, [Minniti et al., 2010]) survey Ks-band image displaying G305.20+0.21 and its surrounding area, supplemented with a schematic labelled with each interferometric baseline. The Ks-band image is included for illustrative purposes only and is not a part of the fitting process. The object's Ks-band flux is considered through the inclusion of the 2MASS flux for the source in the SED. The observations for G305 were taken with baselines between $\sim$42-62m resulting with a resultant range in angular resolution of 12mas (for a 62m baseline at 7.5μm) to 31mas (for a 40m baseline at 12.5μm). The MIDI measurements of G305 show that the object has a comparatively low correlated flux

between 7 and 8μm in the context of the full sample of MYSOs from the Boley et al. [2013] sample. The average overall visibility for the source is 0.03 and the visibility is not constant with wavelength but shows a clear chromatic dependency, in part because of the strongly varying opacity within the silicate absorption wavelength region at 9.7 micron.

G305.20+0.21 was observed with VISIR on 6/7/2016 with good sky conditions (precipitable water vapour (PWV) was 0.78mm) at exposure times of 0.0114s with a total time-on-target of 45 minutes. The observations followed the 2016 upgrade to the instrument and ESO pipelines (version 4.3.1) were used to reduce the data, accounting for chopping and nodding corrections and averaging the subsequent frames to form one image. HD 123139 was observed as PSF standard on the night of the observations with a measured FWHM of 0.48". The Graphical Astronomy and Image Analysis Tool (GAIA, Currie et al. [2014]) was used to perform aperture photometry on G305 and on three other calibrator objects (HD 169916, HD 163376 and HD 111915) observed at the VLT. The amount of counts detected within the apertures were compared to the recorded fluxes of the objects and the difference in aperture size was accounted for. This led to a resultant flux density for G305 of 138$\pm$7Jy at 19.5μm.

G305's source fluxes were compiled from the Red MSX Source (RMS) Survey [Lumsden et al., 2013] and the literature to create an observational SED for the object. The included fluxes are 2MASS J, H and K band data, the WISE 3.4 and 4.6μm fluxes, GLIMPSE data at 3.6μm, MSX 14 and 21μm points, the 18μm flux from De Buizer et al. [2000] (taken with the OSCIR instrument at the Cerro Tololo Inter-American Observatory 4m Blanco Telescope) and the PACS 70μm flux (obtained through the *Herschel*/PACS Point Source Catalog[†]). No GLIMPSE 4.5μm flux is present in archival data for the source and the GLIMPSE 5.8μm image is saturated so neither are included. The WISE fluxes are the colour-corrected fluxes for a 200K black-body emitter. Other wavelength data also exist in the form of the IRAS 60μm

Table 3.2 Fluxes used in the SED. The italicised fluxes are those omitted from the fitting due to the considerations discussed in Section 3.2.

Source	Wavelength (μm)	Flux (Jy)
2MASS J-Band	1.25	$(3.21\pm0.09)\times10^{-3}$
2MASS H-Band	1.662	$(2.09\pm0.1)\times10^{-2}$
2MASS Ks-Band	2.159	0.113 ± 0.004
WISE	3.4	0.293 ± 0.005
GLIMPSE	3.6	2.23 ± 0.07
WISE	4.6	5.71 ± 0.2
MSX	14	$(1.10\pm0.07)\times10^{2}$
OSCIR	18	117.53 ± 0.3
VISIR	19.5	138 ± 7
MSX	21	$(2.66\pm0.2)\times10^{2}$
IRAS	60	$(3.17\pm0.6)\times10^{3}$
PACS	70	$(1.14\pm0.003)\times10^{3}$
IRAS	100	$(8.16\pm1)\times10^{3}$
SIMBA	12000	(18.5 ± 0.04)

and 100μm data points and the SIMBA 1.2mm flux [Faúndez et al., 2004]. These are not considered in the fitting, however, due to the presence of the ATLASGAL core (mentioned in Section 3.1) whose emission is contaminating these measurements. As the two sources cannot be reliably separated, all flux measurements obtained with apertures larger than 20" are discarded. The 19.5μm VISIR flux and the flux calibrated MIDI spectrum are also included in the SED fitting.

3.2.1 Fitting process

Given the success of the envelope-only model of de Wit et al. [2010] in fitting the VISIR profiles of a range of MYSOs in Wheelwright et al. [2012] and the MIDI visibilities of MYSO W33A [de Wit et al., 2010] the same central object, envelope and cavity parameters were used as a starting point for the modelling of G305. However, the model did not immediately present a satisfactory fit, so a large portion of the parameter space was varied in attempts to fit the observational data.

[†]http://archives.esac.esa.int/hsa/legacy/HPDP/PACS/PACS-P/PPSC/HPPSC_Explanatory_Supplement_v2.2.pdf

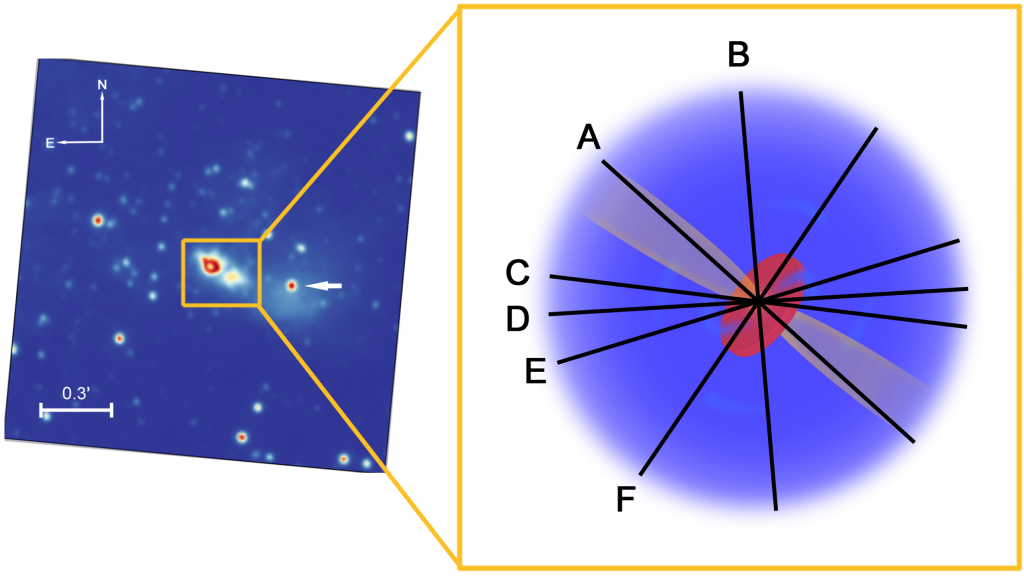

Fig. 3.2 A logarithmically scaled VVV Ks-band image of G305.20+0.21 (left). Two lobes are visible separated by a dark lane. The bright point-source (noted with a white arrow) approximately 0.3' west of the central object surrounded is a known compact HII region. The Ks-band image is supplemented by a schematic of the suspected MYSO geometry overlain with the position angles of each configuration of the MIDI observations (right). In the schematic the envelope is shown in blue, the cavity in yellow and the disk in red.

The VVV Ks-band image shown in Figure 3.2 displays a dark lane between two lobes. The lobes are likely to correspond to the bipolar cavities of the object, implying a dense dusty feature lies between them. This led to the inclusion of a disk in the model but given the size of the dark lane ($\sim$2") it is more likely a result of the shadow of a disk on the surrounding nebulous material than the disk itself. Originally the presence of the lane also led to a prioritisation of close to edge-on inclinations for the source. However, close to edge-on inclinations do not reproduce well the 19.5μm image as too much emission is present in the model images from the red-shifted cavity lobe so ultimately less extreme inclination solutions were explored. Including a disk greatly improved the MIDI visibilities, better recreating the observed upturn towards shorter wavelengths and increasing the visibilities in general. In order to optimise the fit, the added disk was experimented with in a number of respects. Its mass was varied between 0.1-10 solar masses throughout the fitting. The scale-height of the disk was also experimented with and a flatter disk presented improvements to the fits by improving the shape of the visibility profile. The outer radius of the disk was changed on 500-1000au scales in accordance with the expected radii of disks around other objects and the minimum disk radius was varied in intervals beginning with the sublimation radius (18au). The sublimation, or dust destruction radius, is dictated by the luminosity of the source. The chi-squared values allowed us to decide the final MIDI fit and therefore the final, preferred model. The model images and FFTs used to generate the MIDI visibilities are shown in Figure 3.4. Throughout the fitting process Configuration A was consistently the most difficult to fit. In particular, the 7-8μm visibilities proved to be systematically inconsistent with the radiative transfer models that would match the other observables. This configuration has the smallest baseline and is therefore the lowest resolution configuration of the MIDI dataset. It is also the only one aligned with the outflow axis (as displayed in Figure 3.2). The model visibilities at 7-9μm are constantly higher than the observed visibilities meaning that the observed emission is less compact than the model

predicts. Asymmetrical dusty structures along the outflow axis could arise from the entrainment of material during the accretion process. As dynamical processes that depend on local conditions are not covered by the radiative transfer model, one can only speculate about the emission's origin and more data are needed to interpret this plausibly. Another potential source of this emission is entrainment from a collimated jet. It is thought that collimated jets are associated with a number of MYSOs (e.g. Purser et al. [2016], Beuther et al. [2002a]) and such a collimated jet would lie along the position angle of Configuration A. A jet is not included in our model, so dusty material that might have been swept up into such a jet and emit would not be replicated in our simulated visibilities, again explaining the difficulties with fitting this configuration. Given these considerations, the fitting of the other configurations which are more likely to be accurately represented within the model were prioritised over fitting Configuration A.

3.2.2 General observations

This section discusses the observations made while experimenting with the parameter space of the radiative transfer code in the context of each probed scale of G305. The distance is a parameter that affects all simulated observables. The RMS distance of 4kpc for G305 and all the following observations are made for this specific distance.

10mas scales

Any changes to the disk of the object have repercussions on the simulated visibilities but do not affect the simulated VISIR profiles. The scale-height of the disk does not induce large effects and changing the scale-height exponent (which affects the curved shape of the disk at greater radii) also results in small effects. Varying the outer radius of the disk affects the simulated visibilities between 10-13μm only and effects are small between 1000, 2000 and 3000au. This outer radius affects the

emission at longer millimetre wavelengths, which probe the cooler disk regions, but are not simulated in this work. The minimum disk radius has a significant effect on the simulated visibilities, producing a range of visibility values when the minimum radius is varied between R_{sub}-125au. This is due to the fact that a large amount of emission will be reprocessed by the inner rim presenting a turnover. As the minimum radius increases past 100au, the visibilities decrease as more dust is cleared from the inner protostellar regions and the model visibilities become comparable to a no disk-model.

Adding a puffed-up rim increases the visibilities slightly at all wavelengths for the smaller baseline configurations and at 7-8μm for all configurations. This appears consistent as the puffed-up rim provides a greater area of dust available for heating and subsequent emission at MIDI's observed wavelengths. Changing the inner rim shape from flat to curved results in marginally higher visibilities for Configuration A across the entire N-band spectrum. Since the disk is flared and the scale height at the inner rim is small, one would expect the change in visibilities to be small, if the disk was more toroidal then one would expect a bigger change as the curve of the inner rim would be more pronounced.

Increasing the disk density by varying the disk mass from 1 to 5 and then 10 solar masses while maintaining other disk parameters was also investigated. This increases the visibilities at the extreme ends of the N-band range slightly with the most marked effects found at 7, 12 and 13μm, lowering the 7 and 8μm visibilities whilst raising the 13μm visibility, resulting in a flatter visibility spectrum. These wavelengths are the least affected by silicate absorption so one would expect a greater change in these regions of the spectrum. As the disk density increases the inner regions become optically thick extending the τ=1 surface and lowering the visibilities. The improvements here come at the expense of the SED fit, which sees an increase in its 70μm peak and the fluxes between 1-7μm. The modelled N-band visibilities hardly change with the inclusion of disks lower than 1 solar mass. A 0.1 solar mass disk,

i.e. a disk mass within the regime of those found in Herbig Be systems (e.g. Walsh et al. [2014], Kama et al. [2016], Walsh et al. [2016] and Boneberg et al. [2016]), was tried and this generated little change. From these observations it is concluded that the N-band interferometry poorly constrains the total disk mass, which is in agreement with Boley et al. [2016], although they provide important constraints on the inner geometry of the disk.

100mas scales

All the disk parameters mentioned in the previous section have negligible effects on the simulated 19.5μm image. It was found that the most important influences on the emission at this wavelength are the cavity properties, in particular the cavity opening angle and its geometrical shape as captured by the cavity exponent (b in Equation 1). Since the cavity density is lower than the envelope density, the material within it will be more easily illuminated by the central object and the envelope material in the cavity walls will bear the brunt of the stellar emission and be heated. Therefore, the more emission from the cavity that is present, the more extended the emission in the Q-band becomes and the greater the amount of $\sim$20μm flux. When the cavity exponent b equals 1 it will have a conical shape as opposed to the more curved shape of the polynomial cavity that has an exponent other than 1. Because of this change in shape there is less flux at larger scales when modelling a conical cavity as it is essentially narrower, presenting a smaller area of cavity wall available for irradiation and subsequently a smaller solid angle on the sky for re-emission. The envelope infall rate also affects the $\sim$20μm emission. Increasing the envelope infall rate reduces the flux at larger radii. This appears consistent as more of the envelope mass will be present at smaller radii and within a region that is traced at mid-infrared wavelengths, as opposed to remaining in cooler outer regions that would be better traced by radio and sub-mm data. The effect of the envelope infall

rate is less pronounced than the effects of varying the nature of the cavity walls and it is concluded that the 20μm data is predominantly a tracer of cavity wall emission (within the limitations of our adopted dust radiative transfer model).

The remaining factor that influences the $\sim$20μm emission is the inclination, but this affects all types of observation. Pushing to pole-on inclinations raises the MIDI visibilities, while decreasing the amount of $\sim$20μm flux (as one sees less of the illuminated cavity wall) and weakening the silicate absorption feature (as the cavity is optically thin) in the SED and a compromise needed to be found throughout the fitting. If the inclination is increased towards 50° for this source, more 19.5μm emission from the red-shifted cavity lobe is visible in the model images that is not observed. The ultimately adopted value for the inclination of the modelled object is 35°. 35° was chosen as the final value because for higher inclinations the flux short-ward of the silicate absorption feature was too great and the depth of the silicate absorption feature in the SED was slightly too deep. This lies within the range of inclinations found from the five best fitting models of Liu et al. [2019] and is similar to the inclination derived in Ilee et al. [2013] of 43°.

The total flux

MYSOs are very dusty objects so one would expect the silicate absorption to be very prominent, but the N-band spectrum for G305 displays a weak silicate absorption feature. This implies that a closer to pole-on inclination for the model would provide a satisfactory fit to this feature. However, the Ks-band VVV image implies the presence of a second lobe and as such higher inclinations were trialled leading to a final inclination of 35°. The silicate absorption feature has long been an indicator of the extinction towards a source (e.g. Henning and Guertler [1986], Boley et al. [2016]) and the interstellar extinction can be varied within the SED post-processing. A small amount of interstellar extinction best satisfies the model SED's silicate

absorption feature, allowing it to remain small enough to fit the observed MIDI total fluxes. The appearance of two cavity lobes in the Ks-band already implies that the total extinction towards the source is lower than average for MYSOs, and when compared to other MYSOs such as AFGL 2136 [de Wit et al., 2011] the silicate absorption feature is indeed much weaker. This implies that most of the compact (<1") N-band emission suffers very mildly from foreground dust extinction, explaining why both outflow cones are detected in scattered light on scales of several arcseconds. Boley et al. [2013] fit a curve to the N-band spectrum, and find an optical depth of $\tau_{10.2} = 0.5$ in the total flux and a depth of $\tau_{10.2} = 1.71$ in the correlated flux, averaged over all measurements. The authors state that the optical depth of the silicate absorption feature can be significantly lower in the total flux than the correlated flux and postulate that this could be due to the fact that the total flux contains contributions of emission from all scales, while the spatial filtering of MIDI limits this contribution. Boley et al. [2013] also fit a power-law spectrum with an additional foreground screen of material with a column density and dust composition (independent of projected baseline or position angle) to the correlated flux for each of their sources. They found that G305 was one of the few sources whose correlated flux was not adequately reproduced by this model implying that the absorbing material is not largely uniform, detached from the scales traced by MIDI and that spatial effects may be present.

Table 3.3 Parameters of the preferred model. The level of constraint on each of the quoted values is discussed in Section 3.2.2.

$M_\star$ ($M_\odot$)	$L_\star$ ($L_\odot$)	i (°)	d (kpc)	$R_{\rm env}^{\rm min}$ (au)	$R_{\rm env}^{\rm max}$ (au)	R_c (au)	$\dot{M}_{infall}$ ($M_\odot yr^{-1}$)
25	48500	35	4	60	5×10^5	2000	7.5×10^{-4}

The total cavity optical depth in the line of sight (or the cavity density and path length) also affects the silicate absorption feature. The cavity density used in de Wit et al. [2010] of approximately 1×10^{-18}gcm^{-3} results in a very deep silicate

Table 3.4 Parameters of the preferred model (continued). The level of constraint on each of the quoted values is discussed in Section 3.2.2.

θ_{cav} (°)	n_{cav} (gcm^{-3})	M_{disk} ($M_\odot$)	$R_{\rm disk}^{\rm min}$ (au)	$R_{\rm disk}^{\rm max}$ (au)	Dust Fraction	Scale height	$A_{\rm v}^{\rm for}$
12	8.35×10^{-21}	1	60	2000	1	0.1	1

absorption feature (as observed in the case of the MYSO W33A) and our final model uses a lower density. Making the cavity opening angle greater also increases the depth of the silicate absorption feature in the model SED and the largest the cavity opening angle could be was 12°. This is smaller than the angles found by the fitting Liu et al. [2019] of $\geq$27° but their data was of worse resolution.

The envelope parameters affect the SED across its wavelength range. Increasing the infall rate of the envelope deepens the silicate absorption feature and also increases the 70μm peak of the model SED. Increasing the maximum radius of the envelope factor shifts the entire SED to longer wavelengths and severely lowers the 70μm peak of the SED when pushed to sizes of order 10^7au (a value tried during the extreme testing mentioned in Section 3.3). The 70μm peak is an important photometric point to fit as it essentially describes the total flux of the MYSO. The 70μm flux increases because the optical thickness increases, and the colder part of the emission becomes more substantial. Making the disk around the central object more massive slightly increases the flux in the J, H and K bands and results in increases of the flux at the SED peak. As such a lower mass disk provided a more satisfactory fit.

3.2.3 Best-fitting model

The systematic variation of the properties discussed in the previous section and the consideration of the chi-squared values for the MIDI fits finally amounts to the best-fitting model whose parameters are shown in Table 3.3. The central protostellar object of this model possesses a luminosity of 4.85×10^4L$_\odot$ for the RMS distance

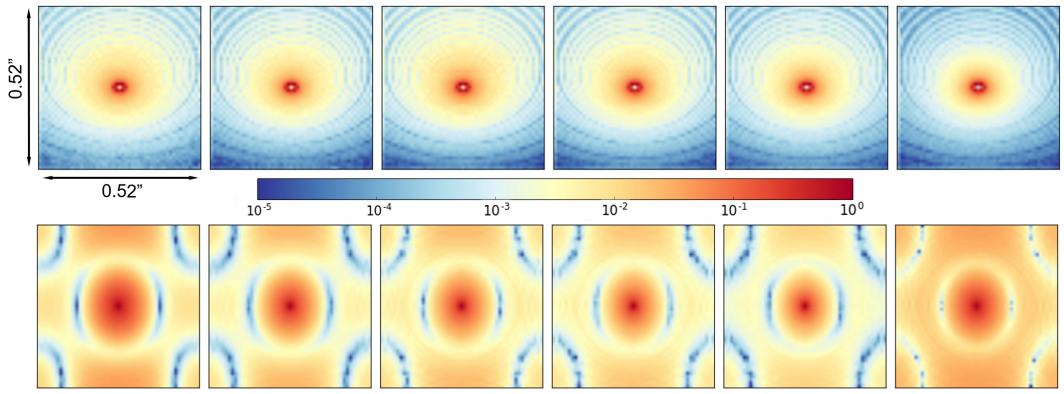

Fig. 3.3 Logarithmically scaled model images (top row) at 7.5, 8.5, 9.5, 10.5, 11.5 and 12.5μm and their corresponding fast Fourier transforms (bottom row). Each image is 0.52" in width corresponding to the interferometric field of view. The colour bar applies to both sets of images and represents the number of counts.

of 4kpc, which is in very good agreement with the RMS bolometric luminosity of $4.9\times10^{4}L_{\odot}$. In order to satisfy the MIDI visibilities, a disk of order $\sim$1 solar mass is required ranging in size from 60-2000au in radius (the exact mass is poorly constrained as discussed in Chapter 2). The envelope has a centrifugal radius of 2000au, chosen to be consistent with the outer radius of the disk, and the infall rate of the envelope is $7.4\times10^{-4}M_{\odot}yr^{-1}$. The cavity opening angle is 12° and the cavity density is $8.35\times10^{-21}gcm^{-3}$.

Figure 3.3 presents the model N-band images and their FFTs for the best-fitting model. Figure 3.4 presents the MIDI visibilities for each observed configuration of G305, with the observed visibilities being shown in black and the simulated model visibilities being shown in red. For all baselines, a depression in the visibility spectrum is seen around the silicate absorption indicating that the emission region at around those wavelengths is larger than the adjacent N-band wavelengths. Telluric absorption impairs flux measurements between 9.3μm and 10.2μm and they have been omitted. Any observations below 7.5μm or above 13.3μm are outside of the N-band and compromised by atmospheric absorption, so our visibilities are plotted between these values only. The errorbars of the simulated visibility points account for the error induced by the artificial ring structures discussed in Chapter 2. The

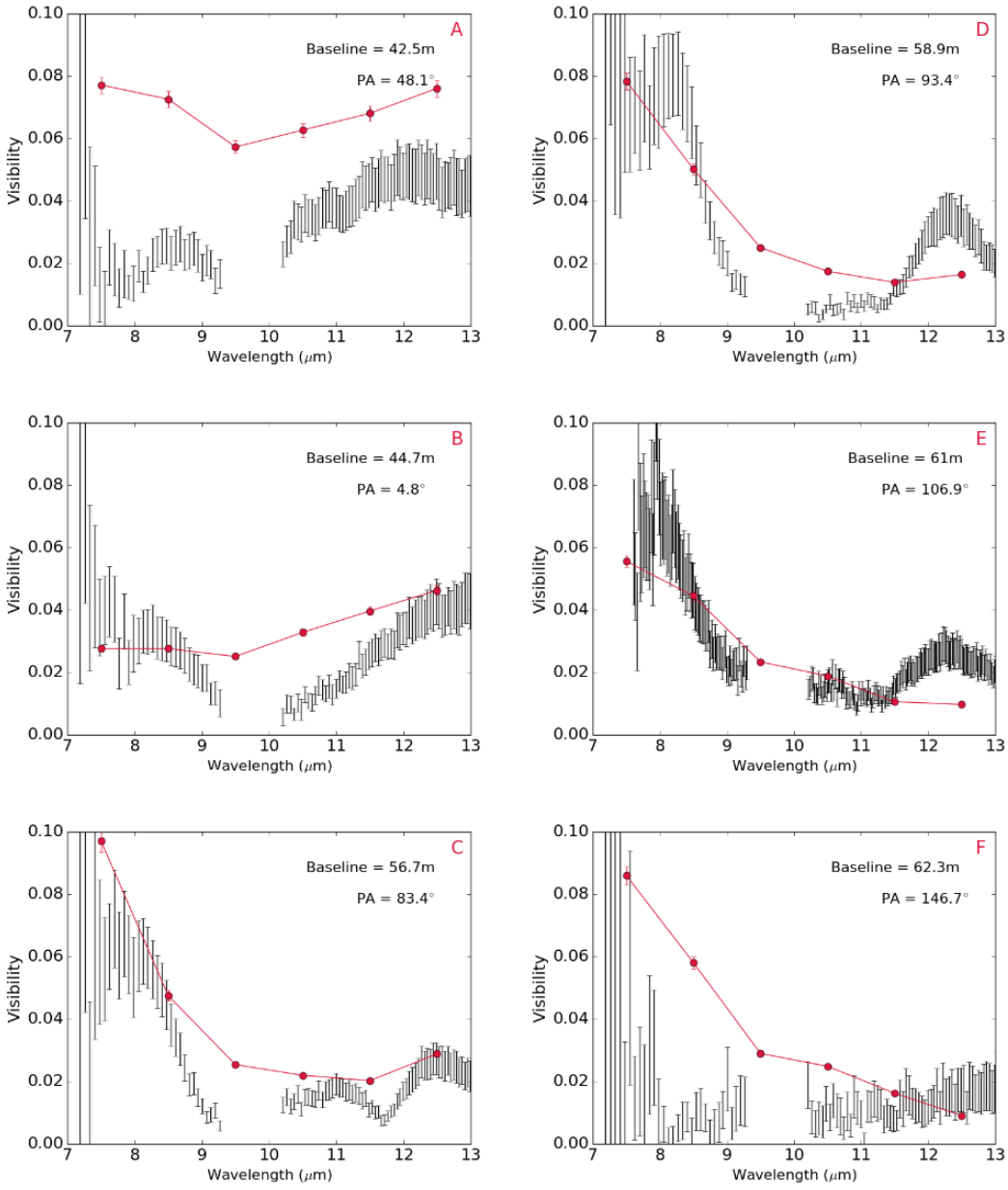

Fig. 3.4 Observed visibilities for each configuration (black) with the simulated visibilities for each model image (red).

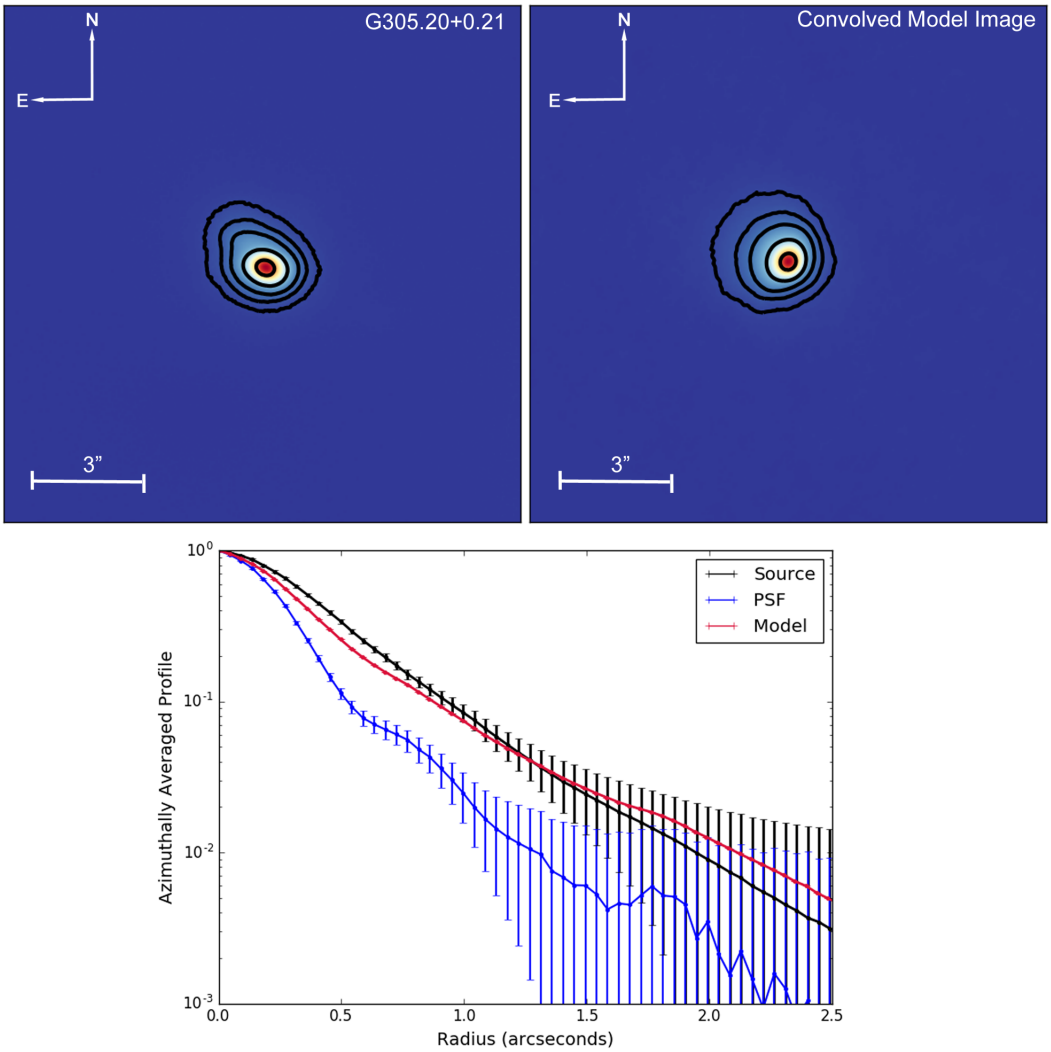

Fig. 3.5 VISIR 19.5μm image (top left), convolved model image (top right) and subsequent radial profiles (bottom). The model image was convolved with the PSF of the observed object to accurately mimic the effects of the telescope specific to the observations.

emission seen in Figure 3.3 is relatively extended resulting in the low visibilities seen in Figure 3.4. The images also suggest that the inner regions of the cavity walls become progressively fainter with wavelength (with the exception of the 9.5 and 10.5μm images) with an increase in the typical emitting size and the subsequent production of lower visibilities.

Figure 3.5 shows the VISIR image for G305, the convolved model image and their subsequent radial profiles. The contours represent 2, 5, 10, 25 and 75% of the peak flux and the error bars represent the rms within a given annulus. The secondary lobe seen in the VVV Ks-band image is also visible in the VISIR image (albeit it at low percentage contours of $\sim$0.2% of the peak flux). Figure 3.6 presents a combination of the two images, illustrating that their emission coincides and confirming the location of the secondary lobe. Given the limits on the pointing accuracy of a UT (3") there was a slight misalignment between the VVV image and the VISIR image. However, the geometry of the brightest lobe of the source matched between the two images and with nothing similar in the local field of view, this was corrected for and the two aligned for the figure by eye. When a Ks-band model image was generated for the source the secondary lobe was not visible in the normal intensity images. However, images detailing the polarised emission, images of the polarised flux and the Q and U Stokes images can also be generated. In these images the second lobe is visible, implying that most of the Ks-band emission from the secondary lobe in the VVV image is scattered light.

Figure 3.7 shows the SED. The fluxes corresponding to the MIDI fluxes are shown as red crosses, included to assure consideration of the silicate absorption feature at 9.7μm. The blue diamonds are fluxes from the RMS, the yellow diamond represents the VISIR flux and unfilled green diamonds represent the fluxes from the RMS survey which were omitted due to the considerations discussed earlier in this chapter. The near-infrared fluxes show a slightly worse fit than the rest of the SED. G305 has an envelope which will be causing significant levels of extinction and in

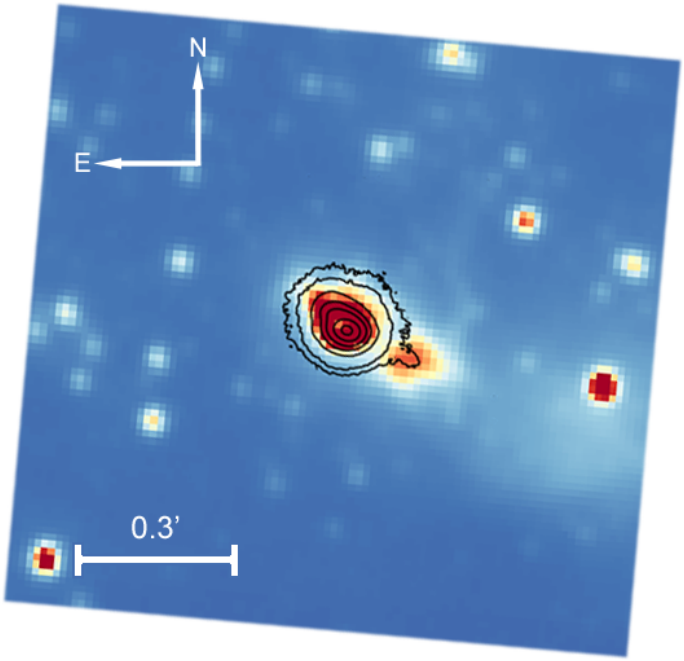

Fig. 3.6 A combined image showing the location and morphology of our VISIR 19.5μm image (black contours) in comparison to the structure observed in the VVV K-s band image. The VISIR contours are 0.2, 0.5, 2, 5, 10, 25 and 75% of the peak flux.

reality this envelope is unlikely to be as smooth as the one presented by the model. The envelope extinction effects will have a much larger effect on the near-infrared fluxes than at longer wavelengths. Given this and the potential for irregularities within the envelope material, fitting of the rest of the SED was prioritised over fitting the near-infrared fluxes.

A temperature/density map of the modelled final MYSO is presented in Figure 3.8, displaying the simulated object at scales corresponding to the three different kinds of observation. The final schematic for the object consists of a dusty envelope with a low-density bipolar cavity carved out by the central protostar and a large-grains disk. Including a small-grains disk worsened the fits of nearly all the MIDI configurations by raising the visibilities significantly, especially in the 8-11μm range. A similar effect occurred when the scale height of the disk was increased, highlighting that the disk of G305 must be flat.

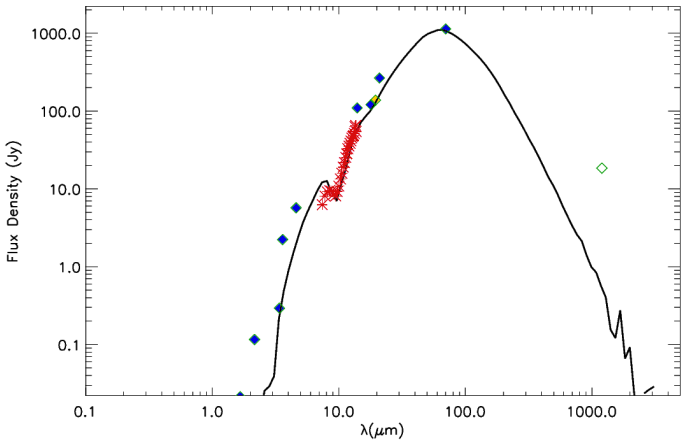

Fig. 3.7 Model spectral energy distribution of the best-fitting model (black). Multi-wavelength flux measurements from the RMS are represented as blue diamonds, the yellow diamond represents the VISIR flux density and the fluxes corresponding to the MIDI visibilities are also shown in red. The unfilled diamonds represent the fluxes that were not considered in the fitting due to their suspected contamination.

3.3 Discussion

3.3.1 Comparisons with previous work

In this section the results presented here for G305 are compared to previous results found for this specific source using different methods/observations and to other MYSOs studied with similar methodologies.

The most notable difference between this final model and the starting point, the envelope-only model of de Wit et al. [2010], is the addition of a disk. Other significant departures from the envelope specification are the centrifugal radius, which is 2000au as opposed to 33au, changed to match the outer radius of the added disk. The cavity has the same polynomial shape as de Wit's work, but in order to successfully fit the silicate absorption feature of the SED the cavity density in our best-fitting model is lower than that presented in de Wit et al. [2010]. The central protostar is 30% dimmer than the central protostar required to fit W33A. The fact that W33A does not require a disk to fit its MIDI visibilities while G305 does could be due to their environments. de Wit et al. [2010] note that while a disk was not

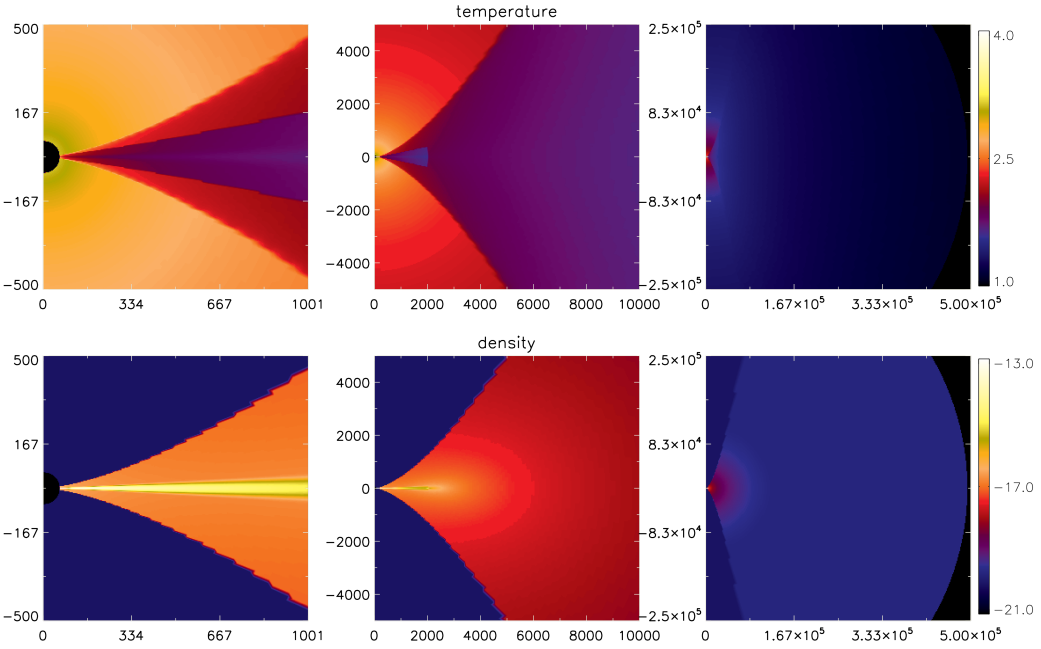

Fig. 3.8 Cut-through, side-on, logarithmically-scaled maps of the temperature and density for the best-fitting model generated with Hochunk (plotted using IDL[§] post-processing scripts written by Whitney et al. [2013]). The temperature colour-bar is Kelvin and the density colour-bar is in gcm^{-3} and both are log scales. The axes for all panels are in au. Each column of images represents a different scale, corresponding to the observations, with the smallest scales traced by MIDI on the left, larger scales traced by VISIR in the centre and the entire envelope displayed on the right.

visible for W33A, MYSOs viewed at smaller inclinations may reveal the presence of a dusty accretion disk and this could be the case for G305. More recently, Maud et al. [2017b] show that at larger scales W33As protostellar environment is very chaotic, with the spiral-like structures wreathing their way around the central source suggesting a highly turbulent, disturbed environment. This is the antithesis of the environment of G305, which appears to be a very 'typical' YSO with clearly defined outflow cavities and the shadow of a disk visible even in near-infrared images. One explanation for the difference between the two MYSOs could be that W33A could have formed a disk like G305 that was then was either disturbed post-formation by the processes creating the spiral structures mentioned above, or alternatively that

[§]IDL is a trademark of Exelis Visual Information Solutions, Inc.

the system has always been so volatile that the disk was never able to form at these scales.

Wheelwright et al. [2012] compare $\sim$20μm profiles generated from the envelope model of de Wit et al. [2010] to the VISIR images of a number of MYSOs. They deduce that this model can reproduce the images and SEDs for the majority of their sample. Adding MIDI, as done in this work, adds a stringent constraint to the interpretation of the geometry of the source. Our analysis highlights the fact that the VISIR data is not sensitive to the disk properties of the YSO but is heavily influenced by the cavity properties, while the MIDI is affected by both. Given this, it is therefore unsurprising that the envelope only model fits the majority of their sample and this does not rule out the presence of disks around the MYSOs, assuming they are at similar distances to G305. MIDI probes the MYSO at scales small enough to trace disk emission, while the sensitivity of VISIR is not high enough for such an endeavour given the MYSOs distances. This indicates that if one wants want to identify the presence of a disk, whilst also accurately constraining the cavity properties of MYSOs in the infrared, a combination of the two observations is invaluable.

As mentioned briefly in the introduction, G305 was also included in a survey of massive star formation by Liu et al. [2019]. In this work an SED of G305 was compiled from fluxes obtained from Gemini/T-ReCS and SOFIA/FORCAST images and was fit using their ZT radiative transfer models [Zhang and Tan, 2018] resulting in five best-fitting models. The stellar mass and inclination of our preferred fit are comparable to the ranges for these values listed for their five best fitting models. Other notable parameters such as cavity opening angle differ between our two works, but the spatial resolution of the N-band data presented here is higher and therefore the work in this thesis is more tightly constrained on this parameter.

Within their deep, single-dish, 3.8-24.5μm images a secondary source (referred to as G305B2) can be seen $\sim$1" to the north-east of G305 whose nature remains unclear.

Interestingly, G305B2 is not present across the entire wavelength range, being absent from the shorter wavelength images, with an increasing relative brightness throughout the N-band and progressively becoming less visible again towards 24.5μm. Liu et al. [2019] mark a silhouette in their 9.7μm image between G305B2 and G305 and postulate that it could be indicative of the silhouette of an inclined disk. If this is a disk silhouette, that would imply that the inclination of the source is the opposite to what is found in this work. Changing the inclination of the model to its opposite (145° instead of 35°) has minimal effects on the MIDI visibilities (as FFTs are symmetric), the VISIR radial profile (which is azimuthally averaged) and the SED. However it does present differences for our images, as the position of the brightest lobe is consistent only if the inclination is 35° for both the VISIR image and the VVV image (illustrated in Figure 3.6). The cavity lobe to the south-west is dimmer, and for a reverse inclination this would be the brighter lobe. This cavity lobe is outside the Gemini imaging field-of-view shown in Liu et al. [2019] and consequently was not discussed in their work. Asymmetry is also present in our 19.5μm VISIR image and the Ks-band image and as such it is possible that they trace this second source.

Earlier in this chapter the poor fitting of the MIDI data for Configuration A was mentioned. The model visibilities were much higher than those observed, implying that extra emission must be present that is not being produced in the model. Given that the secondary source found in the Gemini images lies in the region of the suspected outflow cavity, it therefore appears a good candidate for the source of this emission. Whilst our MIDI data trace only a 0.52" area, one can assume that if material has been entrained out to nearly 1.5", material will be also be present at $\sim$0.5".

Given the confirmed inclination of the source from the VVV and VISIR images, it is concluded that G305B2 is unlikely to be a coherent disk structure. The point-like material could be entrained cavity material, fall-out from potential disk fragmentation

or indicate the presence of a binary companion. The latter two possibilities are addressed further in the following Section 3.3.5.

3.3.2 Definitely a disk?

In Section 3.3 it was mentioned that the unsatisfactory fits presented by the envelope-only model from de Wit et al. [2010] and the fact that a dark lane exists between two apparent cavity lobes in the VVV Ks-band image led to the inclusion of a disk in the model. However, other studies find an insensitivity to disk emission and have shown that cavity emission alone can control the N-band visibilities (e.g. de Wit et al. [2010]). Therefore, for completeness, Figure 3.9 is presented, which includes the best fitting model visibilities and those for the same model with no disk. The VISIR and SED fits for the no-disk model are not added as these change minimally with the inclusion or exclusion of a disk (see Sections 4.1.2 and 4.1.3). When the disk is removed the shape of almost all the model visibilities violates what is observed, especially the peak-like features observed in Configurations C, D and E between 7-8μm. This implies that the illuminated cavity walls represent too large a surface and that a compact component is required to recreate these visibilities. Configuration F is the only configuration satisfied by the no-disk model and constitutes the worst quality dataset of the group. It has already been stated that to satisfy the silicate absorption feature within the SED that the cavity opening angle could not be larger than 12 degrees. Varying the cavity opening angle is the most effective way of changing the model visibilities in an envelope-only model, and with this limitation in place from the SED an envelope-only model could therefore not be found which would satisfy the N-band data as well as the present disk-including model.

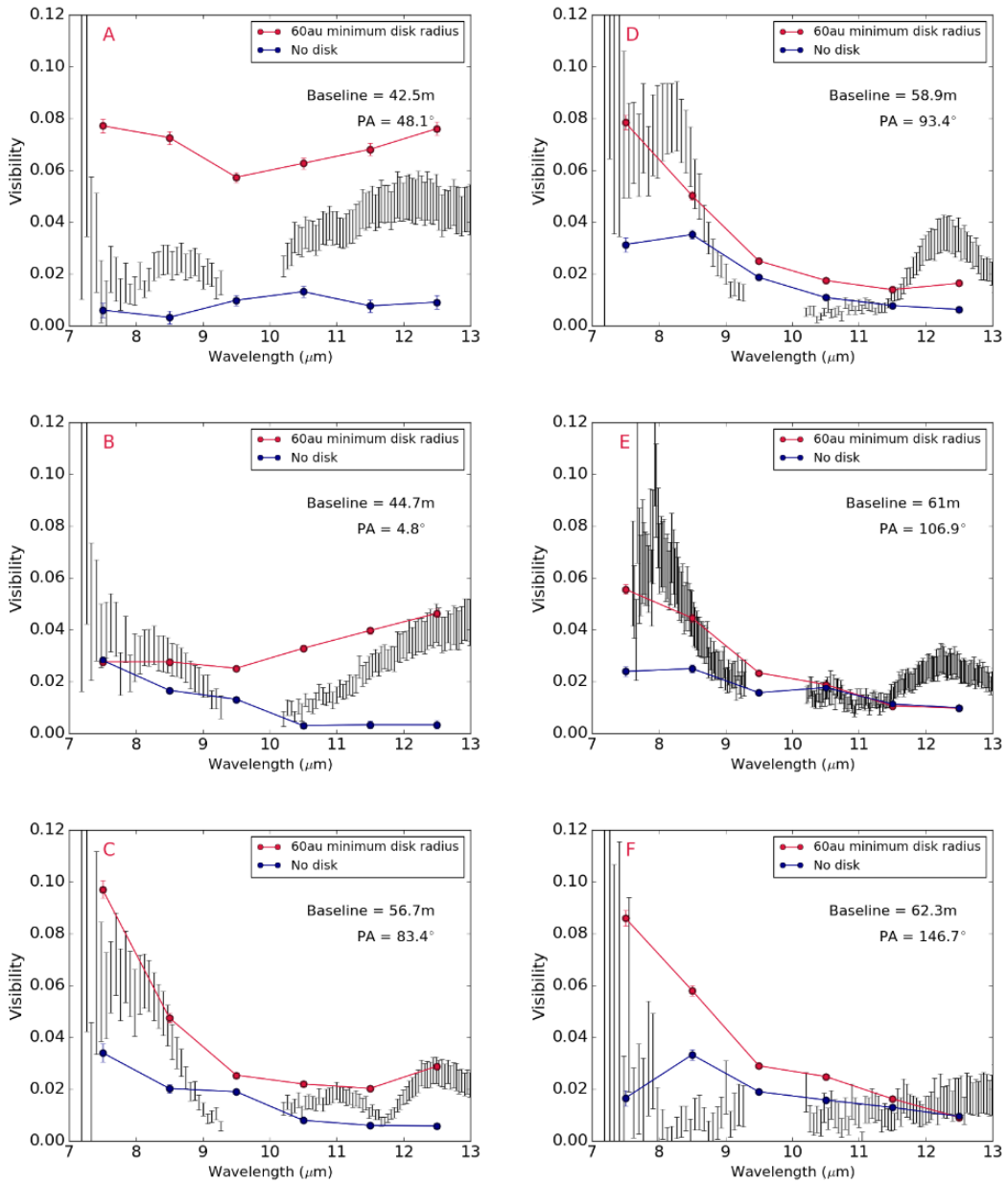

Fig. 3.9 Observed visibilities for each configuration (black) with the simulated visibilities for the best model fit (red) and a model with no-disk (blue).

3.3.3 Testing the possibility of a bloated protostar

While the central luminosity of the protostar is crucial to successfully fitting the SED, the radius and temperature of the central protostar can still be varied whilst maintaining this value. One object that creates the required luminosity is a central object with a temperature of 35000K and radius of $6R_{\odot}$. Such properties are typical

of an O7 zero-age-main-sequence object as defined by the work of Straizys and Kuriliene [1981]. This central object is similar to the object used in de Wit et al. [2010] for W33A, but is dimmer by nearly 30% due to its smaller radius ($6R_\odot$ as opposed to $8R_\odot$) for the same stellar temperature. One could assume that because of the hot nature of the object that the protostar should therefore be able to ionise hydrogen in its surrounding material and create a HII region, contrary to the literature. It is possible to include a protostar that does not have this high temperature, thereby maintaining its luminosity, by 'bloating' the star; expanding its radius and lowering its temperature. This possibility has been modelled extensively (Hosokawa et al. [2010] and Hosokawa and Omukai [2009]). Bloated protostars have been utilised in the fitting of other MYSOs, namely AFGL 2136 [de Wit et al., 2011] and M8EIR [Linz et al., 2009].

Hosokawa et al. [2010] propose the bloating of central protostars as a by product of massive protostellar accretion where the protostellar radius swells to 30-$100R_\odot$. In order for this to occur, Hosokawa et al. [2010] required envelope infall rates of order $10^{-3}M_\odot yr^{-1}$, which are comparable to our model envelope infall rate of $7.4\times10^{-4}M_\odot yr^{-1}$. Therefore the bloating effect Hosokawa postulates is feasible according to our analysis, if the protostellar system manages to retain a large portion of its envelope infall rate and some accretion continues across the 60au gap.

Two models were run where the compact protostar was replaced with two different bloated protostars to assess their affect on our observables. Each bloated central object had the same luminosity as their hotter compact counterpart with the first having a radius of $30R_\odot$ and a temperature of $\sim$16000K and the second a radius of $100R_\odot$ and a temperature of $\sim$9000K, in agreement with the radii estimates of Hosokawa et al. [2010]. Changing the radius of the central protostar while maintaining its luminosity has negligible effects on the VISIR profile but the silicate absorption feature of the SED did becoming marginally deeper for the $100R_\odot$ bloated star. In terms of the MIDI visibilities, differences were seen but the visibil-

ities did not go up and down uniformly, with increases and decreases seen across the same N-band spectrum for each configuration. The $100R_{\odot}$ protostar showed an average difference in visibilities of 0.0025 compared to the compact object, meaning a percentage difference of $\sim$6%. This did not produce significant changes except in the case of Configuration B, where the visibilities at 9.5 and 10.5μm decreased, improving the fit. For a $30R_{\odot}$ bloated star the average change in visibilities was 0.0018, constituting a $\sim$4% change in visibilities compared to the compact central object and the fit of Configuration B was again a slight improvement on the fit for the compact source, although to a lesser degree than the $100R_{\odot}$ protostar.

3.3.4 The weak silicate absorption feature in the SED

The weak silicate absorption and the adjustments required to fit it present further questions about this MYSO. MYSOs are typically extremely dusty environments (with previous works finding deep silicate absorption features in other MYSO environments) yet the feature of G305 is weak. This implies a less dense surrounding environment and indeed, lower cavity densities were required in order to fit the silicate absorption feature of our observational SED. A weak silicate absorption feature can be a result of a combination of emission and absorption in the environment [Whittet et al., 1988]. Levenson et al. [2007] for example note that a deep silicate absorption feature should be the result of a continuous optically and geometrically thick dusty medium while a clumpy medium whose curves are illuminated by from an outside source will have a much weaker feature as the emission compensates for the absorption. A clumpy medium is not replicated in our modelling but it is possible that the real-life geometry of G305 could be suited to this case. It has been previously mentioned that there is a source that is bright at longer wavelengths which could be illuminating the object and contaminating our flux measurements at longer wavelengths, however this source is not bright in the mid-infrared and so one would

not expect this illumination to be filling in the absorption feature. This combined with the fact that a low density environment is required for successful VISIR fitting of G305 contradicts the first case suggested by Levenson et al. [2007] and implies that the weak silicate absorption feature is indicative of the nature of the source, not that of outside illumination, and that this MYSO is less dense than typical examples of its class. YSOs are believed to disperse over time, so the low density environment of G305 implies that this dispersion has begun, and that the MYSO is evolving from an envelope-dominated to disk-dominated system. This is supported by work by Walsh et al. [2007], who conclude that the lack of HC_3N, NH_3, OCS, or H_2O emission observed by ATCA implies that G305 has evolved to the point where it has cleared a significant portion of its surrounding material.

3.3.5 The inner cleared regions

The disk of G305 has an inner rim of 60au as opposed to the ∼6-11au inner radius of the accretion disk found by Kraus et al. [2010] around IRAS 13481-6124 using AMBER observations - almost an order of magnitude difference in size. In order to form a minimum dust radius of 60au through dust sublimation alone, one requires a central object of $\sim 5 \times 10^5 L_\odot$. When such a central source is included in the code the SED fit is violated. The sublimation radius of the central YSO that best fits the SED is ∼18au. However, a model with a sublimation radius of this size results in a much worse fit for the MIDI visibilities (with no change to the VISIR and SED). This implies that the inner disk has been cleared out to the 60au inner radius which best fits the observations.

Such a clearing in the inner regions is typical of the transition disk phase observed for low-mass stars described in the introduction of this chapter, where accretion is ongoing, with the presence of gas but absence of small dust. This is in agreement with the dust types of the successful model which do not contain small grains or

PAHs. Tang et al. [2017], van der Marel et al. [2014], van der Plas et al. [2017] and Fedele et al. [2017] show inner radii of order 10s of au for low-mass transitional objects, in agreement with the size of the inner radius of our best-fitting model. Considering these properties and the weak silicate absorption feature discussed previously, our work suggests that the disk surrounding G305 could present an example of a transition disk around an MYSO. Such a disk has not been reported around a high-mass object and if this disk is transitional in nature this has implications for the massive star formation process, in particular its similarity to the evolutionary sequence of low-mass objects, presenting a new observed evolutionary phase for massive forming stars.

The presence of a pre-transitional disk is also implied by the work of Ilee et al. [2013]. Their CO band-head emission data of G305 is satisfied by a disk of 0.6±0.3au minimum radius, suiting the small gaseous inner disk (scales of order 0.1au) remains close to the inner star expected for this phase [Espaillat et al., 2010]. Further observations of the dust and gas at small radii could confirm whether the disk found in Ilee et al. [2013] and our work coexist and whether G305 presents an example of this evolutionary stage.

While the exact mechanism that has caused the 60au radius gap in this disk cannot be confirmed, various mechanisms for the clearing of the inner region have been proposed for low-mass stars. One such mechanism which translates well to the massive protostellar case is photoevaporation. Photoevaporation is a process whereby high-energy radiation fields heat the uppermost layers of the disk, raising the thermal velocities of its particles above the escape velocity [Hollenbach and Gorti, 2005] resulting in a disk wind. Given that MYSOs have typically large luminosities it seems reasonable to consider that this may be the source of clearing for G305. However it is the gas disk that exists within the dust sublimation radius that will be expelled by photoevaporation and this is not considered by a radiative transfer model, although the work previously mentioned by Ilee et al. [2013] implies that a gas disk

still exists close to the star. Disk theory work suggests that material captured within the resultant disk wind can either be removed from the system or be recaptured and rejoin the disk at larger radii. It has been proposed that the mass-accretion rate decreases with age and will eventually become equal to the amount of mass loss from the disk [Clarke et al., 2001]. After this point, matter is solely lost through the disk wind and is not replenished, meaning that as material from the inner regions continues to accrete the inner regions begin to clear of material. As photoevaporation continues, the inner hole can continue to grow as the rim is irradiated [Alexander and Armitage, 2007]. This model predicts low mass-accretion rates and disk masses and as a result is considered an unlikely mechanism for the formation of low-mass transition disks. However this has not been considered for MYSOs where the relative mass of the disk compared to the star is much smaller than in low-mass cases (for our model of G305 the disk is 5% of the mass of the central MYSO).

Another potential source of clearing proposed for low-mass disks is viscous evolution. The theory postulates that as gas falls towards the central protostar the remainder of the disk spreads outwards to larger radii to conserve angular momentum [Espaillat et al., 2014]. This gas is thought to be 'driven' and in the low-mass case this is attributed to magnetohydrodynamic turbulence, which is not necessarily expected around MYSOs who display little magnetic activity. Arce et al. [2007] however do note the presence of turbulence within and resulting from massive protostellar outflows at varying scales and this mechanism may therefore also present an explanation for the cleared inner regions for G305.

Another mechanism discussed in the context of the cause of the hole in transition disks around low-mass stars is the presence of planets. The detections of planets around higher mass stars are few and tenuous. The NASA Exoplanet archive[¶] provides a comprehensive list of companions detected around other stars. 4055 companions are listed in total and of those objects 3302 have listed stellar masses (as

[¶]https://exoplanetarchive.ipac.caltech.edu/

of 19/9/19). From that subset, only 6 objects (0.229%) are 8 solar masses or larger and the error bars on the determination of these stellar mass are vast and they could, in fact, be low-mass stars. Given that massive forming stars are thought to reach the main sequence in $\sim 10^5$yrs and that planets were not thought to form around low-mass until the late stages of their formation (between $\sim 10^6$-10^7yrs) it would seem that planets could not form around massive stars. However, more studies are appearing that observe gaps and rings in low-mass protoplanetary disks at the Class 0/I stages. For example, Sheehan and Eisner [2018] find that the low-mass Class I protostar GY 91 has multiple rings within its disk and conclude that if planets were sweeping out these rings that they must be able to form within 0.5Myrs of the disk appearing. Harsono et al. [2018] find this implied through the absence of carbon monoxide isotopologues. They conclude that shielding by millimetre-size grains is responsible for the lack of emission and suggests that grain growth and millimetre-size dust grains can be spatially and temporally coincident with a mass reservoir sufficient for giant planet formation. Manara et al. [2018] note that the protoplanetary disks observed around young stars do not have enough mass to form the observed exoplanet population and propose that one implied solution to this problem is that the cores of planets must form in less than 0.1-1Myrs. If the implications of these works are correct, then planets may be able to at least begin to form around massive forming stars and therefore disrupt the disk at small radii.

A potential scenario that perhaps translates better to the massive star formation process is the possibility that a forming companion star could be sweeping out the inner regions of the disk instead of a planet. The multiplicity fraction for massive forming stars is estimated to be large [Sana et al., 2012], although the specific formation mechanisms of these binaries/multiple systems is not confirmed. Pomohaci et al. [2019] include G305 in their pilot survey of binaries and do not class it as a multiple, but their method is suited to detecting wide binaries (separations of 400-46000au) so a companion star could still be forming within the determined 60au

radius which they do not detect. Ilee et al. [2018] detected a body orbiting around MM1 within the G11.92–0.61 high-mass clump using ALMA observations. They conclude that this object, MM1 b, could be one of the first observed companions forming via disk fragmentation based on the extreme mass ratio and orbital properties of the system. Meyer et al. [2018] present 3D gravitation-radiation-hydrodynamic numerical simulations of massive pre-stellar cores. They find that accretion discs of young massive stars violently fragment without preventing accretion onto the protostars and that the migration of some of the disc fragments migrate on to the central massive protostar with dynamical properties comparable to a close massive protobinary system. Given that the mass of the potential disk around G305 is not well constrained by our infrared observations and that the disks observed around other massive stars (e.g. Johnston et al. [2015]) have the potential to be very massive, a forming binary companion could therefore constitute a more realistic body to disrupt the disk at small radii. Meyer et al. [2018] postulate that FU-Orionis-type bursts could happen at the same time as close massive binary formation, with Caratti o Garatti et al. [2017] detecting such a burst around the MYSO S255 NIRS 3. The secondary source, G305B2, mentioned in Section 3.3.1, appears point-like in the single-dish images of Liu et al. [2019] and could potentially be a forming 'proto-companion'. If disk fragmentation is occurring, a piece of dusty material expelled from a fragmenting disk could also cause the presence of G305B2 and explain the poor fitting of Configuration A.

Another possibility is that the winds arising from the MYSO itself could clear the dust within the inner 60au. While these winds would be a result of the luminosity and temperature of the object, which are input parameters within the Hochunk code, such winds are not a component of the models used in this work. Parkin et al. [2009] present hydro-dynamical models investigating how disk and stellar winds interact with envelope material and that reverse-shocks can occur at scales less than 500au. Their work does not look at the 20-100au scales relevant to this work and given the

limits of the models used here, the reason why the outflows disrupting material at 500au would only disrupt material out to 60au cannot be explained.

Given the uncertainty as to the similarity of low-mass and massive star formation it cannot be concluded whether one of the discussed mechanisms or a combination of the effects is a more likely culprit for the cleared the dust within the inner disk regions of G305. Further observations and study will allow for a more detailed discussion of this subject.

3.4 Conclusions

Through the combination of multiple baselines of MIDI interferometric data, VISIR imaging data and an SED the characteristics of the massive YSO G305.20+0.21 are constrained with a 3D radiative transfer model. The best-fitting model indicates that the MYSO is surrounded by a large extended dusty envelope with bipolar cavities and a dusty disk, as per the Class I specification of protostars. This work joins the growing number of publications that suggest that massive stars do indeed form disks as a means of accreting material onto the central protostar. In order to successfully reproduce the observed weak silicate absorption feature in the SED a low-density protostellar environment is required and an inner dust radius of 60au, approximately three times the dust sublimation radius of the source. Since the inclusion of a source which induces a dust sublimation radius of this size completely violates the fit, it can be concluded that some mechanism other than the inherent luminosity of the source must be causing the clearing of dust in these inner regions. This characteristic, and the low densities, are typical characteristics of the transition disk phase observed around low-mass stars. While this source is an MYSO will and will remain embedded for its entire evolutionary sequence, the fact that traits of a transition disk are observed within the MYSO implies that this source could constitute the analogous phase for massive star formation. Further work can help to confirm whether this is the

case. ALMA can be of assistance in ascertaining the stability of the source, by using CH_3CN data to test the kinematics of the protostellar material and image reconstruction with instruments such as GRAVITY and MATISSE can be used to unambiguously confirm the presence of the inner rim.

Chapter 4

A multi-scale analysis of a sample of MYSOs

In previous chapters, the characteristics of two MYSOs were obtained by simultaneously fitting 3D radiative transfer models to N-band interferometric data, Q-band images and an SED. In this section, further results are presented for a sample of MYSOs, the largest of its kind currently within the literature. Just under half of the sample have polyaromatic hydrocarbons in their environment, based on emission features observed in their spectra [Gibb et al., 2004]. A section is dedicated to each object and within each of these 1) the MYSO is introduced 2) any interesting effects on each of the simulated scales when experimenting with the parameter space of the RT code are discussed and 3) the results and final model for each object are presented.

4.1 NGC 2264 IRS1

NGC 2264 IRS1 is one MYSO in a young ($\sim$3Myr) cluster which is in turn located in the Mon OB1 molecular cloud region [Grellmann et al., 2011]. IRS1 is the brightest YSO in NGC 2264 and is suspected to be the source of the radiation pressure creating

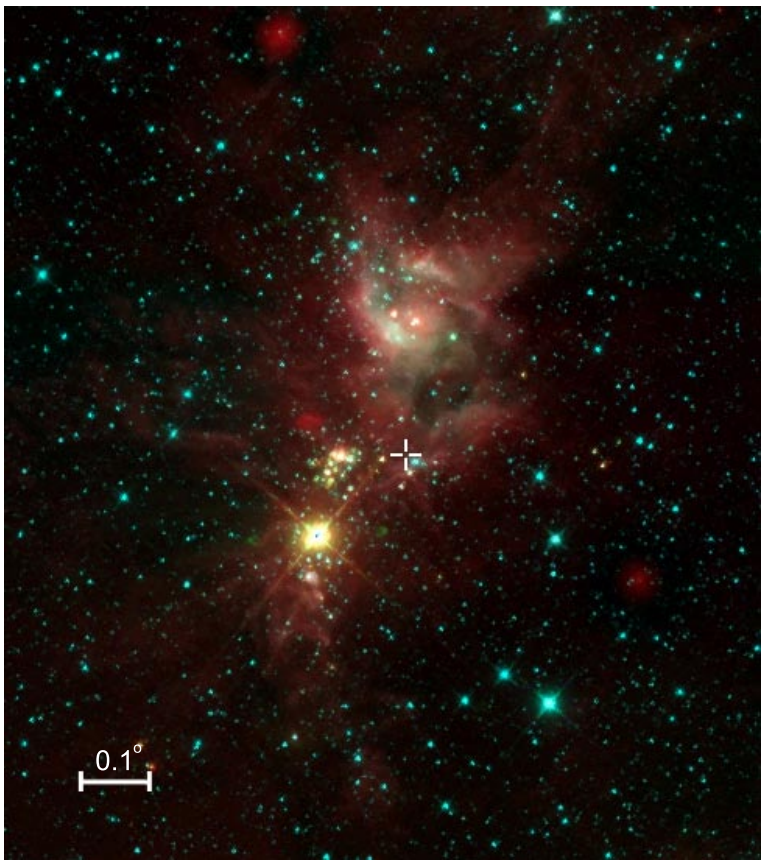

Fig. 4.1 2MASS three-colour image of the Cone Nebula. The location of NGC 2264 IRS1 is shown by a white cross. The image was obtained using SIMBAD and the Aladin Lite viewer [Wenger et al., 2000].

the Cone Nebula observed in the region (Fig. 4.1). Thompson et al. [1998] believe the source to have a mass of $9.5M_{\odot}$ based on its B0-B2 spectral type. The source is reported to have a luminosity of order $10^3 L_{\odot}$ ($3.5\times10^3 L_{\odot}$ determined by far-infrared observations in Harvey et al. [1977a], $4.7\times10^3 L_{\odot}$ determined from isothermal temperature modelling of photometric data Schwartz et al. [1985]). A large visual extinction, between 25-30 magnitudes, casts doubt on the exact luminosity of the source. This lower-limit was determined by Thompson et al. [1998] based on H-K color considerations, while the upper limit was suggested by Thompson and Tokunaga [1978] based on the required reddening needed at 9000Å of 14.3. Schreyer et al. [1997] present evidence for a jet orientated along the line of sight and clumps and large-scale outflows (e.g. Ward-Thompson et al. [2000]) have also been detected

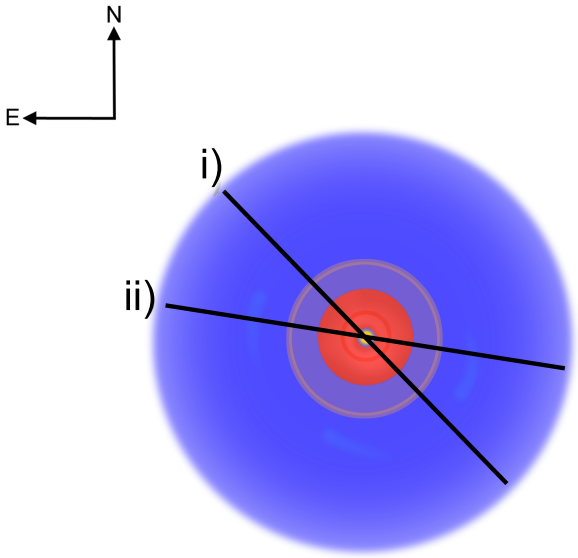

Fig. 4.2 Schematic of the suspected geometry of NGC 2264 IRS1 (a close to pole-on disk-cavity-envelope system) overlain with the position angles of each configuration of the MIDI data. The envelope is shown in blue, the cavity in yellow and the disk in red.

Table 4.1 List of MIDI observations used in the fitting of NGC 2264 IRS1. The configurations are illustrated in Figure 4.2.

Configuration	Date	Telescopes	Projected baseline (m)	Position angle (°)	ESO Run ID
i)	02/15/2009	UT2-UT3	40.2	43.9	082.C-899(A)
ii)	12/23/2005	UT2-UT4	89.1	81.1	076.C-0725(B)

in association with the source. Previous studies have failed to concretely resolve disk structure around the source. NGC 2264 IRS1 was observed with the ISO satellite resulting in a low-resolution infrared spectrum [Gibb et al., 2004]. Within this spectrum, water ice absorption lines (3.1 and 6.0μm), CO_2 ice lines (4.27μm, 15.2μm), solid NH+ lines (6.8μm) and CO_2 gas lines (4.7μm) are visible, suggesting relatively large column densities of cold dense material along the line of sight towards the central source. Some evidence exists for PAHs in the environment of NGC 2264 IRS1 (e.g. Gibb et al. [2004], discussed using an alternative name AFGL 989) but in

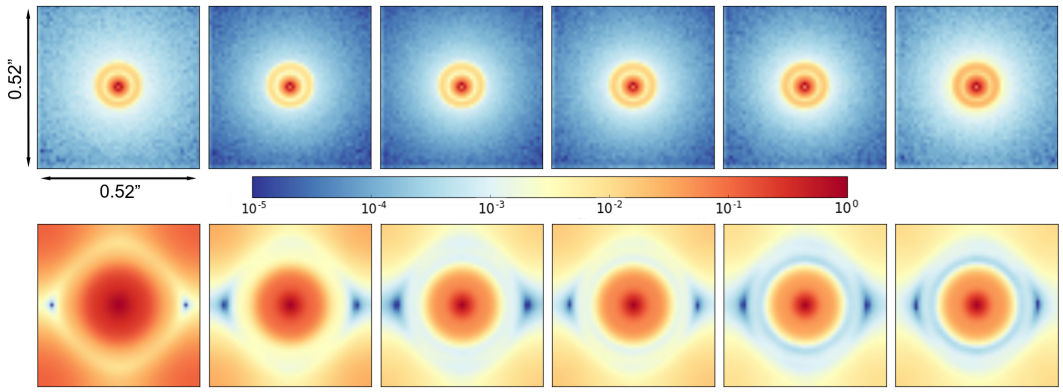

Fig. 4.3 Logarithmically scaled model images (top row) at 7.5, 8.5, 9.5, 10.5, 11.5 and 12.5μm and their resulting fast Fourier transforms (bottom row) that correspond to the preferred model of NGC 2264 IRS1. Each image is 0.52" in width corresponding to the interferometric field of view. The colour bar applies to both sets of images and represents the number of counts.

more recent work while Buckle et al. [2012] note strong PAH emission in sources surrounding IRS1 and extended nebulous regions of the Cone nebula, they do not associate PAHs with the NGC 2264 IRS1 directly.

Grellmann et al. [2011] studied the source using mid-infrared interferometry, using two sets of MIDI data and the source's SED. A variety of models (geometric and 2D radiative transfer with RADMC [Dullemond and Dominik, 2004]) were trialled and ultimately they found that a model including a flat, optically thick circumstellar dust disk allowed sufficient fitting of the datasets. This comes with the caveat of poor fitting of the peak of their SED and they note that an envelope cannot not be ruled out as a possibility as they focus on the regions within 400au. Boley et al. [2013] included one of these MIDI datasets in their work, and determine from their geometrical modelling that the compact mid-IR emission could trace disk structure.

de Wit et al. [2009] present model fitting of a 24.5μm COMICS profile and the SED of the source. They fit a power-law model to the source, and note that a power-law exponent of 1.5 is required to produce reasonable fits to the intensity profiles, mid-IR flux levels and bolometric luminosity. This does not present a good

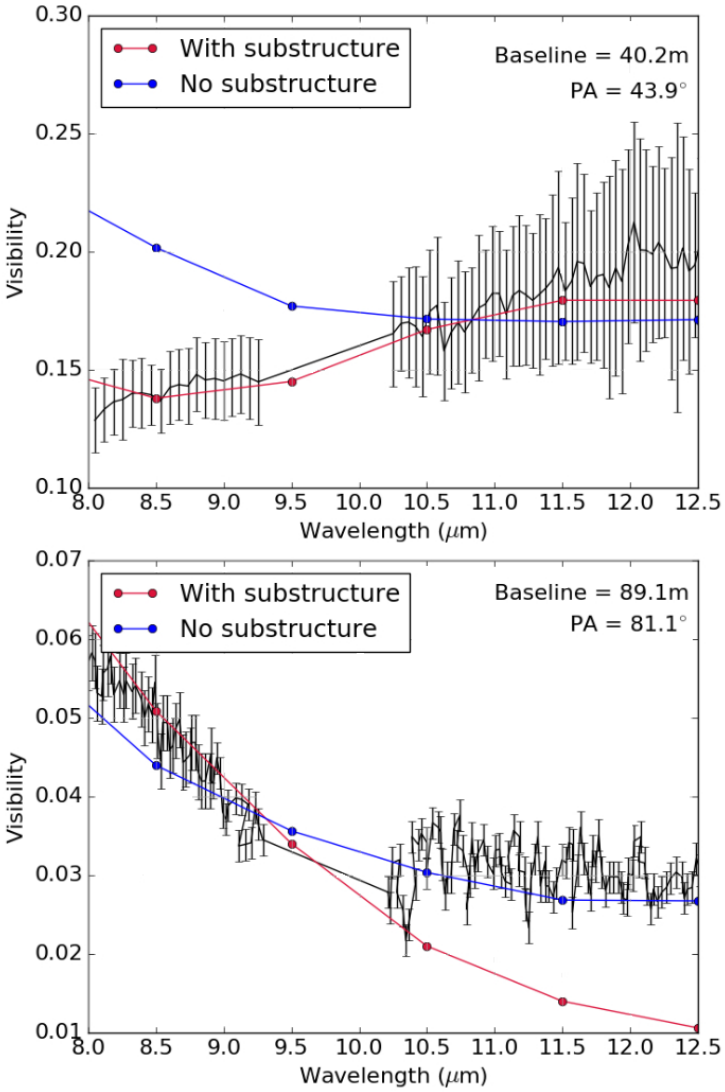

Fig. 4.4 Observed visibilities for each configuration (black) with the simulated visibilities for each model image (coloured).

fit to the far-IR and mm data however and they state that to maintain the spherical model much larger luminosities would be required that violated the fits to the other observations.

4.1.1 Observations

The MIDI data for NGC 2264 IRS1 came from Boley et al. [2013] and Grellmann et al. [2011], meaning that this is the only source studied which uses MIDI data in the

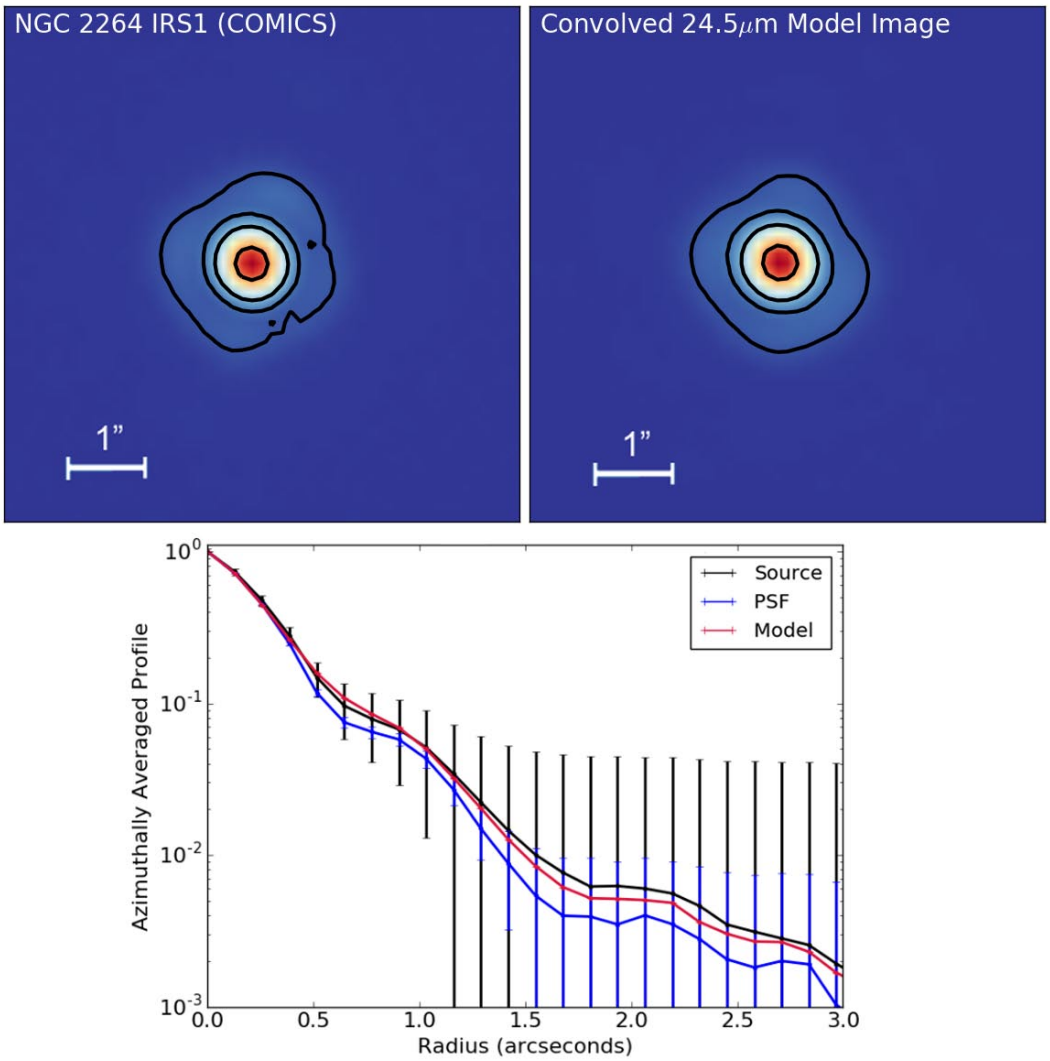

Fig. 4.5 COMICS 24.5μm image (top left), convolved model image (top right) and subsequent radial profiles (bottom). The model image was convolved with the PSF of the observed object to accurately mimic the effects of the telescope specific to the observations. The contours in the images represent 5, 10, 25 and 75% of the peak flux.

SCIPHOT mode. The two configurations are very different in both PA and baseline. The Boley data are of lower resolution whilst the resolution of the Grellmann data is nearly twice as good. Given the baselines of the observations and the source's distance of 738^{+57}_{-50}pc (Kamezaki et al. [2014], determined through H_2O maser parallaxes), the MIDI data traces scales between 0.02" (at 7.5μm for the 89.1m baseline configuration) and 0.07" (at 12.5μm for the 40.2m baselines configuration)

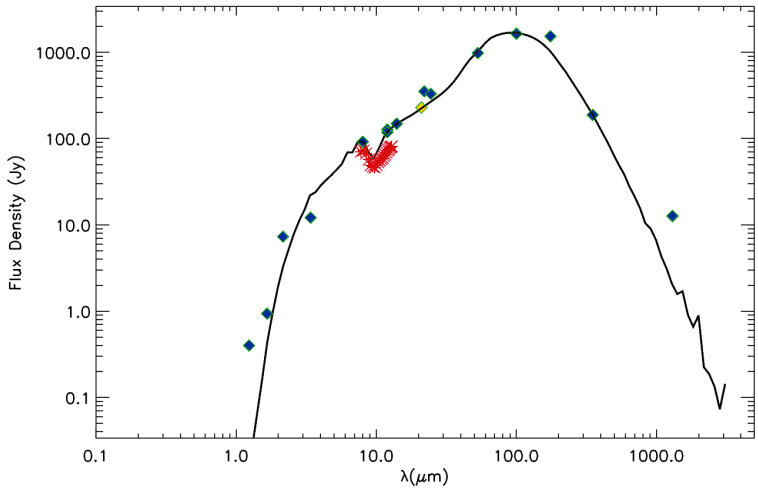

Fig. 4.6 Model spectral energy distribution of the best-fitting model (black). Multi-wavelength flux measurements from the RMS are represented as blue diamonds, the yellow diamond represents the COMICS flux density and the fluxes corresponding to the MIDI visibilities are also shown in red.

or ∼14-55au. When fitting this MIDI data, the PA on the sky of the source varied for each model in intervals from 0-360° throughout the fitting process (as described in Chapter 2) in order to determine the best value.

The COMICS image from de Wit et al. [2009] provided a trace of the ∼20μm emission. The SED fluxes between 1-21μm were obtained from the RMS database. The COMICS flux from de Wit et al. [2009] was included, as well as the long-wavelength data from Harvey et al. [1977a] and Chini et al. [1986b] used in Grellmann et al. [2011].

4.1.2 Results

Through the fitting it was determined that an Ulrich-type density distribution, as opposed to the power-law one of de Wit et al. [2009], can satisfy the fits of all datasets. Including the envelope is necessary to obtain a good fit to the longer wavelength data in the SED, which was not reproduced by the fits of Grellmann et al. [2011]. The final model consists of a disk-outflow system, surrounded by this Ulrich envelope. The central protostar has a luminosity of $4.17\times10^3 L_\odot$ which is in good agreement

with those found in the literature. The stellar mass in the model is $9M_{\odot}$ which also matches previous work. An inclination of 15° was able to successfully fit all the observables, which is consistent with the existence of an outflow in the line-of-sight found by Schreyer et al. [1997]. NGC 2264 IRS1 presented an interesting case for the fitting process due to its close distance of ∼738pc. During the fitting of other objects at more typical MYSO distances (2-4kpc) the COMICS profile was largely unaffected by the variation of disk parameters. In the case of NGC 2264 IRS1 however, the disk had profound effects on the profile and added another level of complexity to the fitting.

Figure 4.3 shows the model images and FFTs for NGC 2264 IRS1. Because the inclination of the source is such that it is nearly face-on, both the images and the FFTs are very symmetric. Figure 4.4 shows the MIDI data and two models which are discussed further in the next section. The two N-band configurations of NGC 2264 IRS1 trace significantly different areas of the protostellar environment, with large differences in both PA and baseline (an illustration is provided in Figure 4.2). Both the MIDI configurations predominately trace disk material. The 40.2m baseline was characterised by its upward trend in visibility which proved challenging to fit. Often the issue was, again, that the model visibilities were too high between 7.5-9μm especially, indicating that the emitting regions at larger scales within the disk were also too compact and needed to be minimised. A near-perfect fit for Configuration ii) could be found when a disk was included with a 500au maximum radius consisting of 20% 'large grains' (Model 1 in Wood et al. [2002]) and 80% 'small grains' (Galactic ISM grains as defined by Kim et al. [1994]) but the fit for the 7-9μm region of the 40.2m baseline fit was poor in comparison. By adding substructure to the disk by using the 3D, spiral capabilities of the code, the fit for configuration i) could be improved. This substructure was induced by using the 'spiral' parameter section of HO-CHUNK3D. The spiral included has a loose pitch angle of 30°, contains 90% of the mass of the disk and begins and ends at 30 and 60au respectively. These

parameters essentially create substructure which manifests as a disk with a gap rather than an obvious spiral. Including this spiral dramatically improves the fit of Configuration i) but worsens the fit of configuration ii) as can be seen in Figure 4.4. The overall change in the simulated visibilities for configuration ii) (V^2 ~0.02) is smaller than the improvement in visibility for configuration i) (V^2 ~0.08) so the model with substructure is referred to as the preferred fit.

Given there is some evidence for PAH emission in the literature, the inclusion of PAH emission in the code was experimented with. Adding PAHs/VSGs to all areas of the model protostellar environment increases the visibilities overall, vastly worsening the fit of configuration i). However, including the PAHs in the cavity and envelopes only results in no change to the MIDI visibilities. This consecrates the fact that the MIDI data is dominated by disk effects for this source. Given that a good fit could not be obtained when including PAHs in the disk, but PAH signatures are observed [Gibb et al., 2004], compromise is made by adding them to the cavity and envelope only. This can be explained physically, as PAHs constitute some of the smallest components of protostellar material and behave like very small dust grains. As a result, they could be vulnerable to the effects of photoevaporation. This means that they could be pushed from the inner environment into the envelope and cavity material at greater distances from the central protostar. Additionally, the PAHs in the further reaches of the envelope material would feel a weaker force from the stellar photons and would not be so easily removed from the environment. Therefore, the idea that PAHs may be present in outer regions of the protostellar environment but not the inner regions, may be consistent. The improvements noted by the inclusion of the spiral exist with or without the presence of PAHs.

Figure 4.5 presents the COMICS image, model 24.5μm image and the resulting radial profiles. The image is symmetrical and appears to show details of substructure, but de Wit et al. [2009] state that most of these are due to diffraction effects. Given its close distance, the 24.5μm emission of NGC 2264 IRS1 is heavily influenced

by the disk included in the model. The close distance, inclination and the need for substructure within the model meant that the disk mass for NGC 2264 IRS1 could be more accurately constrained than other sources. Changing the cavity density exponent, and therefore how evenly the cavity material was distributed, could assist in the fitting of the source. Increasing the exponent from the default value of 0 (constant density throughout the cavity) to 0.25 (meaning the mass was slightly weighted towards the bottom of the cavity, close to the protostar), reduced the amount of 24.5μm emission creating a better fit. This is consistent as more emitting material is at smaller radii within the protostellar environment, making the source appear less extended. A combination of the close-to-pole-on inclination and a foreground A_v of 25 allowed sufficient fitting of the silicate absorption feature in the SED and is close to the A_v values calculated by Thompson et al. [1998] and Thompson and Tokunaga [1978]. Changing the cavity exponent to satisfy the COMICS profile flattened the peak of the SED slightly, improving the fit. The SED fit is shown in Figure 4.6.

4.1.3 Discussion

The fact that including substructure in the model has marked improvements on the fit of the data has significant implications for the massive star formation process. Substructures are rarely detected in disks around massive protostars. Sanna et al. [2019] detect a sub-Keplerian disk and jet system around a different MYSO G023.01-00.41 and find that the CH_3OH emission at scales $\sim$2000au is significantly warped with respect to the plane. Various other disks (e.g. Ilee et al. [2018]) show other irregular features as a result of fragmentation, but disks such as these are unlikely to be examples of a stable stage of the massive star formation process. The substructure which improves the fit of the data for NGC 2264 IRS1 manifests as a gap in the disk, shown in Figure 4.3. For the low-mass case, various causes have been suggested for gaps. The first is the presence of a forming planet. Pinte et al. [2019] present

one of the first confirmations of a planet in a gas and dust gap in the protostellar disk of the 2.4$M_{\odot}$ object HD 97048, but otherwise the presence of planets in these gaps has mostly been inferred. As discussed in the context of G305 in Chapter 3, planets are not observed around massive stars but whether they can never form or cease to exist as the protostar becomes more luminous with age has not been confirmed. An alternative method of gap creation is dust trapping. Dust traps [Whipple, 1972] occur when a local gas pressure maximum in the disk attracts and traps dust grains allowing clearing to occur in the disks and has also been proposed as a mechanism for observed gaps in low-mass disks (e.g. Gonzalez et al. [2017]). Recently van der Marel et al. [2018] show through physical-chemical modelling that the gaps observed in ALMA data of the disk of the Herbig Ae star HD 163296 can be reproduced from dust trapping alone, without the presence of a planetary body. Dust growth presents another avenue of gap formation whereby the amalgamation or pile-up of dust grains clears space in the disk (e.g. Zhang et al. [2015], Okuzumi et al. [2016]). Instabilities, both large-scale [Lorén-Aguilar and Bate, 2016] and gravitational [Takahashi and Inutsuka, 2016], have also been shown through modelling to be able to cause gaps. Out of all of these scenarios perhaps dust growth and instabilities are the most applicable to massive star formation. Toroids, which have been shown to create instabilities in works such as Lorén-Aguilar and Bate [2016], have been observed around massive forming stars (such as those studied in Beltrán et al. [2005]), presenting an avenue for this instability and therefore gap to occur. Gravitational instability is a more likely occurrence in massive systems where the central protostellar mass is higher and when multiple systems are present. Price et al. [2018] have shown through hydrodynamical simulations that spirals, shadows and asymmetrical structures can all be produced by a companion star on an inclined and eccentric orbit approaching periastron. Given that increasing the fraction of large dust grains in the disk improved the fit of the MIDI data for this source, and the high multiplicity fraction for MYSOs [Pomohaci et al., 2019], it is concluded

that dust growth and the presence of a binary/multiple system are the most likely candidates for any substructure in this disk. Both the effects of binaries and dust growth take 10s of thousands of years to occur, implying that NGC 2264 IRS1 may be a more evolved source.

MIDI has only allowed the inference of this substructure. Unambiguously confirming the presence of the substructure and its extent through high-resolution imaging or image reconstruction could provide more data which can allow further discussion of its cause.

4.2 S255 IRS3

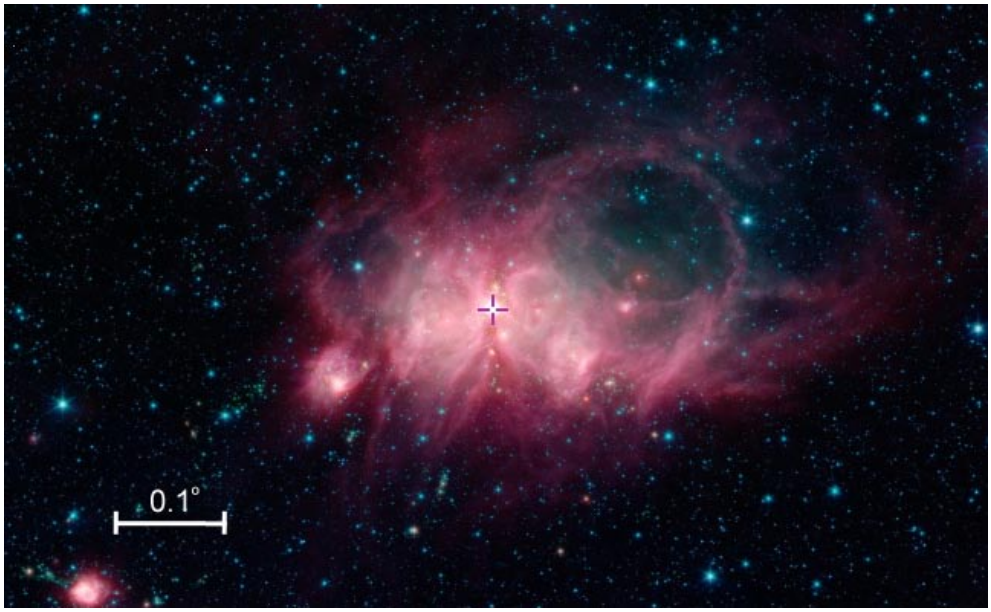

Fig. 4.7 The wider star forming region of S255 IRS3 as taken by GLIMPSE. The location of S255 IRS3 is shown by a purple cross. The image was obtained using SIMBAD and the Aladin Lite viewer [Wenger et al., 2000].

IRS3 is one of a few MYSOs residing within the massive cluster S255IR (Figure 4.7), which lies at a distance of ∼1.8kpc (calculated through water maser parallaxes by Burns et al. [2016]). IRS3 is the dominant source in this region, with a mass of $20M_{\odot}$ [Zinchenko et al., 2015a] and luminosity of order $10^4L_{\odot}$ [Wang et al., 2011],

Table 4.2 List of MIDI observations used in the fitting of S255 IRS3. The configurations are illustrated in Figure 4.8.

Configuration	Date	Telescopes	Projected baseline (m)	Position angle (°)	ESO Run ID
i)	2010-01-15	E0-G0	15.8	74.8	84.C-0183(D)
ii)	2010-01-16	E0-H0	47.8	73.5	84.C-0183(C)
iii)	2010-01-17	G0-H0	30.8	76.7	84.C-0183(B)
iv)	2010-01-17	G0-H0	31.1	76.0	84.C-0183(B)
v)	2010-01-17	E0-H0	47.5	68.9	84.C-0183(B)
vi)	2013-02-13	C1-D0	17.6	32.6	90.C-0717(A)

and is associated with a millimetre source S255IR SMA1. Zinchenko et al. [2017] studied the source with SMA and IRAM-30m continuum and spectral lines and find signatures of rotation and attribute this to a disk-like structure. The outflow is molecular in nature, and a close to edge-on orientation is suspected for the system [Boley et al., 2013]. Caratti o Garatti et al. [2017] present K-band (UKIDSS), Ks-band (PANIC) images of the source displaying the two illuminated cavity lobes, which again supports the notion of a close to edge-on source. Various maser signatures have been detected within the region. A particularly bright 6.7GHz methanol flare is discussed in Fujisawa et al. [2015] and a sub-mm flare was also found in Zinchenko et al. [2017]. This flare was later tied to NIR and radio flares by Caratti o Garatti et al. [2017]. These were determined to be the result of an accretion burst of order $10^{-3}\mathrm{M}_{\odot}\mathrm{yr}^{-1}$. This was the first directly observed accretion burst around an MYSO, which has important implications as episodic accretion is a key component of the low-mass star formation process [Stamatellos et al., 2011]. IRS3 and its neighbouring MYSO IRS1 were captured in COMICS imaging by de Wit et al. [2009]. They too find IRS3 to be the dominant source and that a model consisting of a 1D power-law envelope model exponent $p = 1.25$ best satisfies the fit of their SED and intensity profiles.

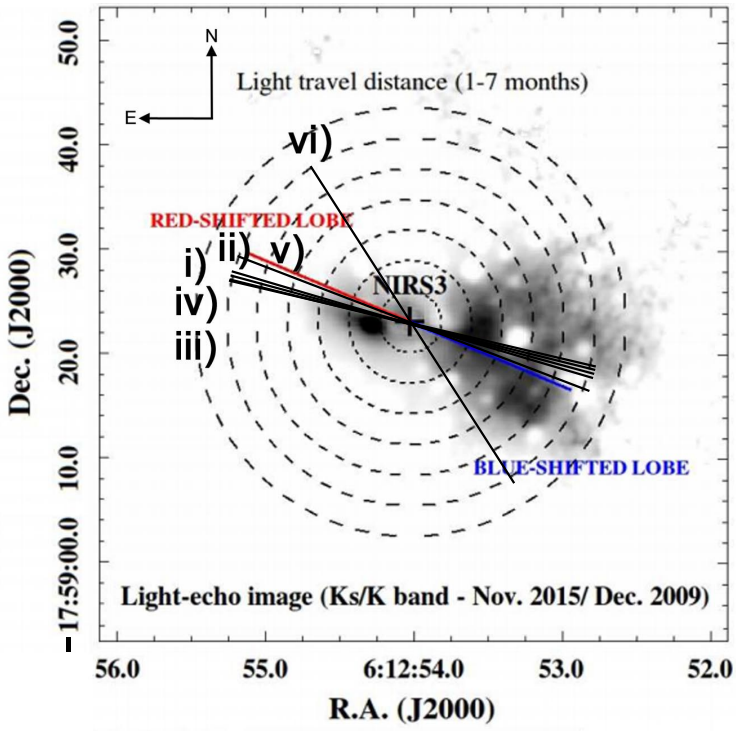

Fig. 4.8 A K-band image of S255 IRS3 from Caratti o Garatti et al. [2017] showing the two cavity lobes of the source. The position angles of each configuration of the MIDI data are overlain in black and labelled in accordance with Table 1.4. IRS1 is present in the field of view ∼2.5" from IRS3 but is not labelled.

4.2.1 Observations

All the MIDI data for S255 IRS3 came from Boley et al. [2013], with six configurations of data available for fitting. All the configurations, save one, trace very similar position angles of around 70°. The remaining configuration traced a position angle of 32.6° and was low-resolution due to its 17.6m baseline. The PA on the sky of 67° from Caratti o Garatti et al. [2017] was used in the fitting of the MIDI data.

The COMICS image from de Wit et al. [2009] is used in the fitting process. Both IRS1 and IRS3 are visible in the COMICS image. In order to exclude scales which may be influenced by the emission of IRS1, the inner 3" of the source is fit as opposed to the whole profile. All of the fitted data were taken at a time which appears to be an accretion lull for S255 IRS3, as the fluxes from the SED (which were taken at similar times to the MIDI and COMICS data) are in much better agreement with

the non-burst fluxes from Caratti o Garatti et al. [2017] than the burst fluxes. Fluxes from the RMS survey and Caratti o Garatti et al. [2017] were incorporated, alongside additional fluxes from de Wit et al. [2009] and the MIDI flux spectrum.

4.2.2 Results

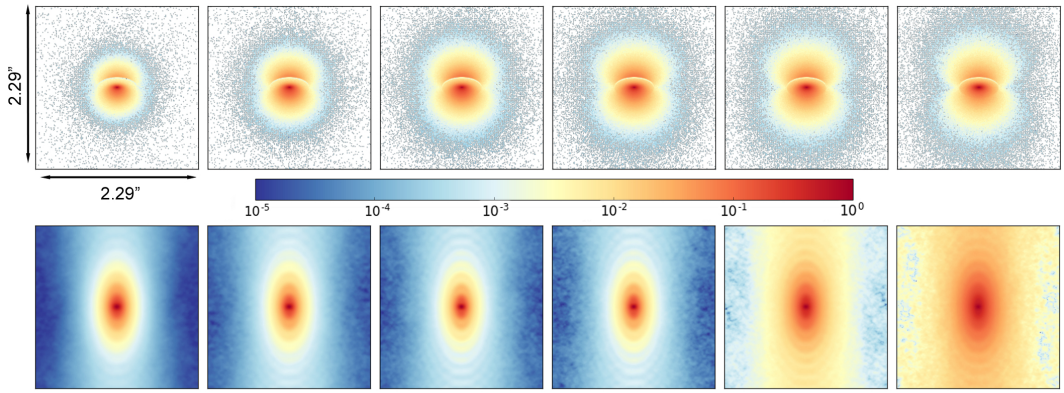

Fig. 4.9 Logarithmically scaled model images (top row) at 7.5, 8.5, 9.5, 10.5, 11.5 and 12.5μm and their corresponding fast Fourier transforms (bottom row). Each image is 2.29" in width corresponding to the AT field of view. The colour bar applies to both sets of images and represents the number of counts.

The plots for the final model are shown in Figures 4.9 - 4.12. The final luminosity for the central source in the model is 2.15 $\times$ $10^4 L_\odot$, which is in excellent agreement with that observed by Wang et al. [2011] of $\sim$2.4$\times$ $10^4 L_\odot$. The overall model is a disk/outflow system, as expected from other observations. An inclination of 120° fit all the observables, which again, is consistent as this is close to the edge-on orientation suspected by Boley et al. [2013]. Similar to G305, the closer to 90° the inclination became, the worse the fit as too much emission was present from the blue-shifted cavity lobe. The foreground extinction towards the source is large (A_v $\sim$70) similar to the findings of Caratti o Garatti et al. [2017]. Given the close to edge-on inclination, a disk mass from 0.1-10$M_\odot$ could be present and satisfy the observables which is poorly constrained due to the limitations of the infrared as a disk mass tracer (see Chapter 2). A compromise was found for the longer wavelength

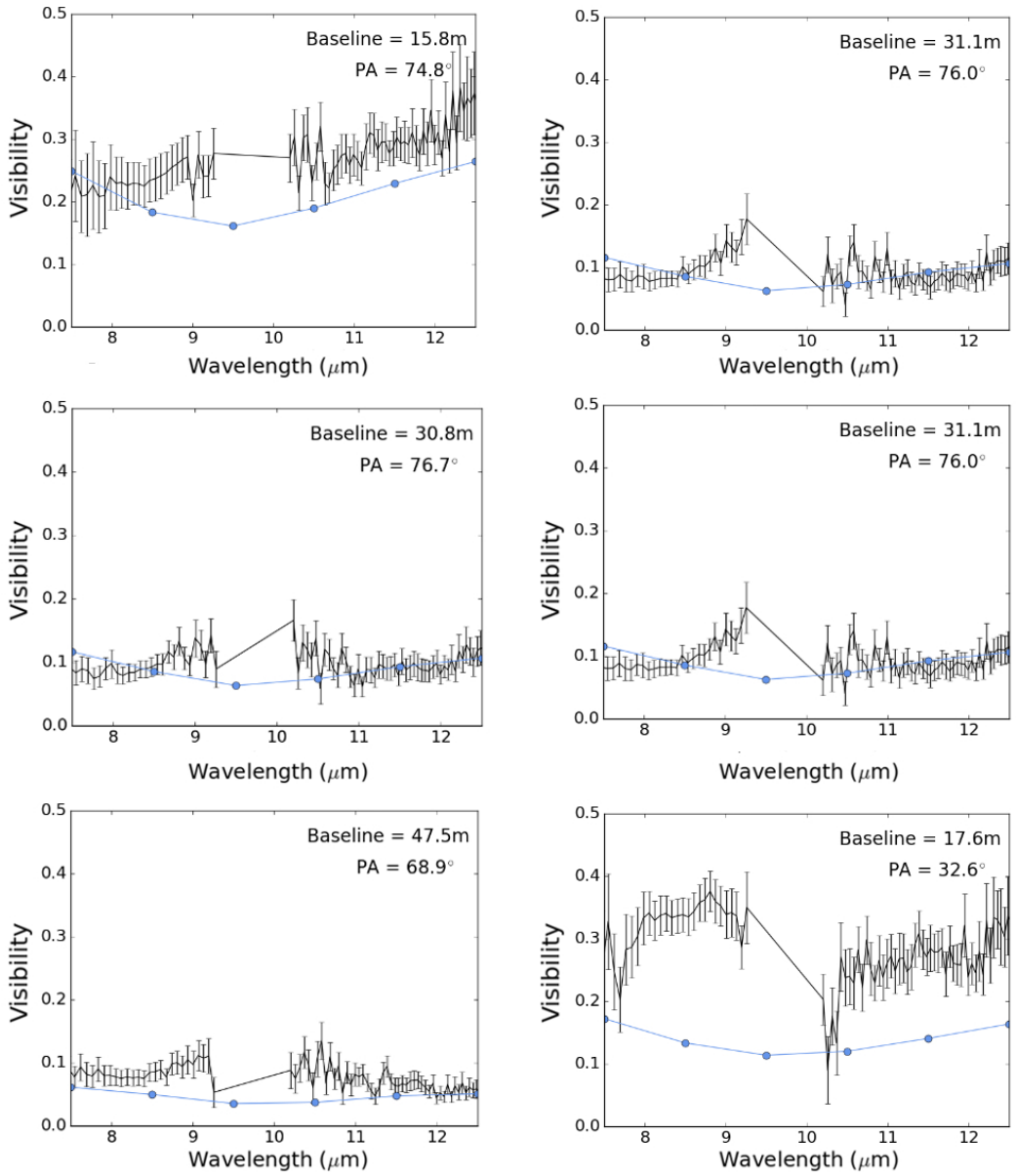

Fig. 4.10 Observed visibilities for each configuration (black) with the simulated visibilities for each model image (coloured).

regime of the SED between the data of Caratti o Garatti et al. [2017] and the data from de Wit et al. [2009] that they do not list as upper limits.

Varying the disk parameter space has negligible effects on the COMICS profile, save for the disk outer radius and the centrifugal radius of the envelope, which is attributed to the sources inclination and distance. It was found that the 2000au maximum disk radius/centrifugal radius used for G305 resulted in too much 24.5μm

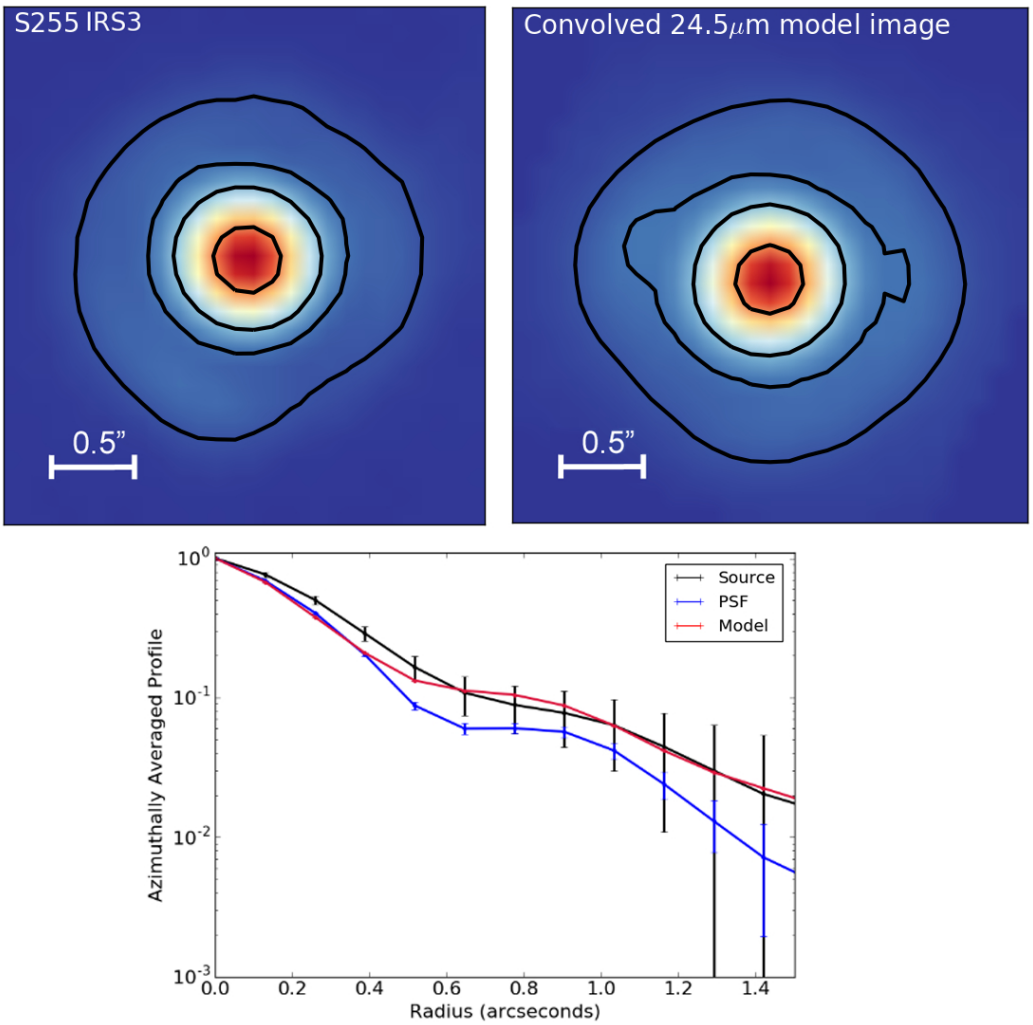

Fig. 4.11 COMICS 24.5μm image (top left), convolved model image (top right) and subsequent radial profiles (bottom). The model image was convolved with the PSF of the observed object to accurately mimic the effects of the telescope specific to the observations. The contours in the images represent 5, 10, 25 and 75% of the peak flux.

emission to successfully fit the radial profile, implying that the disk must be less extended. Reducing these values to 500au allowed a good fit for the COMICS profile.

A large amount of data was available in the literature for the fitting of the SED, however a large number of the fluxes from 70μm and above are likely to include emission from both IRS1 and IRS3 and were not considered in the fitting.

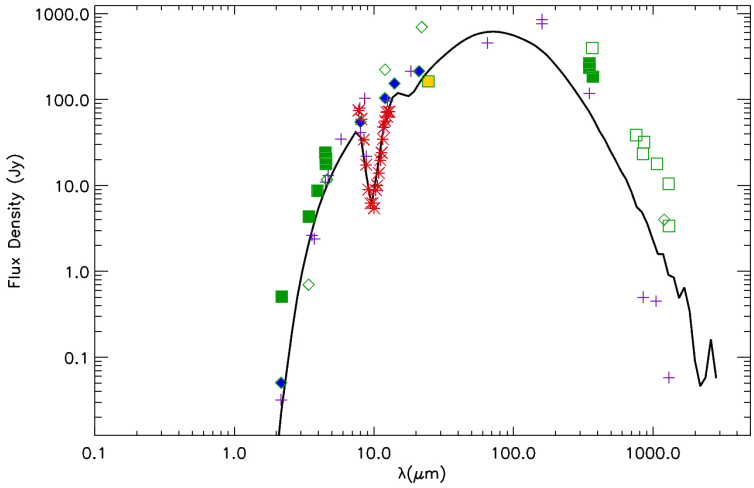

Fig. 4.12 Model spectral energy distribution of the best-fitting model (black) for S255 IRS3. The different symbols correspond to different datasets, purple crosses are data from Caratti o Garatti et al. [2017], blue diamonds are fluxes from th RMS database, squares are data from de Wit et al. [2009] (with the COMICS flux in yellow) and the fluxes corresponding to the MIDI visibilities are also shown in red. Open symbols correspond to upper limits.

4.2.3 Discussion

A model containing a flat disk with no inner clearing allows a good fit to be obtained for the MIDI visibilities of S255 IRS3. Two disk components were included in the successful model, a small grains disk and a large grains disk, both with the same scale height. Configuration vi) is the worst fit of the set. Although different in position angle to its fellow configurations, it is still likely to be tracing cavity material, as illustrated by Figure 4.8. The simulated visibilities are lower than those observed implying that the smooth cavity surface presents too large an area for emission to match the data. This could be explained by the fact that the cavity material is clumpy and irregular (also visible in 4.8). The cavity density of S255 IRS3 is of order 10^{-19}gcm^{-3}, which is comparable to that of W33A.

The wider environment of S255 IRS3 differs compared to the other MYSOs in this sample, with an outer envelope radius that is five times smaller than the other sources and an envelope infall rate that is significantly lower. Raising the infall rate

to a value comparable to those found for the other sources ($\sim 10^{-4} M_{\odot} yr^{-1}$) increases the peak of the SED significantly. While this appears to improve the fit to the SED, the fluxes that are better fit are almost certainly detecting flux from both IRS1 and IRS3 and as a result this envelope infall rate is likely to be an overestimation of what is actually present. As a result, a fit with the lower envelope infall rate which better fits the smaller aperture $\sim 70 \mu$m point is preferred. High-resolution, small aperture observations at $\sim 100 \mu$m could allow separate SEDs for the two MYSOs to be obtained and for this to be better investigated. While this is outside the scope of this work, increasing the envelope infall rate also lowers all the simulated MIDI visibilities which are only tracing IRS3, not IRS1. Using an envelope infall rate of the same order of magnitude as W33A and NGC 2264 IRS1 vastly worsens the fits for all configurations, further showing the need for a lower envelope infall rate.

Increasing the envelope radius reduces the emission at infrared wavelengths and increases the emission and millimetre wavelengths worsening the fit. The fact that S255 IRS3 appears to be the outlier in this respect is discussed further in Chapter 5.

The disk is fairly small as is the envelope in comparison to other MYSOs in this study. One could interpret this as an effect of age, but given that the object is known to be very actively accreting this seems unlikely. The accretion process itself, however, could explain this. Changes in the luminosity and the source's emission from the NIR to the radio will have large affects on the environment. When the source goes through a large accretion burst, an associated outflow event will occur. During this, shocks will propagate throughout the entire protostellar environment, potentially disrupting material and affecting the density of the surrounding envelope. After an accretion event has occurred, the mass of the disk will be depleted, also providing an explanation for the flat nature of the disk around S255 IRS3.

Another reason for the flat nature of the disk could be the fact that the density distributions for the disk in the code are based on that of a stable disk in thermal

equilibrium [Shakura and Sunyaev, 1973]. Since the MYSO is going through large accretion bursts it may be the case that this description does not fit the disk.

The fact that the envelope is rotating and infalling could be linked to the accretion burst of the source. As mentioned in Chapter 1, infall from the wider environment is directly linked to disk accretion in the turbulent core model [Tan et al., 2014]. With a centrifugal radius of 500au as opposed to 2000au, more material is fed closer to the central star, providing a larger reservoir of easily accessible material for accretion. This need not be a constant flow of material, meaning that envelope infall rate and disk accretion rate can fluctuate throughout the life of the stellar system, allowing for low accretion rates.

4.3 IRAS 17216-3801

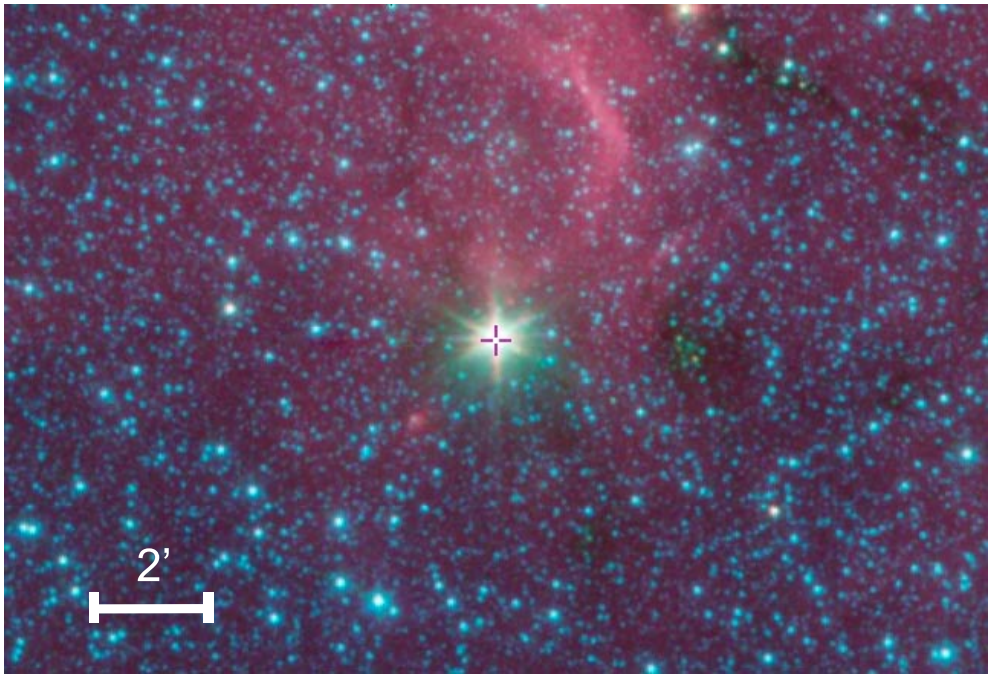

Fig. 4.13 The wider star forming region of IRAS 17216-3801 as taken by GLIMPSE. The location of the source is shown by a purple cross. The image was obtained using SIMBAD and the Aladin Lite viewer [Wenger et al., 2000].

Table 4.3 List of MIDI observations used in the fitting of IRAS 17216-3801. The configurations are illustrated in Figure 4.14.

Configuration	Date	Telescopes	Projected baseline (m)	Position angle (°)	ESO Run ID
i)	2012-05-01	B2-C1	11.3	13.9	89.C-0968(A)
ii)	2012-05-01	A1-B2	11.0	134.1	89.C-0968(A)
iii)	2012-05-01	B2-C1	10.0	40.2	89.C-0968(A)
iv)	2012-05-02	A1-B2	8.9	91.5	89.C-0968(A)
v)	2012-05-02	A1-C1	16.0	69.6	89.C-0968(A)
vi)	2012-05-02	A1-D0	34.2	51.5	89.C-0968(A)
vii)	2012-05-02	B2-D0	30.5	39.5	89.C-0968(A)
viii)	2013-02-12	B2-D0	33.8	165.1	90.C-0717(A)
ix)	2013-02-12	C1-D0	22.6	175.5	90.C-0717(A)
x)	2013-02-13	A1-D0	35.1	176.9	90.C-0717(A)

Persson and Campbell [1987] identified IRAS 17216-3801 as an MYSO. Boley et al. [2013] calculate a distance of 3.08±0.6kpc to the source using APEX measurements of the $H^{13}CO+$ (4-3) line. From the fitting of their mid-infrared emission these authors also postulate that the elongated structure of IRAS 17216-3801 may be caused by a disk/outflow system. This was confirmed by Kraus et al. [2017], who resolved the source into a close binary using a combination of AMBER, CRIRES and GRAVITY data through interferometry and spectro-interferometry. They find that the two stars are separated by ∼170au and that not only is there a disk surrounding the pair of stars but disks surrounding each individual object as well. Geometric modelling was performed to get their characteristics, finding that both circumstellar disks had very different PAs and inclinations but similar sizes, although this may be due to the limitations of the K-band data.

While HO-CHUNK3D does not present the capabilities to include a binary, the circumstellar environment of the sources can still be investigated through this methodology, the results of which are presented in this section.

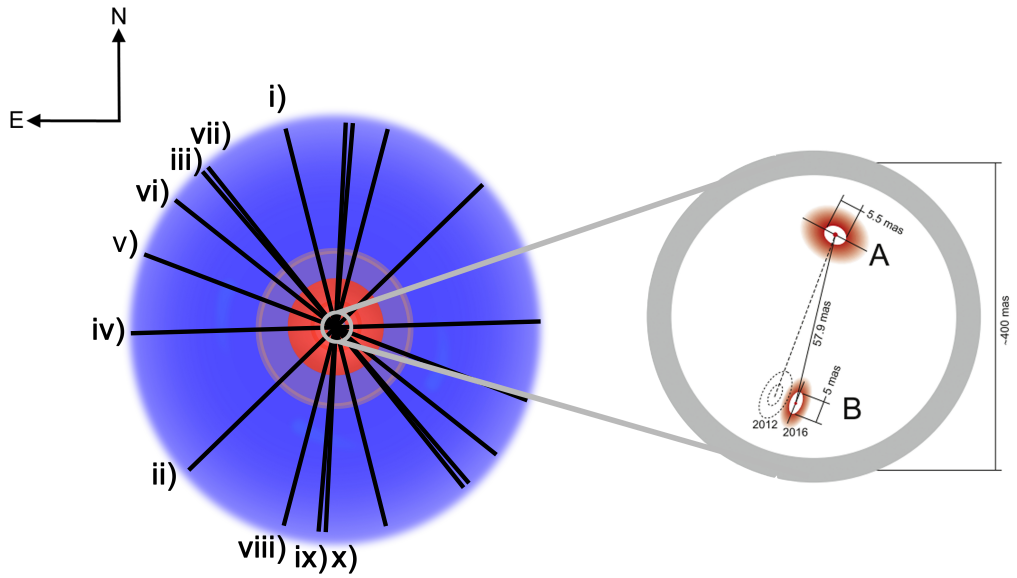

Fig. 4.14 Left: Schematic of the suspected MYSO geometry (a close to pole-on disk-outflow-envelope system) overlain with the position angles of each configuration of the MIDI data. The envelope is shown in blue, the cavity in yellow and the disk in red. Right: An illustration from Kraus et al. [2017] showing the components of their successful model and the suspected orientation of the binary system. While their schematic implies that only the secondary star moves between 2012 and 2016, it is more likely that if the two stars are of similar mass, as Kraus et al. [2017] find, both stars and circumstellar disks will have shifted.

4.3.1 Observations

IRAS 17216-3801 has the largest MIDI dataset of the sample with ten configurations. The position angles of this dataset range from approximately 14-175° but all are fairly low resolution with baselines of 35m or shorter. This means that most of the MIDI configurations are sensitive only to the circumbinary material. As illustrated in Figure 4.14, configurations viii), ix) and x) are the only three with PAs suitable for tracing the circumprimary disk and only configuration viii) has the potential to trace the material around the secondary star. The baselines of configurations viii), ix) and x) are some of the largest among the set; configuration viii) can probe scales of ∼20-35mas, configuration ix) traces scales between ∼20-50mas and configuration x) traces scales between 19-33mas. As such these configurations not only have the PA to trace the circumstellar disks, but also the required resolution. Configurations vi)

and vii) have comparable resolving power to configurations viii), ix) and x) but their PAs mean that they are more likely to be tracing any material within the cavity carved out by the binary. The baselines of the remaining configurations are short, meaning that they would all be tracing the suspected circumbinary disk material. The average visibility across each dataset varies considerably and no trend is observed between the average visibility of the configurations which may be tracing circumstellar disk material and those which will not. When fitting this MIDI data, the PA on the sky of the source varied for each model in intervals from 0-360° throughout the fitting process in order to determine the best value (as described in Chapter 2).

The $\sim$20μm data for this source comes from VISIR. It was observed on the same night as G305, meaning it too benefits from the post-upgrade sensitivity of the instrument (see Chapters 2 and 3 and Appendix A). The image is mostly symmetric and the VISIR flux was quantified using the same method applied to G305. This is included in the SED used in the fitting.

IRAS 17216-3801 was not studied as part of the RMS survey and fluxes for the SED were instead obtained from the VIZieR catalogue [Ochsenbein et al., 2000]. The J, H and K-band fluxes were taken from 2MASS (presented by Zacharias et al. [2004]). Fluxes from the IRAS catalogue [Beichman, 1988] are included, as well as fluxes from the WISE all-sky survey [Cutri and et al., 2012], fluxes from the MSX telescope [Egan et al., 2003] and the ATLASGAL flux [Contreras et al., 2013].

4.3.2 Results and discussion

HO-CHUNK3D does not provide the capabilities for modelling multiple systems but does present the opportunity to investigate the circumbinary material of IRAS 17216-3801. A single central object is included in the model, whose luminosity was obtained through the fitting of the SED as per the other sources in this thesis. The protostellar mass has a less significant effect on the SED but has some effects on its

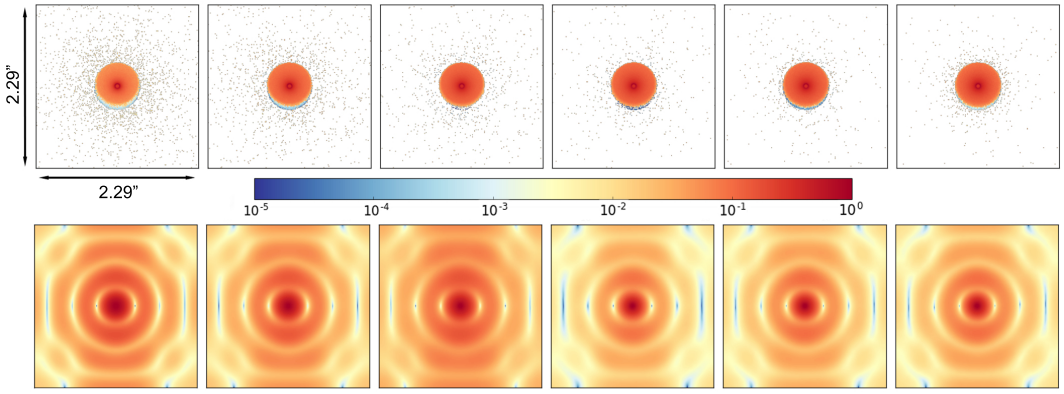

Fig. 4.15 Logarithmically scaled model images (top row) at 7.5, 8.5, 9.5, 10.5, 11.5 and 12.5μm and their corresponding fast Fourier transforms (bottom row) for the preferred fitting model of IRAS 17216-3801. The images are 2.29" in width corresponding to the AT field of view. The colour bar applies to both sets of images and represents the number of counts.

shape. It was found that a mass of 38M$_\odot$, the combined mass of the binary system based on the work of Kraus et al. [2017], did not disrupt the fit.

Surrounding this central source is a disk-outflow-envelope system. The disk scale-height is very similar to that of the default suggested by Whitney et al. [2013], with the small grains disk being slightly flatter. The disk inner radius is 100au, which is in agreement with the estimates of Kraus et al. [2017]. The FFTs of the successful model are shown in 4.15, while visibilities are shown in Figures 4.16 and 4.17. It was found that changing the minimum envelope radius to values smaller than 100au improved the fits of configurations viii), ix) and x) by lowering the simulated visibilities across each configuration. As previously mentioned each of these configurations has the potential to be tracing circumstellar disk material, so the fact that including additional dust within the circumbinary disk improves the fits to these configurations appears consistent. If the configurations are not tracing circumstellar disk material, having a smaller minimum envelope radius than the minimum disk radius implies that the binary stars cannot have destroyed the dust in the inner hole nor accreted it into their binary disks.

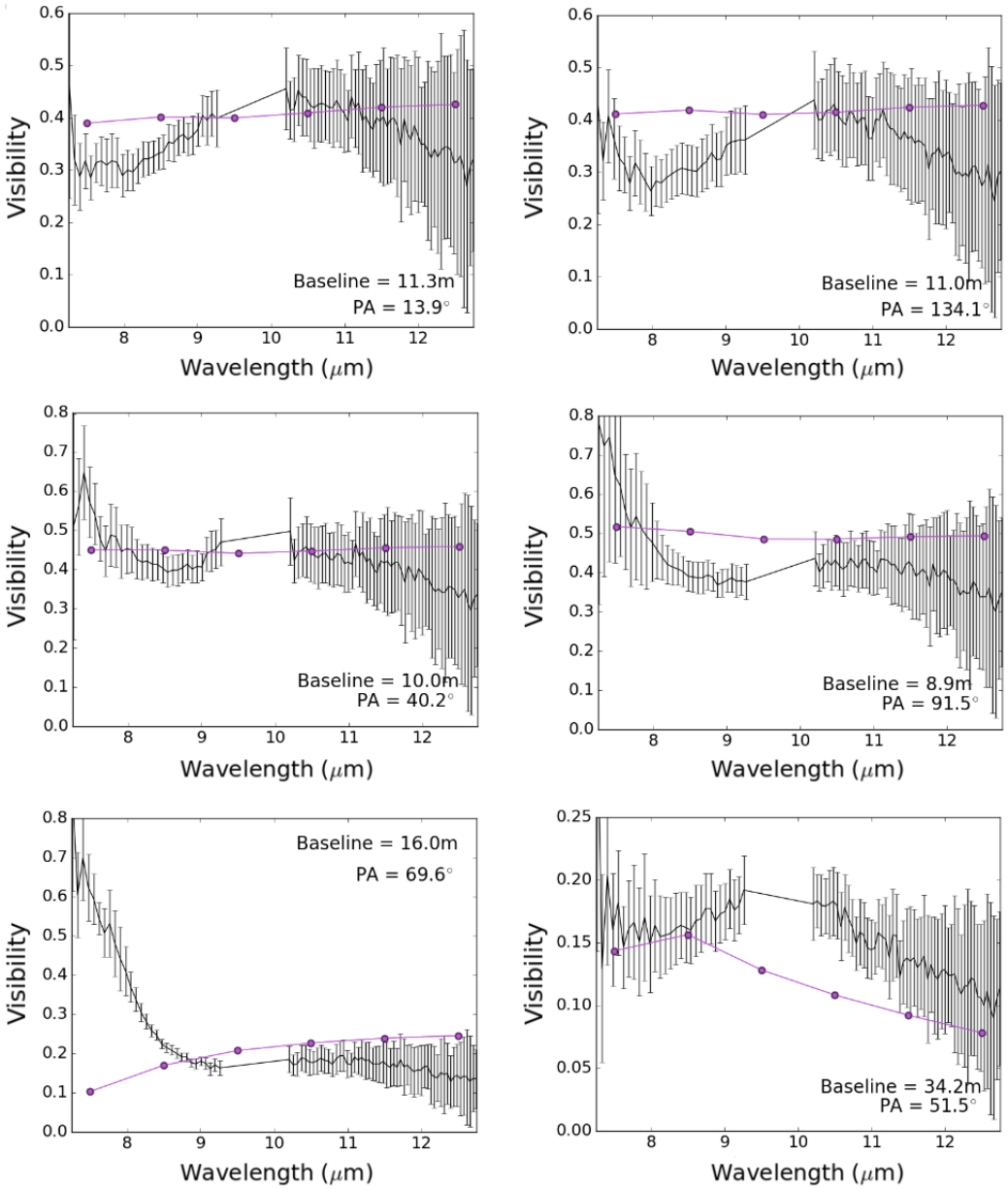

Fig. 4.16 Observed visibilities for each configuration (black) with the simulated visibilities for each model image (coloured) (1)

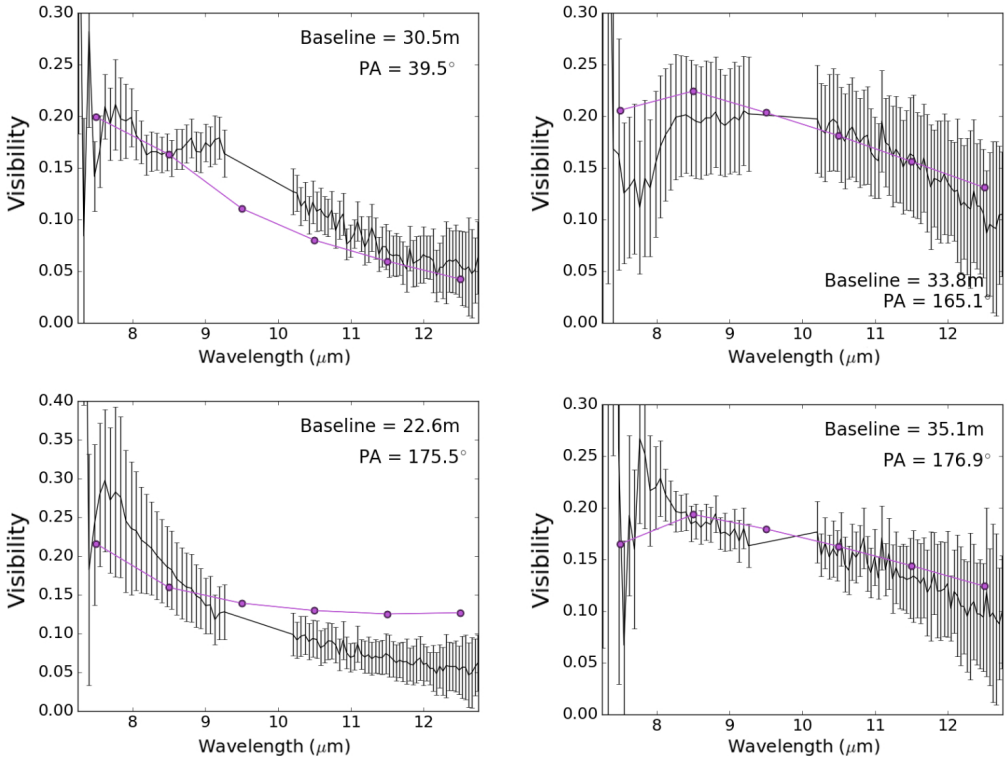

Fig. 4.17 Observed visibilities for each configuration (black) with the simulated visibilities for each model image (coloured) (2)

In order to satisfy the VISIR data (Figure 4.18) a low-inclination was required (15°) and a cavity density exponent of 1. This is because the VISIR profile is barely resolved. A density exponent of 1 as opposed to 0 (the default value) means that the density in the cavity decreases linearly with radius instead of remaining at a constant value. The innermost part of the cavity will then be brighter than its outer regions, reducing the extended emission and lowering the $\sim$20μm flux at larger radii, improving the fit. Similarly, close to pole-on inclinations reduce the extended emission as only one of the cavity lobes is directly visible in the line of sight.

The SED is shown in Figure 4.19. The ATLASGAL 870μm point proved difficult to fit. The aperture of this measurement was 19.2" but the region is fairly uncrowded (Fig. 4.13) with no obvious sources contaminating such a measurement. In an attempt to improve the fit to this data point disks of bigger radius were trialled. The larger the extent of the disk the more cold emission at sub-mm and millimetre wavelengths will be present. A 4000au maximum radius disk showed small improvements in the millimetre of the regions but more substantial changes in the 20μm region of the SED, making the dip-like feature between 10-20μm flatten. This increase in radius caused all the simulated MIDI visibilities to decrease, worsening some fits and but improving the fit of configuration ix). The fit of the VISIR profile was violated however, as the model radial profile displayed more extended emission than the observed profile. This occurred for any disks larger than 2000au so this was the final value chosen for the disk to preserve the quality of the VISIR fit. Making the envelope radius larger improved the fit to longer wavelength end of the SED by shifting the SED to longer wavelengths, but this worsened the fit of the 20μm region of the SED.

The mass of the central source was also found to affect the shape of 10-20μm region of the SED. For example, if a 20 solar mass central source is used this 10-20μm region of the SED is flatter. This is consistent as the density distribution of the TSC envelope (see equation 2.2) is proportional to $M_*^{1/2}$, meaning that as the

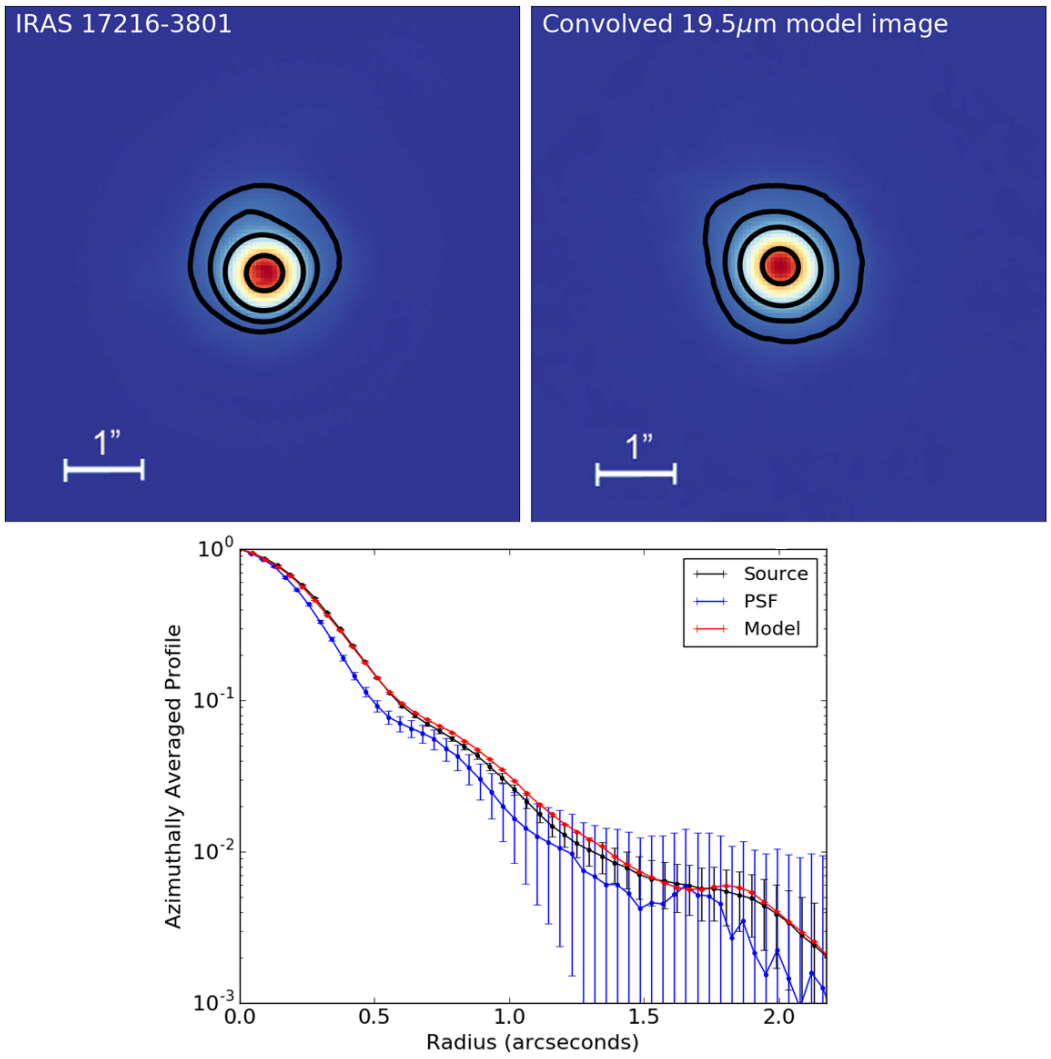

Fig. 4.18 VISIR 19.5μm image (top left), convolved model image (top right) and subsequent radial profiles (bottom). The model image was convolved with the PSF of the observed object to accurately mimic the effects of the telescope specific to the observations. The contours in the images represent 5, 10, 25 and 75% of the peak flux.

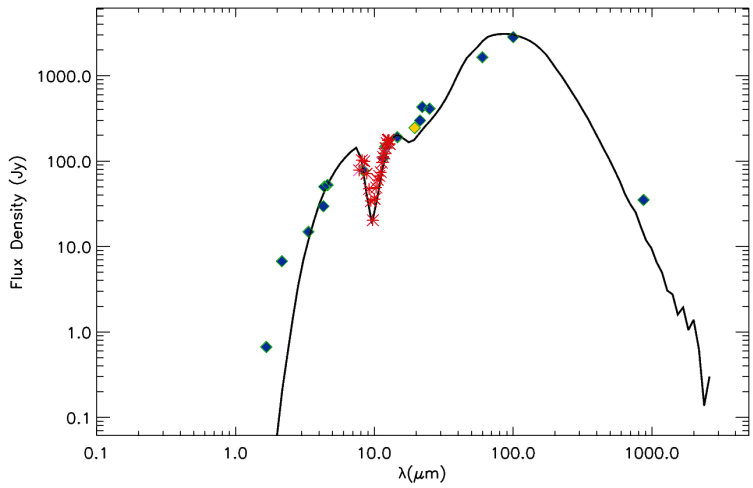

Fig. 4.19 Model spectral energy distribution of the best-fitting model (black) of IRAS 17216-3801. Multi-wavelength flux measurements from the literature are represented as blue diamonds, the yellow diamond represents the VISIR flux density and the fluxes corresponding to the MIDI visibilities are also shown in red.

stellar mass increases, the density will decrease within the infall radius and reduce the amount of 20μm flux.

Configuration v) proved the most difficult to fit. This occurred despite the fact that it is one of the lowest resolution datasets and is likely to be tracing material within the circumbinary disk. A large (nearly eight-fold) upturn is present in the visibilities between 7 and 9μm which is often a hallmark feature of a compact component like a disk. To test whether the very large increase in visibility could be due to the presence of the inner rim specifically, the inner disk radius was changed to the disk to 134au, which is the scale traced by this configuration at 7.5μm. A minor upturn in the visibilities was observed but the fits for the other, higher resolution configurations worsened. When the inner radius of the disk was varied between 100-150au the visibilities changed marginally but the overall goodness of fit changed negligibly.

The upturn in configuration v) could be due to the binary system interacting with the circumbinary disk. Small scale features, such as a puffed-up inner rim and disk-spiral, were tested but also present marginal changes, mostly likely due

to the object's distance. A very specific local substructure must be present at the scales traced by this baseline alone and not the others of similar PA/baseline to induce the observed increase in visibility. Various theoretical works have shown that binary or multiple stellar systems can result in the formation of such a small-scale substructure in protostellar disks. Nelson and Marzari [2016] used the SPH code VINE to model the circumbinary disk of the low-mass source GG Tau A. They found that the binary system 'stirs' the material in the disk, leading to the formation of spiral structures, which extend towards the centre within the inner radius of the disk as streams in the earliest stages. Within the disk itself, they see significant areas of over-density. Thun et al. [2017] find that the inner rims of the circumbinary disks are often unstable, clumpy and recessing from their hydrodynamical modelling. Desai et al. [2019] focus on the study of unequal mass binaries in particular using a 3D hydrodynamics code CHYMERA. Here they find that gravitational instabilities are induced by the binary interaction, with the smaller of the companions creating a density wave at the earliest stages and at later stages also see the generation of spirals. Observationally, Tobin et al. [2016] detect spiral structures surrounding a three-star system. Although low-mass, two of the stars have a separation comparable to that of IRAS 17216-3801 of $\sim$180au. These authors postulate that this distant star is the cause of disk fragmentation in the system and that the disk could have recently undergone a gravitational instability, inducing the formation of one or two of the companion stars. While all these cases focus on low-mass stars, the potential a binary system has to create gravitational instabilities and affect the stability and geometry of its circumbinary disk will be increased if those stars have higher mass. As such, the likelihood of over-densities which could create the compact feature required to fit this configuration is high and could therefore explain the poor fitting of this data.

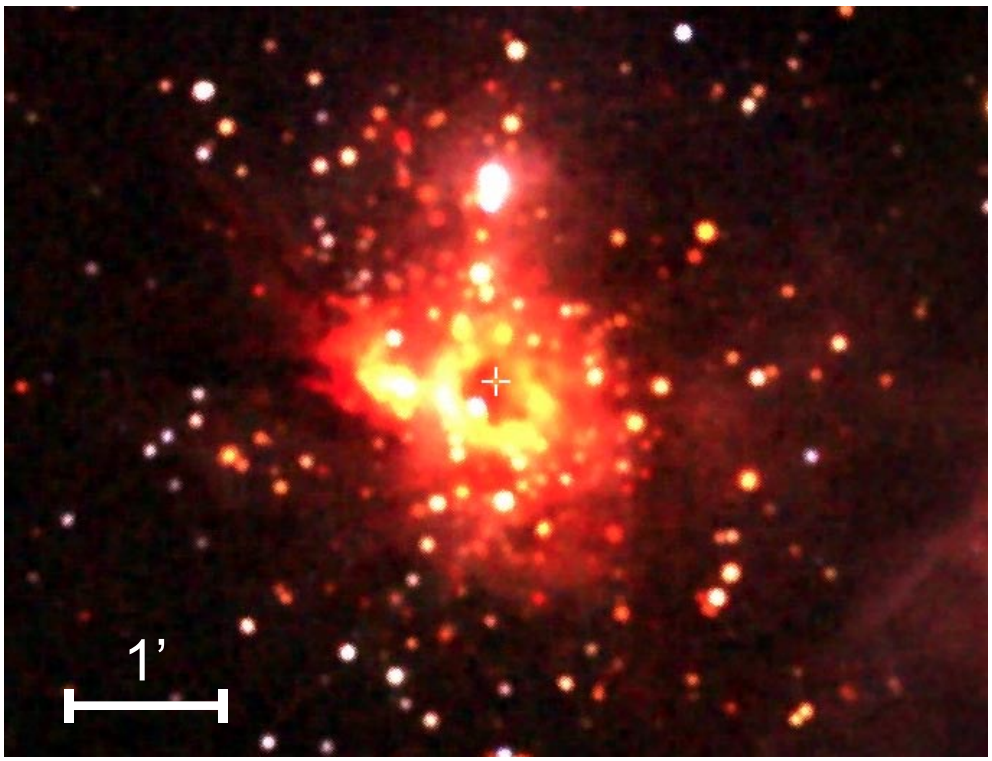

Fig. 4.20 The wider star forming region of Mon R2 IRS2 as taken by 2MASS. The ring-like HII region can be seen in the centre in orange, with Mon R2 IRS2 marked by a cross. The image was obtained using SIMBAD and the Aladin Lite viewer [Wenger et al., 2000].

4.4 Mon R2 IRS2

The Mon R2 region (Figure 4.20) is home to five different sources and located at a distance of 0.84±0.05kpc. This distance was calculated by Herbst and Racine [1976], who fit of the ZAMS of Johnson [1963] to their UBV photometry and MK spectroscopy data for a number of sources in the Mon R2 region. Using this they derived absolute magnitudes and used these to estimate a distance. A large extended HII region covers 30" of the region (visible in both 870μm maps [Giannakopoulou et al., 1997] and the 24.5μm image of de Wit et al. [2009]). Mon R2 IRS2 lies within the centre-north region of this HII region and is its main source of illumination [Aspin and Walther, 1990]. A large CO bipolar outflow is present in the wider environment [Giannakopoulou et al., 1997] but it is unknown which MYSO in the region is responsible for it. Another massive protostellar system, Mon R2 IRS3,

Table 4.4 List of MIDI observations used in the fitting of Mon R2 IRS2. The configurations are illustrated in Figure 4.21.

Configuration	Date	Telescopes	Projected baseline (m)	Position angle (°)	ESO Run ID
i)	2009-02-15	UT2-UT3	44.6	39.9	82.C-0899(A)
ii)	2009-11-14	E0-G0	10.8	55.8	84.C-1072(A)
iii)	2009-11-15	E0-G0	10.7	55.4	84.C-1072(A)
iv)	2009-11-15	G0-H0	26.9	64.9	84.C-1072(B)
v)	2009-11-15	G0-H0	31.1	70.6	84.C-1072(B)

which has been resolved into two sources A and B, is the dominant source of the whole region. No free-free emission is associated with IRS2 and it is unresolved in UKIRT observations [Alvarez et al., 2004]. Boley et al. [2013] find its mid-IR emission to be compact (∼40au), and attribute this to its lower luminosity than IRS3A and B. Henning et al. [1992] find a luminosity of the source of ∼6000$L_{\odot}$.

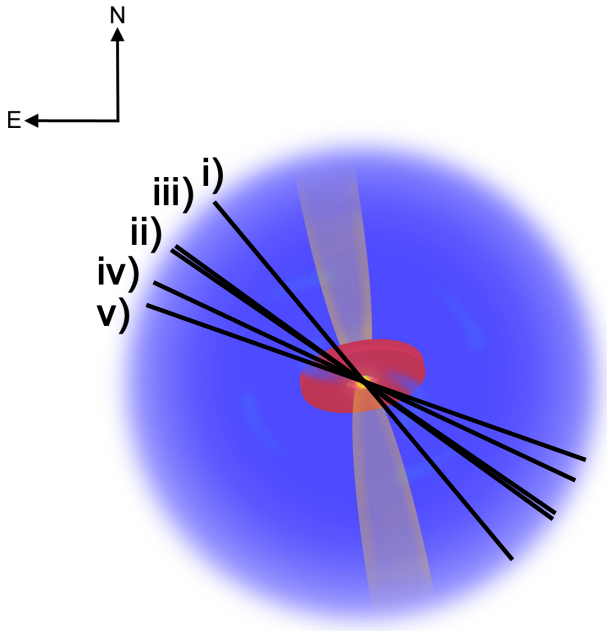

Fig. 4.21 Schematic of the suspected geometry of Mon R2 IRS2 overlain with the position angles of each configuration of the MIDI data. The envelope is shown in blue, the cavity in yellow and the disk in red.

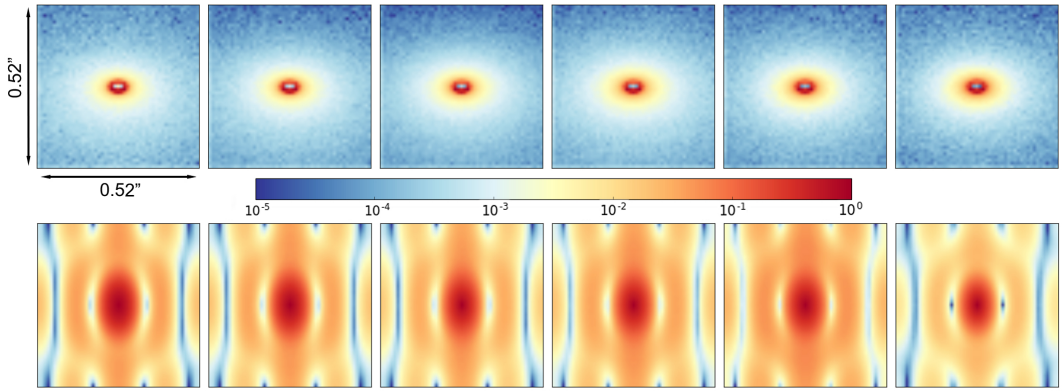

Fig. 4.22 Logarithmically scaled model images (top row) at 7.5, 8.5, 9.5, 10.5, 11.5 and 12.5μm and their corresponding fast Fourier transforms (bottom row) for the best-fitting model of Mon R2 IRS2. Each image is 0.52" in width corresponding to the UT field of view. The colour bar applies to both sets of images and represents the number of counts.

4.4.1 Observations

The MIDI observations for Mon R2 IRS2 consist of five different configurations (illustrated in Figure 4.21) taken from Boley et al. [2013]. The PA of these observations varies from 4-70° and the baseline by 30m, with the smallest configuration of ∼10m and the largest ∼45m. The shortest baseline configurations are largely unresolved with visibilities close to 1 with little variation, while the larger baseline datasets' visibilities range from 0.05-0.2. When fitting the MIDI data, the PA on the sky of the source was varied for each model in 20° intervals from 0-360° until a best-fitting value was found (as described in Chapter 2).

The COMICS image from de Wit et al. [2009] was used in the fitting but they did not fit IRS2 in their work, choosing instead to focus on IRS3. The COMICS image is subject to a large amount of low level contamination, which can be seen in the 5% contours of Figure 4.24. In order to avoid this emission, only the inner regions of the source are considered for the fit.

Like IRAS 17216-3801, Mon R2 IRS2 was not included in the RMS survey. Fluxes were obtained for the SED fitting from ViziER including H and K-band data from UKIDSS and previous work. IRAS measurements exist at 12, 25, 60 and

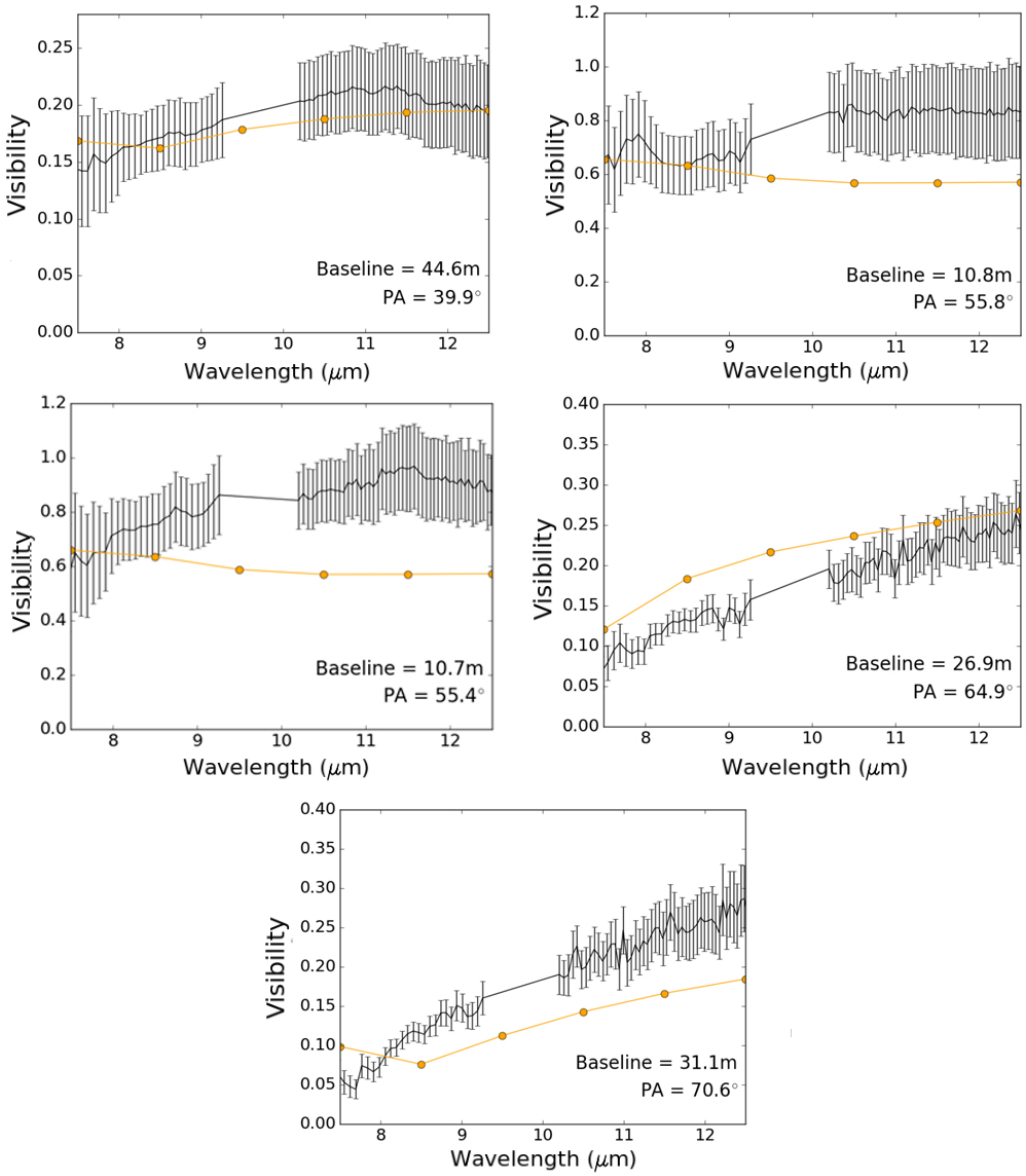

Fig. 4.23 Observed visibilities for each configuration (black) with the simulated visibilities for each model image (coloured) for Mon R2 IRS2.

100μm but given the large apertures of the instrument it is noted that the surrounding HII region is likely to be contaminating at these wavelengths. WISE data also exist but at a nearly 2" offset to the source position and with much larger fluxes at $\sim$3μm compared to the 2MASS and UKIDSS fluxes. As such they are not included in the fitting. Additional fluxes from Henning et al. [1992] were also incorporated in this work, consisting of IRAM-30m measurements and infrared fluxes from Aspin

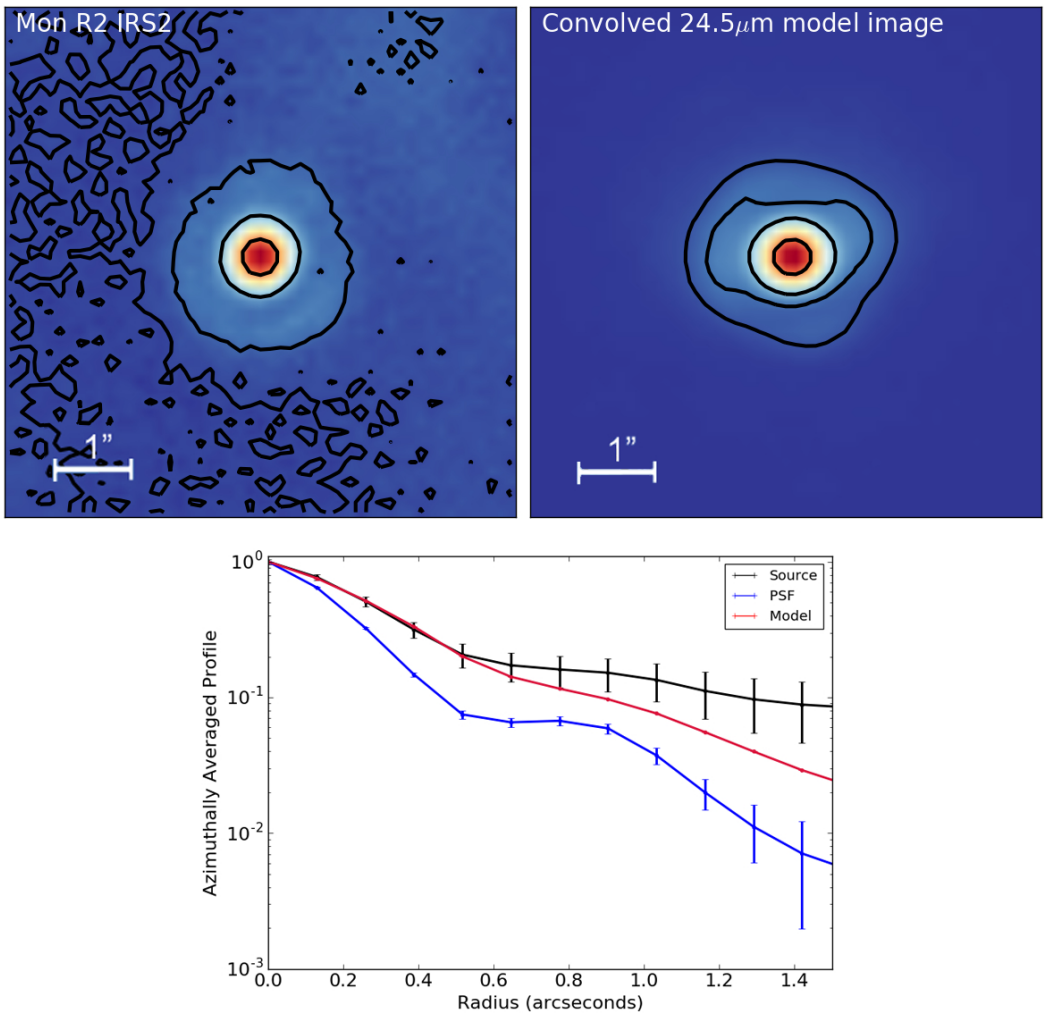

Fig. 4.24 COMICS 24.5μm image (top left), convolved model image (top right) and subsequent radial profiles (bottom). The model image was convolved with the PSF of the observed object to accurately mimic the effects of the telescope specific to the observations. The contours in the images represent 5, 10, 25 and 75% of the peak flux.

and Walther [1990]. Data exists for the source in Mueller et al. [2002], but all the measurements are of such large apertures they encompass nearly the whole Mon R2 region, and as such are not considered in this work.

4.4.2 Results

Mon R2 IRS2 is another source where the fits to the MIDI data are improved by the inclusion of an inner hole (20au in radius). The dust sublimation radius of

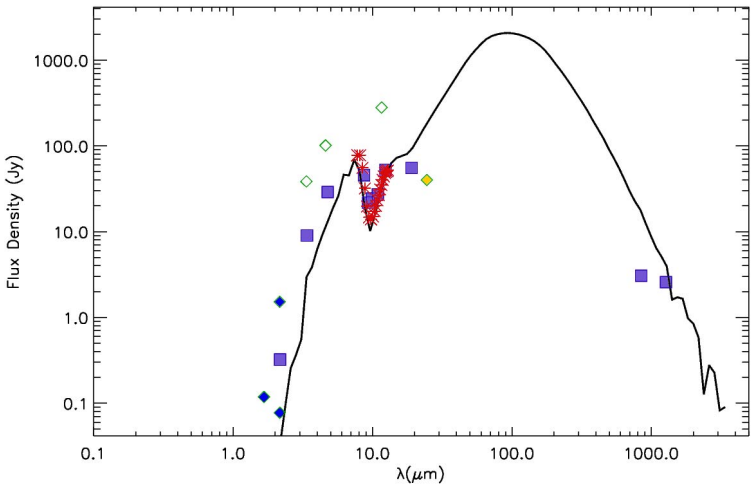

Fig. 4.25 Model spectral energy distribution of the best-fitting model of Mon R2 IRS2 (black). Multi-wavelength flux measurements from the RMS are represented as blue diamonds, the yellow diamond represents the COMICS flux density and the fluxes corresponding to the MIDI visibilities are also shown in red. The unfilled diamonds represent the fluxes that were not considered in the fitting due to their suspected contamination and the fluxes from Henning et al. [1992] are included as squares.

the source is small ($\sim$6au) due to comparatively low source luminosity required to fit the observables. The PAH emission lines for the source are weak [Gibb et al., 2004], and it was found that the MIDI fit could be improved by removing the PAHs from the disk. The final luminosity of $5520 L_{\odot}$ is similar to that of Henning et al. [1992]. The envelope of Mon R2 IRS2 is similar to that of the majority of the sample, with a comparable infall rate and the same outer radius. The cavity density is low ($\sim 10^{-21} \mathrm{gcm}^{-3}$) and the cavity opening angle is 30°. The source is inclined at 130° so both cavity lobes are visible. Through the SED fitting it was difficult to simultaneously fit the silicate absorption feature and the 20μm flux. Eventually the fitting of the silicate absorption feature was prioritised, as this is the higher resolution dataset. The model images and FFTs are shown in Figure 4.22, the visibilities in Figure 4.23, the images in Figure 4.24 and the SED in Figure 4.25.

4.4.3 Discussion

The position angles of the MIDI data for Mon R2 IRS2 mean that all five configurations are likely to be tracing disk material and configuration i) is likely to be tracing cavity material. Three of the MIDI configurations have high visibilities and are tracing an unresolved component of the protostellar environment. The simulated visibilities of configuration i) get lower if the outer radius of the disk is made larger implying that a small, compact disk best satisfies this configuration. However, as $R_c/R_{\rm max}^{\rm disk}$ increased to values of 4000au (in agreement with some of the largest observed disks around MYSOs e.g. Johnston et al. [2015]) improvements were seen to the fit of the COMICS profile as the flux at larger radii increased, so a compromise ultimately had to be made.

Configurations iv) and v) of the MIDI data proved the most difficult to fit and resulted in the inclusion of the hole. Without this the visibilities for both the configurations were too high. This hole is 40au across, in agreement with the size of the compact emission from Boley et al. [2013]. This implies that the mid-IR emission for this source, as traced by their work, is mostly dominated by emission from this inner rim. A compromise was found between the fitting of configurations iv) and v) as opposed to fitting one perfectly and leaving the other poorly fit.

The SED also proved difficult to fit in particular the balance between fitting the silicate absorption feature and the $\sim$20μm slope of the SED. Ultimately the fit of the silicate absorption feature was prioritised as this is traced by higher resolution data and more data points available for the constraint of the fit. Additionally, the only data points for the peak of the SED were large aperture, and definitely contaminated by the obscuring dust. As a result, the SED fit here is poorly constrained.

The hole alone was not able to provide the best fit to the data. The PAH emission features for Mon R2 IRS2 are weak, and it was found that removing some of the PAHs from the environment improved the fit to the visibilities. Removing the PAHs

in the envelope and cavity material had negligible effects on the MIDI fits, implying that the N-band emission of the source is disk-dominated. Removing PAHs from the entire environment greatly worsens the NIR slope of the SED fit. Should the presence of the inner hole be due to dispersal and evolution, the PAHs in the disk could have had time to coagulate into larger grains or have been expelled from the inner regions due to the activity of the protostar. If the PAHs had been expelled this could push them out to larger scales of the protostellar environment like the cavity and envelope, explaining why they still exist in these regions. Alternatively, PAHS/VSGs could exist in the cavity because the effects of the stellar radiation field and winds are most prominent in this low-density region, meaning that the cavity dust could be broken down into smaller grains.

4.5 M8EIR

Simon et al. [1984] distinguished M8E (Fig. 4.26) from a nearby UCHII region. These authors note that M8EIR can be interpreted as consisting of two physically different components (a hot compact one and a broader cooler one) and that it is associated with an optically thin radio source. They also speculate that a disk may be present based on the observed elongation in lunar occultation measurements at 3.8μm. They stated that the broad component is not molecular cloud material, but an 'intermediary phase' of material between molecular cloud and hot disk material. Within the context of the models used in this thesis such material best translates to envelope material. de Wit et al. [2009] note difficulties in their model fitting of the SED and the mid-IR intensity profiles. Ultimately they find that a model with a p=1.5 power-law distribution is the most workable final model. However they also note that a distribution with p=1.75 best satisfies the data that trace scales of 1000-10000au but that this provides an unsatisfactory fit to the 24.5μm profile. Boley et al. [2013] note a significant amount of large grains in the source, deduced from fitting simple

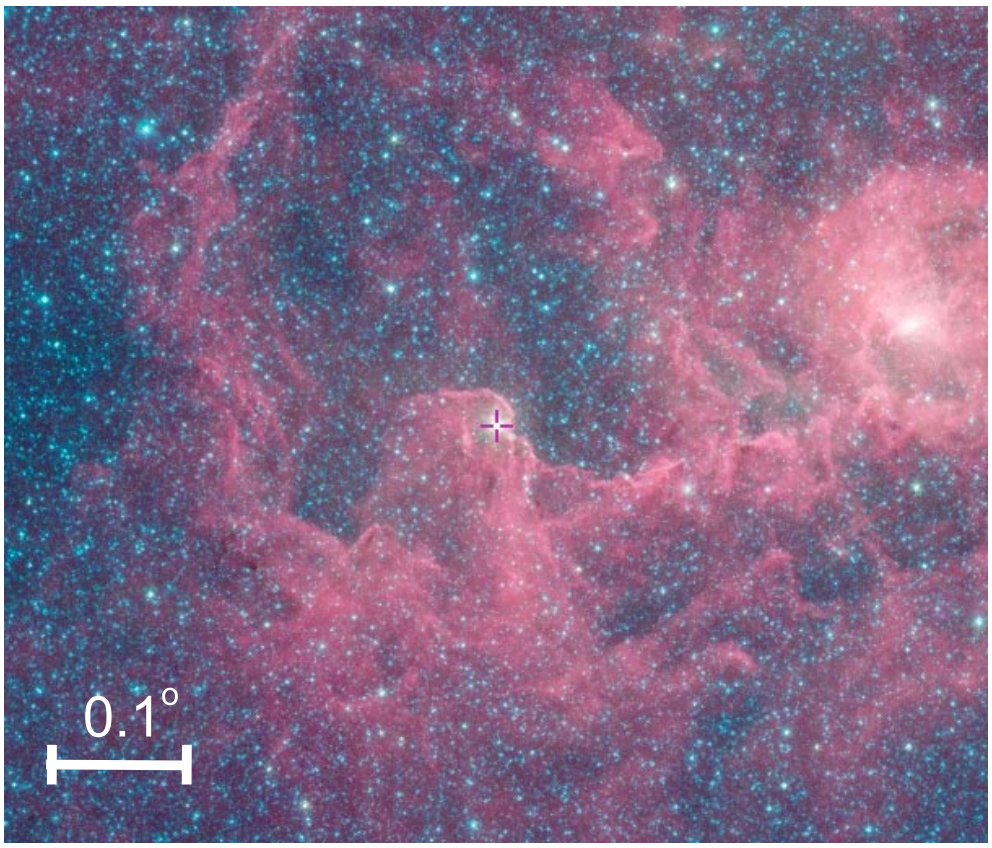

Fig. 4.26 The wider star forming region of M8EIR as taken by GLIMPSE. The location of the source is shown by a purple cross. The image was obtained using SIMBAD and the Aladin Lite viewer [Wenger et al., 2000].

absorption models to the correlated flux of their MIDI data. They find that the MIDI visibilities of M8EIR appear to trace a region aligned with a CO outflow observed in the region [Mitchell et al., 1991] and attribute the infrared emission to this outflow. This appears to be in agreement with the work of Linz et al. [2009], who studied the source by fitting MIDI visibilities and an SED (the 24.5μm COMICS image was also presented but not involved in the fitting process). They state that they cannot rule out the presence of a disk at small scales and note that an extended envelope is required. M8EIR was also studied in Ilee et al. [2013], where its CO bandhead emission was fit and modelled. In their results they find that the 13.5$M_{\odot}$ central object found in Linz et al. [2009] (using the SED models of Robitaille et al. [2007]) and a disk with an outer radius of $\sim$50au (defined where the disk temperature fell

Table 4.5 List of MIDI observations used in the fitting of M8EIR. The configurations are illustrated in Figure 4.27.

Configuration	Date	Telescopes	Projected baseline (m)	Position angle (°)	ESO Run ID
i)	2004-06-05	UT1-UT3	96.8	42.7	60.A-9224(A)
ii)	2004-06-05	UT1-UT3	82.8	44.6	60.A-9224(A)
iii)	2004-08-01	UT2-UT3	46.6	38.4	273.C-5044(A)
iv)	2005-03-02	UT3-UT4	46.8	94.1	74.C-0389(B)
v)	2005-06-24	UT3-UT4	51.6	137.8	75.C-0755(A)
vi)	2005-06-26	UT1-UT2	55.7	173.4	75.C-0755(B)

below 1000K) were sufficient to fit their data. Damiani et al. [2019] calculate a distance to the source of 1.325±0.01kpc using parallax measurements from the Gaia telescope.

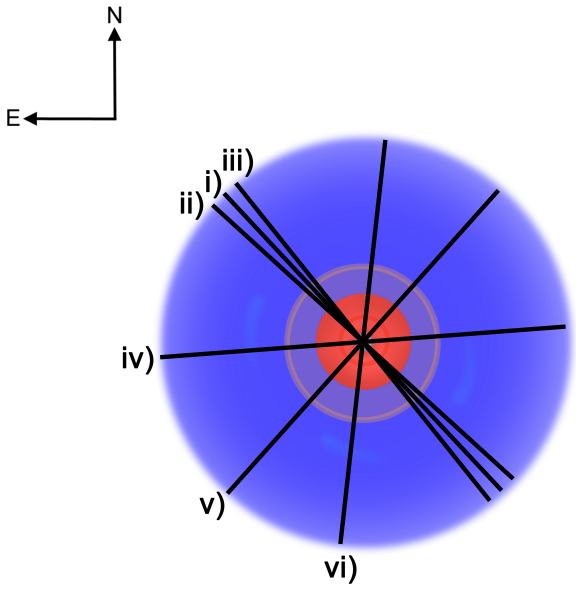

Fig. 4.27 Schematic of the suspected MYSO geometry (a close to pole-on disk-outflow-envelope system) overlain with the position angles of each configuration of the MIDI data. The envelope is shown in blue, the cavity in yellow and the disk in red.

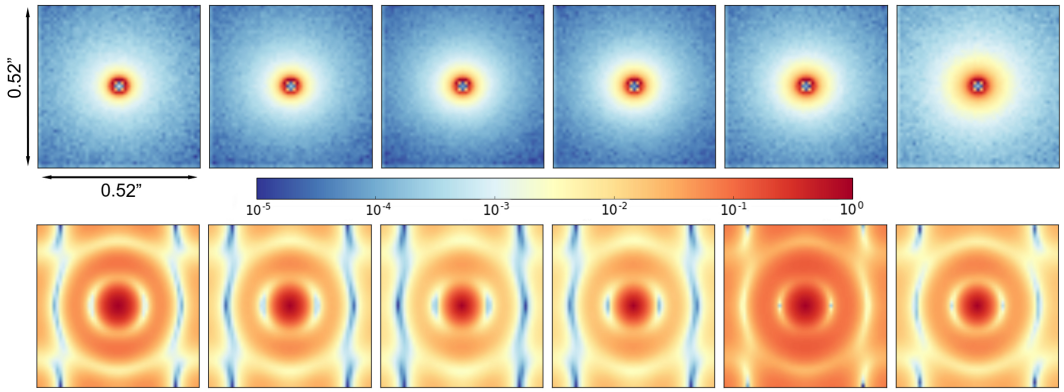

Fig. 4.28 Logarithmically scaled model images (top row) at 7.5, 8.5, 9.5, 10.5, 11.5 and 12.5μm and their corresponding fast Fourier transforms (bottom row) for the best-fitting model of M8EIR. Each image is 0.52" in width corresponding to the interferometric field of view. The colour bar applies to both sets of images and represents the number of counts.

4.5.1 Observations

The MIDI data of M8EIR from Boley et al. [2013], the COMICS image of de Wit et al. [2009] and an SED for M8EIR are fit. Six configurations worth of MIDI data are used, with a variety of PAs and baselines. The COMICS image shows that M8EIR is mostly symmetric. The SED fluxes were collated from de Wit et al. [2009], Linz et al. [2009] and Feldt et al. [2008] and references therein.

4.5.2 Results

This work finds that the 13.5$M_{\odot}$ central object of Ilee et al. [2013] well reproduces the shape of the SED of the source. A luminosity of $\sim$12000$L_{\odot}$ is sufficient to fit the multiple datasets, which is also in good agreement with the value of L obtained for the source in Ilee et al. [2013]. In the preferred model a 5×10^{5}au envelope, infalling at a rate of $1\times10^{-3}M_{\odot}yr^{-1}$, surrounds this protostar, as well as a disk with a maximum radius of 2000au. Outflow cavities are carved out of the envelope with opening angles of 25° and densities of order $10^{-20}gcm^{-3}$. Using a cavity density exponent of 0.25 was found to improve both the simulated 24.5μm profile and the

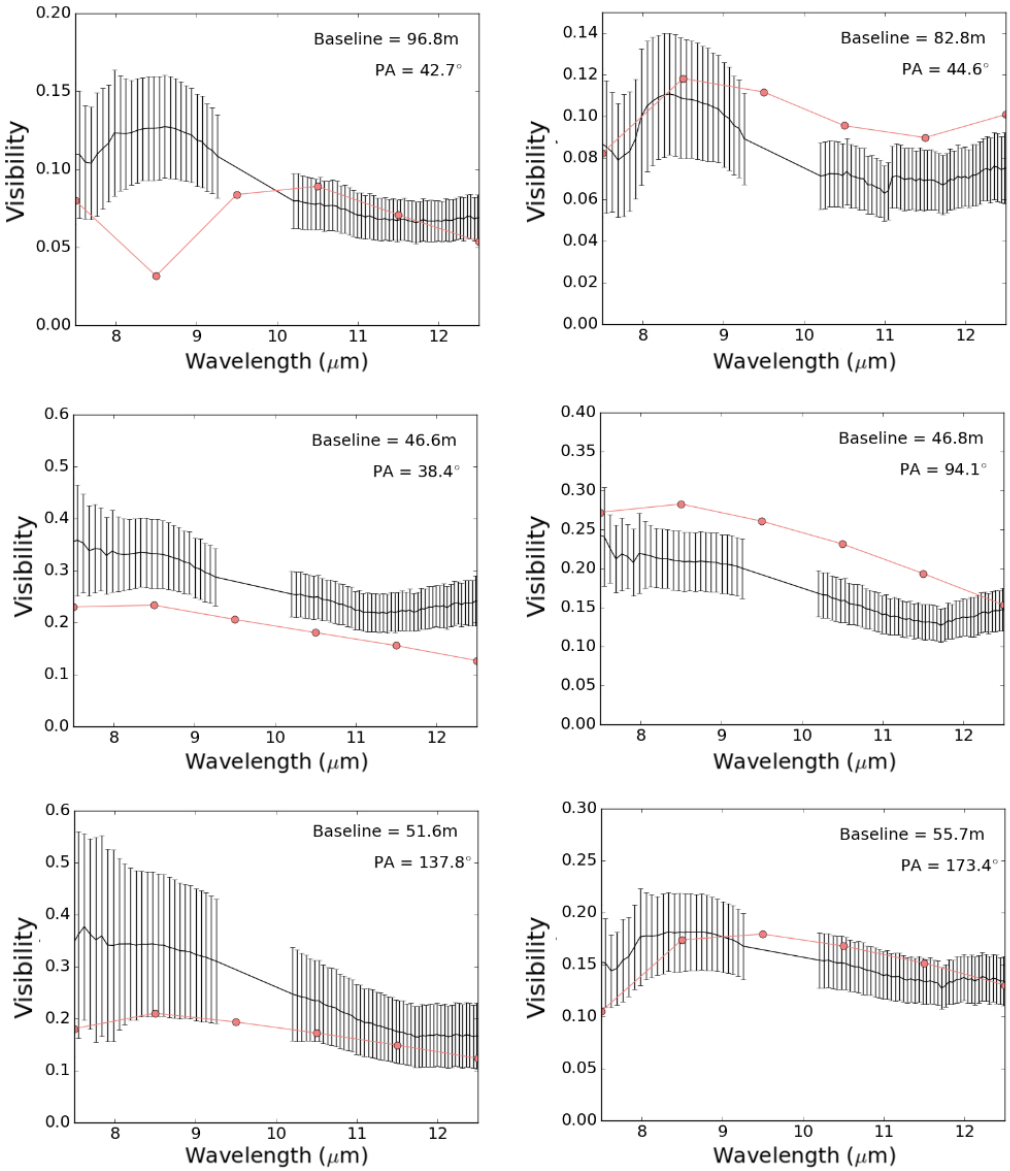

Fig. 4.29 Observed visibilities for each configuration (black) with the simulated visibilities for each model image (coloured) for M8EIR.

shape of the SED, similar to NGC 2264 IRS1 and IRAS 17216-3801. Using an inner hole (radius 30au) again improved the fit of the simulated visibilities. Using the dust sublimation radius (∼15au) as the minimum radius led to the simulated visibilities for all configurations to be lower than those observed, similar to the case of G305 (see Chapter 3). The model images and FFTs for the final model are displayed in

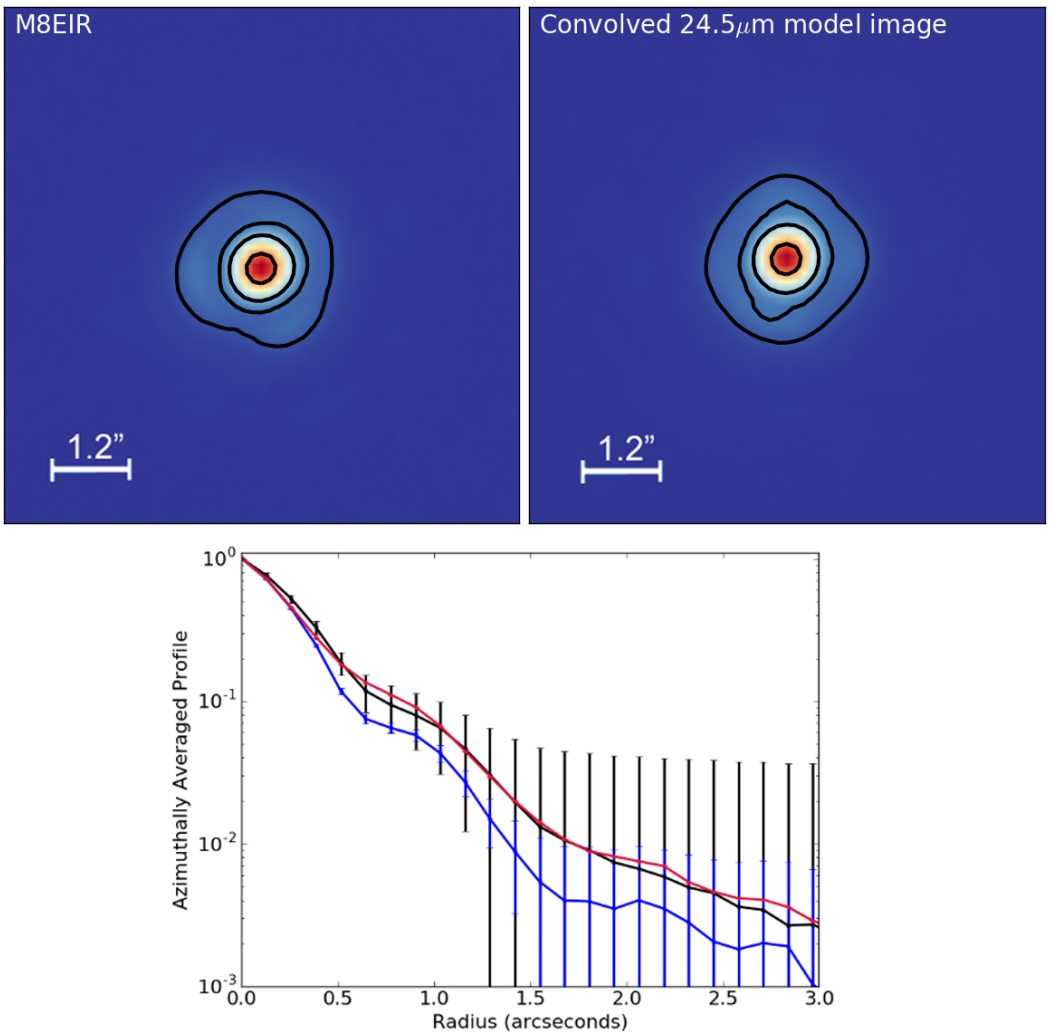

Fig. 4.30 COMICS 24.5μm image (top left), convolved model image (top right) and subsequent radial profiles (bottom). The model image was convolved with the PSF of the observed object to accurately mimic the effects of the telescope specific to the observations. The contours in the images represent 5, 10, 25 and 75% of the peak flux.

Figure 4.28. The visibilities are shown in Figure 4.29, the images in Figure 4.30 and the SED in Figure 4.31.

4.5.3 Discussion

In configuration i) a sharp downturn is found at 8.5μm. Such a quick visibility change can be caused by the turnover induced by the inner rim of the disk. When varying the inner disk radius around 30au similar shapes were observed, but alongside

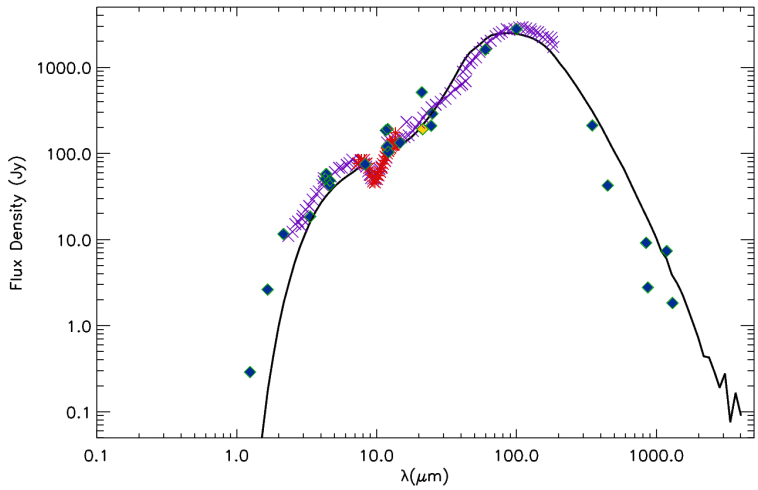

Fig. 4.31 Model spectral energy distribution of the best-fitting model (black) for M8EIR. All fluxes from the literature are shown as diamonds, except for the spectrum from Feldt et al. [2008]. This was sampled electronically and the data are represented as purple crosses. The fluxes corresponding to the MIDI visibilities are shown in red. Open symbols correspond to upper limits.

further detriments to the other visibility datasets. As a result 30au was chosen as the final inner radius. The simulated visibilities between 9-12μm for configuration ii) are $\sim$0.02 higher than those observed, implying that the structure traced by this configuration is slightly larger than that modelled. Given the long baseline length of the configuration this could be explained if the inner rim is not completely smooth but clumpy in nature. If this inner radius were the dust destruction radius a sharp cut off would be expected, but given that an inner hole exists the idea that the medium could also not be perfectly smooth is not unlikely. A compromise was found between the fitting of configurations iii) and iv) as opposed to fitting one perfectly and the other very poorly.

4.6 AFGL 2136

AFGL 2136 IRS1 (hereafter AFGL 2136) resides in a near-IR reflection nebula (known as the Juggler nebula due to its three lobes) and the wider environment surrounding this nebula is shown in Figure 4.32. Around thirty sources accompany

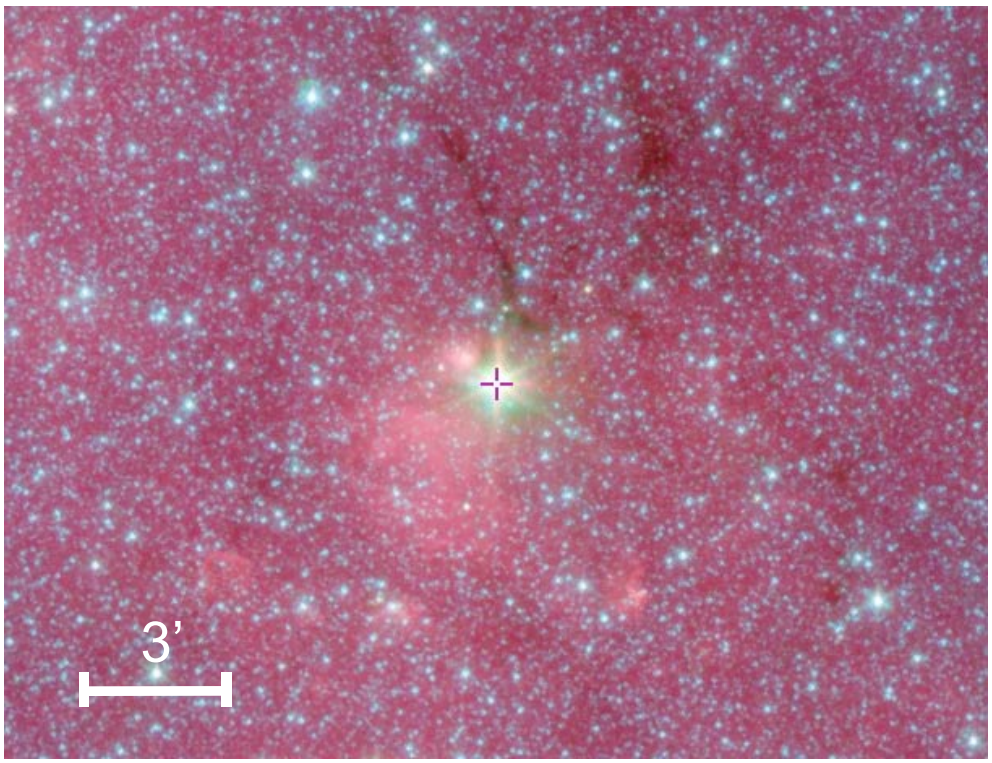

Fig. 4.32 The wider star forming region of AFGL 2136 as taken by GLIMPSE. The location of the source is shown by a purple cross. The image was obtained using SIMBAD and the Aladin Lite viewer [Wenger et al., 2000].

AFGL 2136 in the nebula but it is the dominant source. A CO bipolar outflow of arcminute scales with a PA of 135° is associated with AFGL 2136 [Kastner et al., 1992]. Menten and van der Tak [2004] detected weak, optically thick radio emission from AFGL 2136 which is slightly elongated which could be due to the presence of an ionised jet. Minchin et al. [1991] detected a disk around the source using near-IR polarimetric imaging, and Boley et al. [2013] find the mid-infrared emission to be elongated parallel to this disk. de Wit et al. [2009] image a large portion of the area including and surrounding AFGL 2136. They find the dominant source is mostly symmetric, the envelope can be traced out to scales of 3" and extension of the source in the direction of each lobe of the nebula. Their 1D radiative transfer modelling of the COMICS profile and SED of the sources shows that their intensity profile and SED are best fit by a model with a density distribution of p=1 but note that none of

their models reproduce the emission <10μm well and that a p=1.5 profile can also reproduce adequate fits but worse than those of p=1.

de Wit et al. [2011] applied a similar analysis to the one presented in this thesis to AFGL 2136, using similar datasets and an older version of the same RT code. The main difference is the amount of MIDI data available, as only one configuration was fit in that work as opposed to the four used here. Additional technical differences between the fitting of this thesis and [de Wit et al., 2011] are the multiplication of the model images with a Gaussian and the convolution of the COMICS image with a Gaussian PSF as opposed to an observed one (see Chapter 2). Throughout their fitting de Wit et al. [2011] found that a dust disk violated their MIDI visibilities, making the visibilities too high. Their final geometry consisted of an envelope-cavity system with the inclusion of a dusty torus (implemented through the variation of the size of the cavity launching site within the envelope) and the addition of a gaseous inner disk. The addition of a gaseous inner disk was not possible through HO-CHUNK3D and implemented separately.

Maud et al. [2018] and Maud et al. [2019] studied the source using ALMA observations. Maud et al. [2018] find that the dust emission implies a disk-like structure. They suspect that the ^{13}CO emission traces cavity walls and their CH_3CN and CH_3OH emission trace arc-shaped trails leading away from the disk plane. Using parametric models with the SiO emission they show the presence of Keplerian rotation of a disk between 10-30$M_\odot$. These parametric models must also have a radially expanding component which they explain as a disk wind. They confirm Keplerian rotation in the disk and suspect that the source is an older object due to the presence of H30α emission (indicating ionisation). In Maud et al. [2019] the H_2O emission of the disk was investigated. They again confirmed Keplerian rotation, in addition to a ring-like density enhancement which they postulate could potentially be a spiral structure.

Table 4.6 List of MIDI observations used in the fitting of AFGL 2136. The configurations are illustrated in Figure 4.33.

Configuration	Date	Telescopes	Projected baseline (m)	Position angle (°)	ESO Run ID
i)	2005-06-24	UT3-UT4	61.3	107.0	75.C-0755(A)
ii)	2005-06-26	UT1-UT2	53.5	14.0	75.C-0755(B)
iii)	2006-05-18	UT2-UT3	46.4	45.9	77.C-0440(A)
iv)	2008-06-23	UT2-UT3	42.6	47.4	381.C-0607(A)

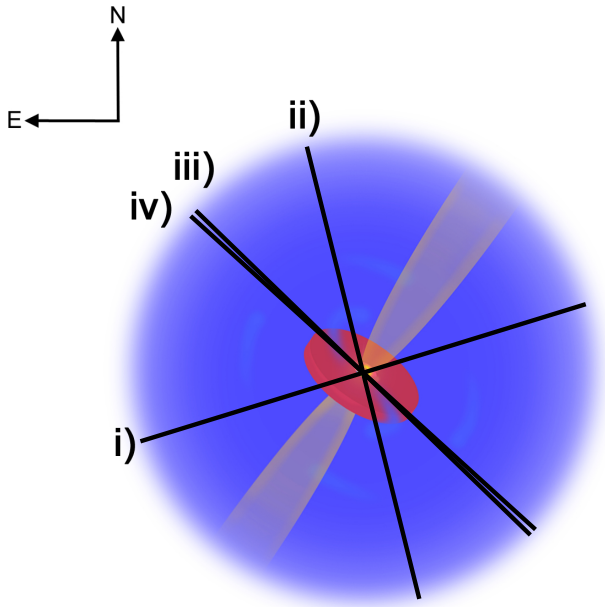

Fig. 4.33 Schematic of the suspected MYSO geometry overlain with the position angles of each configuration of the MIDI data. The envelope is shown in blue, the cavity in yellow and the disk in red.

4.6.1 Observations

The MIDI data for AFGL 2136 from Boley et al. [2013] consists of four configurations (Fig. 4.33) of fairly similar resolution with a minimum baseline of 42.6m and a maximum of 61.3m. The PA range is large, between 14-107°. The visibilities for all four configurations are low, averaging at around 0.03. The visibility profiles are unusual in shape with very sharp variations. The COMICS image from de Wit et al.

[2009] was used. The SED for AFGL 2136 was compiled using the RMS database and the literature. Included fluxes come from 2MASS, MSX and WISE with JCMT data from Kastner et al. [1992], a 350μm flux from Mueller et al. [2002] and 50 and 100μm data presented in Harvey et al. [2000].

4.6.2 Results

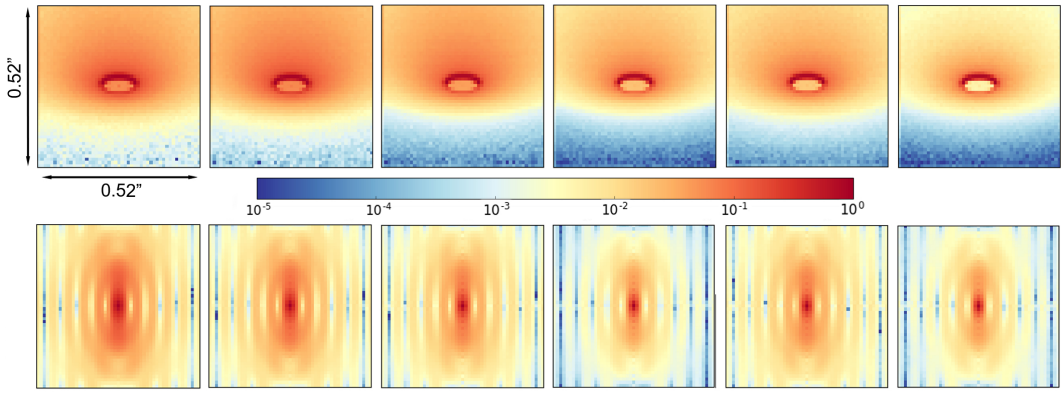

Fig. 4.34 Logarithmically scaled model images (top row) at 7.5, 8.5, 9.5, 10.5, 11.5 and 12.5μm and their corresponding fast Fourier transforms (bottom row) for the best-fitting model of AFGL 2136. Each image is 0.52" in width corresponding to the interferometric field of view. The colour bar applies to both sets of images and represents the number of counts.

The first step in the modelling of this source was to apply the model of de Wit et al. [2011] to the larger dataset. As discussed in Chapter 2, the model images are not multiplied by a Gaussian and it was found that without this, the MIDI configuration common to both this thesis and that work could not be satisfactorily fit using the model of de Wit et al. [2011]. The model also provided poor fits to all the other MIDI configurations which were not included in de Wit et al. [2011].

Given the observations of a disk around the source, various disk-outflow-envelope geometries were trialled during the modelling. Disk masses ranging between 10-30 solar masses are workable components of the model, in agreement with the kinematic measurements of Maud et al. [2018] and Maud et al. [2019]. The larger the mass, the less 24.5μm emission, improving the fit of the radial profile. For a 30 solar mass

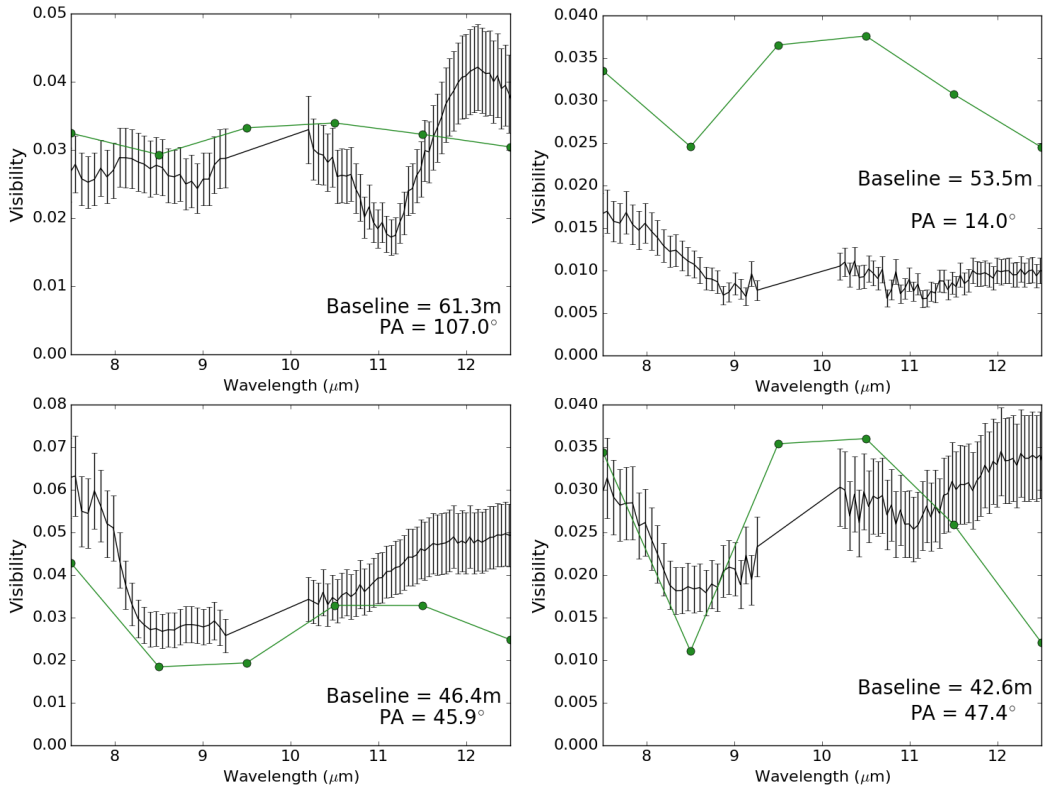

Fig. 4.35 Observed visibilities for each configuration (black) with the simulated visibilities for each model image (coloured) for AFGL 2136.

disk the millimetre slope of the SED fit is worse than for a 10 solar mass disk. The quality of the MIDI fits are comparable across the disk mass range. For the 30 solar disk mass model, fit for configuration ii) improves slightly as the simulated visibility at 8μm increases, but the visibilities for configuration iv) also increase, which further worsens the fit to that configuration by a comparable amount. Given the similarity across the MIDI data a compromise was made between the SED and COMICS fits and 20 solar masses was selected as the final disk mass.

Similarity is found between the preferred best fitting model of this thesis and the model of de Wit et al. [2011] in that the minimum dust radius is larger than that of the dust sublimation radius. This is clearly visible in the model images shown in Figure 4.34. In this work the inner radius is four times larger than the sublimation radius, in theirs it was five. In de Wit et al. [2011] a gaseous disk and bloated star resided within this cleared inner hole. Including a gaseous disk is not part of the

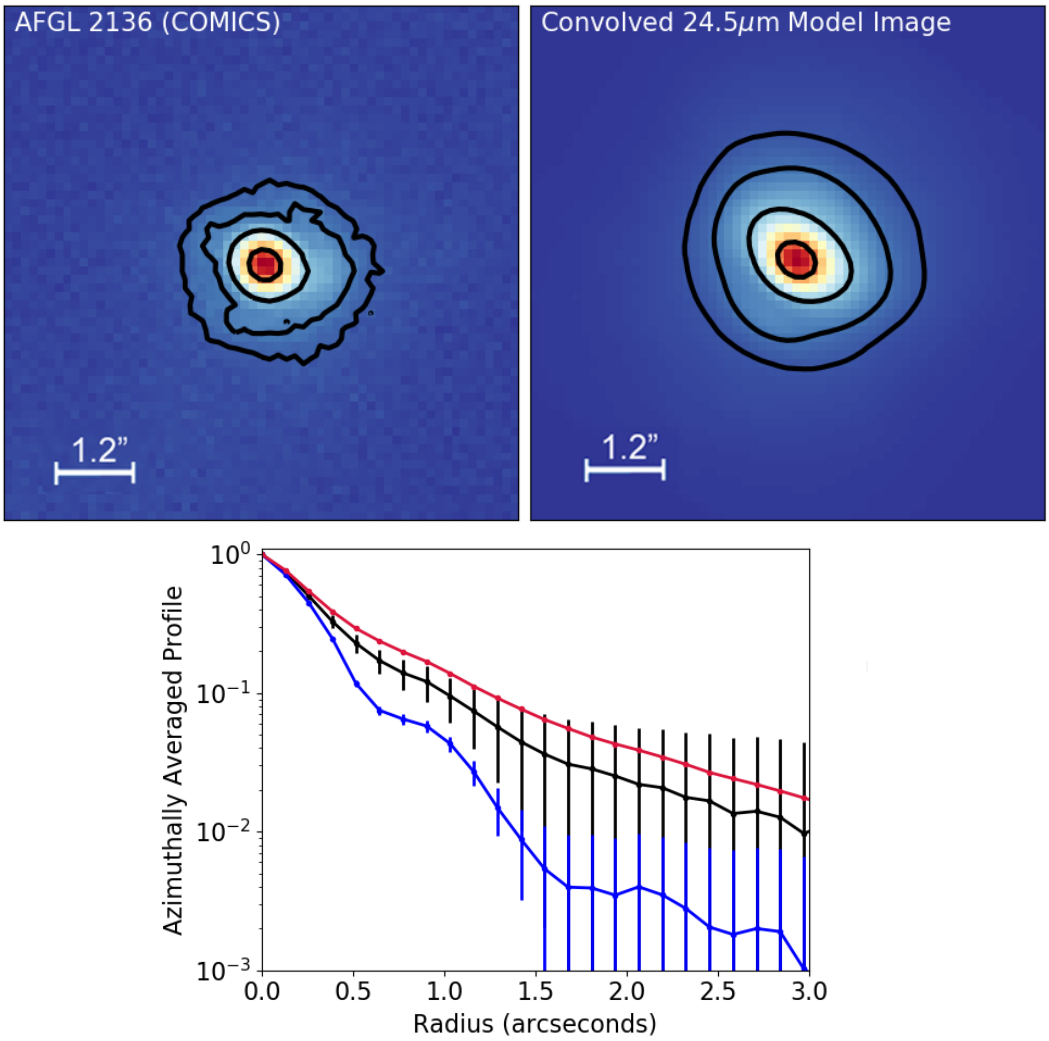

Fig. 4.36 COMICS 24.5μm image (top left), convolved model image (top right) and subsequent radial profiles (bottom). The model image was convolved with the PSF of the observed object to accurately mimic the effects of the telescope specific to the observations. The model is more symmetric than the observed source meaning it has more emission in its eastern regions, explaining the larger amount of 24.5μm flux visible for the model in the radial profiles. The contours in the images represent 5, 10, 25 and 75% of the peak flux.

methodology of this work, but its potential existence cannot be denied. As discussed in the examination of G305 (Chapter 3), the presence of a bloated source can also not be ruled out. Both a large and small grains disk were used in the final model, with matching scale-heights. The outflow cavity opening angle is tightly constrained at 22.5° to maintain the balance of fits of the three observables and the cavity density is of order 10^{-19}gcm^{-3}. The centrifugal radius is 2000au and the infall rate is of order

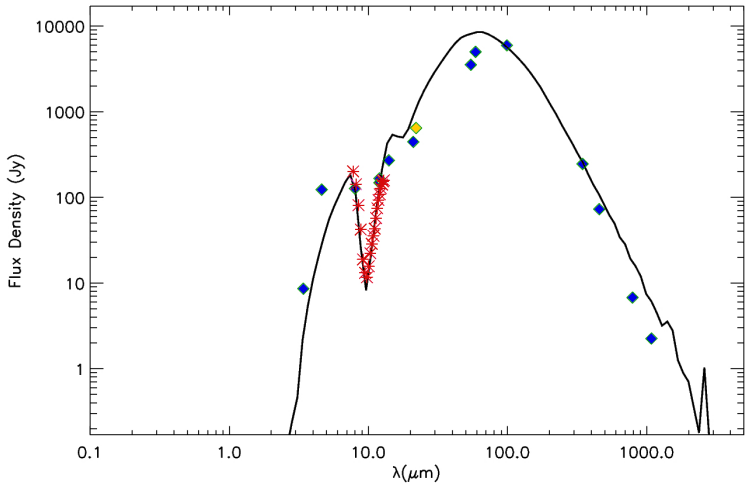

Fig. 4.37 Model spectral energy distribution of the best-fitting model (black). Multi-wavelength flux measurements from the RMS are represented as blue diamonds, the yellow diamond represents the COMICS flux density and the fluxes corresponding to the MIDI visibilities are also shown in red. The unfilled diamonds represent the fluxes that were not considered in the fitting due to their suspected contamination.

10^{-4} solar masses per year. The final model includes an inclination for the system of 60°, and the central object is similar to that of de Wit et al. [2011]; a bloated star of radius $25R_{\odot}$ with an overall luminosity of $1.51\times10^{5}L_{\odot}$. This luminosity matches the O-type classification ascribed by Maud et al. [2018] and Maud et al. [2019] and in good agreement with the bolometric luminosity determined by Lumsden et al. [2013].

4.6.3 Discussion

The visibilities of the final model are shown in Figure 4.35, the images are shown in Figure 4.35 and the SED is shown Figure 4.37. Configuration ii) of the MIDI data proved nigh-impossible to successfully fit. Despite this, the preferred model recreated the shape of the visibilities well and was only V^2=0.015 off in visibility. This implies that the protostellar environment traced by this configuration is larger than that simulated in the model. The PA of this configuration was 14° meaning that, taking into account the source's PA on the sky, it could be tracing envelope material

close to the cavity wall or disk material. Both the continuum and CO contours of Maud et al. [2018] show the medium to be clumpy, despite the disk's stability. Given that only smooth geometries were used in the modelling, it could be that the model is not reproducing this emission leading to this poor fitting. The other three MIDI configurations are matched well by the final geometry.

This work agrees with Maud et al. [2018] and Maud et al. [2019] in that a disk-outflow system suits the source. Maud et al. [2019] detect a ring-like structure at scales of 120au. This is in very good agreement with the inner radius found in this thesis for the disk through the fitting of the infrared data, which is four times the sublimation radius or $\sim$125au. Maud et al. [2019] even compare their inner ring to the inner radius of 60au found for G305. Causes of the large inner rim found for AFGL 2136 could be the presence of a multiple system, which Price et al. [2018] postulate for the source HD 142527 and agrees with the discussions of G305 (as discussed in Chapter 3). Dust trapping (e.g. Pinilla et al. [2018]), whereby grains are trapped in pressure maxima and amalgamate, is also cited as a possible cause of their structure by Maud et al. [2019]. While the exact mechanism cannot be confirmed, the fact that the inner rim has been detected using three different methodologies and in two different wavelength regimes is promising for future study.

4.7 Summary

In conclusion, the multi-scale analysis has determined that the datasets of all of the sources in this sample can be explained by models consisting of a protostellar environment with a disk-outflow-envelope geometry. The final parameters for the sample are listed in Table 4.7. A number of the disks within this sample display substructures of various kinds, but with the most common being an inner hole. All of the envelopes of the sources were of the same Ulrich type, implying actively infalling environments for the sources. Agreement exists between the characteristics

found through this work and those found through previous studies. From the study of this sample it appears that the MIDI data are most sensitive to the inner disk geometry of the sources. This could be determined thanks to the combination of the MIDI data with the VISIR/COMICS data which provides additional constraint on cavity material. The level of constraint could further be improved by using another high-resolution dataset at sub-mm/millimetre wavelengths.

Across the sample, the far-infrared fluxes in the SED were occasionally problematic to fit. One may assume that changing the dust types could aid in the fitting of the far-infrared slope. Olguin [2016] experimented with dust models based on the Kim Martin and Hendry dust model (used in the cavity and small grains disk in this thesis) but with added ice mantles, but found this did not improve the fit. Mottram et al. [2011d] note that the extinction model used in the code will effect the shape of the far-infrared slope. In their work and the work of this thesis a standard interstellar extinction law is used based on the work of Kim et al. [1994]. Using a different extinction law model could also therefore also potentially assist with the fitting of the far-infrared SED fluxes. The fluxes used in the SEDs throughout this chapter are listed in Appendix B.

Table 4.7 Parameters of the preferred models for the full sample of sources. PA is shorthand for position angle and is defined as east from north. Exf. stands for cavity density exponent [Whitney et al., 2013], D1 SH is short for 'Disk 1 scale-height' and D2 SH is short for 'Disk 2 scale-height'.

Source	$M_\star$ ($M_\odot$)	$L_\star$ ($L_\odot$)	i (°)	d (kpc)	$R_{\rm env}^{\rm min}$ (au)	$R_{\rm env}^{\rm max}$ (au)	R_c (au)	$\dot{M}_{infall}$ ($M_\odot yr^{-1}$)	θ_{cav} (°)	n_{cav} (gcm^{-3})	Exf	M_{disk}	$R_{\rm disk}^{\rm min}$ ($M_\odot$)	$R_{\rm disk}^{\rm max}$ (au)	Dust Fraction (au)	D1 SH	D2 SH	$A_{\rm V}^{\rm for}$	PA (°)
W33A	25	49270	120	2.4	18 (R_{sub})	5×10^5	500	7.4×10^{-4}	20	1×10^{-19}	0	1	18 (R_{sub})	500	0.2	0.11	0.22	0	30
G305.20+0.21	25	48500	35	4	60	5×10^5	2000	7.5×10^{-4}	12	8×10^{-21}	0	1	60	2000	1	0.1	-	1	55
NGC 2264 IRS1	8	4200	15	0.74	4 (R_{sub})	5×10^5	500	9×10^{-4}	25	8×10^{-21}	0.25	0.3	4 (R_{sub})	500	0.2	0.4	0.8	25	-18.5
S255 IRS3	20	21550	120	1.8	12 (R_{sub})	1×10^5	500	7.5×10^{-8}	20	6×10^{-19}	0	1	12 (R_{sub})	500	0.2	0.1	0.1	70	67
IRAS 17216-3801	38	172000	15	3.08	1	5×10^5	1000	4×10^{-3}	40	9×10^{-21}	1	1	100	1000	0.2	0.4	0.7	60	320
Mon R2 IRS2	15	5500	130	0.84	20	5×10^5	2000	9.5×10^{-4}	30	3×10^{-21}	0	0.1	20	2000	0.2	0.4	0.8	25	190
M8EIR	13.5	12100	25	1.33	30	5×10^5	2000	1×10^{-3}	25	8×10^{-21}	0.25	0.1	30	2000	0.2	0.4	0.8	25	260
AFGL 2136	20	151000	60	2.2	125	1×10^5	2000	3×10^{-4}	22.5	3×10^{-19}	0	20	125	2000	0.2	0.375	0.375	60	-35

Chapter 5

Looking for trends in the circumstellar environments of MYSOs

5.1 Introduction

In Chapter 1, it was stated that the model of de Wit et al. [2010] had been successfully applied to a number of MYSOs when fitting their VISIR profiles and SEDs [Wheelwright et al., 2012]. This presents the question as to whether all MYSOs can be fit with this model, or a similar family of models. Through the employment of the multi-scale, high-resolution methodology described in Chapter 2, model fits have been obtained for a sample of MYSOs, as presented in Chapters 2, 3 and 4 of this thesis. In doing so, the geometries, characteristics and traits of these MYSOs have been ascertained. This constitutes the largest sample of MYSOs in the literature to be tested with such a multi-scale methodology. Since the sample was analysed in a consistent manner, the results for each object can be directly compared to one another. In this chapter, this analysis is performed. Firstly, the choices made during the fitting process and how these affect the analysis are discussed, and some factors

calculated to allow better interpretation of the parameter space are defined. Secondly, parameters that were identical or very similar across the sample of MYSOs are discussed. Thirdly, correlations are used to quantify the relations within the parameter space. A general investigation of the overall trends between the MYSOs follows, before finishing with a discussion of how the characteristics deduced for this sample relate to classification schemes of previous work.

Table 5.1 A list of the MYSOs analysed in this thesis

Name	RA	DEC	Distance (kpc)
G305.20+0.21	13:11:10.45	-62:34:38.6	4
NGC 2264 IRS1	06:41:10.15	+09:29:33.6	0.7
S255 IRS3	06:12:54.02	17:59:23.60	1.8
Mon R2 IRS2	06:07:45.8	-0.6:22:53.2	0.8
IRAS 17216-3801	17:25:06.51	-38:04:00.4	3.1
M8E-IR	18:04:53.18	-24:26:41.4	1.4
W33A	18:14:39.0	-17:52:03	2.4
AFGL 2136	18:22:26.38	-13:30:12.0	2.2

5.2 Considerations

Before presenting the comparative analysis, it is prudent to first discuss any aspects of the fitting process which may affect the relationships between the characteristics of the sample. Two factors are also defined which were calculated to assist in the interpretation of the parameter space.

5.2.1 Notes on discussed parameters

The luminosity of the central source in the model is calculated from its user-defined temperature and radius. The stellar radii of MYSOs are mostly derived quantities based on model interpretations such as evolutionary tracks and assumptions of the effective temperature of the sources. The derived luminosity however, just depends on the distance of the source. Any results attained within this thesis as function of

luminosity would therefore be much more robust than other derived quantities. It was found during the fitting process that it is the overall luminosity that holds power over the simulated observables and the fits, not the specific temperature and radius. This was discussed in the Chapter 3 during the testing of bloated protostars. Given this, luminosity is compared with other parameters instead of T and R_* separately.

Similarly, central source mass is also usually derived based on model interpretation of evolutionary tracks. The starting point for the masses used throughout this thesis came from the literature and were usually estimated based on assumptions of the mass-luminosity relationship of ZAMS sources and not based on any dynamical information of the protostellar systems. While the mass values from these works were successful components of the preferred model fits, it was found that varying the central object mass did have small effects on the shape of the SEDs of the source, as discussed in Chapter 4.3.2 in regards to IRAS 17216-3801. The central object mass is still discussed later on in this chapter, but with this taken into account.

This methodology combines a variety of techniques with a focus on the mid-infrared for the high-resolution observations. While MYSOs are, as a whole, infrared bright, some of their components will be better traced by longer wavelength observations. The total disk mass is best quantified by modelling the sub-mm/millimetre continuum of sources in combination with dynamical studies which can distinguish it from envelope material. The envelope outer radius will also only be detected at the longest wavelengths given its very cold temperatures. While sub-mm and millimetre fluxes are included in the SEDs used in the fitting process, the fact that these fluxes are not combined with high-resolution data means that the origin of the cold emission cannot be confirmed. As such, the handle on the total disk mass and envelope maximum radius is weaker than other parameters. The fitting process has shown the outer disk radius can have an effect on the VISIR/COMICS profiles of nearer sources. For G305, which was at a distance of 4kpc, the angular size of a disk with an outer radius of 2000au is $\sim$0.5" whereas for NGC 2264 IRS1 (a

nearer source) it is nearly 3". Therefore a disk constitutes a much smaller emitting component for a more distant source, whereas for a nearer source the disk can have effects on the extended 20μm emission.

5.2.2 Calculated factors

Throughout this analysis a number of factors were calculated to give a more pertinent feel of the parameter space. The first is the maximum resolving factor of the MIDI observations. This was calculated by dividing the largest projected baseline used to observe each source by the distance to the source. Calculating whether any of the characteristics obtained from the fitting have only been detected due to fortuitous position/observations is important and this is discussed further in the next section. Another calculated quantity was the flaring factor of the disk. Most of the preferred fit models included two disk components, one made from 'large grains' (disk 1) and one from 'small grains' (disk 2). Whitney et al. [2013] suggest a flaring factor of 2 between the two disks to simulate this, based on the hydrostatic calculations of D'Alessio et al. [1998] and images of observed disks (Cotera et al. [2001] and Wood et al. [2002]). During the fitting process it was found that varying this ratio (as well as varying which disks were used) could improve the fits to the observations. The flaring factor is simply the scale height of disk 2 divided by the scale height of disk 1.

5.3 Notable similarities and groups

After fitting the whole sample, some parameters were the same, or similar, for all the objects. These are excluded from the later correlation discussions, but are discussed here.

5.3.1 Cavity shape exponent

The same cavity shape exponent of 1.5 was a successful component of all the final models. As discussed in Chapter 2, this dictates the shape of the outflow cavity. A streamlined, perfectly conical cavity will have an exponent of 1, a parabolic cavity an exponent of 2 and so on. Both streamlined and curved cavities are observed around YSOs (e.g. Padgett et al. [1999], Stark et al. [2002], Reipurth et al. [2000]), but the mechanisms causing each of them are not entirely clear. Varying the cavity exponent induces effects on the 20μm emission and the shape of the model SED (Chapter 3). It is therefore significant that it was was not required to deviate from a cavity exponent of 1.5 during the fitting process. The shape of the cavities will be controlled by a number of processes specific to the central protostar and the envelope they are carved out of. Therefore, if the shape of the cavity is consistent across a sample of MYSOs this implies that the same processes are occurring in MYSOs that shape these cavities. In the low-mass case, the outflow morphology is essentially dictated by an interplay of magnetic field activity between the star and the disk. The magnetic fields themselves are suspected to be fossil fields from the wider cloud, which become compressed by the gravitational collapse of the core and twisted up by rotation (Königl et al. [2010], Königl et al. [2011]). The field lines within the disk can be amplified by convection and shear in the disk, resulting in an hourglass shape which can be recreated through a cavity exponent of 1.5. However, as previously discussed, the role of magnetic fields lines in massive protostellar environments is still not well understood/observed. Walder et al. [2012] note that magnetic activity is more likely to be sustainable if massive stars/protostars are convective. While the convective stage for massive PMS stars is expected to be short (Chapter 1) convection is possible for lower temperature objects. Bloated MYSOs could be convective enough to generate magnetic dynamos and thick disks are also thought to have the potential to be convective [Ferreira and Pelletier, 1995]. Should

magnetic fields be present in either, they will have implications for both the outflow and disk behaviour.

Kuiper et al. [2015] performed radiation hydrodynamical simulations of massive protostellar outflows and the hourglass morphology associated with a cavity with a shape exponent of 1.5 is present for many different masses of high-mass star (although they do not specifically quantify this exponent). Offner et al. [2011] also perform radiation hydrodynamical simulations of massive protostellar outflows and also find that the cavities carved are curved. Additionally, they find that the cavity opening angle is seen to increase with time between 10^2-10^7years within the context of their models, which are collapsing cores and not fed material from a wider clump. As such, envelope depletion would stop accretion at some point allowing the widening of the cavity opening angle. The majority of the cavity opening angles for the sample lie between 20-30°, placing then between $\sim 10^{3.2}$yrs to $10^{4.5}$yrs according the the models of Offner et al. [2011].

To summarise, a curved polynomial cavity, which is found to be a successful component of all the preferred final models, appears to be consistent with recent simulations of massive protostellar outflows.

5.3.2 Envelope radius and ambient density

All the MYSOs in the sample, save one, have the same outer envelope radius. The outer envelope radius is only probed by the SEDs in the dataset and is therefore not constrained to a high degree of accuracy. All the fits were satisfied by an envelope with radius $5 \times 10^5 R_\odot$ or $1 \times 10^5 R_\odot$. Only S255 IRS3 required the smaller envelope for its SED to be successfully fit. One may assume that a less luminous or massive MYSO may have a smaller surrounding envelope as a smaller reservoir of natal material will provide less material for building the star. This does not appear to be the case however, as far less luminous/massive MYSOs than S255 have larger

envelope radii. One could argue that because S255 IRS3 is observed to go through large accretion events that the smaller envelope radius could be due to periodic mass-accretion events, however the exact cause cannot be determined throughout this work.

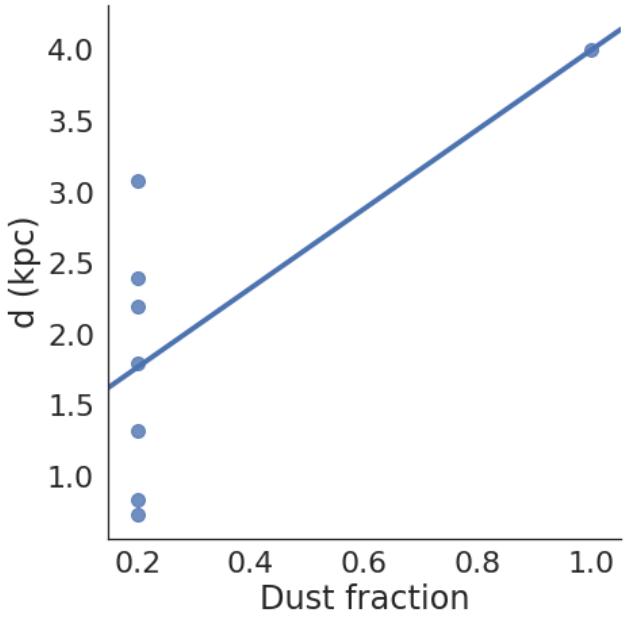

Fig. 5.1 Scatter plot showing the relationship between the dust fraction and the minimum envelope radius. The sub-group mentioned in Section 5.3.3 is clearly visible.

5.3.3 Dust fraction

The dust fraction has one large clear group. Most of the MYSOs could be fit with models which used the default disk dust fraction suggested by Whitney et al. [2013], where 20% of the total disk mass consists of large grains. The remaining MYSO, G305.20+0.21, has a disk consisting only of large grains. A strong correlation is found between dust fraction and distance (Figure 5.1) but when looking at this data visually the correlation is essentially dictated by one source. Therefore, due to this effect and the fact that dust fraction is almost completely consistent across the MYSO

sample, it is not discussed again during in the context of the overall trends of the group.

5.4 Correlations

In this section, correlations are used to compare the parameters spaces of the best-fitting models obtained throughout this thesis. A correlation coefficient is a numerical measure of the relationship between two variables. The Pearson product-moment correlation coefficient (PPMCC) is a commonly used correlation and can be calculated using:

$$r_{xy} = \frac{\Sigma_{i=1}^{n}(x_i - \bar{x})(y_i - \bar{y})}{\sqrt{\Sigma_{i=1}^{n}(x_i - \bar{x})^2}\sqrt{\Sigma_{i=1}^{n}(y_i - \bar{y})^2}} \tag{5.1}$$

where r_{xy} is the coefficient, n is the sample size, x_i and y_i are the data points and $\bar{x}$ and $\bar{y}$ are the sample means. Values for the coefficient can range between -1 and 1. No correlation at all between the variables results in a 0, two completely positively related variables have a correlation coefficient of 1 and two completely negatively correlated variables have a value of -1. The amount of correlation can be classified into three categories; weak, moderate and strong. If the correlation coefficient has a value <0.3 it is weak, if the correlation coefficient lies between 0.3-0.7 it is moderate and if the coefficient is equal to or higher than 0.7 it is strong.

Figure 5.2 presents these correlations in a comparative format, excluding the parameters discussed in Section 5.2.1. The vast majority of the correlation coefficients are <0.5. This implies that for the most part, the objects within this sample are a diverse group. The underlying geometry of the sources however is similar as they all have disk-outflow systems surrounded by Ulrich-type envelopes.

In the remainder of this subsection it is discussed how using different observing configurations may affect the resulting correlations and whether the determined

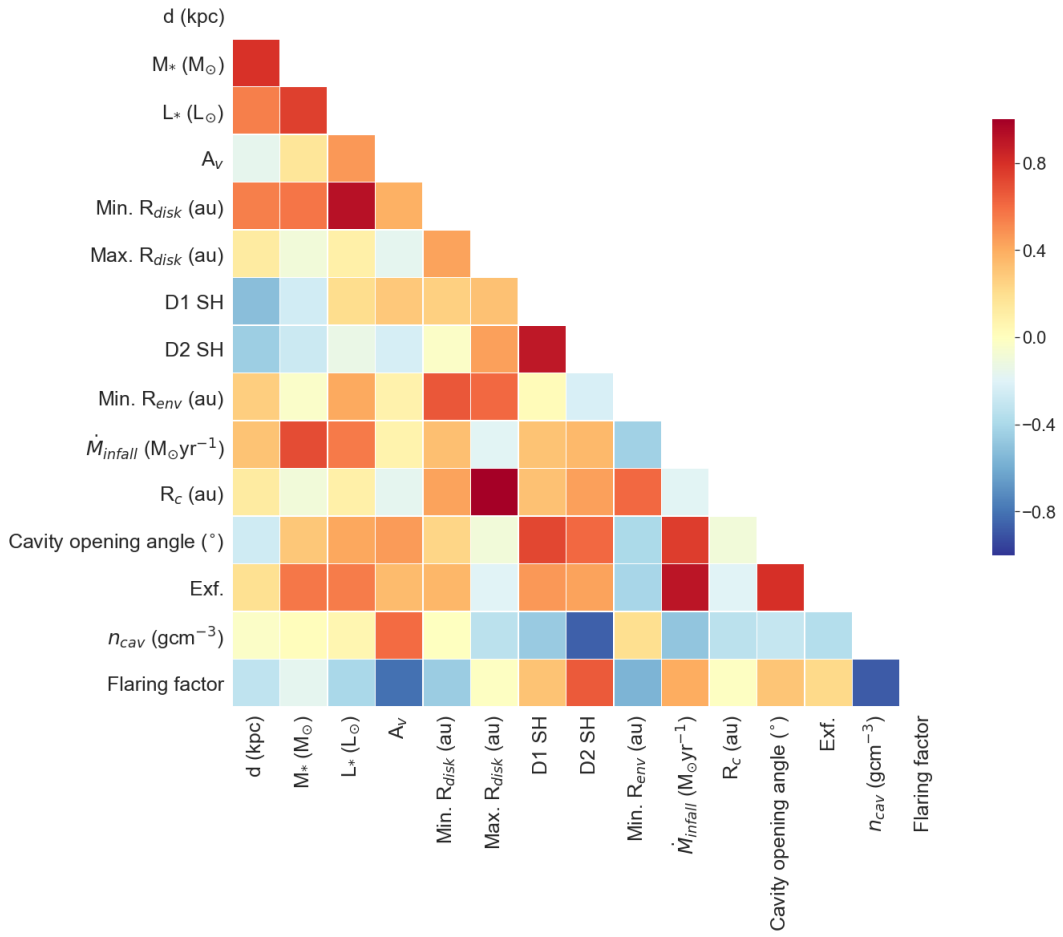

Fig. 5.2 Correlation matrix displaying the relationship between the parameter space. Because of the poor constraint of the disk mass using mid-infrared observations this parameter is omitted. Additionally parameters which were the same or very similar across the entire parameter space (e.g. cavity shape exponent, maximum envelope radius, dust fraction) are also not included. Exf. is the shorthand used for the cavity density exponent by Whitney et al. [2013].

parameters are biased by their inclinations. Groups within the parameter space are also noted, and correlations that were unexpected and strong correlations are presented.

5.4.1 Checking for biases

Before considering the correlations they were checked for bias. The sample, presented in Chapter 4, includes MYSOs at a variety of distances and inclinations, and they were all observed using different baseline configurations. As such, it was of interest to determine whether the parameter space was affected by the resolving power of the observations and whether specific parameters were only detected at certain inclinations.

For the resolving factor, strong correlations were detected for two characteristics - the distance and stellar mass. This is consistent, as a very distant source needs to be more massive or luminous to be detectable, but if a source is close and observed with small baseline lengths it may be comparably resolved as a source that is distant but observed with the largest baselines. The flaring shows a moderate correlation, which again seems consistent as the more flared the disk, the larger the area available for irradiation and subsequently the larger solid angle on the sky for re-emission, meaning that more flared disks will be more easily detectable. This would have a larger effect for disk-only systems, but the fact that the disk is enclosed in an envelope for all of the observations will reduce the importance of this effect, possibly explaining why a moderate, and not strong, correlation is observed. All other protostellar characteristics display weak correlations, implying that the characteristics obtained for the sources are not just due to the specifics of their MIDI observations.

The inclination was examined in four ways. Firstly, the base inclination (as included in the table of model fits for the sample in the previous chapter) was

compared with other properties. Secondly, the difference in inclination from 90° was investigated. When viewed edge on (90°) the line of sight traces the densest region of the protostellar environment which harbours the disk. As the inclination deviates from 90° the column density in the line of sight decreases. Therefore, investigating the distance from 90° can tell us if there is a bias towards MYSOs viewed at a certain line of sight. Finally, the sine and cosine of the inclination were also checked for consistency. Overall, all the correlation coefficients for inclination when compared with other parameters were weak or moderate, implying that the derived characteristics are not determined by the inclination of the source.

5.4.2 Effects of fitting choices

Throughout the fitting process a few decisions were made which affect the correlations. One such decision was to equate the centrifugal radius and outer disk radius during the fitting process. This was done as the centrifugal radius essentially dictates where material which is infalling in the envelope will be deposited. As discussed in Chapter 1, it is thought that infall from the wider environment will occur at similar rates to accretion onto the central protostar. As such, the envelope and disk scales may be linked. The deposition of material at the centrifugal radius provides the most logical source of material for the formation of a disk and the most likely reservoir of material which will ultimately be fed into the accretion process. Based on these considerations the centrifugal radius and outer disk radius were made equal, resulting in a correlation between the two values of 1.

Another assumption made during the fitting was that the distribution of large grains would be flatter than the distribution of small grains in the disk. Whitney et al. [2013] suggest a flaring factor of 2 between the two large and small grains disk components to simulate this, based on the hydrostatic calculations of D'Alessio et al. [1998] and images of observed disks (Cotera et al. [2001] and Wood et al.

[2002]). This ratio of 2 for the flaring factor was therefore used as a starting point for the fitting process and varied if required. It was found that this ratio could provide suitable fits to most of the datasets, meaning that there is a strong correlation (0.89) between the scale heights of disk 1 and disk 2. The implications of having different disk scale heights in massive protostellar disks is discussed in more detail in Section 5.5.

Similarly, the minimum disk radius and minimum envelope radius were also linked during the fitting, as it was assumed that if something was disrupting the dust in the inner regions of the envelope this would also disrupt material in the inner regions of the disk. Therefore, one would expect a strong correlation between these two parameters. The values were kept the same unless a noticeable improvement in the fit was obtained by changing them and this occurred for IRAS 17216-3801 (discussed in Chapter 4). The difference between the minimum disk radius and envelope radius for this source is large, resulting in a moderate correlation (0.67) between these two parameters for the whole sample, but this increases to 1 if IRAS 17216-3801 is removed.

5.4.3 Unexpected relationships

One correlation that was expected to be present but was not is that concerning distance and luminosity. If a source is distant, one would assume it must be brighter to remain detectable. From this sample it was found that the distance-luminosity relationship was moderate (0.54). If the two most luminous sources (IRAS 17216-3801 and AFGL 2136) are removed, however, the relationship becomes strong (0.89). While these two sources are particularly bright within the scope of this sample, they are not unusually bright for massive protostars in general. As such the moderate correlation for distance-luminosity when these sources is included is put down to sample size, not the presence of outliers.

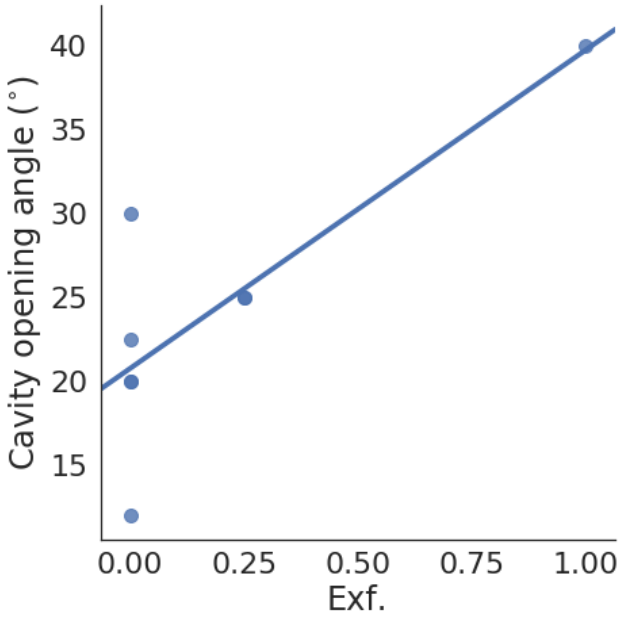

Fig. 5.3 Scatter plot showing the relationship between the cavity density exponent and the cavity opening angle. Exf. is the shorthand used for the cavity density exponent as used by Whitney et al. [2013].

A strong negative correlation is found between A_v and flaring factor (-0.81). The foreground extinction is not an intrinsic property of an MYSO and describes more about its surrounding environment. Such a strong correlation between A_v and any specific protostellar parameters induces skepticism and a wider number of sources would need to be considered to investigate whether this is a tangible correlation or not.

A strong (0.80) correlation is found between the cavity density exponent and the cavity opening angle. This, at first glance, does not appear to have a physically consistent explanation. However, similar to the dust fraction, one source appears to be cause of this strong correlation. IRAS 17216-3801 has the highest cavity opening angle of the sample and also the highest cavity density exponent, inducing a strong correlation across the group. When this source is removed, the relationship is weak (0.36). Similarly, IRAS 17216-3801 has the highest envelope infall rate of the sample, so the same effect occurs. A strong correlation coefficient of 0.91 exists for

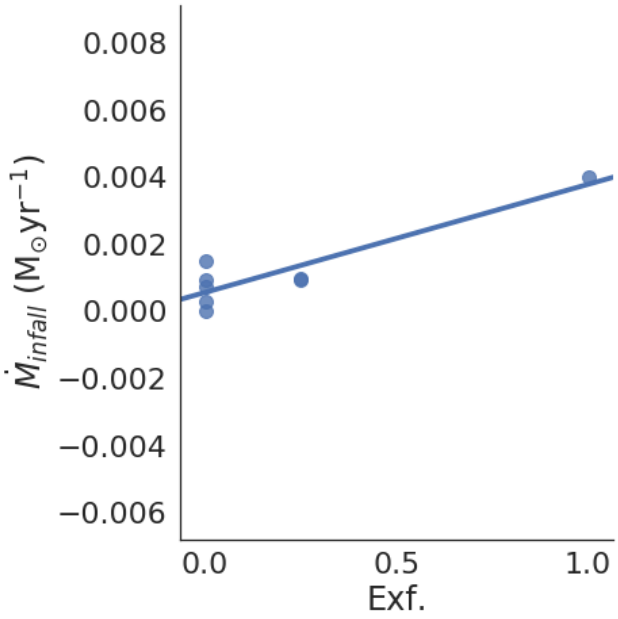

Fig. 5.4 Scatter plot showing the relationship between the cavity density exponent and the envelope infall rate. Exf. is the shorthand used for the cavity density exponent as used by Whitney et al. [2013].

the sample when IRAS 17216-3801 is included, but this decreases to 0.27 when it is removed. As such neither of these correlations are given much consideration. These correlations can be viewed in Figure 5.3 and 5.4 respectively.

5.4.4 Strong correlations

Excluding the strong correlations mentioned which are a result of decisions described above and the resolving power of the observations, a number of strong correlations exist within the sample which, post these checks, are tangible results from the parameter space. These are discussed in the following subsections.

Distance and central object mass (Fig. 5.5)

The first strong correlation (0.79) implies that as a source becomes more distant, its mass increases. Larger mass objects will have larger environments and therefore be

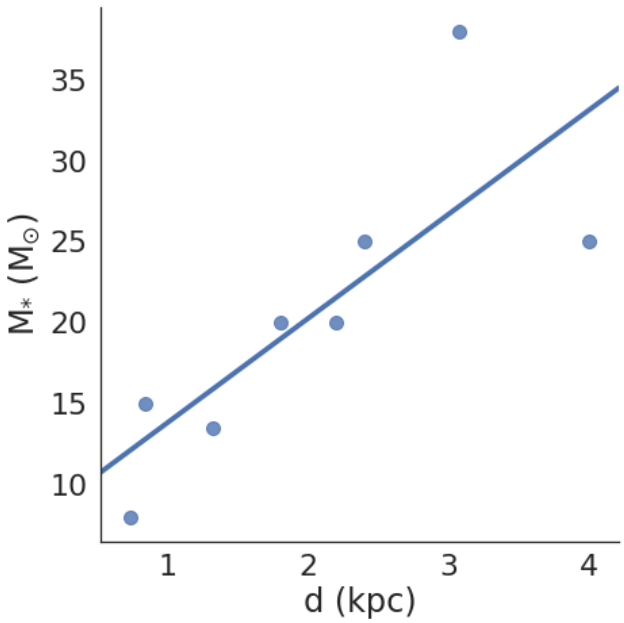

Fig. 5.5 Scatter plot showing the relationship between distance of the sources and the suspected central object masses.

easier to detect at large distances, meaning this correlation appears consistent. This same reasoning can be applied to the luminosity, as a more luminous source will be remain detectable at larger distances, explaining the distance/luminosity relationship as discussed in Section 5.4.3.

Disk scale height and cavity opening angle (Figs. 5.6)

A strong correlation is detected between the scale height of disk 1 and the cavity opening angle (0.72) implying that the more flared the disk, the larger the cavity opening angle. If the disk scale height is large, the disk is more flared and a larger emitting surface will be visible. This same affect occurs if the cavity opening angle increases, as this too increases the available area for irradiation by the protostar and therefore generates a larger emitting region. The correlation between disk 2 scale height and cavity opening angle is moderate (0.62) because one model does not possess this second disk component.

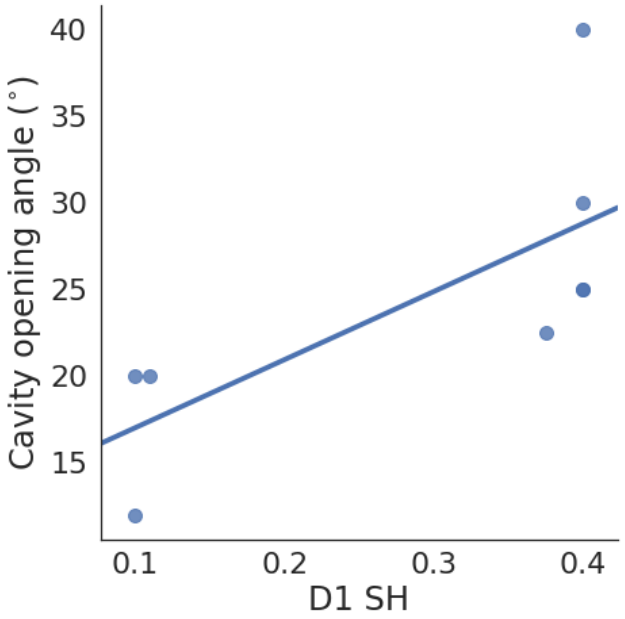

Fig. 5.6 Scatter plot showing the relationship between the scale height of disk component 1 and the cavity opening angle.

Cavity density vs. flaring factor (Fig. 5.7) and disk scale height (Fig. 5.8)

A strong negative correlation (-0.88) exists between the flaring factor and the cavity density, implying that if the disk is more flared, the cavity density will be lower. A similarly strong correlation of -0.86 is detected between the cavity density and the disk 2 scale height, implying that the lower the cavity density, the larger the disk scale height and the greater the volume of the disk. These relationships are discussed in an evolutionary context in Section 5.6.

Disk minimum radius and luminosity (Fig. 5.9)

A strong correlation (0.92) exists between disk minimum radius with luminosity. At a first glance, this appears consistent; a more luminous star will be able to sublimate dust at larger distances compared to a less luminous source, increasing the minimum radius of the circumstellar material. However, as has been discussed in previous chapters, the minimum radius quoted here is not the dust sublimation radius for the

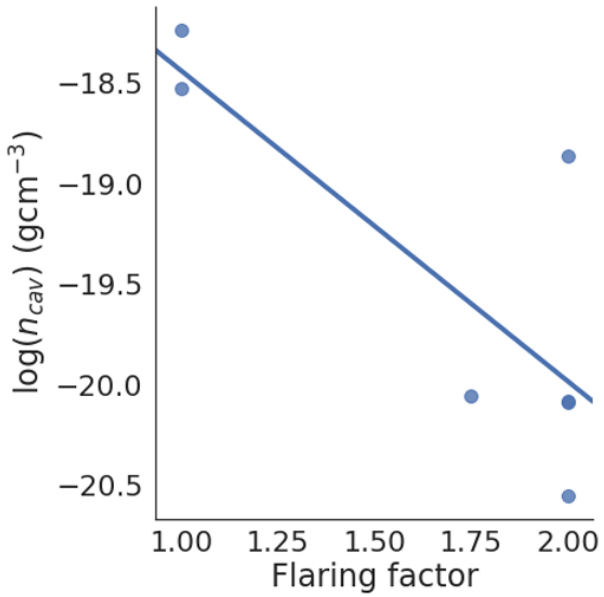

Fig. 5.7 Scatter plot showing the relationship between the flaring factor of the disks and the cavity density.

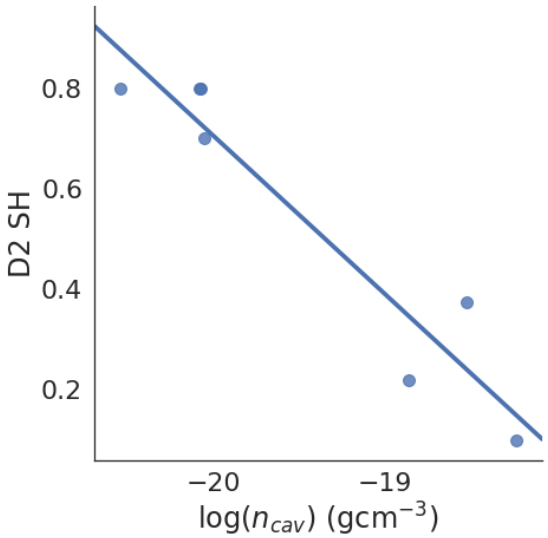

Fig. 5.8 Scatter plot showing the relationship between cavity density and the scale height of the disk.

majority of these sources. In Chapter 3 causes of inner holes in disks were discussed at length and it was determined that the most likely causes for inner holes in massive stars are 1) photoevaporation and 2) the presence of binary/multiple companions. Of these two causes, photoevaporation as a mechanism seems to be in agreement with this correlation. If a source is more luminous, then it will have a greater capacity to generate photons of high-enough energies to dissociate the inner disk material and create cleared inner regions. Therefore, the large luminosity leading to a large inner hole makes sense as the star has another mechanism with which to destroy the disk. This comes with the caveat, however, that the star must not also be creating UV photons to the point where an ionising ultra-compact HII region has begun to form around the source, as that is not observed for any of these sources. A strong correlation does not exist between minimum envelope radius and luminosity, as the minimum envelope radius of the final model for IRAS 17216-3801 vastly differs from its minimum disk radius (as discussed in Chapter 4). If IRAS 17216-3801 is removed, the correlation between minimum envelope radius and luminosity is becomes strong and the correlations between luminosity and both disk and envelope minimum radius become 0.93.

Mass and luminosity (Fig. 5.10)

A strong relationship exists between the central object mass and its luminosity (0.74). The mass-luminosity relationship varies for different masses of main-sequence stars but always follows the same general relation of $L \sim M^N$ where N is an exponent that varies for different masses of star. For stars lower than $0.43 M_\odot$ the exponent is low (2.3) due to their convective nature, for stars between 2 and 55 solar masses it increases to 3.5 and the relationship becomes linear as stars surpass this mass and approach the Eddington luminosity [Salaris and Cassisi, 2005]. While these specific relationships apply to main-sequence stars and there will be some variation

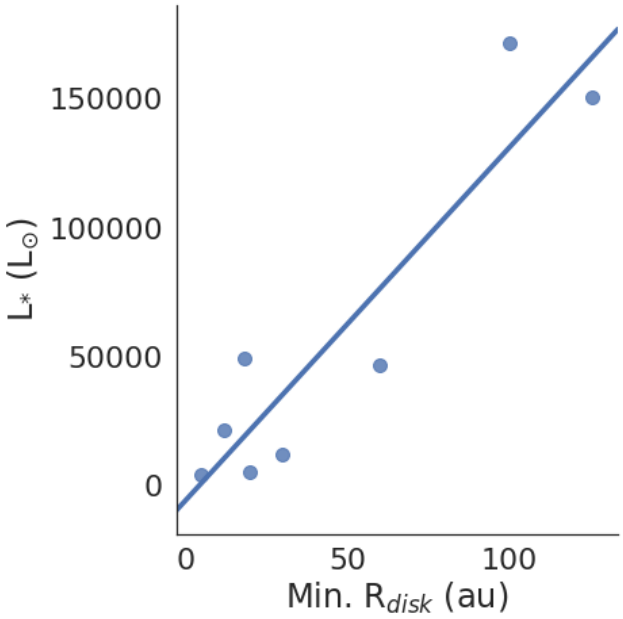

Fig. 5.9 Scatter plot showing the relationship between the luminosity of the source and the minimum disk radius.

in the luminosity of a protostar as it increases, by the time MYSOs are observable they will be approaching the main sequence, so using these approximations is not unreasonable. Additionally, a relationship is to be expected between central object mass and luminosity. As discussed in Chapter 1, the luminosity comes from gravitational potential energy, which will be larger for a greater mass. Also the more massive a core, the more difficult it is for radiation to escape it, as more material is in the way. As a result its temperature and luminosity will be larger than for a low-mass protostar. Therefore, the fact that a strong correlation exists between the mass and luminosity for this sample is unsurprising.

Envelope infall rate vs. central object mass (Fig. 5.11)

A strong correlation (0.71) is seen between envelope infall rate and the mass of the central source. This seems consistent, as the central object is the focal point for gravitational contraction of the wider protostellar environment. If the central

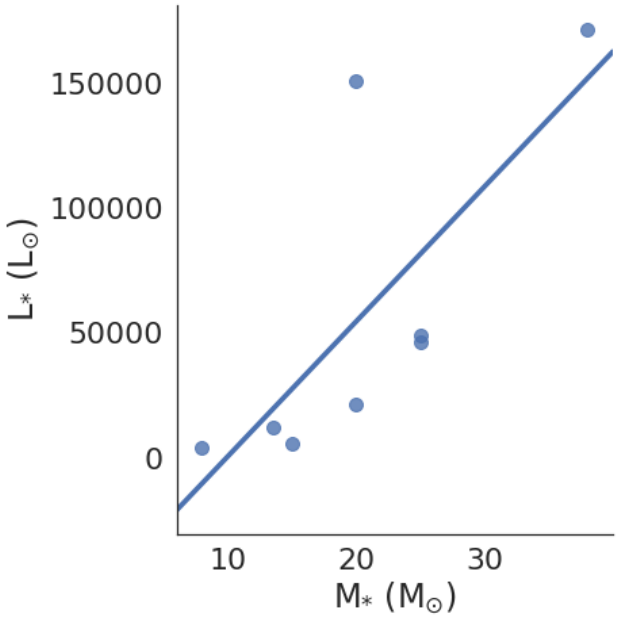

Fig. 5.10 Scatter plot showing the relationship between the luminosity of the source and the central object mass.

source mass increases a greater gravitational force will be exerted on the mass in its surrounding envelope, and the larger the amount of infall will be.

Envelope infall rate vs. cavity opening angle (Fig. 5.12)

A correlation of 0.75 implies that as the envelope infall rate increases, the cavity opening angle will get larger. One possible explanation for this relation is as follows. If the envelope infall rate is high, the envelope is more concentrated towards the midplane and the regions closer to the poles of the envelope will therefore be less dense. The remaining envelope material would then be more vulnerable to the effects of any outflow activity, meaning that more material could be carved of the envelope, thereby widening the outflow cavity such that it has a larger opening angle.

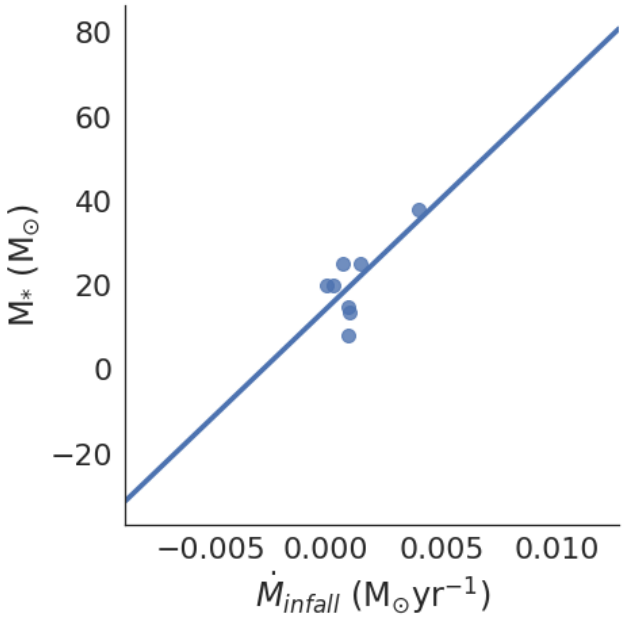

Fig. 5.11 Scatter plot showing the relationship between the envelope infall rate and the mass of the central source.

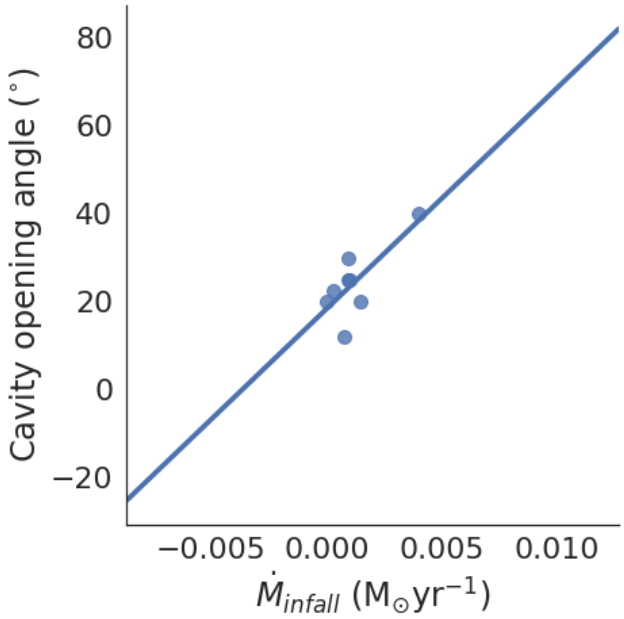

Fig. 5.12 Scatter plot showing the relationship between the envelope infall rate and the cavity opening angle.

5.5 Discussion

The central objects of the models in this study cover a range of masses, temperatures, radii and luminosities. The protostellar masses were only varied to improve the SED fits, as they had effects on the TSC properties of the envelopes. The stars with lower luminosities and therefore lower fluxes in their SEDs were better fit (shape-wise) if their models included lower mass stars, which is consistent as the luminosity of a star is expected to increase with mass.

The envelope properties of the MYSOs were traced predominately by the longer wavelength emission of the SED and the 20μm emission, which was sensitive to the centrifugal radius (for closer sources, following the same discussion 5.2.1) and the envelope infall rate. The larger the envelope infall rate, the larger the density within the infall radius (according to the Ulrich density distribution (Chapter 2, equation 2.2)) and the larger the mount of material available for re-emission of the 20μm flux. All the MYSOs studied within this thesis have observables that can be fit with an Ulrich-type envelope, implying that all of the MYSOs are actively infalling and contain the subsequent density enhancements in the midplane that affect the 20μm emission. Follow-up kinematic studies could confirm this to be the case following methods such as those detailed in Ohashi [2004] (e.g. searching for inverse P Cygni line profiles in the sources' spectra). S255 IRS3 appears to be the exception in terms of envelope parameters, given its low envelope infall rate and small outer radius. S255 is the only source confirmed to be episodically accreting so the fact that differences exist between this source and the others is not surprising, and may be temporary effects induced by this accretion process.

Of the disk parameters, the disk inner and outer radii, flaring factor, dust content of the disks present the most discussion as the other parameters are less well constrained. One weaker constrained parameter is the disk mass. The only source where the disk mass was constrained to a factor smaller than 10 was NGC 2264

IRS1. This is likely due to the fact that it is near, has a close to face-on inclination and has a mass-dependent substructure. AFGL 2136's disk mass was also tested more rigorously to allow comparison with previous work. As expected, very little change was observed between the observables and it was still only constrained to a factor of 10.

The outer disk radius, as discussed in Chapter 2, is only loosely constrained by the observables. A larger disk creates more millimetre emission which can affect the longer wavelength regime of the SED and the maximum disk radius is also tied to the centrifugal radius which affects the shape of the SED particularly at its 70μm peak and around 20μm. The imaging profiles also proved decent outer disk radii tracers, but mostly for the nearer sources. As such, the outer radius is still discussed but it is noted that this is not as constrained as the inner radius, which heavily affects the MIDI emission in all cases.

All the MYSOs in this sample had disks as a component of their final models. These disks are not toroids which are 100s of solar masses and 1000s of au in size [Beltrán and de Wit, 2016], but are objects which (while they could exist at larger radii) are present in the innermost regions of the protostellar environment and within the accreting regions. The fact that all of the sample harbour a disk, lends support to the idea that massive forming stars accrete their mass through similar mechanisms to low-mass stars. The flaring and inner geometry of the disks had the greatest effects on the MIDI visibilities, in agreement with with the postulations for low-mass disks from Dullemond and Monnier [2010] and Mulders and Dominik [2012].

The majority of the model disks have a flaring factor of 2, meaning that the small grains disk has twice the scale height of the large grains disk. Given that this flaring factor is in agreement with the hydrostatic calculations of D'Alessio et al. [1998] and models of observed images (Cotera et al. [2001] and Wood et al. [2002]), this result is encouraging. IRAS 17216-3801 had a flaring factor very close to 2 (1.75) but given that the binary system is likely to be having dynamical effects on this disk,

this slight deviation is not concerning. Two of the remaining disks were flat (scale heights of the disks were 0.1) and one of them required no small grains to be present in the disk to successfully fit the datasets.

Whitney et al. [2013] recommended that the distribution of the dust be split such that 20% of the grains are in disk 1 (the large grains disk component) the remainder are in disk 2 (the small grain component). This approximation suited all of the observations well, save for those of G305. The fact that no disk 2 was required to fit the MIDI visibilities for this source was discussed as a feature of its evolving nature in Chapter 3.

Of these disks, 75% showed substructure. This took the form of inner holes for over half of the sources. The degree of clearing (or the ratio between R_{sub} of the central objects in comparison to R_{disk}) ranged between 1.5-4 across the sample and is shown in Figure 5.13. When the correlation coefficient between minimum disk radius and luminosity was calculated solely for the objects which harboured inner holes, a very strong positive correlation was found. This is interesting because this is not a result of dust sublimation. The potential origin of the inner holes has already been discussed in the previous section and Chapter 3, with photoevaporation and dynamical interaction between a binary and the disk determined as likely causes of the holes in massive protostellar disks. Since this strong correlation exists specifically between luminosity and the minimum radius, one could interpret this as a sign that photoevaporation may be the more likely cause.

Price et al. [2018] note that the observed substructures (including holes, asymmetries and streams) in one Herbig star (HD 142527) can all be explained through the interaction of binary stars with their disks. They find that the more eccentric the binary orbit, the larger the hole and note that it is primarily the dynamical interaction of the stars with the disk that causes the holes observed in their models, not the photoevaporation of said stars. Only one of the sources (IRAS 17216-3801) has been confirmed observationally to be a binary system [Kraus et al., 2017]. Through the

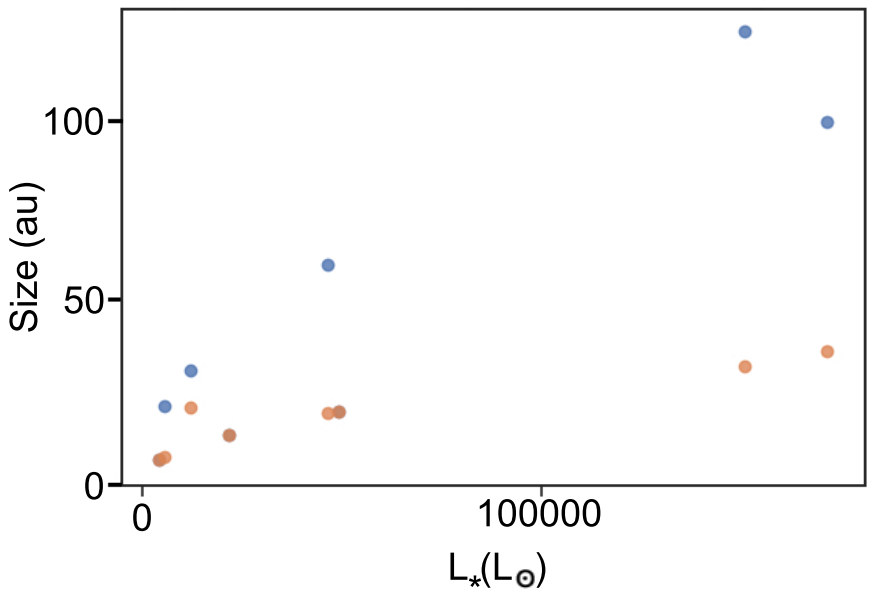

Fig. 5.13 Scatter plot showing the difference between R_{sub} (orange) and the minimum radius of the disk (blue).

employment of this methodology it was found that a satisfactory fit could be found to the majority of the datasets using a one-star model. It then stands to reason that the rest of the sources in the sample could also be binaries and, indeed, studies such as Sana et al. [2012] and Pomohaci et al. [2019] suspect a very high multiplicity fraction for massive stars. It might be fair to assume that the more massive the binary companions, the larger their dynamical effects on the disk and the bigger the hole, but holes are seen across the luminosity and stellar mass range of the models with little pattern. It could be the case that not all of these MYSOs are part of multiple systems or that the binaries are on low eccentricity orbits which disturb the disk less. Determining which of these could be the case would require a direct investigation into the multiplicity of the MYSOs specifically, and is beyond the scope of this thesis.

The remaining substructure takes the form of the 'spiral'/gap substructure in NGC 2264 IRS1. Potential explanations for this have been discussed previously and follow-up observations are required to confirm the precise nature of this environment.

Table 5.2 Type classifications following Cooper [2013] for the sample. No relevant spectra for Mon R2 IRS2 were present so it was not classified.

Name	Type
G305.20+0.21	II
NGC 2264 IRS1	III
S255 IRS3	I
IRAS 17216-3801	III (tentative)
M8E-IR	III
W33A	II
AFGL 2136	II/III

5.6 Evolutionary discussion

Various similarities and dissimilarities are present between the best fitting models of the MYSOs. Characteristics such as cavity opening angle have been observed to change with age through theoretical works, but how do the characteristics of the MYSOs found through this thesis align with previous classification studies?

Cooper [2013] examined the NIR spectra of over one hundred MYSOs from the RMS survey. Various emission signatures were observed throughout the objects, allowing them to be categorised into three main different types. The emission lines which allowed this were H_2, Brγ, Br10 and fluorescent Fe II (hereafter fl-FeII). Other lines were also noted to have relevance, for example it is not that Br10 in particular was a signature, more the presence of Bracket series lines in general that had significance. According to Cooper's classification, Type I MYSOs display strong H_2 emission lines but no others. Type II have H_2 and Brγ present, weak or absent Br10 emission and absent fl-FeII. Type III show weak or absent H_2, strong Brγ emission and a presence of Br10 and fl-FeII emission.

Each of these types is classed as a different evolutionary phase. Type I would correspond to the youngest, with the strong H_2 emission attributed to shock activity where outflow material and envelope material collide. As the MYSO evolves through the Type II and Type III stages the amount of H_2 emission decreases, perhaps because the outflow itself is weakening, the amount of circumstellar material is

depleting due to dispersion and/or because the molecules of H_2 are being dissociated as the protostar gets hotter. This increase in temperature also induces (Type II) and increases (Type III) the Brγ emission. By the time an MYSO is at Type III, either the outflow is too weak or there is not enough material to form shocks of H_2. At this stage the star would be hot enough to produce UV photons to such a degree that a line driven wind is generated, along with HI emission and fl-FeII emission at 1.6878μm. Past this point ionisation would be prevalent enough to create a HII region.

The spectra for the MYSOs (where available in the literature) were inspected for the sample of MYSOs in this thesis in an attempt to see if certain geometries and characteristics were typical of MYSOs within each of these types. Spectra were obtained to a complete enough degree for 6 of the 8 studied sources from Pomohaci [2017], Porter et al. [1998] and Cooper et al. [2013]. A 2μm spectra for IRAS 17216-3801 [Kraus et al., 2017] was also examined.

The sample and their types are listed in Table 5.2. S255 IRS3 was classified as Type I in Cooper [2013] and the fact that it is known to be actively accreting [Caratti o Garatti et al., 2017] corroborates this. The inner geometry of the disk of S255 IRS3 appears consistent with an object at early evolution, as it is not one of the sources which displays a hole in its inner disk. The fact that its disk still harbours small grains again supports this. The envelope infall rate is low, but since the datasets used in this study are from an accretion lull for the source, this may not be problematic. The cavity density for the source is one of the higher among the sample, implying a lack of dispersal of the wider environment and, again, an earlier age for the source. The cavity opening angle is one of the smaller of the sample at 20°. This corresponds to a protostellar age of $\sim 10^{3.2}$yrs according to the modelling of Offner et al. [2011].

G305.20+0.21 and W33A are both spectrally classified as Type II sources, but show very different geometries. G305 has a large inner hole and a low density environment, while W33A is much denser and has a minimum disk radius of its

sublimation radius. Their envelope properties are comparable but with differing centrifugal radii. The cavity opening angle for G305 is the smallest of the sample, but this value may have been be affected by the secondary source detected in the cavity by Liu et al. [2019]. W33A also has a 20° cavity putting it at the younger end of the evolutionary track of Offner et al. [2011].

As said in Cooper [2013], no classification is absolute and AFGL 2136 could be interpreted as either a Type II or Type III source. Its spectrum displays a lack of H_2, implying it is an older Type III object but Br-γ is is only weakly observed, implying it would be a younger Type II object. Some CO lines are present, but most of these are absorption lines. Hoffmeister et al. [2006] find CO absorption in a number of MYSOs in the M17 region and attribute this to heavy accretion ($>10^{-5}$Myr^{-1}, consistent with the final model rate found through the methodology of this thesis). Emission lines like the Br-γ could appear weak if the source has a high column density, which would increase the amount of continuum emission making the lines look fainter and could be the source of this confusion. The continuum emission of AFGL 2136 is high but its column density is not directly measured in this work. Ultimately AFGL 2136 was listed as a borderline Type II/III source.

The remaining sources are classified as Type III. All the disks within this type display substructure. While without the Br series it was hard to completely classify IRAS 17216-3801, the absence of H2 emission and the strength of the Br-γ line suggests that this is a Type III source. It also displays an inner hole and possesses a wide cavity opening angle consistent with what is expected from older sources. NGC 2264 IRS1 is the only source to show a substructure other than an inner hole, but as discussed in Chapter 4 this substructure can be interpreted as consistent with an aging source. All of the disks for this type are highly flared. A decrease in disk flaring has been presented as a diagnostic for evolution with the low-mass disk community, but the topic remains controversial. For lower-mass sources, it has been proposed that once the gas in a disk has gone it will quickly flatten [Williams and Cieza, 2011].

This is expected to occur at the very end of the protostellar/protoplanetary disk phase just before a disk becomes a debris disk, when the systems are between 10^5-10^6yrs. Meeus et al. [2001], through the study of infrared excess in the SEDs of Herbig disks, divided a sample of 14 disks into two groups. The concluded that the earlier disks (dubbed Group I disks) were more likely to be flared and the second group (Group II) were more likely to be flat. They attributed the two groups to different ages and the change in flaring between the two to dust growth. However, recent high-resolution imaging finds no observational support for this postulate. Garufi et al. [2017] in particular find within a large sample of Herbig disks (half of all known at the time) that over half the flared disks are older than 10Myr and state that the idea of evolution from flared to flat disks must be revised. The flaring of the disk could then be due to some other characteristic of the protostellar environment. The results of this thesis therefore agree with the findings of Garufi et al. [2017] for lower-mass sources.

Most of the Type III sources have low density environments which is to be expected of older sources as they would have time to dissipate. The cavity opening angles for these sources are also the larger of the sample, and according to the work of Offner et al. [2011] they would be between $\sim 10^{4.5}$yrs old, which is again consistent with them being more evolved. In Section 5.3 the strong negative correlation (-0.93) between flaring factor and cavity density was noted. Now that it has become apparent through this classification that most of the more evolved sources have flared disks, this correlation appears consistent, as more evolved MYSOs will have lower density environments as they disperse. As most of the Type III MYSOs have highly flared disks within this sample, the fact that the correlation is so strong is consistent. Similarly, a strong correlation between cavity density and disk scale height was found. This again makes sense within this evolutionary context, as all of the Type III sources have low cavity densities (as previously discussed) and highly flared disks. In summary, Type III sources (the most evolved sources), display lower densities,

larger cavity opening angles, a large degree of disk flaring and all display some level of substructure in their disk.

5.7 Summary

In conclusion, the analysis of the full sample has unveiled the following:

- That the characteristics determined by the multi-scale analysis are not dependent on the inclination of the source and the resolving power of the observations.
- That the objects all follow the same basic geometry (Ulrich-type envelope, polynomial bipolar outflow cavities and a disk) which is comparable to the Class I phase of low-mass star formation.
- That there are a lot of small variations within this base geometry, implying that MYSOs are still diverse objects at least on small scales.
- That all the older sources either have holes in their disks or substructure, wider cavity opening angles and lower cavity densities. This is consistent with the idea that substructure evolves over time, due to processes such as disk dispersal.

These conclusions could only be drawn because all the objects were modelled and analysed in the same way. Comparison of the work described in this thesis with that of Cooper [2013] allowed the physical parameters of the MYSOs to be put into an evolutionary perspective. Determining the cause of the holes observed within the evolved MYSO disks presents an avenue of further work.

A graphical presentation of how the parameters of the final models for the sample vary with their classified type is shown in Figure 5.14.

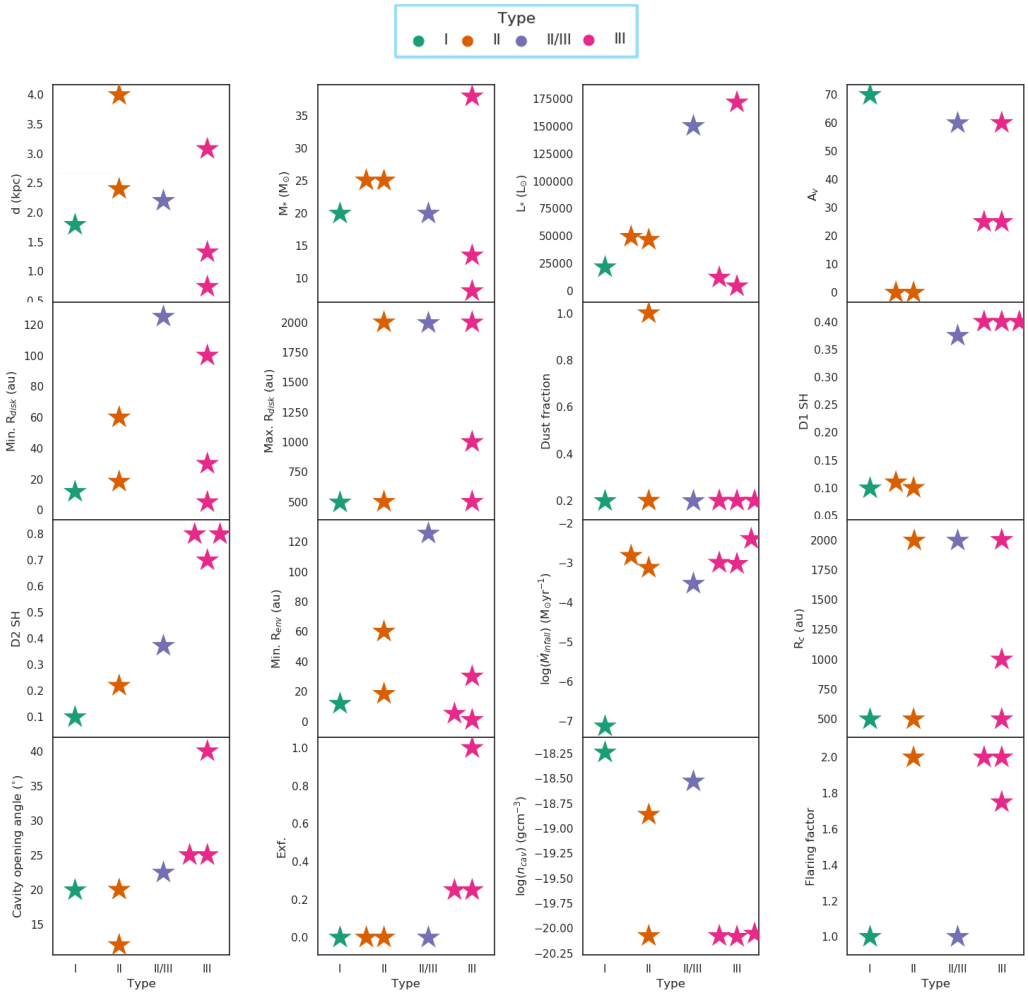

Fig. 5.14 Plots displaying how the parameter space varies with the classified type of the MYSOs.

Chapter 6

Conclusions

This work presented in this thesis used a variety of high-resolution infrared observations, spectral energy distributions and radiative transfer modelling to constrain the properties of Massive Young Stellar Objects (MYSOs), pre-main sequence objects with ongoing accretion who are yet to generate HII regions [Oudmaijer and de Wit, 2014]. The high-resolution data consisted of visibilities from N-band two-telescope interferometry (MIDI, VLTI) and near diffraction limited Q-band images (VISIR/VLT, COMICS/Subaru). The mid-infrared wavelength regime is optimal for the study of MYSOs, as these objects are deeply embedded in dusty material which is infrared bright and at temperatures of $\sim$100K meaning their environments can be studied despite the fact the stars themselves are optically invisible. The combination of the high-resolution infrared datasets with the spectral energy distribution allowed a sample of MYSOs to be probed at 10mas and 100mas scales and as a whole. 3D radiative transfer models (generated using HO-CHUNK3D [Whitney et al., 2013]) consolidated the observations and enabled the specific characteristics of the MYSOs to be investigated. The work presented throughout this thesis tackled a variety of massive protostellar environments of differing distances, luminosities and masses. The number of observations simultaneously fit, the complexity of the modelling and

the number of sources included make this work unique in the literature, increasing the number of studies of MYSOs that fit multiple datasets simultaneously by eight.

In Chapter 2, the methodology was described in full and an example of its implication was presented through the fits of W33A. This source had previously been subject to a similar methodology in de Wit et al. [2010] where just MIDI data and the SED were fit with 2D radiative transfer models (using an older version of the code used in this thesis). Their methodology was built upon and revised, through the inclusion of the imaging data and decision to not multiply the N-band model images with a Gaussian in the simulation process. The previous work also used an older distance for W33A of 3.8kpc which has since be superseded by maser parallax measurements and determined to be 2.4kpc. When fitting the source for the different distance, the model for the old 3.8kpc distance of W33A could not simply be scaled down to provide a best fit and the geometry of the model had to be revised. It can therefore be concluded from this chapter that accurate distance measurements are crucial in the determination of the characteristics of MYSOs. Another conclusion of this chapter is that the dust type included in the models can have a large effect on the mid-IR visibilities obtained for a source. When PAHs are included in the dust composition of the disks, they present an additional density component, simulating a more compact source which increases the visibilities. This is a similar effect to adding a disk to the model. It can therefore be concluded that obtaining proper information on the dust composition of a source, and accurately modelling this, could improve the constraint on the parameters of MYSOs.

In Chapter 3, the results obtained when this methodology was applied to one source, G305.20+0.21, were presented. Models were fit to the interferometric data, imaging data and SED of the methodology, and a VVV Ks-band image was also separately considered. Through the employment of the methodology described in Chapter 2, it was found that the source required clearing within its inner regions such that the minimum dust radius was over three times the size of the dust sublimation

radius (as dictated by the luminosity of the central source which was in agreement with observations). From the VVV image, it was deduced that the environment must be lower density than most typical MYSO environments, as two cavity lobes were visible at $\sim 2\mu$m, which is not possible in a denser environment with higher levels of extinction. This was in agreement with the lower densities found for the protostellar environment through the fitting process. Lower densities imply dispersal and that this could be a more evolved source. An older evolutionary state and inner clearing are two characteristics of transition disks found around low-mass stars, which mark the evolution of the source from a Class II to Class III objects (Chapter 1). Such a disk has not been classified for a high-mass object and the likely causes for the clearing were discussed. The possibilities for bloated protostars were also tested for this source. It was found that the overall luminosity, not the specific stellar radius and temperatures, of the sources has the dominant affect on the observables, with negligible differences seen between the datasets for the inclusion of a cool bloated star vs. a hot compact star.

In Chapter 4, the results obtained for six more MYSOs who had been subject to the methods of the thesis, were presented, resulting in a full sample of eight sources. The sources in this chapter range in distance between 0.74-3.06kpc their luminosities between $\sim 10^3$-$10^5 L_\odot$. The MIDI data, imaging data and SED and the simulated observables of the preferred final models were all presented and their geometries discussed. For the nearer sources it was found the combination of the imaging and interferometric data in particular was invaluable as it allowed a distinction to be made between cavity and disk emission, which have both been claimed to be the main source of N-band emission at small scales in previous work. It was found that substructure was present in the disks of the vast majority of the sources and the most common form of this was an inner hole. Many of the objects are well known sources which had been previously studied, and the characteristics found through my fitting process were compared with previous work.

In Chapter 5, the results of Chapters 2, 3 and 4 were combined and a comparative analysis was performed of all the objects. The relationship between the different characteristics of the MYSO were investigated through the calculation of Pearson's correlation coefficient and through discussions of common characteristics and observed groups in the sample. Every object required a disk to produce a satisfactory fit to its observables. This implies that a scaled-up schematic of low-mass star formation can explain the formation process of these sources and that massive forming stars grow through disk accretion, as the disks were required to fit the MIDI data which traces 2-20au scales which would be involved in the accretion process. All the objects (save one) were classified according to the evolutionary types of Cooper et al. [2013] by using NIR spectra from the literature with most of the sources dubbed as Type III sources (the most evolved type). All of the disks for the Type III sources had substructure with the most common being an inner hole. Given that the Type III sources are defined by emission features associated with line-driven winds induced by UV photons, this may suggest that photoevaporation is the main cause of these inner holes.

6.1 Future Work

6.1.1 Massive protostellar disks

As discussed in Chapters 2, 3 and 4, some disk characteristics are constrained better than others. Follow-up studies at longer wavelengths would help to constrain the larger scale disk parameters such as mass and outer radius.

High-resolution interferometers such as the Atacama Large Millimetre Array (ALMA) and the Northern Extended Millimetre Array (NOEMA) could assist in the quantification of disk mass through continuum emission. NOEMA 1.3mm observations can trace the coldest regions of the protostellar environment most

distant from the central protostars. As such, most of the protostellar material will be encompassed and an accurate value for the dust mass can be obtained through methods such as those utiltised by Ubach et al. [2012]. The CORE project [Beuther et al., 2018] is one project that is actively investigating the nature of fragmentation for MYSOs and the presence of disks using NOEMA. Recent results of the project include the discovery of evidence for rotation in massive protostellar cores similar to low-mass star forming regions which harbour disks [Bosco et al., 2019].

When observing at the same wavelength with ALMA, scales of 0.01" can be traced given the size of the array allowing details of the disk to be resolved at larger scales, thereby probing small details of the MYSOs at high resolution. A variety of hot-core tracing molecular lines could also be investigated using this instrument. CH_3CN ladders have been successfully utilised to study the morphology, kinematics and physical conditions in discs around other MYSOs (e.g. Ilee et al. [2018]). Modelling with the CASSIS local thermodynamic equilibrium (LTE) radiative transfer package on the CH_3CN and $CH_3^{13}CN$ emission line ladders can allow investigations into the physical properties of massive protostellar disks such as column density which were not possible with the infrared data used in this thesis. Additionally, spectral analysis can help to determine whether the disks are Keplerian. Multiple studies (e.g. Ilee et al. [2018], Maud et al. [2018] and Johnston et al. [2015]) use PV diagrams of spectral lines and comparisons with Keplerian rotation curves as a marker of stability for protostellar disks and performing this same analysis can help to ascertain whether the disks studied in this thesis are stable or fragmenting. Calculation of the Toomre Q parameter can assist with the latter (e.g. Maud et al. [2019]). If the parameter is less than 1, the disk is unstable to axisymmetric perturbations and prone to fragmentation [Toomre, 1964]. Analysis of the gas kinematics and dust emission can also allow the calculation of the mass of the main source and the disc, following the method of studies such as Cesaroni et al. [2011].

Image reconstruction provides an alternative way of providing further evidence of the presence of disks around the sources. The Multi AperTure mid-Infrared Spectro-Scopic Experiment (MATISSE) provides one opportunity to pursue this. Operating in the L, M (as of April 2020) and N-band simultaneously, MATISSE is particularly suited to follow-up studies of the sources studied throughout this thesis. The instrument uses four of the VLTI telescopes as opposed to the two used by MIDI, providing a vast improvement in the level of u-v coverage of the observations. The L and M band data also push to higher resolution given their shorter wavelengths, meaning a more detailed picture of the sources can be obtained. All these observations can be consolidated through previous work by obtaining N-band visibilities, which can be compared to the previous work from MIDI. As such observing with MATISSE results in an expanded dataset which can illuminate further details of the protostellar environments but that can be consistently checked with the work of this thesis. Image reconstruction with ALMA and NOEMA can also be performed, and in combination with MATISSE could provide a near-complete image of the environments from infrared to millimetre wavelengths.

Direct imaging at milliarcsecond resolution will also soon be possible with the advent of the Extremely Large Telescope. Its infrared imaging instrument METIS (the Mid-infrared ElT Imager and Spectrograph) will provide images between 3-20μm, overlapping with both the MIDI and VISIR data used in this work. Thanks to the $\sim$40m mirror on the ELT, the resolution of these images will be of a resolution comparable to long-baseline observations with VLTI at $\sim$0.01". These direct images will also provide more spatial information than the reconstructed images of the VLTI and be less expensive to perform time-wise given the smaller overheads of imaging observations. The JWST is the only instrument that could produce images of MYSOs of a similar quality to METIS in the future, but given the high luminosities of the MYSOs, these images may fall victim to over saturation.

6.1.2 Circumbinary or transitional disks?

In chapters 3, 4 and 5 the presence of the inner holes found in the circumstellar environments of a number of these MYSOs was discussed. One avenue of future work is to determine their cause. One possible cause of holes in disks is the presence of a binary system. The enlarged inner radius would then be caused by dynamical effects of the binary on the protostellar environment so one can either study the dynamics of the system or attempt to directly detect the presence of the binary. Pomohaci et al. [2019] classified a number of RMS sources as binary systems through K-band adaptive optics, but there is little overlap between the objects of this thesis and that work. G305 was included in the work of Pomohaci et al. [2019] but not classified as a binary, but their methods are sensitive to wide binaries only , so a close binary system could exist. Other methods exist which allow the detection of closer binaries such as interferometry, spectroscopy and sparse aperture masking. Geometric modelling of infrared visibilities and closure phases in particular can allow the detection of binaries (e.g. Koumpia et al. [2019], Kraus et al. [2017]). Sparse aperture masking can detect binaries in a similar way. Sparse aperture masking is a technique whereby an imaging telescope is manipulated to generate interferometric observables through the use of a mask. The mask has a configuration of holes, and when light passes through these it interferes, creating visibilities and closure phases similar that are more robust to atmospheric turbulence. As such, similar geometric modelling can be performed and used to detect the presence of disks, binaries and, for low-mass stars, substructures such as warps within disks (e.g. Sallum et al. [2019]). Image reconstruction from interferometric data and imaging in the NIR has also been used to detect high-mass protobinary systems [Sridharan et al., 2002] and could also be used for fortuitously inclined sources.

In terms of dynamics, spectral imaging can allow investigations into the kinematics of the sources, allowing the detection of companions. Ilee et al. [2018]

found a companion surrounding G11.92-0.61 MM1 through the examination of the continuum and CH_3CN emission of the source, resolving MM1 into two sources. This method also allowed the dynamics of the disk to be investigated and it was found to be unstable and fragmenting. If a disk is fragmenting it may not be a stable disk which can be accreting and a key component of the massive star formation process. As such, a follow-up study of the MYSOs in this sample with ALMA in a similar manner could not only reveal the presence of any companions, but also provide information on whether they are true representatives of a stable evolutionary class or not. AFGL 2136 has already been studied with ALMA (Maud et al. [2018], Maud et al. [2019]) and appears to be mostly stable and W33A has been studied with ALMA [Maud et al., 2017a] and shown to be turbulent on large scales, but with a possibility for a disk to exist at small scales within these spiralling outer regions.

Based on the above, a comprehensive observing program with ALMA of the remaining disks in the sample will allow investigations into their stability, allow the detection of protobinary companions and therefore determine whether these disks found around the sample are circumbinary or transitional.

6.1.3 Expanding the methodology

While the methodology provides a level of analysis and coverage of the sources seldom seen in the literature, it, like any method, could be expanded upon. The first obvious way to do so would be to apply the approach to more sources. More MYSOs with both MIDI and VISIR data exist and studying them with this methodology would provide a larger dataset for statistical analysis. Additionally, the methodology could include more forms of high-resolution data to better constrain the fits of the sources. This could be provided by MATISSE (as discussed in the Section 6.1.1) or GRAVITY, which would push to even higher resolution and trace hotter material thanks to its K-band operating wavelengths. As previously mentioned the addition

of longer wavelength data (e.g. from ALMA and NOEMA) would also be beneficial, as it would provide tighter constraints on important parameters such as disk mass and radius. Including different forms of long-wavelength data such as sub-mm and millimetre data could help distinguish between cold disk material and cold envelope material, put a constraint on the envelope radius for these sources and further constrain the characteristics of these sources.

As well as exploring different wavelengths for the techniques used within this thesis, different observational methods could also be investigated. Ilee et al. [2013] used CRIRES data between 1-5μm to investigate the CO bandhead emission of a number of MYSOs and through the modelling of this emission were able to infer the presence of disks around many of the sources. X-SHOOTER also provides spectroscopy at near-infrared wavelengths which can be used to detect binary systems, accretion and trace material close in to the central star. Given that only a couple of sources from this thesis overlap with the work of Ilee et al. [2013], their methodology could be adapted and applied to X-SHOOTER data to see if similar results can be obtained for the group of MYSOs studied in this thesis.

6.2 Closing Remarks

In conclusion, this thesis has constrained the characteristics of a number of MYSOs to a new level, probing multiple scales and the different accreting regions of the massive protostellar environment. Information about the circumstellar environment at 10mas, 100mas and as a whole has been gained. Disks are ubiquitous for the sample and the presence of inner holes in the disks is common. The work of this thesis finds that the bloating MYSO models of Hosokawa et al. [2010] are viable within these protostellar environments. If the central object in the model is made larger in radius and cooler in temperature in line with the models of Hosokawa et al. [2010], minimal differences are seen to the fits of the observables. Large envelope infall rates are

present for nearly the entire sample, and the outflow cavities for all sources have been shown to have the same shape, with implications for their formation mechanisms. While some underlying trends exist between the sources, the sources also display a significant degree of diversity. The sources have been compared to the evolutionary classifications of Cooper et al. [2013], linking their physical characteristics to the evolutionary stages determined throughout that work. Expanding this work to more MYSOs can build on the comparative analysis presented here and allow comments on the wider population of MYSOs.

During the timescale of this thesis and in the years to come a variety of instrumentation has come and will come online which will allow improvements upon to this work. MATISSE, the new 4-telescope beam-combining interferometer at the VLTI, serves as MIDI's successor and will improve upon the u-v coverage obtainable for the study of MYSOs and allow the community to move away from visibility studies as the only means of studying massive protostellar environments in the N-band at milliarcsecond resolution. On the theoretical side, radiative hydrodynamical models which include magnetic fields, turbulence and other important effects can be used to model more completely simulate massive protostellar environments. With all these tools combined, the view of massive protostellar environments will be greatly improved in the years to come and so too will the community's understanding of the massive star formation process.

References

Ahmadi, A., Beuther, H., Mottram, J. C., Bosco, F., and CORE Team (2017). Disk properties in high-mass star formation. *Mem. Soc. Astron. Italiana*, 88:763.

Alexander, R. D. and Armitage, P. J. (2007). Dust dynamics during protoplanetary disc clearing. *MNRAS*, 375:500–512.

ALMA Partnership, Brogan, C. L., Pérez, L. M., Hunter, T. R., Dent, W. R. F., Hales, A. S., Hills, R. E., Corder, S., Fomalont, E. B., Vlahakis, C., Asaki, Y., Barkats, D., Hirota, A., Hodge, J. A., Impellizzeri, C. M. V., Kneissl, R., Liuzzo, E., Lucas, R., Marcelino, N., Matsushita, S., Nakanishi, K., Phillips, N., Richards, A. M. S., Toledo, I., Aladro, R., Broguiere, D., Cortes, J. R., Cortes, P. C., Espada, D., Galarza, F., Garcia-Appadoo, D., Guzman-Ramirez, L., Humphreys, E. M., Jung, T., Kameno, S., Laing, R. A., Leon, S., Marconi, G., Mignano, A., Nikolic, B., Nyman, L.-A., Radiszcz, M., Remijan, A., Rodón, J. A., Sawada, T., Takahashi, S., Tilanus, R. P. J., Vila Vilaro, B., Watson, L. C., Wiklind, T., Akiyama, E., Chapillon, E., de Gregorio-Monsalvo, I., Di Francesco, J., Gueth, F., Kawamura, A., Lee, C.-F., Nguyen Luong, Q., Mangum, J., Pietu, V., Sanhueza, P., Saigo, K., Takakuwa, S., Ubach, C., van Kempen, T., Wootten, A., Castro-Carrizo, A., Francke, H., Gallardo, J., Garcia, J., Gonzalez, S., Hill, T., Kaminski, T., Kurono, Y., Liu, H.-Y., Lopez, C., Morales, F., Plarre, K., Schieven, G., Testi, L., Videla, L., Villard, E., Andreani, P., Hibbard, J. E., and Tatematsu, K. (2015). The 2014 ALMA Long Baseline Campaign: First Results from High Angular Resolution Observations toward the HL Tau Region. *ApJ*, 808:L3.

Alvarez, C., Hoare, M., Glindemann, A., and Richichi, A. (2004). Near-IR speckle imaging of massive young stellar objects. *A&A*, 427:505–518.

André, P., Di Francesco, J., Ward-Thompson, D., Inutsuka, S.-I., Pudritz, R. E., and Pineda, J. E. (2014). From Filamentary Networks to Dense Cores in Molecular Clouds: Toward a New Paradigm for Star Formation. *Protostars and Planets VI*, pages 27–51.

André, P., Men'shchikov, A., Bontemps, S., Könyves, V., Motte, F., Schneider, N., Didelon, P., Minier, V., Saraceno, P., Ward-Thompson, D., di Francesco, J., White, G., Molinari, S., Testi, L., Abergel, A., Griffin, M., Henning, T., Royer, P., Merín, B., Vavrek, R., Attard, M., Arzoumanian, D., Wilson, C. D., Ade, P., Aussel, H., Baluteau, J.-P., Benedettini, M., Bernard, J.-P., Blommaert, J. A. D. L., Cambrésy, L., Cox, P., di Giorgio, A., Hargrave, P., Hennemann, M., Huang, M., Kirk, J., Krause, O., Launhardt, R., Leeks, S., Le Pennec, J., Li, J. Z., Martin, P. G., Maury, A., Olofsson, G., Omont, A., Peretto, N., Pezzuto, S., Prusti, T., Roussel, H., Russeil, D., Sauvage, M., Sibthorpe, B., Sicilia-Aguilar, A., Spinoglio, L., Waelkens, C., Woodcraft, A., and Zavagno, A. (2010). From filamentary clouds to

prestellar cores to the stellar IMF: Initial highlights from the Herschel Gould Belt Survey. *A&A*, 518:L102.

Arce, H. G., Shepherd, D., Gueth, F., Lee, C.-F., Bachiller, R., Rosen, A., and Beuther, H. (2007). Molecular Outflows in Low- and High-Mass Star-forming Regions. *Protostars and Planets V*, pages 245–260.

Aspin, C. and Walther, D. M. (1990). Infrared imaging polarimetry of Monoceros R2 IRS. *A&A*, 235:387.

Barsony, M. (1994). *Class 0 Protostars*, volume 65 of *Astronomical Society of the Pacific Conference Series*, page 197.

Barvainis, R. (1992). Dust Reverberation: A Model for the Infrared Variations of Fairall 9. *ApJ*, 400:502.

Bass, M. (1995). Books-Received - Handbook of Optics. *Science*, 267:1195.

Baumgardt, H. and Klessen, R. S. (2011). The role of stellar collisions for the formation of massive stars. *MNRAS*, 413:1810–1818.

Beichman, C. A. (1988). The Infrared Universe Revealed by IRAS. *Astrophysical Letters and Communications*, 27:67.

Beltrán, M. T., Brand, J., Cesaroni, R., Fontani, F., Pezzuto, S., Testi, L., and Molinari, S. (2006). Search for massive protostar candidates in the southern hemisphere. II. Dust continuum emission. *A&A*, 447(1):221–233.

Beltrán, M. T., Cesaroni, R., Neri, R., Codella, C., Furuya, R. S., Testi, L., and Olmi, L. (2005). A detailed study of the rotating toroids in G31.41+0.31 and G24.78+0.08. *A&A*, 435(3):901–925.

Beltrán, M. T. and de Wit, W. J. (2016). Accretion disks in luminous young stellar objects. *A&A Rev.*, 24:6.

Beuther, H., Mottram, J. C., Ahmadi, A., Bosco, F., Linz, H., Henning, T., Klaassen, P., Winters, J. M., Maud, L. T., Kuiper, R., Semenov, D., Gieser, C., Peters, T., Urquhart, J. S., Pudritz, R., Ragan, S. E., Feng, S., Keto, E., Leurini, S., Cesaroni, R., Beltran, M., Palau, A., Sánchez-Monge, Á., Galvan-Madrid, R., Zhang, Q., Schilke, P., Wyrowski, F., Johnston, K. G., Longmore, S. N., Lumsden, S., Hoare, M., Menten, K. M., and Csengeri, T. (2018). Fragmentation and disk formation during high-mass star formation. IRAM NOEMA (Northern Extended Millimeter Array) large program CORE. *A&A*, 617:A100.

Beuther, H., Schilke, P., Gueth, F., McCaughrean, M., Andersen, M., Sridharan, T. K., and Menten, K. M. (2002a). IRAS 05358+3543: Multiple outflows at the earliest stages of massive star formation. *A&A*, 387:931–943.

Beuther, H., Schilke, P., Menten, K. M., Motte, F., Sridharan, T. K., and Wyrowski, F. (2002b). High-Mass Protostellar Candidates. II. Density Structure from Dust Continuum and CS Emission. *ApJ*, 566:945–965.

Bjorkman, J. E. (1997). *Circumstellar Disks*, volume 497, page 239.

Bjorkman, J. E. and Wood, K. (2001). Radiative Equilibrium and Temperature Correction in Monte Carlo Radiation Transfer. *ApJ*, 554:615–623.

Blandford, R. D. and Payne, D. G. (1982). Hydromagnetic flows from accretion disks and the production of radio jets. *MNRAS*, 199:883–903.

Blitz, L. (1993). Giant molecular clouds. In Levy, E. H. and Lunine, J. I., editors, *Protostars and Planets III*, pages 125–161.

Blitz, L. and Shu, F. H. (1980). The origin and lifetime of giant molecular cloud complexes. *ApJ*, 238:148–157.

Boley, P. A., Kraus, S., de Wit, W.-J., Linz, H., van Boekel, R., Henning, T., Lacour, S., Monnier, J. D., Stecklum, B., and Tuthill, P. G. (2016). A multi-wavelength interferometric study of the massive young stellar object IRAS 13481-6124. *A&A*, 586:A78.

Boley, P. A., Linz, H., van Boekel, R., Henning, T., Feldt, M., Kaper, L., Leinert, C., Müller, A., Pascucci, I., Robberto, M., Stecklum, B., Waters, L. B. F. M., and Zinnecker, H. (2013). The VLTI/MIDI survey of massive young stellar objects . Sounding the inner regions around intermediate- and high-mass young stars using mid-infrared interferometry. *A&A*, 558:A24.

Boneberg, D. M., Panić, O., Haworth, T. J., Clarke, C. J., and Min, M. (2016). Determining the mid-plane conditions of circumstellar discs using gas and dust modelling: a study of HD 163296. *MNRAS*, 461:385–401.

Bonnell, I. A., Bate, M. R., Clarke, C. J., and Pringle, J. E. (1997). Accretion and the stellar mass spectrum in small clusters. *MNRAS*, 285:201–208.

Bonnell, I. A., Bate, M. R., Clarke, C. J., and Pringle, J. E. (2001). Competitive accretion in embedded stellar clusters. *MNRAS*, 323:785–794.

Bonnell, I. A., Bate, M. R., and Zinnecker, H. (1998). On the formation of massive stars. *MNRAS*, 298:93–102.

Bosco, F., Beuther, H., Ahmadi, A., Mottram, J. C., Kuiper, R., Linz, H., Maud, L., Winters, J. M., Henning, T., Feng, S., Peters, T., Semenov, D., Klaassen, P. D., Schilke, P., Urquhart, J. S., Beltrán, M. T., Lumsden, S. L., Leurini, S., Moscadelli, L., Cesaroni, R., Sánchez-Monge, Á., Palau, A., Pudritz, R., Wyrowski, F., and Longmore, S. (2019). Fragmentation, rotation, and outflows in the high-mass star-forming region IRAS 23033+5951. A case study of the IRAM NOEMA large program CORE. *A&A*, 629:A10.

Buckle, J. V., Richer, J. S., and Davis, C. J. (2012). The structure of molecular gas associated with NGC 2264: wide-field ^{12}CO and H_2 imaging. *MNRAS*, 423(2):1127–1143.

Bunn, J. C., Hoare, M. G., and Drew, J. E. (1995). Observations of the IR recombination line emission from massive young stellar objects. *MNRAS*, 272:346–354.

Burns, R. A., Handa, T., Nagayama, T., Sunada, K., and Omodaka, T. (2016). H_2O masers in a jet-driven bow shock: episodic ejection from a massive young stellar object. *MNRAS*, 460(1):283–290.

Campbell, B., Persson, S. E., and Matthews, K. (1989). Identification of new young stellar objects associated with IRAS point sources. III - The northern Galactic plane. *AJ*, 98:643–658.

Caratti o Garatti, A., Stecklum, B., Garcia Lopez, R., Eislöffel, J., Ray, T. P., Sanna, A., Cesaroni, R., Walmsley, C. M., Oudmaijer, R. D., de Wit, W. J., Moscadelli, L., Greiner, J., Krabbe, A., Fischer, C., Klein, R., and Ibañez, J. M. (2017). Disk-mediated accretion burst in a high-mass young stellar object. *Nature Physics*, 13:276–279.

Carroll, B. W. and Ostlie, D. A. (1996). *An Introduction to Modern Astrophysics*.

Carruthers, G. R. (1970). Atomic and Molecular Hydrogen in Interstellar Space. *Space Sci. Rev.*, 10:459–482.

Cesaroni, R. (2005). Hot molecular cores. In Cesaroni, R., Felli, M., Churchwell, E., and Walmsley, M., editors, *Massive Star Birth: A Crossroads of Astrophysics*, volume 227 of *IAU Symposium*, pages 59–69.

Cesaroni, R., Beltrán, M. T., Zhang, Q., Beuther, H., and Fallscheer, C. (2011). Dissecting a hot molecular core: the case of G31.41+0.31. *A&A*, 533:A73.

Chini, R., Kreysa, E., Mezger, P. G., and Gemuend, H. P. (1986a). 1.3 MM continuum observations of compact H II regions detected by IRAS I. *A&A*, 154:L8–L11.

Chini, R., Kruegel, E., and Kreysa, E. (1986b). Dust emission spectra from star-forming regions. *A&A*, 167:315–324.

Churchwell, E. (2002). Ultra-Compact HII Regions and Massive Star Formation. *ARA&A*, 40:27–62.

Churchwell, E. (2006). Recent Results from GLIMPSE. In Armus, L. and Reach, W. T., editors, *The Spitzer Space Telescope: New Views of the Cosmos*, volume 357 of *Astronomical Society of the Pacific Conference Series*, pages 116–123.

Churchwell, E., Watson, D. F., Povich, M. S., Taylor, M. G., Babler, B. L., Meade, M. R., Benjamin, R. A., Indebetouw, R., and Whitney, B. A. (2007). The Bubbling Galactic Disk. II. The Inner 20°. *ApJ*, 670:428–441.

Cieza, L. A., Schreiber, M. R., Romero, G. A., Mora, M. D., Merin, B., Swift, J. J., Orellana, M., Williams, J. P., Harvey, P. M., and Evans, Neal J., I. (2010). The Nature of Transition Circumstellar Disks. I. The Ophiuchus Molecular Cloud. *ApJ*, 712:925–941.

Clarke, C. J., Gendrin, A., and Sotomayor, M. (2001). The dispersal of circumstellar discs: the role of the ultraviolet switch. *MNRAS*, 328:485–491.

Cohen, M., Walker, R. G., Carter, B., Hammersley, P., Kidger, M., and Noguchi, K. (1999). Spectral Irradiance Calibration in the Infrared. X. A Self-Consistent Radiometric All-Sky Network of Absolutely Calibrated Stellar Spectra. *AJ*, 117:1864–1889.

Contreras, Y., Schuller, F., Urquhart, J. S., Csengeri, T., Wyrowski, F., Beuther, H., Bontemps, S., Bronfman, L., Henning, T., Menten, K. M., Schilke, P., Walmsley, C. M., Wienen, M., Tackenberg, J., and Linz, H. (2013). ATLASGAL - compact source catalogue: 330° < ℓ < 21°. *A&A*, 549:A45.

Cooper, H. D. B. (2013). *Observational studies of regions of massive star formation*. PhD thesis, University of Leeds.

Cooper, H. D. B., Lumsden, S. L., Oudmaijer, R. D., Hoare, M. G., Clarke, A. J., Urquhart, J. S., Mottram, J. C., Moore, T. J. T., and Davies, B. (2013). The RMS survey: near-IR spectroscopy of massive young stellar objects. *MNRAS*, 430:1125–1157.

Cotera, A. S., Whitney, B. A., Young, E., Wolff, M. J., Wood, K., Povich, M., Schneider, G., Rieke, M., and Thompson, R. (2001). High-Resolution Near-Infrared Images and Models of the Circumstellar Disk in HH 30. *ApJ*, 556(2):958–969.

Crowther, P. A., Caballero-Nieves, S. M., Bostroem, K. A., Maíz Apellániz, J., Schneider, F. R. N., Walborn, N. R., Angus, C. R., Brott, I., Bonanos, A., de Koter, A., de Mink, S. E., Evans, C. J., Gräfener, G., Herrero, A., Howarth, I. D., Langer, N., Lennon, D. J., Puls, J., Sana, H., and Vink, J. S. (2016). The R136 star cluster dissected with Hubble Space Telescope/STIS. I. Far-ultraviolet spectroscopic census and the origin of He II λ1640 in young star clusters. *MNRAS*, 458:624–659.

Cunningham, A. J., Klein, R. I., Krumholz, M. R., and McKee, C. F. (2011). Radiation-hydrodynamic Simulations of Massive Star Formation with Protostellar Outflows. *ApJ*, 740:107.

Currie, M. J., Berry, D. S., Jenness, T., Gibb, A. G., Bell, G. S., and Draper, P. W. (2014). Starlink Software in 2013. In Manset, N. and Forshay, P., editors, *Astronomical Data Analysis Software and Systems XXIII*, volume 485, page 391.

Cutri, R. M. and et al. (2012). VizieR Online Data Catalog: WISE All-Sky Data Release (Cutri+ 2012). *VizieR Online Data Catalog*, page II/311.

D'Alessio, P., Cantö, J., Calvet, N., and Lizano, S. (1998). Accretion Disks around Young Objects. I. The Detailed Vertical Structure. *ApJ*, 500(1):411–427.

Damiani, F., Prisinzano, L., Micela, G., and Sciortino, S. (2019). Wide-area photometric and astrometric (Gaia DR2) study of the young cluster NGC 6530. *A&A*, 623:A25.

Davies, B., Lumsden, S. L., Hoare, M. G., Oudmaijer, R. D., and de Wit, W.-J. (2010). The circumstellar disc, envelope and bipolar outflow of the massive young stellar object W33A. *MNRAS*, 402(3):1504–1515.

De Buizer, J. M. (2006). The Remarkable Mid-Infrared Jet of the Massive Young Stellar Object G35.20-0.74. *ApJ*, 642:L57–L60.

De Buizer, J. M., Liu, M., Tan, J. C., Zhang, Y., Beltrán, M. T., Shuping, R., Staff, J. E., Tanaka, K. E. I., and Whitney, B. (2017). The SOFIA Massive (SOMA) Star Formation Survey. I. Overview and First Results. *ApJ*, 843(1):33.

De Buizer, J. M., Piña, R. K., and Telesco, C. M. (2000). Mid-Infrared Imaging of Star-forming Regions Containing Methanol Masers. *ApJS*, 130:437–461.

de Wit, W. J., Hoare, M. G., Fujiyoshi, T., Oudmaijer, R. D., Honda, M., Kataza, H., Miyata, T., Okamoto, Y. K., Onaka, T., Sako, S., and Yamashita, T. (2009). Resolved 24.5 micron emission from massive young stellar objects. *A&A*, 494:157–178.

de Wit, W. J., Hoare, M. G., Oudmaijer, R. D., and Lumsden, S. L. (2010). The origin of mid-infrared emission in massive young stellar objects: multi-baseline VLTI observations of W33A. *A&A*, 515:A45.

de Wit, W. J., Hoare, M. G., Oudmaijer, R. D., and Mottram, J. C. (2007). VLTI/MIDI 10 μm Interferometry of the Forming Massive Star W33A. *ApJ*, 671:L169–L172.

de Wit, W. J., Hoare, M. G., Oudmaijer, R. D., Nürnberger, D. E. A., Wheelwright, H. E., and Lumsden, S. L. (2011). Mid-infrared interferometry towards the massive young stellar object CRL 2136: inside the dust rim. *A&A*, 526:L5.

Desai, K. M., Steiman-Cameron, T. Y., Michael, S., Cai, K., and Durisen, R. H. (2019). A 3D hydrodynamics study of gravitational instabilities in a young circumbinary disc. *MNRAS*, 483(2):2347–2361.

Di Francesco, J., Johnstone, D., Kirk, H., MacKenzie, T., and Ledwosinska, E. (2008). The SCUBA Legacy Catalogues: Submillimeter-Continuum Objects Detected by SCUBA. *ApJS*, 175:277–295.

Dobbs, C. L., Bonnell, I. A., and Clark, P. C. (2005). Centrally condensed turbulent cores: massive stars or fragmentation? *MNRAS*, 360:2–8.

Draine, B. T. and Li, A. (2007). Infrared Emission from Interstellar Dust. IV. The Silicate-Graphite-PAH Model in the Post-Spitzer Era. *ApJ*, 657(2):810–837.

Dullemond, C. P. and Dominik, C. (2004). Flaring vs. self-shadowed disks: The SEDs of Herbig Ae/Be stars. *A&A*, 417:159–168.

Dullemond, C. P. and Monnier, J. D. (2010). The Inner Regions of Protoplanetary Disks. *ARA&A*, 48:205–239.

Egan, M. P., Price, S. D., Kraemer, K. E., Mizuno, D. R., Carey, S. J., Wright, C. O., Engelke, C. W., Cohen, M., and Gugliotti, M. G. (2003). VizieR Online Data Catalog: MSX6C Infrared Point Source Catalog. The Midcourse Space Experiment Point Source Catalog Version 2.3 (October 2003). *VizieR Online Data Catalog*, page V/114.

Egan, M. P., Shipman, R. F., Price, S. D., Carey, S. J., Clark, F. O., and Cohen, M. (1998). A Population of Cold Cores in the Galactic Plane. *ApJ*, 494:L199–L202.

Espaillat, C., D'Alessio, P., Hernández, J., Nagel, E., Luhman, K. L., Watson, D. M., Calvet, N., Muzerolle, J., and McClure, M. (2010). Unveiling the Structure of Pre-transitional Disks. *ApJ*, 717:441–457.

Espaillat, C., Muzerolle, J., Najita, J., Andrews, S., Zhu, Z., Calvet, N., Kraus, S., Hashimoto, J., Kraus, A., and D'Alessio, P. (2014). An Observational Perspective of Transitional Disks. *Protostars and Planets VI*, pages 497–520.

Evans, Neal J., I., Allen, L. E., Blake, G. A., Boogert, A. C. A., Bourke, T., Harvey, P. M., Kessler, J. E., Koerner, D. W., Lee, C. W., Mundy, L. G., Myers, P. C., Padgett, D. L., Pontoppidan, K., Sargent, A. I., Stapelfeldt, K. R., van Dishoeck, E. F., Young, C. H., and Young, K. E. (2003). From Molecular Cores to Planet-forming Disks: An SIRTF Legacy Program. *PASP*, 115(810):965–980.

Faúndez, S., Bronfman, L., Garay, G., Chini, R., Nyman, L.-Å., and May, J. (2004). SIMBA survey of southern high-mass star forming regions. I. Physical parameters of the 1.2 mm/IRAS sources. *A&A*, 426:97–103.

Fazio, G., Ashby, M., Ashby, M. L. N., Barmby, P., Chakrabarti, S., Gonzalez-Alfonso, E., Huang, J.-S., Madden, S., Noeske, K., Pahre, M., Papovich, C., Robitaille, T., Smith, H., Sturm, E., Surace, J., Wang, Z., Whitney, B., Willner, S., Wu, H., and Zezas, A. (2008). The Spitzer/IRAC Star Formation Reference Survey.

Fedele, D., Carney, M., Hogerheijde, M. R., Walsh, C., Miotello, A., Klaassen, P., Bruderer, S., Henning, T., and van Dishoeck, E. F. (2017). ALMA unveils rings and gaps in the protoplanetary system <ASTROBJ>HD 169142</ASTROBJ>: signatures of two giant protoplanets. *A&A*, 600:A72.

Feldt, M., Pascucci, I., Chesneau, O., Apai, D., Henning, T., Leinert, C., Linz, H., Men'shchikov, A., and Stecklum, B. (2008). Interferometry of M8E-IR with MIDI - Resolving the Dust Emission. In Richichi, A., Delplancke, F., Paresce, F., and Chelli, A., editors, *The Power of Optical/IR Interferometry: Recent Scientific Results and 2nd Generation*, page 263.

Ferreira, J. and Pelletier, G. (1995). Magnetized accretion-ejection structures. III. Stellar and extragalactic jets as weakly dissipative disk outflows. *A&A*, 295:807.

Fujisawa, K., Yonekura, Y., Sugiyama, K., Horiuchi, H., Hayashi, T., Hachisuka, K., Matsumoto, N., and Niinuma, K. (2015). A flare of methanol maser in S255. *The Astronomer's Telegram*, 8286.

Galván-Madrid, R., Zhang, Q., Keto, E., Ho, P. T. P., Zapata, L. A., Rodríguez, L. F., Pineda, J. E., and Vázquez-Semadeni, E. (2010). From the Convergence of Filaments to Disk-outflow Accretion: Massive Star Formation in W33A. *ApJ*, 725(1):17–28.

Garufi, A., Meeus, G., Benisty, M., Quanz, S. P., Banzatti, A., Kama, M., Canovas, H., Eiroa, C., Schmid, H. M., Stolker, T., Pohl, A., Rigliaco, E., Ménard, F., Meyer, M. R., van Boekel, R., and Dominik, C. (2017). Evolution of protoplanetary disks from their taxonomy in scattered light: Group I vs. Group II. *A&A*, 603:A21.

Giannakopoulou, J., Mitchell, G. F., Hasegawa, T. I., Matthews, H. E., and Maillard, J.-P. (1997). The Star-forming Core of Monoceros R2. *ApJ*, 487(1):346–364.

Gibb, E. L., Whittet, D. C. B., Boogert, A. C. A., and Tielens, A. G. G. M. (2004). Interstellar Ice: The Infrared Space Observatory Legacy. *ApJS*, 151:35–73.

Gonzalez, J. F., Laibe, G., and Maddison, S. T. (2017). Self-induced dust traps: overcoming planet formation barriers. *MNRAS*, 467(2):1984–1996.

Grellmann, R., Ratzka, T., Kraus, S., Linz, H., Preibisch, T., and Weigelt, G. (2011). Mid-infrared interferometry of the massive young stellar object NGC 2264 IRS 1. *A&A*, 532:A109.

Guertler, J., Henning, T., Kruegel, E., and Chini, R. (1991). Dust continuum radiation from luminous young stellar objects. *A&A*, 252:801–811.

Haguenauer, P., Alonso, J., Bourget, P., Brillant, S., Gitton, P., Guisard, S., Poupar, S., Schuhler, N., Abuter, R., Andolfato, L., Blanchard, G., Berger, J.-P., Cortes, A., Dérie, F., Delplancke, F., Di Lieto, N., Dupuy, C., Gilli, B., Glindemann, A., Guniat, S., Huedepohl, G., Kaufer, A., Le Bouquin, J.-B., Lévque, S., Ménardi, S., Mérand, A., Morel, S., Percheron, I., Phan Duc, T., Pino, A., Ramirez, A., Rengaswamy, S., Richichi, A., Rivinius, T., Sahlmann, J., Schoeller, M., Schmid, C., Stefl, S., Valdes, G., van Belle, G., Wehner, S., and Wittkowski, M. (2010). The very large telescope Interferometer: 2010 edition. In *Optical and Infrared Interferometry II*, volume 7734 of *Proc. SPIE*, page 773404.

Harries, T. J., Douglas, T. A., and Ali, A. (2017). Radiation-hydrodynamical simulations of massive star formation using Monte Carlo radiative transfer - II. The formation of a 25 solar-mass star. *MNRAS*, 471:4111–4120.

Harsono, D., Bjerkeli, P., van der Wiel, M. H. D., Ramsey, J. P., Maud, L. T., Kristensen, L. E., and Jørgensen, J. K. (2018). Evidence for the start of planet formation in a young circumstellar disk. *Nature Astronomy*, 2:646–651.

Hartmann, L. (1998). Accretion processes in star formation. *Cambridge Astrophysics Series*, 32.

Harvey, P. M., Butner, H. M., Colomé, C., Di Francesco, J., and Smith, B. J. (2000). Far-Infrared Observations of AFGL 2136: Simple Dust Toroid Models. *ApJ*, 534(2):846–853.

Harvey, P. M., Campbell, M. F., and Hoffmann, W. F. (1977a). Far-infrared emission from compact sources in NGC 2264 and the Rosette nebula. *ApJ*, 215:151–154.

Harvey, P. M., Campbell, M. F., and Hoffmann, W. F. (1977b). Far-infrared emission from compact sources in NGC 2264 and the Rosette nebula. *ApJ*, 215:151–154.

Heckman, T. M., Armus, L., and Miley, G. K. (1990). On the Nature and Implications of Starburst-driven Galactic Superwinds. *ApJS*, 74:833.

Henning, T., Chini, R., and Pfau, W. (1992). Submm/mm observations of the Monoceros R2 cloud core. *A&A*, 263:285–291.

Henning, T. and Guertler, J. (1986). BN objects - A class of very young and massive stars. *Ap&SS*, 128:199–215.

Henshaw, J. D., Caselli, P., Fontani, F., Jiménez-Serra, I., Tan, J. C., Longmore, S. N., Pineda, J. E., Parker, R. J., and Barnes, A. T. (2016). Investigating the structure and fragmentation of a highly filamentary IRDC. *MNRAS*, 463(1):146–169.

Henshaw, J. D., Ginsburg, A., Haworth, T. J., Longmore, S. N., Kruijssen, J. M. D., Mills, E. A. C., Sokolov, V., Walker, D. L., Barnes, A. T., Contreras, Y., Bally, J., Battersby, C., Beuther, H., Butterfield, N., Dale, J. E., Henning, T., Jackson, J. M., Kauffmann, J., Pillai, T., Ragan, S., Riener, M., and Zhang, Q. (2019). 'The Brick' is not a brick: a comprehensive study of the structure and dynamics of the central molecular zone cloud G0.253+0.016. *MNRAS*, 485(2):2457–2485.

Herbst, W. and Racine, R. (1976). R-associations. V. Monoceros R2. *AJ*, 81:840–844.

Hindson, L., Thompson, M. A., Urquhart, J. S., Clark, J. S., and Davies, B. (2010). The G305 star-forming complex: wide-area molecular mapping of NH_3 and H_2O masers. *MNRAS*, 408:1438–1451.

Hoare, M. G. (2005). Ultra-Compact H II Regions. *Ap&SS*, 295:203–215.

Hoffmeister, V. H., Chini, R., Scheyda, C. M., Nürnberger, D., Vogt, N., and Nielbock, M. (2006). 2.3 μm CO emission and absorption from young high-mass stars in M 17. *A&A*, 457(3):L29–L32.

Hollenbach, D. and Gorti, U. (2005). The Photoevaporation of Protoplanetary Disks by Their Central Stars. In *Protostars and Planets V Posters*, volume 1286, page 8433.

Hosokawa, T. and Omukai, K. (2009). Evolution of Massive Protostars with High Accretion Rates. *ApJ*, 691:823–846.

Hosokawa, T., Yorke, H. W., and Omukai, K. (2010). Evolution of Massive Protostars Via Disk Accretion. *ApJ*, 721:478–492.

Ilee, J. D., Cyganowski, C. J., Brogan, C. L., Hunter, T. R., Forgan, D. H., Haworth, T. J., Clarke, C. J., and Harries, T. J. (2018). G11.92-0.61 MM 1: A Fragmented Keplerian Disk Surrounding a Proto-O Star. *ApJ*, 869:L24.

Ilee, J. D., Cyganowski, C. J., Nazari, P., Hunter, T. R., Brogan, C. L., Forgan, D. H., and Zhang, Q. (2016). G11.92-0.61 MM1: a Keplerian disc around a massive young proto-O star. *MNRAS*, 462:4386–4401.

Ilee, J. D., Wheelwright, H. E., Oudmaijer, R. D., de Wit, W. J., Maud, L. T., Hoare, M. G., Lumsden, S. L., Moore, T. J. T., Urquhart, J. S., and Mottram, J. C. (2013). CO bandhead emission of massive young stellar objects: determining disc properties. *MNRAS*, 429:2960–2973.

Immer, K., Reid, M. J., Menten, K. M., Brunthaler, A., and Dame, T. M. (2013). Trigonometric parallaxes of massive star forming regions: G012.88+0.48 and W33. *A&A*, 553:A117.

Isella, A. (2007). High angular resolution observations of circumstellar disks. *Mem. Soc. Astron. Italiana*, 78:677.

Ishihara, D., Onaka, T., Kataza, H., Salama, A., Alfageme, C., Cassatella, A., Cox, N., Garcia-Lario, P., Stephenson, C., Cohen, M., Fujishiro, N., Fujiwara, H., Hasegawa, S., Ita, Y., Kim, W., Matsuhara, H., Murakami, H., Muller, T. G., Nakagawa, T., Ohyama, Y., Oyabu, S., Pyo, J., Sakon, I., Shibai, H., Takita, S., Tanab, T., Uemizu, K., Ueno, M., Usui, F., Wada, T., Watarai, H., Yamamura,

I., and Yamauchi, C. (2010). VizieR Online Data Catalog: AKARI/IRC mid-IR all-sky Survey (ISAS/JAXA, 2010). *VizieR Online Data Catalog*, 2297.

Itoh, Y., Tamura, M., Suto, H., Hayashi, S. S., Murakawa, K., Oasa, Y., Nakajima, Y., Kaifu, N., Kosugi, G., Usuda, T., and Doi, Y. (2001). Near-Infrared Observations of S 255-2 : The Heart of a Massive YSO Cluster. *PASJ*, 53(3):495–500.

Ivezic, Z. and Elitzur, M. (1997). Self-similarity and scaling behaviour of infrared emission from radiatively heated dust - I. Theory. *MNRAS*, 287(4):799–811.

Jackson, J. M., Finn, S. C., Chambers, E. T., Rathborne, J. M., and Simon, R. (2010). The "Nessie" Nebula: Cluster Formation in a Filamentary Infrared Dark Cloud. *ApJ*, 719(2):L185–L189.

Jaffe, W. J. (2004). Coherent fringe tracking and visibility estimation for MIDI. In Traub, W. A., editor, *New Frontiers in Stellar Interferometry*, volume 5491 of *Proc. SPIE*, page 715.

Johnson, H. L. (1963). *Photometric Systems*, page 204.

Johnston, K. G., Robitaille, T. P., Beuther, H., Linz, H., Boley, P., Kuiper, R., Keto, E., Hoare, M. G., and van Boekel, R. (2015). A Keplerian-like Disk around the Forming O-type Star AFGL 4176. *ApJ*, 813:L19.

Johnston, K. G., Shepherd, D. S., Robitaille, T. P., and Wood, K. (2013). The standard model of low-mass star formation applied to massive stars: a multi-wavelength picture of AFGL 2591. *A&A*, 551:A43.

Kama, M., Bruderer, S., van Dishoeck, E. F., Hogerheijde, M., Folsom, C. P., Miotello, A., Fedele, D., Belloche, A., Güsten, R., and Wyrowski, F. (2016). Volatile-carbon locking and release in protoplanetary disks. A study of TW Hya and HD 100546. *A&A*, 592:A83.

Kamezaki, T., Imura, K., Omodaka, T., Hand a, T., Tsuboi, Y., Nagayama, T., Hirota, T., Sunada, K., Kobayashi, H., Chibueze, J. O., Kawai, E., and Nakano, M. (2014). Annual Parallax Determination toward a New X-Ray-emitting Class 0 Candidate with the Water Maser in the NGC 2264 Star-forming Region. *ApJS*, 211(2):18.

Kashi, A. and Soker, N. (2010). Periastron Passage Triggering of the 19th Century Eruptions of Eta Carinae. *ApJ*, 723:602–611.

Kastner, J. H., Weintraub, D. A., and Aspin, C. (1992). The Juggler: A Three-lobed Near-Infrared Reflection Nebula toward CRL 2136 = OH 17.6+0.2. *ApJ*, 389:357.

Käufl, H. U., Kerber, F., Asmus, D., Baksai, P., Di Lieto, N., Duhoux, P., Heikamp, S., Hummel, C., Ives, D., Jakob, G., Kirchbauer, J.-P., Mehrgan, L., Momany, Y., Pantin, E., Pozna, E., Riquelme, M., Sandrock, S., Siebenmorgen, R., Smette, A., Stegmeier, J., Taylor, J., Tristram, K., Valdes, G., van den Ancker, M., Weilenmann, U., and Wolff, B. (2015). The Return of the Mid-infrared to the VLT: News from the VISIR Upgrade. *The Messenger*, 159:15–18.

Kaufmann, W. J. (1991). *Universe*.

Kennicutt, R. C. (2005). The role of massive stars in astrophysics. In Cesaroni, R., Felli, M., Churchwell, E., and Walmsley, M., editors, *Massive Star Birth: A Crossroads of Astrophysics*, volume 227 of *IAU Symposium*, pages 3–11.

Kim, S.-H., Martin, P. G., and Hendry, P. D. (1994). The size distribution of interstellar dust particles as determined from extinction. *ApJ*, 422:164–175.

Kolpak, M. A. (2003). *The large-scale galactic structure of star formation tracers*. PhD thesis, BOSTON UNIVERSITY.

Königl, A., Romanova, M. M., and Lovelace, R. V. E. (2011). Are the outflows in FU Orionis systems driven by the stellar magnetic field? *MNRAS*, 416(1):757–766.

Königl, A., Salmeron, R., and Wardle, M. (2010). Wind-driving protostellar accretion discs - I. Formulation and parameter constraints. *MNRAS*, 401(1):479–499.

Koumpia, E., Ababakr, K. M., de Wit, W. J., Oudmaijer, R. D., Caratti o Garatti, A., Boley, P., Linz, H., Kraus, S., Vink, J. S., and Le Bouquin, J. B. (2019). Resolving the MYSO binaries PDS 27 and PDS 37 with VLTI/PIONIER. *Astronomy and Astrophysics*, 623:L5.

Kraus, S., Hofmann, K.-H., Menten, K. M., Schertl, D., Weigelt, G., Wyrowski, F., Meilland, A., Perraut, K., Petrov, R., Robbe-Dubois, S., Schilke, P., and Testi, L. (2010). A hot compact dust disk around a massive young stellar object. *Nature*, 466:339–342.

Kraus, S., Kluska, J., Kreplin, A., Bate, M., Harries, T. J., Hofmann, K. H., Hone, E., Monnier, J. D., Weigelt, G., Anugu, A., de Wit, W. J., and Wittkowski, M. (2017). A High-mass Protobinary System with Spatially Resolved Circumstellar Accretion Disks and Circumbinary Disk. *ApJ*, 835(1):L5.

Krishnan, V., Ellingsen, S. P., Reid, M. J., Bignall, H. E., McCallum, J., Phillips, C. J., Reynolds, C., and Stevens, J. (2017). Parallaxes of 6.7-GHz methanol masers towards the G 305.2 high-mass star formation region. *MNRAS*, 465:1095–1105.

Krumholz, M. R. (2006). High Mass Star Formation by Gravitational Collapse of Massive Cores. *ArXiv Astrophysics e-prints*.

Krumholz, M. R., Bate, M. R., Arce, H. G., Dale, J. E., Gutermuth, R., Klein, R. I., Li, Z.-Y., Nakamura, F., and Zhang, Q. (2014). Star Cluster Formation and Feedback. *Protostars and Planets VI*, pages 243–266.

Krumholz, M. R., Klein, R. I., and McKee, C. F. (2007). Radiation-Hydrodynamic Simulations of Collapse and Fragmentation in Massive Protostellar Cores. *ApJ*, 656:959–979.

Krumholz, M. R., Klein, R. I., McKee, C. F., Offner, S. S. R., and Cunningham, A. J. (2009). The Formation of Massive Star Systems by Accretion. *Science*, 323:754.

Krumholz, M. R., McKee, C. F., and Klein, R. I. (2005). How Protostellar Outflows Help Massive Stars Form. *ApJ*, 618:L33–L36.

Kuiper, R., Klahr, H., Beuther, H., and Henning, T. (2011). Three-dimensional Simulation of Massive Star Formation in the Disk Accretion Scenario. *ApJ*, 732(1):20.

Kuiper, R. and Yorke, H. W. (2013). On the Simultaneous Evolution of Massive Protostars and Their Host Cores. *ApJ*, 772(1):61.

Kuiper, R., Yorke, H. W., and Turner, N. J. (2015). Protostellar Outflows and Radiative Feedback from Massive Stars. *ApJ*, 800(2):86.

Kurtz, S. (2005). Hypercompact HII regions. In Cesaroni, R., Felli, M., Churchwell, E., and Walmsley, M., editors, *Massive Star Birth: A Crossroads of Astrophysics*, volume 227 of *IAU Symposium*, pages 111–119.

Labeyrie, A. (1975). Interference fringes obtained on Vega with two optical telescopes. *ApJ*, 196:L71–L75.

Lada, C. J. and Lada, E. A. (2003). Embedded Clusters in Molecular Clouds. *ARA&A*, 41:57–115.

Lagage, P. O., Pel, J. W., Authier, M., Belorgey, J., Claret, A., Doucet, C., Dubreuil, D., Durand, G., Elswijk, E., Girardot, P., Käufl, H. U., Kroes, G., Lortholary, M., Lussignol, Y., Marchesi, M., Pantin, E., Peletier, R., Pirard, J.-F., Pragt, J., Rio, Y., Schoenmaker, T., Siebenmorgen, R., Silber, A., Smette, A., Sterzik, M., and Veyssiere, C. (2004). Successful Commissioning of VISIR: The Mid-Infrared VLT Instrument. *The Messenger*, 117:12–16.

Lawrence, A., Warren, S. J., Almaini, O., Edge, A. C., Hambly, N. C., Jameson, R. F., Lucas, P., Casali, M., Adamson, A., Dye, S., Emerson, J. P., Foucaud, S., Hewett, P., Hirst, P., Hodgkin, S. T., Irwin, M. J., Lodieu, N., McMahon, R. G., Simpson, C., Smail, I., Mortlock, D., and Folger, M. (2007). The UKIRT Infrared Deep Sky Survey (UKIDSS). *MNRAS*, 379(4):1599–1617.

Leinert, C. (2003). MIDI on the VLTI: Interferometry at 10μm. In *GENIE - DARWIN Workshop - Hunting for Planets*, volume 522 of *ESA Special Publication*, page 27.

Leinert, C. (2004). Scientific observations with MIDI on the VLTI: present and future. In *New Frontiers in Stellar Interferometry*, volume 5491, page 19.

Leitherer, C. (1994). Massive Stars in Starburst Galaxies and the Origin of Galactic Superwinds. In Klare, G., editor, *Reviews in Modern Astronomy*, volume 7 of *Reviews in Modern Astronomy*, pages 73–102.

Levenson, N. A., Sirocky, M. M., Hao, L., Spoon, H. W. W., Marshall, J. A., Elitzur, M., and Houck, J. R. (2007). Deep Mid-Infrared Silicate Absorption as a Diagnostic of Obscuring Geometry toward Galactic Nuclei. *ApJ*, 654:L45–L48.

Linz, H., Henning, T., Feldt, M., Pascucci, I., van Boekel, R., Men'shchikov, A., Stecklum, B., Chesneau, O., Ratzka, T., Quanz, S. P., Leinert, C., Waters, L. B. F. M., and Zinnecker, H. (2009). Mid-infrared interferometry of massive young stellar objects. I. VLTI and Subaru observations of the enigmatic object M8E-IR. *A&A*, 505:655–661.

Linz, H., Stecklum, B., Follert, R., Henning, T., van Boekel, R., Men'shchikov, A., Pascucci, I., and Feldt, M. (2008). Mid-infrared interferometry of massive young stellar objects. In *Journal of Physics Conference Series*, volume 131, page 012024.

Liu, M., Tan, J. C., De Buizer, J. M., Zhang, Y., Beltrán, M. T., Staff, J. E., Tanaka, K. E. I., Whitney, B., and Rosero, V. (2019). The SOFIA Massive (SOMA) Star Formation Survey. II. High Luminosity Protostars. *arXiv e-prints, 901.01958, ApJ, submitted*.

Longmore, S. N., Burton, M. G., Minier, V., and Walsh, A. J. (2006). Mid-infrared source multiplicity within hot molecular cores traced by methanol masers. *MNRAS*, 369(3):1196–1200.

Lorén-Aguilar, P. and Bate, M. R. (2016). Toroidal vortices as a solution to the dust migration problem. *MNRAS*, 457(1):L54–L58.

Lucy, L. B. (1999). Computing radiative equilibria with Monte Carlo techniques. *A&A*, 344:282–288.

Lumsden, S. L., Hoare, M. G., Oudmaijer, R. D., and Richards, D. (2002). The population of the Galactic plane as seen by MSX. *MNRAS*, 336:621–636.

Lumsden, S. L., Hoare, M. G., Urquhart, J. S., Oudmaijer, R. D., Davies, B., Mottram, J. C., Cooper, H. D. B., and Moore, T. J. T. (2013). The Red MSX Source Survey: The Massive Young Stellar Population of Our Galaxy. *ApJS*, 208:11.

Lynden-Bell, D. and Pringle, J. E. (1974). The evolution of viscous discs and the origin of the nebular variables. *MNRAS*, 168:603–637.

Machida, M. N. (2017). Protostellar Jets and Outflows in low-mass star formation. *arXiv e-prints*.

Maddalena, R. J. and Thaddeus, P. (1985). A large, cold and unusual molecular cloud in Monoceros. *ApJ*, 294:231–237.

Manara, C. F., Morbidelli, A., and Guillot, T. (2018). Why do protoplanetary disks appear not massive enough to form the known exoplanet population? *A&A*, 618:L3.

Maud, L. T., Cesaroni, R., Kumar, M. S. N., Rivilla, V. M., Ginsburg, A., Klaassen, P. D., Harsono, D., Sánchez-Monge, Á., Ahmadi, A., Allen, V., Beltrán, M. T., Beuther, H., Galván-Madrid, R., Goddi, C., Hoare, M. G., Hogerheijde, M. R., Johnston, K. G., Kuiper, R., Moscadelli, L., Peters, T., Testi, L., van der Tak, F. F. S., and de Wit, W. J. (2019). Substructures in the Keplerian disc around the O-type (proto-)star G17.64+0.16. *A&A*, 627:L6.

Maud, L. T., Cesaroni, R., Kumar, M. S. N., van der Tak, F. F. S., Allen, V., Hoare, M. G., Klaassen, P. D., Harsono, D., Hogerheijde, M. R., Sánchez-Monge, Á., Schilke, P., Ahmadi, A., Beltrán, M. T., Beuther, H., Csengeri, T., Etoka, S., Fuller, G., Galván-Madrid, R., Goddi, C., Henning, T., Johnston, K. G., Kuiper, R., Lumsden, S., Moscadelli, L., Mottram, J. C., Peters, T., Rivilla, V. M., Testi, L., Vig, S., de Wit, W. J., and Zinnecker, H. (2018). Chasing discs around O-type (proto)stars. ALMA evidence for an SiO disc and disc wind from G17.64+0.16. *A&A*, 620:A31.

Maud, L. T., Hoare, M. G., Galván-Madrid, R., Zhang, Q., de Wit, W. J., Keto, E., Johnston, K. G., and Pineda, J. E. (2017a). The ALMA view of W33A: a spiral filament feeding the candidate disc in MM1-Main. *MNRAS*, 467(1):L120–L124.

Maud, L. T., Hoare, M. G., Galván-Madrid, R., Zhang, Q., de Wit, W. J., Keto, E., Johnston, K. G., and Pineda, J. E. (2017b). The ALMA view of W33A: a spiral filament feeding the candidate disc in MM1-Main. *MNRAS*, 467:L120–L124.

McKee, C. F. and Tan, J. C. (2003). The Formation of Massive Stars from Turbulent Cores. *ApJ*, 585(2):850–871.

Meeus, G., Waters, L. B. F. M., Bouwman, J., van den Ancker, M. E., Waelkens, C., and Malfait, K. (2001). ISO spectroscopy of circumstellar dust in 14 Herbig Ae/Be systems: Towards an understanding of dust processing. *A&A*, 365:476–490.

Menten, K. M. and van der Tak, F. F. S. (2004). Very compact radio emission from high-mass protostars. I. CRL 2136: Continuum and water maser observations. *A&A*, 414:289–298.

Merello, M., Evans, Neal J., I., Shirley, Y. L., Rosolowsky, E., Ginsburg, A., Bally, J., Battersby, C., and Dunham, M. M. (2015). The Bolocam Galactic Plane Survey. XI. Temperatures and Substructure of Galactic Clumps Based On 350 μM Observations. *ApJS*, 218(1):1.

Meyer, D. M.-A., Kuiper, R., Kley, W., Johnston, K. G., and Vorobyov, E. (2018). Forming spectroscopic massive protobinaries by disc fragmentation. *MNRAS*, 473:3615–3637.

Mezger, P. G., Chini, R., Kreysa, E., Wink, J. E., and Salter, C. J. (1988). Dust emission at submillimeter wavelengths from cloud cores and protostellar condensations in NGC 2024 and S 255IR. *A&A*, 191:44–56.

Michelson, A. A. and Pease, F. G. (1921). Measurement of the Diameter of α Orionis with the Interferometer. *ApJ*, 53.

Minchin, N. R., Hough, J. H., Burton, M. G., and Yamashita, T. (1991). Near-infrared imaging polarimetry of bipolar nebulae - IV. GL 490, GL 2789 and GL 2136. *MNRAS*, 251:522–528.

Minniti, D., Lucas, P. W., Emerson, J. P., Saito, R. K., Hempel, M., Pietrukowicz, P., Ahumada, A. V., Alonso, M. V., Alonso-Garcia, J., Arias, J. I., Bandyopadhyay, R. M., Barbá, R. H., Barbuy, B., Bedin, L. R., Bica, E., Borissova, J., Bronfman, L., Carraro, G., Catelan, M., Clariá, J. J., Cross, N., de Grijs, R., Dékány, I., Drew, J. E., Fariña, C., Feinstein, C., Fernández Lajús, E., Gamen, R. C., Geisler, D., Gieren, W., Goldman, B., Gonzalez, O. A., Gunthardt, G., Gurovich, S., Hambly, N. C., Irwin, M. J., Ivanov, V. D., Jordán, A., Kerins, E., Kinemuchi, K., Kurtev, R., López-Corredoira, M., Maccarone, T., Masetti, N., Merlo, D., Messineo, M., Mirabel, I. F., Monaco, L., Morelli, L., Padilla, N., Palma, T., Parisi, M. C., Pignata, G., Rejkuba, M., Roman-Lopes, A., Sale, S. E., Schreiber, M. R., Schröder, A. C., Smith, M., , Jr., L. S., Soto, M., Tamura, M., Tappert, C., Thompson, M. A., Toledo, I., Zoccali, M., and Pietrzynski, G. (2010). VISTA Variables in the Via Lactea (VVV): The public ESO near-IR variability survey of the Milky Way. *New A*, 15:433–443.

Mitchell, G. F., Maillard, J. P., and Hasegawa, T. I. (1991). Episodic Outflows from High-Mass Protostars. *ApJ*, 371:342.

Molinari, S., Brand, J., Cesaroni, R., and Palla, F. (1996). A search for precursors of ultracompact HII regions in a sample of luminous IRAS sources. I. Association with ammonia cores. *A&A*, 308:573–587.

Molinari, S., Brand, J., Cesaroni, R., Palla, F., and Palumbo, G. G. C. (1998). A search for precursors of ultracompact H II regions in a sample of luminous IRAS sources. II. VLA observations. *A&A*, 336:339–351.

Mottram, J. C., Hoare, M. G., Davies, B., Lumsden, S. L., Oudmaijer, R. D., Urquhart, J. S., Moore, T. J. T., Cooper, H. D. B., and Stead, J. J. (2011a). The RMS Survey: The Luminosity Functions and Timescales of Massive Young Stellar Objects and Compact H II Regions. *ApJ*, 730:L33.

Mottram, J. C., Hoare, M. G., Lumsden, S. L., Oudmaijer, R. D., Urquhart, J. S., Sheret, T. L., Clarke, A. J., and Allsopp, J. (2007). The RMS survey: mid-infrared observations of candidate massive YSOs in the southern hemisphere. *A&A*, 476:1019–1111.

Mottram, J. C., Hoare, M. G., Urquhart, J. S., Lumsden, S. L., Oudmaijer, R. D., Robitaille, T. P., Moore, T. J. T., Davies, B., and Stead, J. (2011b). The Red MSX Source survey: the bolometric fluxes and luminosity distributions of young massive stars. *A&A*, 525:A149.

Mottram, J. C., Hoare, M. G., Urquhart, J. S., Lumsden, S. L., Oudmaijer, R. D., Robitaille, T. P., Moore, T. J. T., Davies, B., and Stead, J. (2011c). The Red MSX Source survey: the bolometric fluxes and luminosity distributions of young massive stars. *A&A*, 525:A149.

Mottram, J. C., Hoare, M. G., Urquhart, J. S., Lumsden, S. L., Oudmaijer, R. D., Robitaille, T. P., Moore, T. J. T., Davies, B., and Stead, J. (2011d). The Red MSX Source survey: the bolometric fluxes and luminosity distributions of young massive stars. *A&A*, 525:A149.

Mueller, K. E., Shirley, Y. L., Evans, Neal J., I., and Jacobson, H. R. (2002). The Physical Conditions for Massive Star Formation: Dust Continuum Maps and Modeling. *ApJS*, 143(2):469–497.

Mulders, G. D. and Dominik, C. (2012). Probing the turbulent mixing strength in protoplanetary disks across the stellar mass range: no significant variations. *A&A*, 539:A9.

Nelson, A. F. and Marzari, F. (2016). Dynamics of Circumstellar Disks. III. The Case of GG Tau A. *ApJ*, 827(2):93.

Neugebauer, G., Beichman, C. A., Soifer, B. T., Aumann, H. H., Chester, T. J., Gautier, T. N., Gillett, F. C., Hauser, M. G., Houck, J. R., Lonsdale, C. J., Low, F. J., and Young, E. T. (1984). Early results from the Infrared Astronomical Satellite. *Science*, 224:14–21.

Ochsenbein, F., Bauer, P., and Marcout, J. (2000). The VizieR database of astronomical catalogues. *A&AS*, 143:23–32.

Offner, S. S. R., Lee, E. J., Goodman, A. A., and Arce, H. (2011). Radiation-hydrodynamic Simulations of Protostellar Outflows: Synthetic Observations and Data Comparisons. *ApJ*, 743(1):91.

Ohashi, N. (2004). Infall in Protostellar Envelopes. In Burton, M. G., Jayawardhana, R., and Bourke, T. L., editors, *Star Formation at High Angular Resolution*, volume 221 of *IAU Symposium*, page 75.

Okuzumi, S., Momose, M., Sirono, S.-i., Kobayashi, H., and Tanaka, H. (2016). Sintering-induced Dust Ring Formation in Protoplanetary Disks: Application to the HL Tau Disk. *ApJ*, 821(2):82.

Olguin, F. A. (2016). *The circumstellar matter distribution of massive young stellar objects*. PhD thesis, University of Leeds.

Olguin, F. A., Hoare, M. G., Wheelwright, H. E., Clay, S. J., de Wit, W. J., Rafiq, I., Pezzuto, S., and Molinari, S. (2015). Herschel Hi-GAL imaging of massive young stellar objects. *MNRAS*, 449(3):2784–2793.

Oudmaijer, R. D. and de Wit, W.-J. (2014). Star Formation at milli-arcsecond resolution. In *EAS Publications Series*, volume 69 of *EAS Publications Series*, pages 319–331.

Padgett, D. L., Brandner, W., Stapelfeldt, K. R., Strom, S. E., Terebey, S., and Koerner, D. (1999). HUBBLE SPACE TELESCOPE/NICMOS Imaging of Disks and Envelopes around Very Young Stars. *AJ*, 117(3):1490–1504.

Pandian, J. D., Momjian, E., Xu, Y., Menten, K. M., and Goldsmith, P. F. (2011). The Arecibo Methanol Maser Galactic Plane Survey. IV. Accurate Astrometry and Source Morphologies. *ApJ*, 730:55.

Parkin, E. R., Pittard, J. M., Hoare, M. G., Wright, N. J., and Drake, J. J. (2009). The interactions of winds from massive young stellar objects: X-ray emission, dynamics and cavity evolution. *MNRAS*, 400:629–645.

Perault, M., Omont, A., Simon, G., Seguin, P., Ojha, D., Blommaert, J., Felli, M., Gilmore, G., Guglielmo, F., Habing, H., Price, S., Robin, A., de Batz, B., Cesarsky, C., Elbaz, D., Epchtein, N., Fouque, P., Guest, S., Levine, D., Pollock, A., Prusti, T., Siebenmorgen, R., Testi, L., and Tiphene, D. (1996). First ISOCAM images of the Milky Way. *A&A*, 315:L165–L168.

Persson, S. E. and Campbell, B. (1987). Identification of New Young Stellar Objects Associated with IRAS Point Sources. I. The Southern Galactic Plane. *AJ*, 94:416.

Pinilla, P., Tazzari, M., Pascucci, I., Youdin, A. N., Garufi, A., Manara, C. F., Testi, L., van der Plas, G., Barenfeld, S. A., Canovas, H., Cox, E. G., Hendler, N. P., Pérez, L. M., and van der Marel, N. (2018). Homogeneous Analysis of the Dust Morphology of Transition Disks Observed with ALMA: Investigating Dust Trapping and the Origin of the Cavities. *ApJ*, 859(1):32.

Pinte, C., van der Plas, G., Menard, F., Price, D. J., Christiaens, V., Hill, T., Mentiplay, D., Ginski, C., Choquet, E., Boehler, Y., Duchene, G., Perez, S., and Casassus, S. (2019). Kinematic detection of a planet carving a gap in a protoplanetary disc. *arXiv e-prints*, page arXiv:1907.02538.

Poglitsch, A., Waelkens, C., Geis, N., Feuchtgruber, H., Vandenbussche, B., Rodriguez, L., Krause, O., Renotte, E., van Hoof, C., Saraceno, P., Cepa, J., Kerschbaum, F., Agnèse, P., Ali, B., Altieri, B., Andreani, P., Augueres, J. L., Balog, Z., Barl, L., Bauer, O. H., Belbachir, N., Benedettini, M., Billot, N., Boulade, O., Bischof, H., Blommaert, J., Callut, E., Cara, C., Cerulli, R., Cesarsky, D., Contursi, A., Creten, Y., De Meester, W., Doublier, V., Doumayrou, E., Duband , L., Exter, K., Genzel, R., Gillis, J. M., Grözinger, U., Henning, T., Herreros, J., Huygen, R., Inguscio, M., Jakob, G., Jamar, C., Jean, C., de Jong, J., Katterloher, R., Kiss, C., Klaas, U., Lemke, D., Lutz, D., Madden, S., Marquet, B., Martignac, J., Mazy, A., Merken, P., Montfort, F., Morbidelli, L., Müller, T., Nielbock, M., Okumura, K., Orfei, R., Ottensamer, R., Pezzuto, S., Popesso, P., Putzeys, J., Regibo, S., Reveret, V., Royer, P., Sauvage, M., Schreiber, J., Stegmaier, J., Schmitt, D., Schubert, J., Sturm, E., Thiel, M., Tofani, G., Vavrek, R., Wetzstein, M., Wieprecht, E., and Wiezorrek, E. (2010). The Photodetector Array Camera and Spectrometer (PACS) on the Herschel Space Observatory. *A&A*, 518:L2.

Pomohaci, R. (2017). *A near-infrared view of the evolution, environment and multiplicity of Massive Young Stellar Objects*. PhD thesis, University of Leeds.

Pomohaci, R., Oudmaijer, R. D., and Goodwin, S. P. (2019). A pilot survey of the binarity of Massive Young Stellar Objects with K-band adaptive optics. *MNRAS*, 484:226–238.

Porter, J. M., Drew, J. E., and Lumsden, S. L. (1998). Broad band infrared spectroscopy of massive young stellar objects. *A&A*, 332:999–1016.

Price, D. J., Cuello, N., Pinte, C., Mentiplay, D., Casassus, S., Christiaens, V., Kennedy, G. M., Cuadra, J., Sebastian Perez, M., Marino, S., Armitage, P. J., Zurlo, A., Juhasz, A., Ragusa, E., Laibe, G., and Lodato, G. (2018). Circumbinary, not transitional: on the spiral arms, cavity, shadows, fast radial flows, streamers, and horseshoe in the HD 142527 disc. *MNRAS*, 477(1):1270–1284.

Pudritz, R. E. and Norman, C. A. (1986). Bipolar Hydromagnetic Winds from Disks around Protostellar Objects. *ApJ*, 301:571.

Purser, S. J. D., Lumsden, S. L., Hoare, M. G., Urquhart, J. S., Cunningham, N., Purcell, C. R., Brooks, K. J., Garay, G., Gúzman, A. E., and Voronkov, M. A. (2016). A search for ionized jets towards massive young stellar objects. *MNRAS*, 460:1039–1053.

Rathborne, J. M., Jackson, J. M., and Simon, R. (2006). Infrared Dark Clouds: Precursors to Star Clusters. *ApJ*, 641:389–405.

Reipurth, B., Yu, K. C., Heathcote, S., Bally, J., and Rodríguez, L. F. (2000). Hubble Space Telescope NICMOS Images of Herbig-Haro Energy Sources: [Fe II] Jets, Binarity, and Envelope Cavities. *AJ*, 120(3):1449–1466.

Richardson, K. J., White, G. J., Gee, G., Griffin, M. J., Cunningham, C. T., Ade, P. A. R., and Avery, L. W. (1985). Submillimetre line and continuum observations of the S 255 molecular cloud. *MNRAS*, 216:713–733.

Rivera-Ingraham, A., Martin, P. G., Polychroni, D., Motte, F., Schneider, N., Bontemps, S., Hennemann, M., Men'shchikov, A., Nguyen Luong, Q., André, P.,

Arzoumanian, D., Bernard, J. P., Di Francesco, J., Elia, D., Fallscheer, C., Hill, T., Li, J. Z., Minier, V., Pezzuto, S., Roy, A., Rygl, K. L. J., Sadavoy, S. I., Spinoglio, L., White, G. J., and Wilson, C. D. (2013). Herschel Observations of the W3 GMC: Clues to the Formation of Clusters of High-mass Stars. *ApJ*, 766(2):85.

Robitaille, T. P. (2011). HYPERION: an open-source parallelized three-dimensional dust continuum radiative transfer code. *A&A*, 536:A79.

Robitaille, T. P. (2017). A modular set of synthetic spectral energy distributions for young stellar objects. *A&A*, 600:A11.

Robitaille, T. P., Meade, M. R., Babler, B. L., Whitney, B. A., Johnston, K. G., Indebetouw, R., Cohen, M., Povich, M. S., Sewilo, M., Benjamin, R. A., and Churchwell, E. (2008). Intrinsically Red Sources Observed by Spitzer in the Galactic Midplane. *AJ*, 136:2413–2440.

Robitaille, T. P., Whitney, B. A., Indebetouw, R., and Wood, K. (2007). Interpreting Spectral Energy Distributions from Young Stellar Objects. II. Fitting Observed SEDs Using a Large Grid of Precomputed Models. *ApJS*, 169:328–352.

Rosen, A. L., Krumholz, M. R., McKee, C. F., and Klein, R. I. (2016). An unstable truth: how massive stars get their mass. *MNRAS*, 463(3):2553–2573.

Rybicki, G. B. and Lightman, A. P. (1986). *Radiative Processes in Astrophysics*.

Salaris, M. and Cassisi, S. (2005). *Evolution of Stars and Stellar Populations*.

Sallum, S., Skemer, A., Eisner, J., van der Marel, N., Sheehan, P., Close, L., Ireland, M., Males, J., Morzinski, K., Bailey, V., Briguglio, R., and Puglisi, A. (2019). New Spatially Resolved Imaging of the SR 21 Transition Disk and Constraints on the Small-Grain Disk Geometry. *arXiv e-prints*, page arXiv:1908.07427.

Sana, H., de Mink, S. E., de Koter, A., Langer, N., Evans, C. J., Gieles, M., Gosset, E., Izzard, R. G., Le Bouquin, J. B., and Schneider, F. R. N. (2012). Binary Interaction Dominates the Evolution of Massive Stars. *Science*, 337(6093):444.

Sana, H., Ramírez-Tannus, M. C., de Koter, A., Kaper, L., Tramper, F., and Bik, A. (2017). A dearth of short-period massive binaries in the young massive star forming region M 17. Evidence for a large orbital separation at birth? *A&A*, 599:L9.

Sanna, A., Kölligan, A., Moscadelli, L., Kuiper, R., Cesaroni, R., Pillai, T., Menten, K. M., Zhang, Q., Caratti o Garatti, A., and Goddi, C. (2019). Discovery of a sub-Keplerian disk with jet around a 20 $M_{\odot}$ young star. ALMA observations of G023.01-00.41. *A&A*, 623:A77.

Schleicher, D. R. G., Sur, S., Banerjee, R., Klessen, R. S., Federrath, C., Arshakian, T., Beck, R., and Spaans, M. (2011). Magnetic fields during primordial star formation. *ArXiv e-prints*.

Schreyer, K., Helmich, F. P., van Dishoeck, E. F., and Henning, T. (1997). A molecular line and infrared study of NGC 2264 IRS 1. *A&A*, 326:347–365.

Schwartz, P. R., Thronson, H. A., J., Odenwald, S. F., Glaccum, W., Loewenstein, R. F., and Wolf, G. (1985). Active star formation in NGC 2264. *ApJ*, 292:231–237.

Shakura, N. I. and Sunyaev, R. A. (1973). Reprint of 1973A&A....24..337S. Black holes in binary systems. Observational appearance. *A&A*, 500:33–51.

Sheehan, P. D. and Eisner, J. A. (2018). Multiple Gaps in the Disk of the Class I Protostar GY 91. *ApJ*, 857:18.

Shepherd, D. S. and Churchwell, E. (1995). Bipolar Molecular Outflows from Massive Stars. In *American Astronomical Society Meeting Abstracts*, volume 27 of *Bulletin of the American Astronomical Society*, page 1318.

Shu, F. H. (1977). Self-similar collapse of isothermal spheres and star formation. *ApJ*, 214:488–497.

Simon, M., Peterson, D., Longmore, A., Storey, J., and Tokunaga, A. (1984). Lunar Occultation Observations of M8E-IR. In *BAAS*, volume 16, page 938.

Simpson, J. P., Burton, M. G., Colgan, S. W. J., Cotera, A. S., Erickson, E. F., Hines, D. C., and Whitney, B. A. (2009). Hubble Space Telescope NICMOS Polarization Observations of Three Edge-on Massive Young Stellar Objects. *ApJ*, 700(2):1488–1501.

Skrutskie, M. F., Cutri, R. M., Stiening, R., Weinberg, M. D., Schneider, S., Carpenter, J. M., Beichman, C., Capps, R., Chester, T., Elias, J., Huchra, J., Liebert, J., Lonsdale, C., Monet, D. G., Price, S., Seitzer, P., Jarrett, T., Kirkpatrick, J. D., Gizis, J. E., Howard, E., Evans, T., Fowler, J., Fullmer, L., Hurt, R., Light, R., Kopan, E. L., Marsh, K. A., McCallon, H. L., Tam, R., Van Dyk, S., and Wheelock, S. (2006). The Two Micron All Sky Survey (2MASS). *AJ*, 131(2):1163–1183.

Solomon, P. M., Edmunds, M. G., and Turner, B. E. (1980). Book-Review - Giant Molecular Clouds in the Galaxy. *Nature*, 287:176.

Sridharan, T. K., Beuther, H., Schilke, P., Menten, K. M., and Wyrowski, F. (2002). High-Mass Protostellar Candidates. I. The Sample and Initial Results. *ApJ*, 566:931–944.

Stamatellos, D., Whitworth, A. P., and Hubber, D. A. (2011). The Importance of Episodic Accretion for Low-mass Star Formation. *ApJ*, 730(1):32.

Stark, D. P., Whitney, B. A., Stassun, K. G., and Wood, K. (2002). Near-IR Model Images of Disks and Envelopes. In *American Astronomical Society Meeting Abstracts #200*, volume 200 of *American Astronomical Society Meeting Abstracts*, page 71.13.

Straizys, V. and Kuriliene, G. (1981). Fundamental stellar parameters derived from the evolutionary tracks. *Ap&SS*, 80:353–368.

Takahashi, S. Z. and Inutsuka, S.-i. (2016). An Origin of Multiple Ring Structure and Hidden Planets in HL Tau: A Unified Picture by Secular Gravitational Instability. *AJ*, 152(6):184.

Tan, J. C., Beltrán, M. T., Caselli, P., Fontani, F., Fuente, A., Krumholz, M. R., McKee, C. F., and Stolte, A. (2014). Massive Star Formation. In Beuther, H., Klessen, R. S., Dullemond, C. P., and Henning, T., editors, *Protostars and Planets VI*, page 149.

Tang, Y.-W., Guilloteau, S., Dutrey, A., Muto, T., Shen, B.-T., Gu, P.-G., Inutsuka, S.-i., Momose, M., Pietu, V., Fukagawa, M., Chapillon, E., Ho, P. T. P., di Folco, E., Corder, S., Ohashi, N., and Hashimoto, J. (2017). Planet Formation in AB Aurigae: Imaging of the Inner Gaseous Spirals Observed inside the Dust Cavity. *ApJ*, 840:32.

Terebey, S., Shu, F. H., and Cassen, P. (1984). The collapse of the cores of slowly rotating isothermal clouds. *ApJ*, 286:529–551.

Thompson, A. R., Moran, J. M., and Swenson, Jr., G. W. (2017). *Interferometry and Synthesis in Radio Astronomy, 3rd Edition*.

Thompson, R. I., Corbin, M. R., Young, E., and Schneider, G. (1998). NGC 2264 IRS: Evidence for Triggered Star Formation. *ApJ*, 492(2):L177–L179.

Thompson, R. I. and Tokunaga, A. T. (1978). Analysis of obscured infrared objects. II. Allen's infrared source in NGC 2264. *ApJ*, 226:119–123.

Thun, D., Kley, W., and Picogna, G. (2017). Circumbinary discs: Numerical and physical behaviour. *A&A*, 604:A102.

Tobin, J. J., Hartmann, L., Bergin, E., Chiang, H.-F., Looney, L. W., Chandler, C. J., Maret, S., and Heitsch, F. (2012). Complex Structure in Class 0 Protostellar Envelopes. III. Velocity Gradients in Non-axisymmetric Envelopes, Infall, or Rotation? *ApJ*, 748(1):16.

Tobin, J. J., Kratter, K. M., Persson, M. V., Looney, L. W., Dunham, M. M., Segura-Cox, D., Li, Z.-Y., Chandler, C. J., Sadavoy, S. I., Harris, R. J., Melis, C., and Pérez, L. M. (2016). A triple protostar system formed via fragmentation of a gravitationally unstable disk. *Nature*, 538(7626):483–486.

Tody, D. (1986). The IRAF Data Reduction and Analysis System. In Crawford, D. L., editor, *Proc. SPIE*, volume 627 of *Society of Photo-Optical Instrumentation Engineers (SPIE) Conference Series*, page 733.

Toomre, A. (1964). On the gravitational stability of a disk of stars. *ApJ*, 139:1217–1238.

Ubach, C., Maddison, S. T., Wright, C. M., Wilner, D. J., Lommen, D. J. P., and Koribalski, B. (2012). Grain growth signatures in the protoplanetary discs of Chamaeleon and Lupus. *MNRAS*, 425(4):3137–3161.

Ulrich, R. K. (1976). An infall model for the T Tauri phenomenon. *ApJ*, 210:377–391.

Urquhart, J. S., Busfield, A. L., Hoare, M. G., Lumsden, S. L., Clarke, A. J., Moore, T. J. T., Mottram, J. C., and Oudmaijer, R. D. (2007a). The RMS survey. Radio observations of candidate massive YSOs in the southern hemisphere. *A&A*, 461:11–23.

Urquhart, J. S., Busfield, A. L., Hoare, M. G., Lumsden, S. L., Oudmaijer, R. D., Moore, T. J. T., Gibb, A. G., Purcell, C. R., Burton, M. G., and Marechal, L. J. L. (2007b). The RMS survey. ^{13}CO observations of candidate massive YSOs in the southern Galactic plane. *A&A*, 474:891–901.

Urquhart, J. S., Busfield, A. L., Hoare, M. G., Lumsden, S. L., Oudmaijer, R. D., Moore, T. J. T., Gibb, A. G., Purcell, C. R., Burton, M. G., Maréchal, L. J. L., Jiang, Z., and Wang, M. (2008). The RMS survey. ^{13}CO observations of candidate massive YSOs in the northern Galactic plane. *A&A*, 487:253–264.

Urquhart, J. S., Figura, C. C., Moore, T. J. T., Hoare, M. G., Lumsden, S. L., Mottram, J. C., Thompson, M. A., and Oudmaijer, R. D. (2014a). The RMS survey: galactic distribution of massive star formation. *MNRAS*, 437:1791–1807.

Urquhart, J. S., Hoare, M. G., Lumsden, S. L., Oudmaijer, R. D., Moore, T. J. T., Mottram, J. C., Cooper, H. D. B., Mottram, M., and Rogers, H. C. (2012). The RMS survey: resolving kinematic distance ambiguities towards a sample of compact H ii regions using H i absorption*. *MNRAS*, 420:1656–1672.

Urquhart, J. S., Hoare, M. G., Purcell, C. R., Lumsden, S. L., Oudmaijer, R. D., Moore, T. J. T., Busfield, A. L., Mottram, J. C., and Davies, B. (2009). The RMS survey. 6 cm continuum VLA observations towards candidate massive YSOs in the northern hemisphere. *A&A*, 501:539–551.

Urquhart, J. S., Moore, T. J. T., Csengeri, T., Wyrowski, F., Schuller, F., Hoare, M. G., Lumsden, S. L., Mottram, J. C., Thompson, M. A., Menten, K. M., Walmsley, C. M., Bronfman, L., Pfalzner, S., König, C., and Wienen, M. (2014b). ATLASGAL - towards a complete sample of massive star forming clumps. *MNRAS*, 443(2):1555–1586.

Urquhart, J. S., Moore, T. J. T., Schuller, F., Wyrowski, F., Menten, K. M., Thompson, M. A., Csengeri, T., Walmsley, C. M., Bronfman, L., and König, C. (2013). ATLASGAL - environments of 6.7 GHz methanol masers. *MNRAS*, 431:1752–1776.

van der Marel, N., van Dishoeck, E. F., Bruderer, S., Andrews, S. M., Pontoppidan, K. M., Herczeg, G. J., van Kempen, T., and Miotello, A. (2016). Resolved gas cavities in transitional disks inferred from CO isotopologs with ALMA. *A&A*, 585:A58.

van der Marel, N., van Dishoeck, E. F., Bruderer, S., Pérez, L., and Isella, A. (2015). Gas density drops inside dust cavities of transitional disks around young stars observed with ALMA. *A&A*, 579:A106.

van der Marel, N., van Dishoeck, E. F., Bruderer, S., and van Kempen, T. A. (2014). Warm formaldehyde in the Ophiuchus IRS 48 transitional disk. *A&A*, 563:A113.

van der Marel, N., Williams, J. P., and Bruderer, S. (2018). Rings and Gaps in Protoplanetary Disks: Planets or Snowlines? *ApJ*, 867(1):L14.

van der Plas, G., Ménard, F., Canovas, H., Avenhaus, H., Casassus, S., Pinte, C., Caceres, C., and Cieza, L. (2017). An 80 au cavity in the disk around HD 34282. *A&A*, 607:A55.

van der Walt, D. J. (2011). On the periodic class II methanol masers in the high mass star forming region G9.62+0.20E. *Bulletin de la Societe Royale des Sciences de Liege*, 80:260–264.

Vehoff, S., Nürnberger, D. E. A., Hummel, C. A., and Duschl, W. J. (2008). VLTI / MIDI Observations of the Massive Protostellar Candidate NGC 3603 IRS 9A. In *Massive Star Formation: Observations Confront Theory*, volume 387, page 444.

Walder, R., Folini, D., and Meynet, G. (2012). Magnetic Fields in Massive Stars, Their Winds, and Their Nebulae. *Space Sci. Rev.*, 166(1-4):145–185.

Walsh, A. J. (2002). G305.20+0.21: A very young class II methanol maser source. In Migenes, V. and Reid, M. J., editors, *Cosmic Masers: From Proto-Stars to Black Holes*, volume 206 of *IAU Symposium*, page 155.

Walsh, A. J. and Burton, M. G. (2006). Mopra observations of G305.2+0.2: massive star formation at different evolutionary stages? *MNRAS*, 365:321–326.

Walsh, A. J., Chapman, J. F., Burton, M. G., Wardle, M., and Millar, T. J. (2007). Australia Telescope Compact Array 1.2-cm observations of the massive star-forming region G305.2+0.2. *MNRAS*, 380:1703–1714.

Walsh, C., Juhász, A., Meeus, G., Dent, W. R. F., Maud, L. T., Aikawa, Y., Millar, T. J., and Nomura, H. (2016). ALMA Reveals the Anatomy of the mm-sized Dust and Molecular Gas in the HD 97048 Disk. *ApJ*, 831:200.

Walsh, C., Juhász, A., Pinilla, P., Harsono, D., Mathews, G. S., Dent, W. R. F., Hogerheijde, M. R., Birnstiel, T., Meeus, G., Nomura, H., Aikawa, Y., Millar, T. J., and Sandell, G. (2014). ALMA Hints at the Presence of two Companions in the Disk around HD 100546. *ApJ*, 791:L6.

Wang, Y., Beuther, H., Bik, A., Vasyunina, T., Jiang, Z., Puga, E., Linz, H., Rodón, J. A., Henning, T., and Tamura, M. (2011). Different evolutionary stages in the massive star-forming region S255 complex. *A&A*, 527:A32.

Ward-Thompson, D. and Whitworth, A. P. (2015). *An Introduction to Star Formation*.

Ward-Thompson, D., Zylka, R., Mezger, P. G., and Sievers, A. W. (2000). Dust emission from star-forming regions. VI. The submillimetre YSO cluster in NGC 2264. *A&A*, 355:1122–1128.

Wenger, M., Ochsenbein, F., Egret, D., Dubois, P., Bonnarel, F., Borde, S., Genova, F., Jasniewicz, G., Laloë, S., Lesteven, S., and Monier, R. (2000). The SIMBAD astronomical database. The CDS reference database for astronomical objects. *A&AS*, 143:9–22.

Wheelwright, H. E., de Wit, W. J., Oudmaijer, R. D., Hoare, M. G., Lumsden, S. L., Fujiyoshi, T., and Close, J. L. (2012). Probing the envelopes of massive young stellar objects with diffraction limited mid-infrared imaging. *A&A*, 540:A89.

Whipple, F. L. (1972). On certain aerodynamic processes for asteroids and comets. In Elvius, A., editor, *From Plasma to Planet*, page 211.

White, R. L. (1979). Polarization in reflection nebulae. I. Scattering properties of interstellar grains. *ApJ*, 229:954–961.

Whitney, B. A. (2011). *Monte Carlo radiative transfer*, pages 151–176. World Scientific Publishing Co.

Whitney, B. A., Robitaille, T. P., Bjorkman, J. E., Dong, R., Wolff, M. J., Wood, K., and Honor, J. (2013). Three-dimensional Radiation Transfer in Young Stellar Objects. *ApJS*, 207:30.

Whitney, B. A. and Wolff, M. J. (2002). Scattering and Absorption by Aligned Grains in Circumstellar Environments. *ApJ*, 574:205–231.

Whitney, B. A., Wood, K., Bjorkman, J. E., and Wolff, M. J. (2003). Two-dimensional Radiative Transfer in Protostellar Envelopes. I. Effects of Geometry on Class I Sources. *ApJ*, 591:1049–1063.

Whittet, D. C. B., Bode, M. F., Longmore, A. J., Adamson, A. J., McFadzean, A. D., Aitken, D. K., and Roche, P. F. (1988). Infrared spectroscopy of dust in the Taurus dark clouds - Ice and silicates. *MNRAS*, 233:321–336.

Whittet, D. C. B., Gerakines, P. A., Hough, J. H., and Shenoy, S. S. (2001). Interstellar Extinction and Polarization in the Taurus Dark Clouds: The Optical Properties of Dust near the Diffuse/Dense Cloud Interface. *ApJ*, 547(2):872–884.

Williams, J. P., Blitz, L., and McKee, C. F. (2000). The Structure and Evolution of Molecular Clouds: from Clumps to Cores to the IMF. *Protostars and Planets IV*, page 97.

Williams, J. P. and Cieza, L. A. (2011). Protoplanetary Disks and Their Evolution. *ARA&A*, 49:67–117.

Wood, K., Wolff, M. J., Bjorkman, J. E., and Whitney, B. (2002). The Spectral Energy Distribution of HH 30 IRS: Constraining the Circumstellar Dust Size Distribution. *ApJ*, 564:887–895.

Wyatt, M. C. (2008). Evolution of Debris Disks. *ARA&A*, 46:339–383.

Yorke, H. W. and Sonnhalter, C. (2002). On the Formation of Massive Stars. *ApJ*, 569:846–862.

Yusef-Zadeh, F., Morris, M., and White, R. L. (1984). Bipolar reflection nebulae : Monte Carlo simulations. *ApJ*, 278:186–194.

Zacharias, N., Monet, D. G., Levine, S. E., Urban, S. E., Gaume, R., and Wycoff, G. L. (2004). The Naval Observatory Merged Astrometric Dataset (NOMAD). In *American Astronomical Society Meeting Abstracts*, volume 205, page 48.15.

Zhang, K., Blake, G. A., and Bergin, E. A. (2015). Evidence of Fast Pebble Growth Near Condensation Fronts in the HL Tau Protoplanetary Disk. *ApJ*, 806(1):L7.

Zhang, Y. and Tan, J. C. (2018). Radiation Transfer of Models of Massive Star Formation. IV. The Model Grid and Spectral Energy Distribution Fitting. *ApJ*, 853:18.

Zinchenko, I., Liu, S. Y., Su, Y. N., Kurtz, S., Ojha, D. K., Samal, M. R., and Ghosh, S. K. (2012). A Multi-wavelength High-resolution study of the S255 Star-forming Region: General Structure and Kinematics. *ApJ*, 755(2):177.

Zinchenko, I., Liu, S. Y., Su, Y. N., Salii, S. V., Sobolev, A. M., Zemlyanukha, P., Beuther, H., Ojha, D. K., Samal, M. R., and Wang, Y. (2015a). The Disk-outflow System in the S255IR Area of High-mass Star Formation. *ApJ*, 810(1):10.

Zinchenko, I., Liu, S. Y., Su, Y. N., Salii, S. V., Sobolev, A. M., Zemlyanukha, P., Beuther, H., Ojha, D. K., Samal, M. R., and Wang, Y. (2015b). The Disk-outflow System in the S255IR Area of High-mass Star Formation. *ApJ*, 810(1):10.

Zinchenko, I., Liu, S. Y., Su, Y. N., and Sobolev, A. M. (2017). Detection of a new methanol maser line with ALMA. *A&A*, 606:L6.

Zinnecker, H. (1982). Prediction of the protostellar mass spectrum in the Orion near-infrared cluster. *Annals of the New York Academy of Sciences*, 395:226–235.

Zinnecker, H. and Yorke, H. W. (2007). Toward Understanding Massive Star Formation. *Annual Review of Astronomy and Astrophysics*, 45:481–563.

Appendix A

VISIR images of MYSOs

A.1 Introduction

In Chapters 3 and 4, VISIR data was presented for two MYSOs studied throughout this thesis. This data was obtained as part of the successful proposal 097.C-0320(A) (PI: Frost) which obtained near-diffraction limited images of a number of MYSOs. A further proposal 095.C-0595(A) (PI: Oudmaijer) also obtained VISIR images for a number of MYSOs but prior to the instrument upgrade of VISIR (as described in Chapter 2). Within this proposal a number of other MYSOs were observed. In this appendix, the images and azimuthally averaged profiles for the remainder of the images obtained during these observing runs are presented.

Table A.1 Details of the observations

Source	Period	Date	Grade
AFGL 4716	P97	27-28/07/2016	A
V1028 Cen	P97	5-6/07/2016	A
V921 Sco	P97	14-15/07/2016	A
RCra	P95	18-19/07/2015	A
MWC 300	P95	26-27/07/2015	A
M17 SW IRS1	P95	19-20/07/2015	A
M17 UC1	P95	11-12/09/2015	B

Table A.2 FWHMs of the different sources.

Source	FWHM (")
AFGL 4716	0.690
V1028 Cen	0.498
V921 Sco	0.462
RCrA	0.646
MWC 300	0.438
M17 SW IRS1	0.468
M17 UC1	0.908

A.2 Observations

At the time of these observations VISIR was mounted on the Cassegrain focus of the UT3 at the VLT/I. The observations were taken using the Q3 filter (central wavelength of 19.5μm) and the observations were taken using the normal imaging mode. A new detector (a Raytheon 1024x1024 pixel Aquarius array) was introduced between P95 and P97 which improved the instrument's efficiency by a factor of six and increased its sensitivity [Käufl et al., 2015]. As such the P95 observations are less sensitive than those taken in P97. The exposure was 0.011s and time on target was 40-60mins per object for both the P95 and P97 observations. The VISIR images presented in Figure A.1 were reduced using ESO pipelines version 4.3.1. The field of view of the VISIR observations is around 30", but the images have been cropped to better illuminate their structure here. The profiles of the sources can be found in Figure A.2. Table A.1 provides further details on the observations.

A.3 Comments

These images of the circumstellar environments of the MYSOs show variation. Some are obviously extended, while some are more point-like and others (such as M17 UC1) show a large degree of complexity. These differences were similarly observed in the sample of Wheelwright et al. [2012]. Most of the sources display a close to

circular geometry and are mostly symmetric. They also appear as a single source within the field of view. Table A.2 lists the FWHMs of the sources.

AFGL 4176 has been previously studied by Johnston et al. [2015]. They find that the source has an inclination of 30° and a large disk ($12M_{\odot}$, 2000au in radius), which poses the question as to whether the extended nature of the source may be due to the presence of this large disk. Given the distance to the source of 4.2kpc [Boley et al., 2013] I conclude that the extended nature of the source is not due to this large disk, as this would only constitute ∼1" of the VISIR image and the outer regions would likely not be traced by this dataset. Upcoming work from the same authors notes the presence of a large tail of material to the north of the source (private communication) and this may contribute to the extension seen in the VISIR image presented here, although contributions from cavity material are almost definitely contributing given the findings of this thesis. V921 Sco and MWC 300 are uncertainly classified in the literature, with some studies postulating that they may in fact be Herbig Ae/Be sources. This may explain their smaller extent in comparison to the rest of the sample.

M17 UC1 displays multiple sources who are not very symmetric. This may be related to suspected high multiplicity fraction for this region as suggested by Sana et al. [2017] based on radial-velocity dispersion measurements and the consideration of the young age (1Myr) of the M17 region. From their work they conclude that binaries in the region are at large separations ($>100R_{\odot}$) and given that the two sources in the VISIR image of M17 UC1 are many arcseconds apart supports this. The complex structure observed in the sources in this image could also be a result of dynamical interactions between wide binary sources. However, another source from the region, M17 SW IRS1, is also presented in this appendix and does not show multiple sources, although it does show some asymmetry.

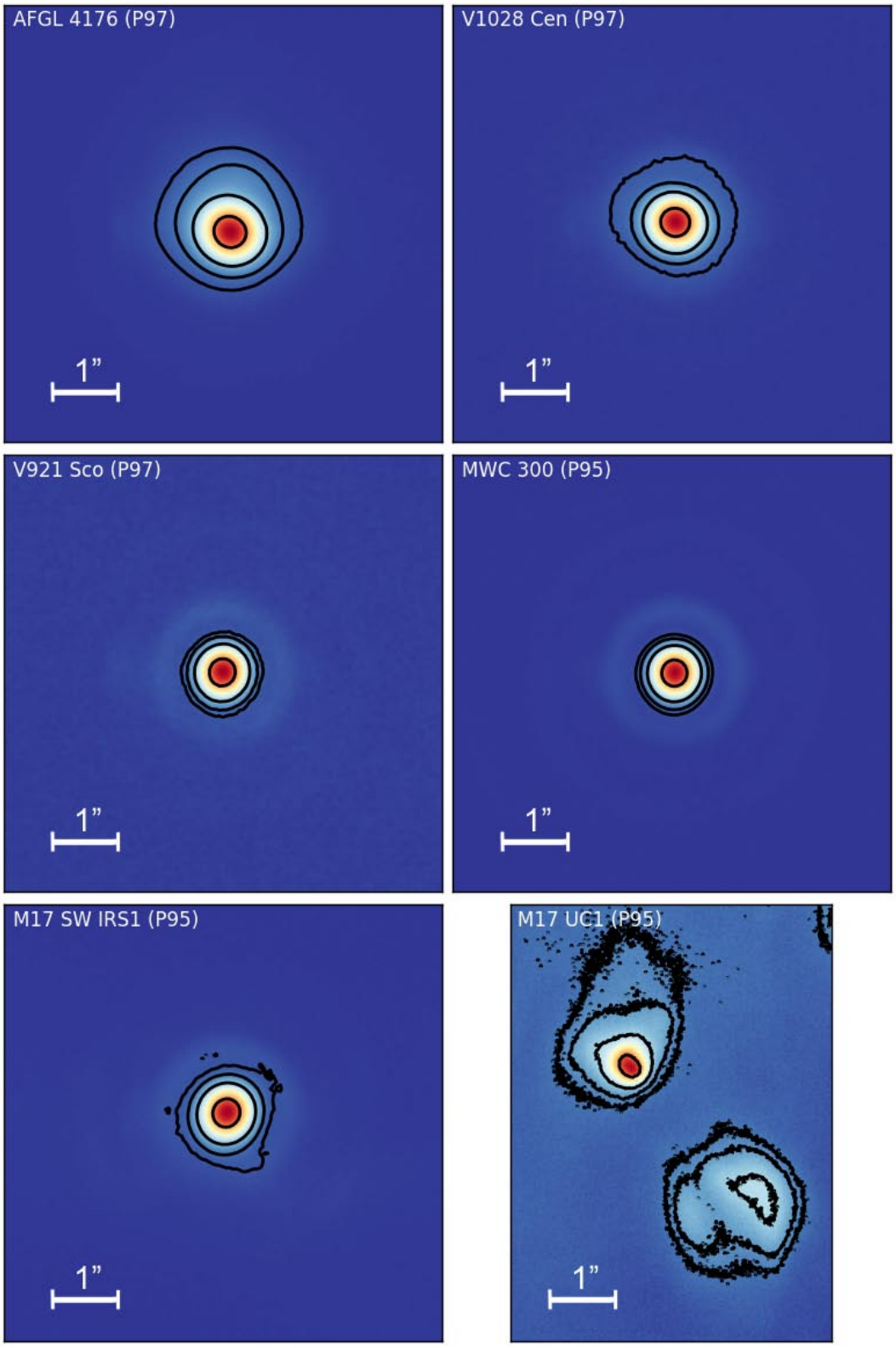

Fig. A.1 VISIR images at 19.5μm images of the sources from 097.C-0320(A) and 095.C-0595(A). The contours represent 5, 10, 15, 25 and 75% of the peak flux.

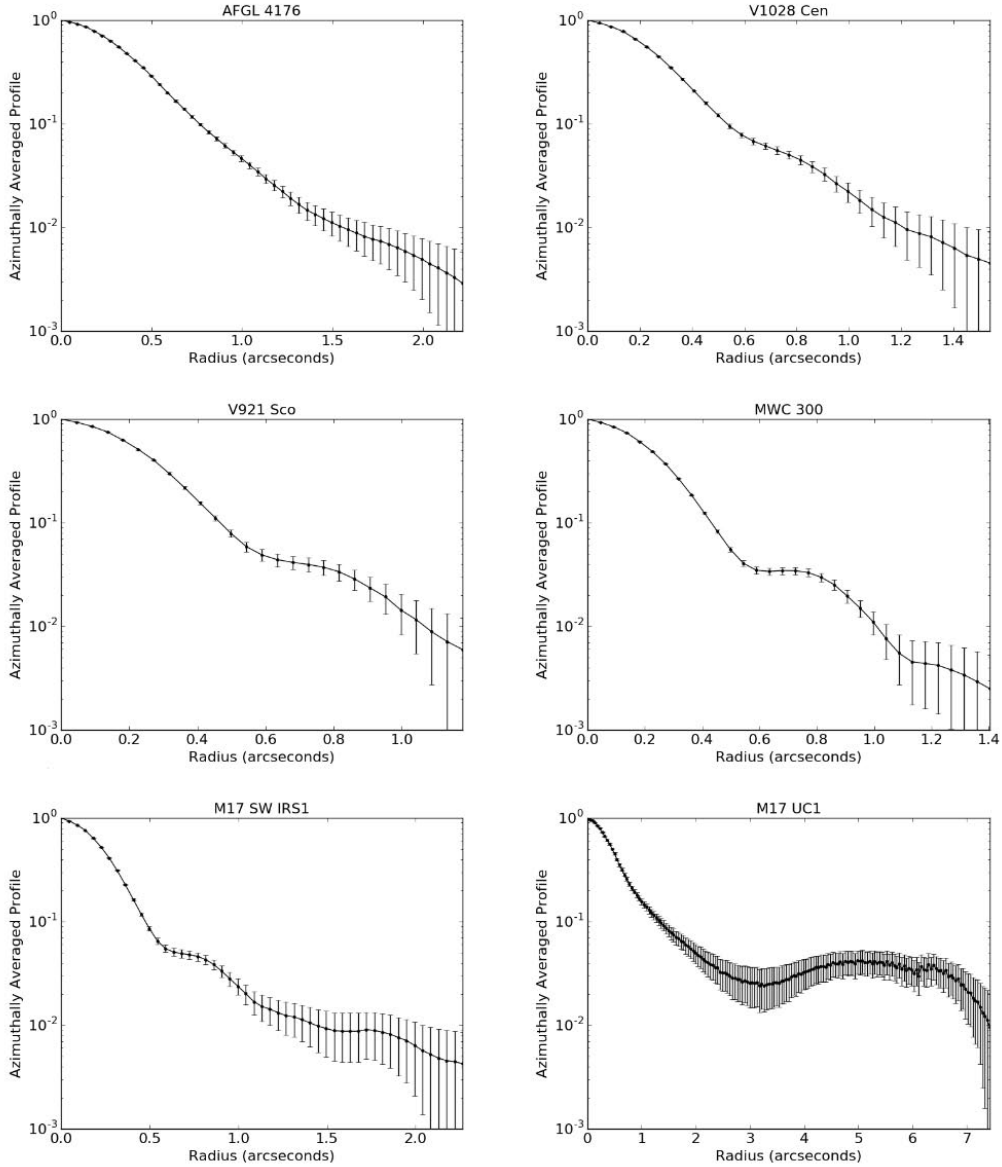

Fig. A.2 Azimuthally averaged profiles of the sources and PSF presented in Figure A.1.

Appendix B

Data tables

This appendix displays the SED data tables used in the fitting of the sample.

Table B.1 Fluxes available for use in the SED fitting of W33A

Origin	Wavelength (μm)	Flux (Jy)
2MASS	1.235	$(1.21\pm0.07)\times10^{-3}$
	1.66	$(5.37\pm0.3)\times10^{-3}$
	2.159	0.139±0.01
WISE	3.4	0.714±0.001
	4.6	20.8±3
	12	33.3±2
MSX	8	15.6±4
	12	23.2±5
	14	50.0±6
	21	144±6
IRAS	60	2230±500
MIPS	70	2137±6
SHARC	350	597±30
JCMT	850	40.5±0.11
SIMBA	1200	15.7±3

Table B.2 Fluxes available for use in the SED fitting of NGC 2264 IRS1

Origin	Wavelength (μm)	Flux (Jy)	Reference
2MASS	1.24	0.040±0.002	Skrutskie et al. [2006]
	1.66	0.898±0.03	
	2.16	7.15±0.04	
WISE	3.35	12.1±1	Cutri and et al. [2012]
	4.6	132	
	11.6	127±40	
	22	353±0.4	
MSX	8	91.4±4	Egan et al. [1998]
	12	119±6	
	14	148±9	
	21	13.7±14	
COMICS	24.5	330±33	de Wit et al. [2009]
KAO	53	980±5	Harvey et al. [1977b]
KAO	100	1645±82	
KAO	175	1530±77	
IRTF	350	188±7	Chini et al. [1986b]

Table B.3 Fluxes available for use in the SED fitting of S255 IRS3

Origin	Wavelength (μm)	Flux (Jy)	Reference
NICMOS	2	0.00283±0.0003	Simpson et al. [2009]
CIAO (Subaru)	2.2	0.010±0.0001	Itoh et al. [2001]
	3.75	2.38±0.002	
	4.70	13.1±0.013	
Michelle (Gemini)	7.9	79.5±0.7	Longmore et al. [2006]
	8.8	21.8±0.2	
	11.6	47.7±0.4	
	12.5	95.3±1	
UKIDSS	1.64	0.00865±0.0005	Lawrence et al. [2007]
	2.16	0.032±0.001	
ISACC	1.66	0.00237±0.004	Caratti o Garatti et al. [2017]
	2.16	0.0153±0.0002	
IRAC	3.6	2.62±0.01	Fazio et al. [2008]
	4.5	10.91±0.03	
	5.8	34.5±0.04	
	8.0	41.2±0.04	
AKARI/IRC	8.6	103±0.3	Ishihara et al. [2010]
	18.4	213±0.2	
AKARI	65	455±10	Caratti o Garatti et al. [2017]
	160	760±3	
PACS	70	1465±150	Poglitsch et al. [2010]
	160	849±80	
SHARC	350	118±9	Merello et al. [2015]
IRAM	850	0.5±0.07	Zinchenko et al. [2015b]
SMA	1050	0.45±0.06	Zinchenko et al. [2012]
SMA	1300	0.058±0.01	Zinchenko et al. [2015b]
2MASS	1.24	$(1.01\pm0.2)\times10^{-3}$	Skrutskie et al. [2006]
	1.66	$(6.46\pm1)\times10^{-3}$	
	2.16	$(5.06\pm0.5)\times10^{-2}$	
WISE	3.35	0.689±0.01	Cutri and et al. [2012]
	4.6	11.7±0.1	
	11.6	222±70	
	22	695±0.8	
MSX	8	55.0±2	Egan et al. [1998]
	12	104.0±5	
	14	154±9	
	21	213±10	
COMICS	24.5	163±20	de Wit et al. [2009]
UKIRT	350	230±9	Richardson et al. [1985]
	370	180±2	
	760	36±2	
	1070	17±1	
SCUBA	450	224±0.2	Di Francesco et al. [2008]
	850	22.0±0.02	
IRTF	350	190	Mezger et al. [1988]
	1300	3.3±0.8	Chini et al. [1986a]
	1300	7.5	Mezger et al. [1988]

Table B.4 Fluxes available for use in the SED fitting of IRAS 17216-3801

Origin	Wavelength (μm)	Flux (Jy)	Reference
2MASS J-Band	1.24	0.0134±0.0005	Skrutskie et al. [2006]
H-Band	1.66	0.666±0.04	
Ks-Band	2.16	6.73±0.1	
WISE	3.35	14.9±0.9	Cutri and et al. [2012]
	4.60	52.5±20	
	11.6	108±20	
	22.1	430±4	
MSX	4.29	29.6±3	Egan et al. [1998]
	4.35	50.1±5	
	8.28	78.1±3	
	12.1	145±7	
	14.7	190±10	
	21.34	299±20	
VISIR	19.5	245±10	This work
ATLASGAL	870	35.1±5	Urquhart et al. [2014b]
IRAS	12	148±7	Beichman [1988]
	25	410±20	
	60	1640±200	
	100	2820±400	

Table B.5 Fluxes available for use in the SED fitting of Mon R2 IRS2

Origin	Wavelength (μm)	Flux (Jy)	Reference
UKIDSS H-band	1.662	0.002 (2±0.006)$\times 10^{-3}$	Lawrence et al. [2007]
K-band	2.159	0.0771±0	
WISE	3.35	38.5±5	Cutri and et al. [2012]
	4.60	101±15	
	11.6	281±30	
	22.1	4935.874 (upper limit)	
COMICS	24.5	40±4	de Wit et al. [2009]
MRT	870	3070±122	Henning et al. [1992]
	1300	2640±37	

Table B.6 Fluxes available for use in the SED fitting of M8EIR (1)

Origin	Wavelength (μm)	Flux (Jy)	Reference
2MASS J-Band	1.24	$(3.05\pm0.008)\times10^{-3}$	Skrutskie et al. [2006]
H-Band	1.66	2.62±0.1	
Ks-Band	2.16	11.6±0.4 (poor quality (E flag))	
MSX	4.29	50.7±5	Egan et al. [1998]
	4.35	57.6±6	
	8.28	75.0±7	
	12.1	104±10	
	14.7	133±10	
	21.34	191±10	
COMICS	24.5	210±20	de Wit et al. [2009]
IRTF	1.24	$(6.7\pm0.07)\times10^{-2}$	Simon et al. [1984]
	1.66	0.83±0.008	
	2.16	5.7±0.06	
SHARC	12	119±7	Mueller et al. [2002]
IRAS	25	289±20	
	60	1611±200	
	100	2783±700	
FCRAO	350	210±42	Kastner et al. [1992]
	450	42.4±15	
	850	9.14±1	
SEST	1200	7.36	Beltrán et al. [2006]
MRT	870	2.79±0.1	Guertler et al. [1991]
SEST	1300	1.85±0.02	

Table B.7 Fluxes available for use in the SED fitting of M8EIR (2)

Origin	Wavelength (μm)	Flux (Jy)	Reference
ISO SWS	16.4	232±70	Feldt et al. [2008]
ISO LWS	2.34	11.0±2	
	2.50	12.3±2	
	2.62	15.1±3	
	2.74	16.2±3	
	2.90	14.3±3	
	2.94	17.3±3	
	2.97	18.8±4	
	3.11	22.1±4	
	3.29	24.5±5	
	3.48	29.1±6	
	3.69	33.8±7	
	3.86	36.2±7	
	4.09	43.0±9	
	4.18	47.2±9	
	4.19	51.8±10	
	4.43	49.9±10	
	4.69	54.1±11	
	5.03	60.7±12	
	5.38	68.1±13	
	6.11	73.8±15	
	6.39	77.2±15	
	6.69	84.7±17	
	7.09	71.2±14	
	7.34	75.4±15	
	7.68	82.7±17	
	8.13	76.2±15	
	8.42	70.3±14	
	8.72	61.9±12	
	8.92	56.4±11	
	9.13	51.5±10	
	9.45	50.9±10	
	9.78	50.3±10	
	10.0	56.4±11	
	10.5	66.3±13	
	10.8	70.2±14	
	11.5	81.5±16	
	11.7	89.4±18	
	11.9	134±27	
	12.4	140±28	
	13.3	143±29	
	13.9	147±29	
	14.9	153±31	
	15.8	155±31	
	16.9	162±32	
	18.1	182±36	
	19.0	200±40	

Table B.8 Fluxes available for use in the SED fitting of M8EIR (3)

Origin	Wavelength (μm)	Flux (Jy)	Reference
ISO LWS	20.1	227±45	Feldt et al. [2008]
	21.5	260±52	
	22.8	295±59	
	24.7	343±69	
	26.5	367±73	
	28.7	398±80	
	31.1	431±86	
	33.7	500±100	
	36.5	555±100	
	39.5	615±100	
	40.9	637±100	
	43.3	690±100	
	41.3	889±200	
	43.8	963±200	
	46.4	1120±200	
	51.4	1300±200	
	57.6	1670±300	
	54.4	1510±300	
	48.0	1210±200	
	61.0	1900±400	
	65.4	2030±400	
	70.8	2300±500	
	75.0	2440±500	
	78.5	2560±500	
	85.1	2770±600	
	89.0	2700±500	
	96.5	2800±600	
	105	2900±600	
	111	2930±600	
	117	2830±600	
	125.6	2764±600	
	127	2610±500	
	136	2610±500	
	143	2550±500	
	147	2400±500	
	154	2240±400	
	167	22670±500	
	177	2190±400	
	179	1970±400	
	184	1720±300	

Table B.9 Fluxes available for use in the SED fitting of AFGL 2136

Origin	Wavelength (μm)	Flux (Jy)	Reference
2MASS J-Band	1.24	1.59×10^{-3}	Skrutskie et al. [2006]
H-Band	1.66	$(8.52\pm0.01)\times10^{-2}$	
Ks-Band	2.16	0.123 ± 0.001	
WISE	3.35	8.6 ± 1	Cutri and et al. [2012]
	4.6	123	
	11.6	148 ± 40	
	22	644 ± 1	
MSX	8	127 ± 5	Egan et al. [1998]
	12	166 ± 8	
	14	270 ± 20	
	21	444 ± 30	
COMICS	24.5	140 ± 10	de Wit et al. [2009]
IRAS	60	4810 ± 900	Beichman [1988]
	100	5700 ± 1000	
SHARC	350	240 ± 50	Mueller et al. [2002]
	450	72.7 ± 6	
	800	6.66 ± 0.15	Kastner et al. [1992]
	1100	2.35 ± 0.09	